

Proceedings of
2019 9th International Conference on Bioscience,
Biochemistry and Bioinformatics

ICBBB 2019

Singapore

January 7-9, 2019

ISBN: 978-1-4503-6654-0

The Association for Computing Machinery
2 Penn Plaza, Suite 701
New York New York 10121-0701



ACM ISBN: 978-1-4503-6654-0

ACM COPYRIGHT NOTICE. Copyright © 2019 by the Association for Computing Machinery, Inc. Permission to make digital or hard copies of part or all of this work for personal or classroom use is granted without fee provided that copies are not made or distributed for profit or commercial advantage and that copies bear this notice and the full citation on the first page. Copyrights for components of this work owned by others than ACM must be honored. Abstracting with credit is permitted. To copy otherwise, to republish, to post on servers, or to redistribute to lists, requires prior specific permission and/or a fee. Request permissions from Publications Dept., ACM, Inc., fax +1 (212) 869-0481, or permissions@acm.org.

For other copying of articles that carry a code at the bottom of the first or last page, copying is permitted provided that the per-copy fee indicated in the code is paid through the Copyright Clearance Center, 222 Rosewood Drive, Danvers, MA 01923, +1-978-750-8400, +1-978-750-4470 (fax).

Table of Contents

Proceedings of 2019 9th International Conference on Bioscience, Biochemistry and Bioinformatics (ICBBB 2019)

Preface.....	V
Conference Committees.....	VI

• ***Session 1- Biomedical Imaging and Image Processing***

An Unsupervised Learning with Feature Approach for Brain Tumor Segmentation Using Magnetic Resonance Imaging	1
<i>Khurram Ejaz, Mohd Shafy Mohd Rahim, Usama Ijaz Bajwa, Nadim Rana and Amjad Rehman</i>	
Bessel-Gauss Beam Light Sheet Assisted Fluorescence Imaging of Trabecular Meshwork in the Iridocorneal Region Using Long Working Distance Objectives	8
<i>C. S. Suchand Sandeep, Sarangapani Sreelatha, Mani Baskaran, Xun Jie Jeessmond Hong, Tin Aung and Vadakke Matham Murukeshan</i>	
Semantic Segmentation of Colon Gland with Conditional Generative Adversarial Network	12
<i>Liye Mei, Xiaopeng Guo and Chaowei Cheng</i>	
Image Processing, Textural Feature Extraction and Transfer Learning based detection of Diabetic Retinopathy	17
<i>Anjana Umopathy, Anusha Sreenivasan, Divya S. Nairy, S Natarajan and B Narasinga Rao</i>	

• ***Session 2- Bioinformatics and Biosignal Analysis***

Establishment of an Integrated Computational Workflow for Single Cell RNA-Seq Dataset	22
<i>Miaomiao Jiang, Qichao Yu, Jianming Xie and Shiping Liu</i>	
An Interactive Gameplay to Crowdsourcing Multiple Sequence Alignment of Genome Sequences: Genenigma	28
<i>D. A. Meedeniya, S. A. P. A. Rukshan and A. Welivita</i>	
A Hybrid Approach to Optimize the Number of Recombinations in Ancestral Recombination Graphs	36
<i>Nguyen Thi Phuong Thao and Le Sy Vinh</i>	
CNN-SVR for CRISPR-Cpf1 Guide RNA Activity Prediction with Data Augmentation	43
<i>Guishan Zhang and Xianhua Dai</i>	
Extraction of Respiration from PPG Signals Using Hilbert Vibration Decomposition	48
<i>Hemant Sharma</i>	

• ***Session 3- Biological Systems Modeling and Simulation***

Calcium Signaling and Finite Element Technique	53
<i>Devanshi D. Dave and Brajesh Kumar Jha</i>	

A Fractional Mathematical Model to Study the Effect of Buffer on Calcium Distribution in Parkinson's Disease	58
<i>Hardik Joshi and Brajesh Kumar Jha</i>	
Computational Modelling of Calcium Buffering in a Star Shaped Astrocyte	63
<i>Amrita Jha and Brajesh Kumar Jha</i>	
Stability of Mitotic Spindle Using Computational Mechanics	67
<i>Andrii Iakovliev, Srinandan Dasmahapatra and Atul Bhaskar</i>	
• Session 4- Bioscience and Biotechnology	
Research on Response Surface Optimization of Culture Medium for Antibacterial Substances Produced by <i>Bacillus Amyloliquefaciens</i> GN59	75
<i>Liu Yaping, Zhao Bo, Emiliya Kalamiyets, Wu Peng and Chu Jie</i>	
Effect of Brewing Time and Temperature of <i>Centella Asiatica</i> Tea on Antioxidant Activity and Consumer Acceptance	82
<i>Rungnattakan Ploenkutham, Preeyapa Sripromma, Suksan Amornraksa, Patchanee Yasurin, Malinee Sriariyanun, Suvaluk Asavasanti and Aussama Soontrunnarudrungsri</i>	
β -Cyclodextrin Inclusion Complex with Dimethyl[4-hydroxypiperidin-4-yl]Phosphonates as Green Plant Growth Stimulators	86
<i>A. Ye. Malmakova, V. K. Yu, N. U. Kystaubayeva, A. G. Zazybin and T. E. Li</i>	
Antimicrobial Activity of Lichens-Associated Actinomycetes Strain LC-23	91
<i>Agustina E. Susanti, Shanti Ratnakomala, W. Mangunwardoyo and Puspita Lisdiyanti</i>	
Comparative Studies Between Hydrothermal Carbonation and Torrefaction for Biofuel Production from Poultry Litter	97
<i>Rafail Isemin, Aleksandr Mikhalev, Oleg Milovanov, Dmitry Klimov, Natalia Muratova, Kristina Krysanova, Yuri Teplitskii, Anatolii Greben'kov and Vadim Kogh-Tatarenko</i>	
• Session 5- Statistical Ecology	
Ecological Informatics Approach to Analyze Habitat Preferences of <i>Auricularia delicata</i> in Bingungan Forest, Turgo Natural Forest Conservation Area	102
<i>Dwiki Prasetya and Tien Aminatun</i>	
Author Index	109

ICBBB 2019

Biomedical Imaging and Image Processing

An Unsupervised Learning with Feature Approach for Brain Tumor Segmentation Using Magnetic Resonance Imaging

Khurram Ejaz
Faculty of Computing, UTM
Johor Bahru
Malaysia
kejaz2@live.utm.my

Mohd Shafy Mohd Rahim
Faculty of Computing, UTM
Johor Bahru
Malaysia
shafry@utm.my

Usama Ijaz Bajwa
Computer Science department,
COMSATS University Islamabad
Lahore Campus, Pakistan
usamabajwa@ciitlahore.edu.pk

Nadim Rana
Faculty of CCIS, Jazzan University
Jazzan, Saudi Arabia
nadimrana@jazanu.edu.sa

Amjad Rehman
Faculty of CCIS
Al Yamama University, Riyadh, Saudi Arabia
a_khane@yu.edu.sa

ABSTRACT

Segmentation methods are so much efficient to segment complex tumor from challenging datasets. MACCAI BRATS 2013-2017 brain tumor dataset (FLAIR, T2) had been taken for high grade glioma (HGG). This data set is challenging to segment tumor due to homogenous intensity and difficult to separate tumor boundary from other normal tissues, so our goal is to segment tumor from mixed intensities. It can be accomplished step by step. Therefore image maximum and minimum intensities has been adjusted because need to highlight the tumor portion then thresholding perform to localize the tumor region, has applied statistical features(kurtosis, skewness, mean and variance) so tumor portion become more visualize but can't separate tumor from boundary and then apply unsupervised clusters like kmean but it gives hard crisp membership and many tumor membership missed so texture features(Correlation, energy, homogeneity and contrast) with combination of Gabor filter has been applied but dimension of data increase and intensities became disturb due high dimension operation over MRI. Tumor boundary become more visualize if combine FLAIR over T2 sequence image then we apply FCM and result is: tumor boundaries become more visualized then applied one statistical feature (Kurtosis) and one texture feature(Energy) so tumor portion separate from other tissue and better segmentation accuracy have been checked with comparison parameters like dice overlap and Jaccard index.

CCS Concepts

Applied computing → Life and medical sciences → Computational biology → Imaging

Keywords

SOM-FKM; Magnetic Resonance Imaging (MRI); Texture

Permission to make digital or hard copies of all or part of this work for personal or classroom use is granted without fee provided that copies are not made or distributed for profit or commercial advantage and that copies bear this notice and the full citation on the first page. Copyrights for components of this work owned by others than ACM must be honored. Abstracting with credit is permitted. To copy otherwise, or republish, to post on servers or to redistribute to lists, requires prior specific permission and/or a fee. Request permissions from Permissions@acm.org.

ICBBB '19, January 7–9, 2019, Singapore, Singapore

© 2019 Association for Computing Machinery.

ACM ISBN 978-1-4503-6654-0/19/01...\$15.00

DOI: <https://doi.org/10.1145/3314367.3314384>

features, statistical features, Kmean, FCM. Dice index (DOI), Jaccard Index(JI)

1. INTRODUCTION

Images are composing of voxel of pixels, it has been seen in field of image processing. Segmentation is one of performance-oriented technique to segment within boundary or detect edge in image and its application also exhibits in medical imaging like MRI, CT scan to segment region of interest.

Magnetic Resonance Imaging (MRI) gives important information inside human body like brain and other organ which are scanned by doctor using MRI machine, abnormalities are investigated for treatment. These machines have scanner and capture image intensities, normally they get variation therefore MRI resultant image possess intensity biasness and machine creates image which consists of more homogenous pattern and organ become hide, therefore we need to handle intensity distribution to see our region of interest.

MRI sequences are T1, T1CE, T2, FLAIR (Fluid attenuated inversion recovery). T1 weighted depict white matter (as inner) and grey matter (as outer) tissues region whereas t2 weighted images are more contrast or darker image and their boundaries are clearer with darkness. T2 and FLAIR images have been segmented in this paper.

Features plays important role for identification of variability among different shapes, they work with combination of un supervised clustering techniques to give better segmentation results for detection of brain tumor.

The organization of this paper is as, section number 2 is consisting of related work which give very clear picture, section number 3 is pertaining material which have taken from BRATS MACCAI 2017-2013 brain tumor dataset. Section number four reflects methodology of our work, section number 5 'RESULT AND Discussion's analysis portion of this work and last portion is conclusion and future work.

2. RELATED WORK

The identification of tumor tissue in MRI of brain has been possible with segmentation methods like automatic segmentation [21]-[26]. It is important to see the tumor portion in those images which is clearer like in MACCAI BRATS brain tumor dataset and for verification point of view they have been cross check with already available tagged data. Therefore, this work has been

divided into four streams, first to check either brain tumor MRI image skull has been already stripped? So, this part is for preprocessing. Second thing is to check also for preprocessing which technique is better for enhancement of dataset. For segmentation which is next step. Clustering is one of best unsupervised technique for segmentation technique of brain tumor [1] 'a benchmark', used SOM-FKM for segmentation purpose. Third step is to check the most coherent features to FKM-SOM for tumor segmentation purpose and last thing is evaluation of results. In following paragraphs, we will check them one by one.

It is important to understand which preprocessing (enhancement of MRI) required for our experiment dataset (MACCAI BRAIN TUMOR DATASET), for brain generally three preprocessing practice, one is skull removal second is denoising and third one is intensity normalization. For this dataset skull is already removed or stripped by ITK, it is a skull removal filter. ITK (insight segmentation registration toolkit) is firstly register with atlas image then brain mask has been erode and present as refined brain, brain has been extracted with level set. Level set evolve towards brain edges dedicatedly [2].

Intensity distribution is required for image correction. If MRI imaging have been acquisition for same patient image with same MRI scanner then check other patients with same scanner, discrepancy exist therefore no standard tool available for segmentation to check intensity range so we have applied Intensity normalization is best for MACCAI brain tumor dataset [3]. Sampling performed with nearest neighbor pixels interpolation, all 2mm isotropic resolution has been compared with ground truth 1mm resolution therefore intensities are sampled [4]. Different algorithms have been checked over Brats MACCAI brain tumor glioma dataset and limitation remain due to variability if tumor shape and intensity biasness. Therefore, with such dataset we need to cope with biased intensities so conclusively we need this dataset and preprocessing by using intensity normalization.

Focusing [1] a benchmark dataset, the best automatic technique for segmentation is basically FKM and FKM is hybrid with SOM. For accurate segmentation, it is important to target the features which are closer to segmentation like FKM and SOM. One feature is consisting of ten to thousands of variables of data which are related to other variable [6]. Feature is like structure of object which directs region of interest of brain tumor. Different kind of features exist like texture features, statistical feature and histogram features. Therefore, need of time is to explore those features which are nearer to brain tumor segmentation. Problem occurs when segmentation of image is performed with texture, so problem has been resolved using unsupervised method Fuzzy c mean. Features are mean, variance, third and fourth ordered moments [7]. Texture analysis has been performed for segmentation and checked one nearer feature is homogeneity which help to find out region of interest in image [8]. Texture features like Horlick thirteen features (angular momentum, contrast, correlation, variance, entropy, inverse difference moment, sum average, sum variance, entropy information, measure of correlation, max correlation coefficient, inertia, cluster shade, cluster prominence, local homogeneity, and energy) and these features are called over Grey level co-occurrence matrix (GLCM) [9]. The features which are statistical, texture, histogram gradient features over MRI they are coherent if apply unsupervised technique for segmentation of brain tumor. K mean cluster gives segmentation without miss cluster region due to hard clustering, but their membership is low [10]. K mean sometimes as hard

crisp cluster, fuzzy or soft clustering in which feature vector X has degree of membership in each cluster. At first step it guesses the mean from $m_1, m_2, m_3 \dots m_k$ the from estimated mean to find out degree of membership [11]. Kmean is not suitable due to hard clustering. FCM need large CPU times computation. FCM clustering with kohonen mean cluster overlap grayscale intensity and not clearly boarder between tissues successfully. FCM is sensitive for noise but FKM improves segmentation degradation when noise corrupt the image. Statistical features like histogram features and gradient based parameters. Histogram is computed without considering spatial relationship. Histogram features are mean, variance, skewness and kurtosis [12]. Statistical features are better for detection of region of interest (brain tumor) than Gabor texture feature because of they consume low space than Gabor which have high dimension [13].

Un supervised clustering technique for segmentation of brain tumor they never work good if work individually or performance degrades. Like If we have used Self Optimization mapping (SOM) then overhead occurs but if combine with some unsupervised clustering technique so performance increase. SOM is initially assigned weights then train data, after training best match unit node has been selected to draw radius around central nodes but this method is more computation with minimum accuracy [14]. The drawback of SOM is that competitive neural layer become equal to desire regions. It is possible to determine correct number of regions of detected tumor [15] so it is limitation of conventional SOM but with FCM a fuzzy partitioning technique which check member of tumor in multiple cluster of datasets and give better segmentation. Hybrid SOM-FKM gives accurate segmentation with evaluation parameters like Jaccard index, DOI, sensitivity, specificity, recall, precision [16]. [19] SOM-FKM gives better segmentation whereas SOM reduce dimension and FKM gives maximum membership for segmentation, but tumor segmentation has not discussed. FCM and KMean both are combine to achieve better results of segmentation but m_k memberships can be missed [20]. Clustered have been calculated then correct intensity to find out tumor region then joint label fused for accurate segmentation of tumor performed [21].

From all above issue it have been observed that hybrid SOM-FKM and other segmentation techniques gives better accurate segmentation with comparison parameters but problem still remains in region of interest where mixed intensities occurs as mentioned in bench mark paper [1].

3. MATERIAL

For experimentation, dataset which has been used it is Brats 2013-2017 MACCAI brain tumor dataset. This is published dataset which have been used by different researchers across the world. For detection of tumor, the dataset is consisting of low grades glioma as well as high grade glioma. Dataset pertains 285 MRI patients known as volume. Their naming convention is like BRATS 17-2013-8-1. This dataset is consisting of images from year 2013 to 2017. In dataset 210 patients are high grades glioma whereas 75 are low grade glioma. MRI images sequences are Flair, T1, T1CE, T2. Mostly images in this dataset are axial orientation where some of orientations are sagittal and coronal. Total number of HGG are $210 * 155 * 4 = 130200$ whereas low grade glioma are $75 * 155 * 4 = 46500$. Tagged images are already segmented images, they have been used to check already given segmentation with already selected sequence. For every sequence one tagged image is available for test or validate the result of segmentation. Dataset is publically available for experiments [5].

Table 1 is a list of HGG and LGG images of 285 patients, for every patient tagged segmented images available for test so 285 tagged images are available. Figure 1 is axil orientation (FLAIR) image for volume number 2, in Figure 2 that FLAIR image have been normalized with adjusted intensity from normalization purpose to segment region of interest. Figure 3 for T2 sequence image and in Figure 4 it has been normalized to separate tumor tissues from normal tissues and Figure 5 is available tagged tumor for testing.

Table 1. MACCAI BRATS 2017-2013 dataset

Types of folder	patients x sequences x slices)	Total Number of images
HGG	210x4x155(patients x sequences x slices)	130200
LGG	75x4x155(patients x sequences x slices)	46500
Tagged (already segmented)	285 x1 x 155 (patients x sequences x slices))	44175
Subtotal (Validation)	46x1x155(patients x sequences x slices))	28520
Grand total		220875

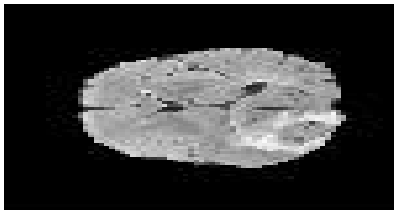


Figure 1. Flair (Brats17_2013_2_1)

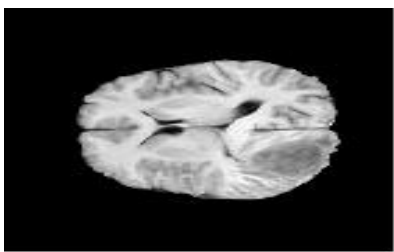


Figure 2. T1(Brats17_2013_2_1)

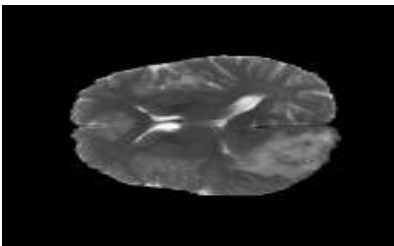


Figure 3. T2(Brats17_2013_2_1)

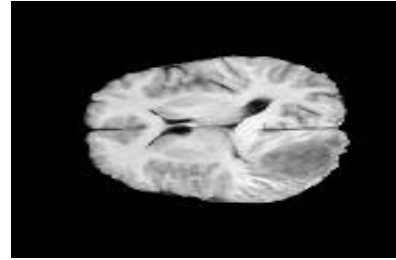


Figure 4. (T1CE(Brats17_2013_2_1))

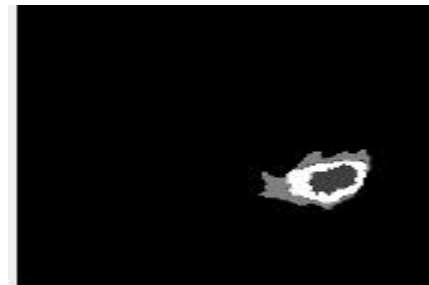


Figure 5. Tagged image (Brats17_2013_2_1)

4. METHODOLOGY

Figure 14 is a frame work diagram. Unsupervised clustering techniques have been checked across features to get good segmentation results of segmentation over BRATS MACCAI brain tumor dataset over T2 and Flair images. We have selected slice number 75th because layer of tumor boundary is roughly visible from rest of 155 slices. Ten more close slices of tumor have been checked. Firstly, input image is converted greyscale using mat2gray function. Intensities have been adjusted to max and min pixel values of image so that tumor portion can be prominent. We have three cases and in third case, better segmentation has been achieved. At first case, for localization of tumor adjusted image have been thresholded so that region of interest can be seen. Over thresholder region statistical features (mean, variance, skewness, kurtosis) are applied, tumor become highlight but couldn't separate from other brain tissues then in second case Kmean has been applied but due to hard crisp many memberships of tumor region are missed. In another case two texture features after GLCM with combination of Gabor filter applied but dimension of image become higher and more complex. At last segmentation with good result achieve when from adjusted intensities we have applied FCM. We have concatenate flair image intensities with T2, T2 is darker whereas flair is light so tumor boundaries become more visible then we have applied FCM with different class of intensities and tumor is segmented with intensity of 0.1. Before FCM statistical feature kurtosis has been applied and after FCM segmentation texture feature Energy is applied so tumor has been segmented.

Segmentation for Flair image: -

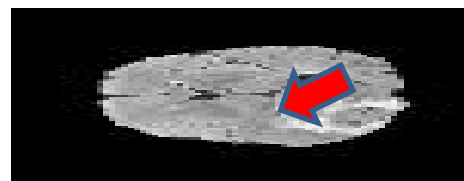


Figure 6. Original flair image 75 number slice

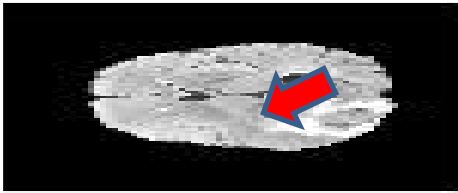


Figure 7. Intensity Normalize

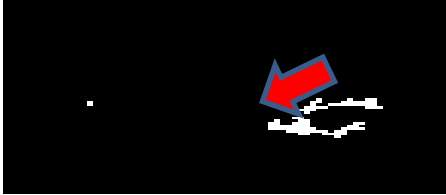


Figure 8. Binary Tumor Segmented Image

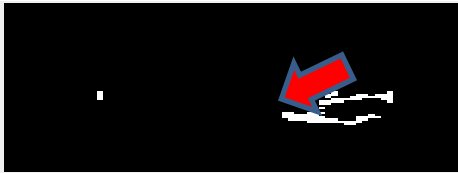


Figure 9. With Homogeneity feature of texture detection of Tumor

Two cases are important to see for contributed segmentation. Figure 6 is Flair orientation image and its intensity has been adjusted in Figure 7 then in Figure 8 we can see using thresholding tumor boundary has been segmented. In Figure 9 we can see clearly that after applying homogeneity a texture feature tumor boundaries become more prominent. During our experiment over Figure 6 we have noted, original Flair image is given Contrast and variance feature values over flair images are very low over for tumor segmentation whereas Kurtosis feature very high.

Segmentation for T2 number of slice for same patient as same slice of Flair: -

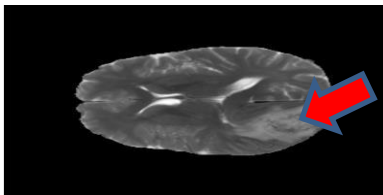


Figure 10. T2 sequence

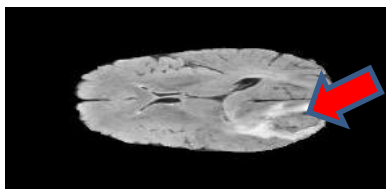


Figure 11. Contrast

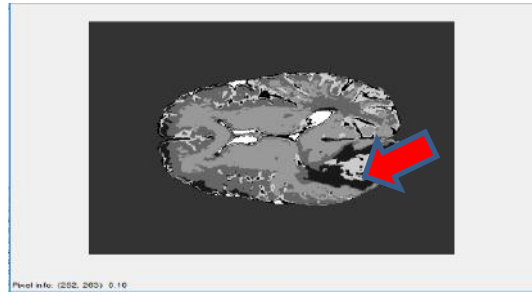


Figure 12. Tumor headlight with black color using FCM with intensity of 0.1

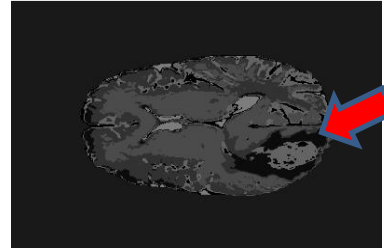


Figure 13. More highlighted with applying energy feature with black region boundary around grey fluid

In Figure 10, experiment have been performed over T2 sequence of image and tumor is more contrast and intensities are more homogenous to segment so in this case step by step tumor have been segmented, in next step Figure 11 average intensities then combine Flair sequence with T2, apply FCM therefore tumor has been segmented with black portion with intensity of 0.1 in Figure 12 and at last after applying energy feature tumor boundary segmented with black portion, it can be seen in figure 13.

Statistical features give illusion with minimum cost [17].

Table 2 is showing statistical features whereas Table 3 is showing for texture features.

Table 2. Statistical Features

Feature Name	Formula
Kurtosis	$\text{Kurtosis} = \left\{ \frac{n(n+1)}{(n-1)(n-2)(n-3)} \sum \left(\frac{x_j - \bar{x}}{s} \right)^4 \right\} - \frac{3(n-1)^2}{(n-2)(n-3)}$
Skewness	$\text{Skew} = \frac{n}{(n-1)(n-2)} \sum \left(\frac{x_j - \bar{x}}{s} \right)^3$
Variance	$\tilde{f}(x, y) = \frac{1}{mn-1} \sum_{(r,c) \in W} \left(g(r, c) - \frac{1}{mn-1} \sum_{(r,c) \in W} g(r, c) \right)^2$
Mean	$f(x, y) = \frac{1}{mn} \sum_{(r,c) \in W} g(r, c)$

Texture feature can be seen from [18] over GLCM, here subset have been used.

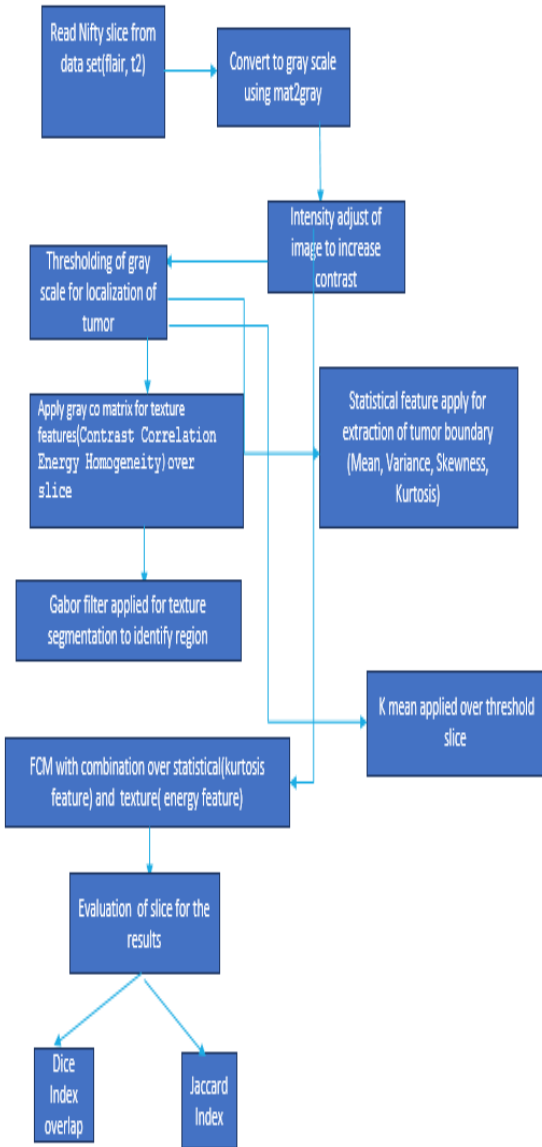


Figure 14. Frame work diagram

5. RESULTS AND DISCUSSION

In MACCAI BRATS brain tumor dataset segmented tag images are provided to checked and validate for every single patient. We have performed segmentation through FCM and results from FCM with eight features like texture (Energy, homogeneity, contrast, correlation) and statistical (Mean, variance, kurtosis, skewness). They are subset features from their main class but give help for better segmentation. The output results have been compared with given tagged images of every patient individually. For comparison and evaluation dice overlap and Jaccard index have been used. Then we are comparing our results with [1] benchmark and draw conclusion. Table 4 and Table 5, for Flair and T2 ten images 75th to 85th sequence ten features (**Contrast, Homogeneity, Energy, Variance, Mean, skewness, kurtosis**) have been checked whereas Table 6 is comparison among benchmark and

this paper result values. Figure 15 and Figure 16 shows features over this dataset whereas Figure 17 is comparison among this paper result versus benchmark results.

Table 3. Texture features

Feature name	Formula
Energy	$\sum_{i,j=0}^{N-1} (P_{ij})^2$
Contrast	$\sum_{i,j=0}^{N-1} P_{ij} (i-j)^2$
Homogeneity	$\sum_{i,j=0}^{N-1} \frac{P_{ij}}{1+(i-j)^2}$
Correlation	$\sum_{i,j=0}^{N-1} P_{ij} \frac{(i-\mu)(j-\mu)}{\sigma^2}$

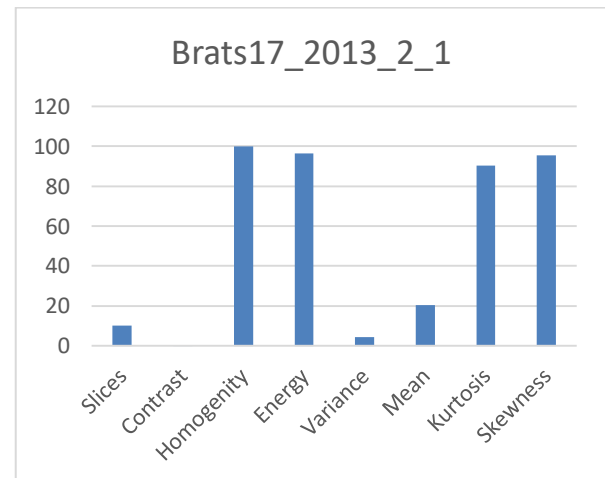


Figure 15. Statistical and Texture feature over 10 images of volume number Flair sequence (Brats17_2013_2_1)

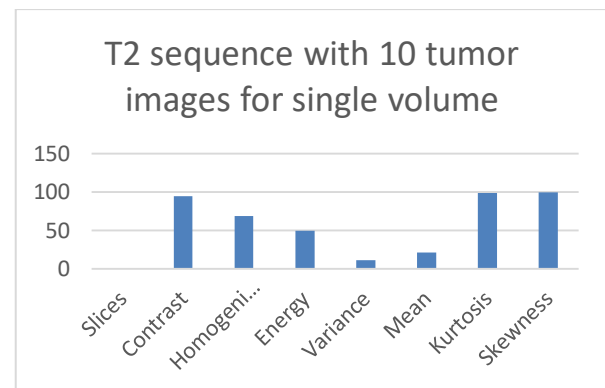


Figure 16. With T2 sequence

Table 4. Flair sequence image across features

Slices	Contrast	Homogeneity	Energy	Variance	Mean	Kurtosis	Skewness
75	0.01	0.9988722	0.9689	0.091314	0.1975	2.05732	0.9546
76	0.0032	0.9983835	0.9574	0.019642	0.2055	47.9113	0.9546
77	0.0037	0.9981391	0.9559	0.020122	0.2063	46.6976	0.9546
78	0.0029	0.9985276	0.9624	0.017296	0.2063	54.8159	0.9546
79	0.0023	0.9988283	0.9697	0.013944	0.2048	68.717	0.9546
80	0.0027	0.9986341	0.9678	0.014708	0.2048	64.9888	0.9546
81	0.0017	0.9991353	0.975	0.011612	0.204	83.1183	0.9546
82	0.0036	0.9981892	0.9591	0.018597	0.2087	50.7724	0.9546
83	0.0036	0.9981955	0.9585	0.01891	0.2071	49.8835	0.9546
84	0.0041	0.9979261	0.9548	0.020481	0.2071	45.8254	0.9546
	0.0381	9.9848308	9.6296	0.246627	2.0521	514.787	9.5456

Table 5. T2 sequence image across features

Slices	Contrast	Homogeneity	Energy	Variance	Mean	Kurtosis	Skewness
75	0.788324	0.13	0.490745	0.116	0.22142	2.128872	0.985862
76	0.999896	0.782292798	0.491435	0.115	0.22	2.130904	0.9888
77	2.525444	0.135	0.491435	0.114098	0.219034	2.137703	0.988837
78	2.433906	0.142091685	0.489172	0.11119	0.215939	2.147838	0.993262
79	2.34915	0.785769993	0.491075	0.113917	0.218271	2.157703	0.997835
80	2.332344	0.786765506	0.491416	0.115429	0.219257	2.166712	12.16933
81	2.423925	0.78529869	0.493503	0.119781	0.222866	2.174276	7.286939
82	2.672338	0.781041972	0.494175	0.121017	0.223501	2.182282	6.483036
83	2.713894	0.779862143	0.496041	0.107486	0.210274	2.184867	1.016572
84	2.650975	0.496312765	0.496313	0.079189	0.180368	2.180669	1.016187

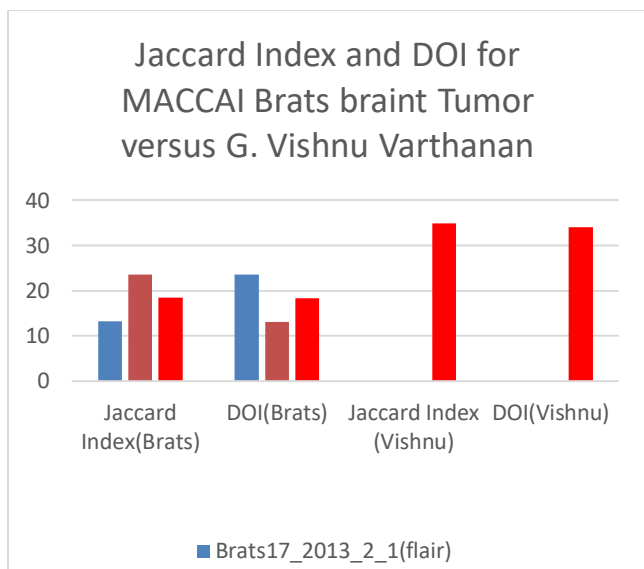


Figure 17. Comparison with benchmark

Table 6. Bench mark comparison table

Jaccard Index(Brats)	DOI(Brats)	Jaccard Index (Vishnu)	DOI(Vishnu)
13.3	23.5	34.85	34

In Figure 17 it is clear cut seen for DOI and jaccard index of our results are 23.58, 23.5 whereas for benchmark they are 34.85 and 34 so we have some motivations and result can be improve if we reduce dimension with SOM and then using FKM for more accurate segmentation can be achieve.

6. CONCLUSION AND FUTURE WORK

We can conclude this work as using segmentation methods with help of feature gives better accurate segmentation over Brats MACCAI brain tumor dataset over Flair and T2 sequence, when both sequence combine then better picture of tumor visualize and when applies subset of texture and statistical feature with FCM therefore tumor boundaries separate from normal brain. But this work compromise because we are solving mixed intensity issues and FCM with texture and statistical feature has been used but if

we used SOM for feature reduction and also reduce noise then apply FKM then will be able to get more better segmentation.

7. ACKNOWLEDGEMENT

I acknowledge to my supervisor Dr. Mohd Shafry Mohd Rahim, Dr. Usama Ejaz Bajwa and my brother Chaudhry Farhan Ejaz senior optimizer, R&D member NSN, Alkhobar , Saudi Arabia who supported me and more moral support from my mother.

8. REFERENCES

- [1] Vishnuvarthanan, G., Rajasekaran, M. P., Subbaraj, P., and Vishnuvarthanan, A. (2016). An unsupervised learning method with a clustering approach for tumor identification and tissue segmentation in magnetic resonance brain images. *Applied Soft Computing*, 38, 190-212.
- [2] Bauer, S., Fejes, T., and Reyes, M. (2013). A skull-stripping filter for ITK. *Insight Journal*, 2012.
- [3] Pereira, S., Pinto, A., Alves, V., and Silva, C. A. (2016). Brain tumor segmentation using convolutional neural networks in MRI images. *IEEE transactions on medical imaging*, 35(5), 1240-1251.
- [4] Cordier, N., Menze, B., Delingette, H., and Ayache, N. (2013). Patch-based segmentation of brain tissues. Paper presented at the MICCAI challenge on multimodal brain tumor segmentation, 6-17.
- [5] Menze, B. H., Jakab, A., Bauer, S., Kalpathy-Cramer, J., Farahani, K., Kirby, J., et al. (2015). The multimodal brain tumor image segmentation benchmark (BRATS). *IEEE transactions on medical imaging*, 34(10), 1993.
- [6] Chandrashekar, G., and Sahin, F. (2014). A survey on feature selection methods. *Computers & Electrical Engineering*, 40(1), 16-28.
- [7] Sayadi, M., Tlig, L., and Fnaiech, F. (2007). A new texture segmentation method based on the fuzzy c-mean algorithm and statistical features. *Applied Mathematical Sciences*, 1(60), 2999-3007.
- [8] Texture Segmentation. (Texture based features).
- [9] al, H. E. (2017). Haralick texture features calculated from GLCMs.
- [10] Joseph, R. P., Singh, C. S., and Manikandan, M. (2014). Brain tumor MRI image segmentation and detection in image processing. *International Journal of Research in Engineering and Technology*, 3(1), 1-5.
- [11] Kohonen, r. (2007). Self optimisation mapping and Kmean. page1-page5.
- [12] Christe, S. A., Malathy, K., and Kandaswamy, A. (2010). Improved hybrid segmentation of brain MRI tissue and tumor using statistical features. *ICTACT J Image Video Process*, 1(1), 34-49.
- [13] Nabizadeh, N., and Kubat, M. (2015). Brain tumors detection and segmentation in MR images: Gabor wavelet vs. statistical features. *Computers & Electrical Engineering*, 45, 286-301.
- [14] Guthikonda, S. M. (2005). Kohonen self-organizing maps. Wittenberg University, 98.
- [15] Ahirwar, A. and Jadon, R.S., 2011. Characterization of tumor region using SOM and Neuro Fuzzy techniques in Digital Mammography. *International Journal of Computer Science and Information Technology*, 3(1), pp.199-211.
- [16] Isselemou Abd El Kader, S. Z. (2017). A Hybrid Self-Organizing Map With Fuzzy K-Means Algorithm For BrainTumor Identification And Analysis Using Magnetic Resonance Brain Images. *IJAR*, 1572-1578.
- [17] Kumar, V., and Gupta, P. (2012). Importance of statistical measures in digital image processing. *International Journal of Emerging Technology and Advanced Engineering*, 2(8), 56-62.
- [18] Khurram ejaz. Mohd Shafry Mohd Rahim, H. C., Amjad Rehman. (2018). Segmentation method for pathological brain tumor and accurate detection using MRI. *IJACSA*, 9(Segmentation method for pathological brain tumor and accurate detection using MRI), 394-401.
- [19] Khosro Jalali, M. H., Asma Tanavar. (2014). Image Segmentation with Improved Distance Measure in Som and K Means Algorithms. *JMCS*, Volume 8(4), pp 367 - 376.
- [20] Abdel-Maksoud, E., Elmogy, M., and Al-Awadi, R. (2015). Brain tumor segmentation based on a hybrid clustering technique. *Egyptian Informatics Journal*, 16(1), 71-81
- [21] Pei, L., Reza, S. M., and Iftekharuddin, K. M. (2015). Improved brain tumor growth prediction and segmentation in longitudinal brain MRI. Paper presented at the Bioinformatics and Biomedicine (BIBM), 2015 IEEE International Conference on, 421-424.
- [22] Sneha Dhurkunde , S. P. (2016). Segmentation of Brain Tumor in Magnetic Resonance Images using Various Techniques *International Journal of Innovative Research in Science, Engineering and Technology* Vol. 5,(Iaauw no. 1).
- [23] Saleha Masood*, M. S., Afifa Masood, Mussarat Yasmin and Mudassar Raza (2015). A Survey on Medical Image Segmentation. *Current Medical Imaging Reviews*(Segmentation in medical imaging), 3-14
- [24] Norouzi, A., Rahim, M. S. M., Altameem, A., Saba, T., Rad, A. E., Rehman, A., et al. (2014). Medical image segmentation methods, algorithms, and applications. *IETE Technical Review*, 31(3), 199-213.
- [25] Rajaei, A., Rangarajan, L., and Dallalzadeh, E. (2012). Medical Image Texture Segmentation Usingrange Filter. *computer science and information technology*, 2(1).
- [26] Padma, A., and Sukanesh, R. (2011). Automatic classification and segmentation of brain tumor in CT images using optimal dominant gray level run length texture features. *International Journal of Advanced Computer Science and Applications*, 2(10), 53-59.

Bessel-Gauss Beam Light Sheet Assisted Fluorescence Imaging of Trabecular Meshwork in the Iridocorneal Region Using Long Working Distance Objectives

C. S. Suchand Sandeep
Singapore Centre for 3D Printing,
School of Mechanical & Aerospace
Engineering,
Nanyang Technological University,
Singapore

Sarangapani Sreelatha
Centre for Optical and Laser
Engineering (COLE), School of
Mechanical & Aerospace Engineering,
Nanyang Technological University,
Singapore

Mani Baskaran
Singapore Eye Research Institute,
Singapore National Eye Centre,
Duke-NUS Medical School,
Singapore

Xun Jie Jeessmond Hong
Centre for Optical and Laser
Engineering (COLE), School of
Mechanical & Aerospace Engineering,
Nanyang Technological University,
Singapore

Tin Aung
Singapore Eye Research Institute,
Singapore National Eye Centre,
National University of Singapore,
Singapore

Vadakke Matham Murukeshan*
Centre for Optical and Laser
Engineering (COLE), School of
Mechanical & Aerospace Engineering,
Nanyang Technological University,
Singapore
*MMurukeshan@ntu.edu.sg

ABSTRACT

Glaucoma is one of the leading cause of blindness characterized by increased intra ocular pressure (IOP), visual field defects and irreversible loss of vision. Remedial intervention of glaucoma primarily aims at the reduction of IOP and subsequent examination concerning the related anomalies in the aqueous outflow system (AOS) especially with newer angle procedures. Thus, high resolution imaging of the iridocorneal angle (ICA) region comprising trabecular meshwork (TM) is extremely valuable to clinicians and vision analysts in comprehending the disease state for the efficacious analysis and treatment of glaucoma. Imaging of the AOS inside the eye using the digitally scanned Bessel-Gauss beam light sheet microscopy has been used in this study to obtain high resolution optical sections with minimal phototoxicity and photobleaching. This paper investigates the effect of long working distance objectives in obtaining high resolution TM images while offering non-contact and non-invasive approach in imaging. A series of experiments were conducted to optimize various imaging parameters using porcine eyes as test samples. Investigations carried out by illuminating both the anterior segment region and limbal region resulted in promising results. A delineated network of collagen fibers in a meshwork fashion can be clearly seen in the obtained images of the TM. The optical sectioning capability of this technique is demonstrated and the structural features match well

Permission to make digital or hard copies of all or part of this work for personal or classroom use is granted without fee provided that copies are not made or distributed for profit or commercial advantage and that copies bear this notice and the full citation on the first page. Copyrights for components of this work owned by others than the author(s) must be honored. Abstracting with credit is permitted. To copy otherwise, or republish, to post on servers or to redistribute to lists, requires prior specific permission and/or a fee. Request permissions from Permissions@acm.org.

ICBBS '19, January 7–9, 2019, Singapore, Singapore

© 2019 Copyright is held by the owner/author(s). Publication rights licensed to ACM.

ACM ISBN 978-1-4503-6654-0/19/01...\$15.00

DOI: <https://doi.org/10.1145/3314367.3314380>

with previous literature reports.

CCS Concepts

Applied computing → **Life and medical sciences** → **Consumer health**

Applied computing → **Physical sciences and engineering** → **Physics**

Keywords

Bio optics; Bessel-Gauss beam; Glaucoma; Iridocorneal angle; Trabecular mesh work

1. INTRODUCTION

High resolution imaging and ultra-sensitive detection techniques in biomedical optics are remodeling the medical landscape with newly developed clinical instruments [1-3]. There are various methodologies and techniques that have been developed over the last few decades towards resolution improvement, and aberration and curvature correction for bio optic applications [1, 4-8]. Vision researchers around the globe have been constantly striving to innovate better diagnostics and treatment methods for various eye ailments. Primary angle closure glaucoma is one of the major eye diseases causing blindness worldwide [9]. Glaucoma is an eye disease caused by irregularities in the ocular aqueous outflow system (AOS) causing an elevated intraocular pressure (IOP) that may result in the decay of retinal ganglion cells, resulting in loss of vision. Primary angle closure glaucoma may occur when the iris is pushed or pulled against the drainage channels at the iridocorneal angle (ICA) region [10]. The aqueous outflow system at ICA consists of the trabecular meshwork (TM), the Schlemm's canal and the collector channels [11]. Imaging of ICA in high resolution is of great diagnostic value to clinicians for the assessment of the disease state. The main diagnostic techniques currently available for ICA visualization can be broadly classified into photographic (gonioscopic photography [12], EyeCAMTM [13], pentacam [14] etc.) and optical tomographic methods (Ultrasound biomicroscopy [15], optical coherence tomography (OCT) [16] etc.). All these imaging modalities allow visualization of ICA and help in the diagnosis and management of glaucoma.

There are advantages and inadequacies in measurement reliability and repeatability associated with each of these techniques. The widely used clinical reference standard for ICA assessment is gonioscopy. However patient discomfort and physician compliance are two main concerns of this technique. Since this technique is quite tedious and requires cumbersome methods and expertise to record the data, ICA images from gonioscopy are often not documented. In addition multiple reflections from the gonioscopic lens or mirrors used along with the coupling gel affects the image quality of the gonioscopic system [17]. To be able to resolve the TM structures, a spatial resolution of about 1–5 μm is required. Another clinically effective, state of the art tool used in the assessment of ICA to investigate angle closure is OCT. Even though OCT can image features on a micrometer scale, the low image contrast of the OCT images restricts the visualization of TM structures [18]. In other words, these commonly used techniques usually cannot deliver high resolution images required for the visualization of the TM structures.

In this regard, we consider light sheet fluorescence microscopy (LSFM), as a potential imaging solution that has the ability to produce high resolution optical images with minimal photobleaching and phototoxicity [19]. In conventional static LSFM, a stationary sheet of light is projected onto the sample plane utilizing a cylindrical optics. The fluorescence signal emitted by the sample is then imaged using an imaging optics placed perpendicular to the illumination axis. This technique can generate two dimensional optical sections of the samples under investigation with high resolution in large field of view. A thinner and high signal to noise ratio light sheet with an extended depth of focus can be realized by digitally scanning a Bessel–Gauss beam in one dimension [20]. The superiority of Bessel-Gauss beam based LSFM had been demonstrated by several research groups. [21, 22]. Here we present our recent advances in Bessel-Gauss beam light sheet microscopy for high resolution imaging of the ICA, in particular, the trabecular meshwork. By incorporating long working distance (WD), high numerical aperture (NA) objectives, this method provides a non-contact and non-invasive technique for high resolution imaging of the TM.

2. EXPERIMENTAL

2.1 Preparation of Samples

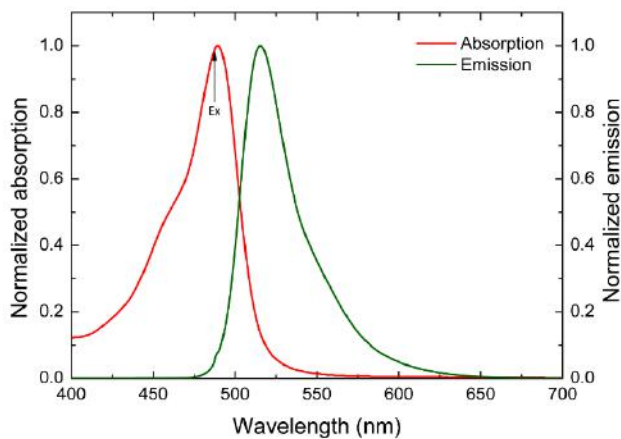


Figure 1. Absorption and emission spectra of aqueous fluorescein sodium solution

We randomly collected porcine eye samples (*Sus scrofa domestica*) to use them as ex-vivo samples for the measurements. The samples were collected from a local abattoir to be transported and kept in ice boxes till investigations began for maintaining the freshness. The samples were mounted on to a custom made eye holder and the anterior chamber of the eye samples was injected with 0.2 ml of 0.05% w/v fluorescein sodium (Bausch & Lomb, UK). The experiments were completed within 8 hours of the death of the animal. We have taken proper precautions on bio safety, according to the regulations of Nanyang Technological University (NTU) and Agri-Food and Veterinary Authority (AVA) of Singapore. The absorption and emission spectra of aqueous fluorescein sodium solution are shown in Figure 1. The emission spectrum shown here is obtained by exciting the fluorescein solution at 488 nm, corresponding to the excitation wavelength used for the measurements.

2.2 Optical Setup for Imaging

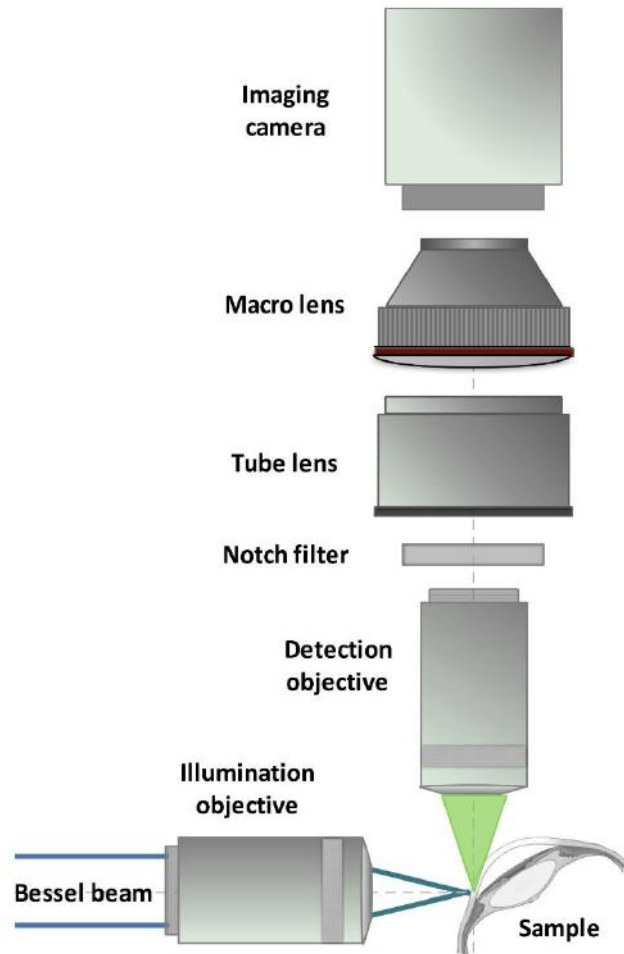


Figure 2. Schematic of the Bessel-Gauss beam light sheet microscopy used for the imaging of ICA

For the fluorescence excitation, a fiber coupled continuous wave (CW) laser diode of 488 nm emission wavelength (LUX-488 Omicron, Germany) was used. The beam was expanded and collimated to the required size with the help of an external beam expander. A 176° apex angle plano convex axicon lens (Thorlabs) was used for the generation of the Bessel-Gauss beam. The

generated Bessel-Gauss beam was made incident on a two axis Galvano scanner and directed to the illumination objective using a tele-centric scan lens followed by a tube lens. An infinity corrected, long working distance (WD = 20 mm) apochromatic objective of 20X magnification was used (Plan Apo, NA 0.42, Mitutoyo, Japan) for sample excitation. The Bessel-Gauss light sheet was created by scanning the vertical mirror of the Galvano scanner. The imaging arm consisted of an identical infinity corrected long working distance objective and a tube lens ($f = 200$ mm, WD = 148 mm, Thorlabs) with the optical axis orthogonal to the excitation arm. A 60 mm macro lens (Nikon AF Micro Nikkor 60 mm) was used for an easier collection adjustment at the camera end. Scattered excitation laser was isolated with the help of a 488 nm notch filter in the imaging system. A 5.5 megapixel sCMOS camera (Andor Neo, UK) was used for recording the images. The illumination laser power was always kept lower than the maximum permissible exposure (MPE) limit recommended by the American National Standards Institute (ANSI) and the International Commission on Non-Ionizing Radiation Protection (ICNIRP) [23, 24]. The experimental setup used for the measurements is outlined in Figure 2.

3. RESULTS AND DISCUSSION

Compared to a conventional Gaussian beam, the Bessel-Gauss beam can maintain a focused spot over a relatively larger distance [25, 26]. Additionally, the use of self-reconstructing Bessel beam results in the improvement of the sample image contrast and the reduction in shadowing and scattering artifacts. The use of fluorescence dye enhances the contrast of the images further. In addition, the digitally scanned light sheet technique offers a better control over the intensity profile and size of the generated light sheet compared to conventional static light sheet microscopy.

The images obtained using the digitally scanned Bessel-Gauss beam light sheet from a porcine eye sample are presented in Figure 3. These images clearly show the ICA region and the trabecular meshwork can be distinctly identified in these images. The optical sectioning capability of this technique is presented in a series of images (Figure 3b - 3d). These images are obtained by progressively moving the detection objective towards the sample in steps of 50 μ m.

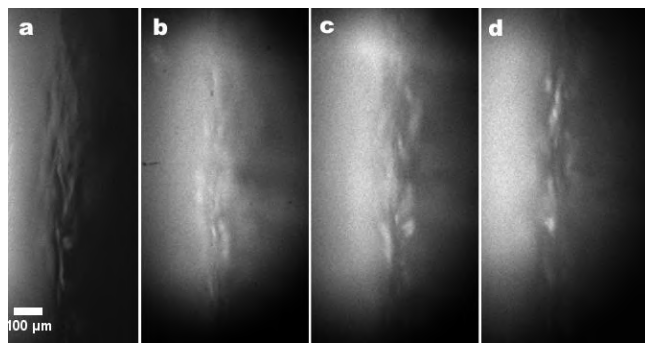


Figure 3. Optically sectioned Images (at 50 μ m steps) of porcine TM obtained using the Bessel-Gauss beam light sheet microscopy

4. CONCLUSION

An imaging system based on digitally scanned Bessel-Gauss beam light sheet for the high resolution visualization of the iridocorneal angle region in the eye is presented with illustrative examples. The results shows a delineated network of collagen fibers in a meshwork design. Structural details of the obtained TM images

are found to be in good agreement with previous reports in literature [27-29]. The optical sectioning capability of this technique is also demonstrated. High resolution imaging of the ICA and TM can help in the early and accurate detection of glaucomatous disease process, which empowers clinicians and vision researchers to comprehend the pathology and diverse conditions of the eye disease for ensuing treatment and follow-up methodology. Improved direct high quality visualization of the TM region through this system can be used for Laser trabeculoplasty, and further glaucoma management.

5. ACKNOWLEDGMENTS

The authors acknowledge the financial support received through A*STAR-MIG project (BMRC1619077002) and the facilities and research manpower provided through COLE-EDB funding.

6. REFERENCES

- [1] Mendez A. 2016. *Optics in Our Time*. Mohammad D. A., Mohamed E., and Zubairy M. S. Ed, Springer. DOI = http://doi.org/10.1007/978-3-319-31903-2_13
- [2] Sujatha N., Murukeshan V.M., Ong L.S., and Seah L.K. 2003. *An all fiber optic system modeling for the gastrointestinal endoscopy: design concepts and fluorescent analysis*. Optics Communications, 219, 1 (April 2003), 71-79. DOI= [http://doi.org/10.1016/S0030-4018\(03\)01198-2](http://doi.org/10.1016/S0030-4018(03)01198-2)
- [3] Hong X. J. J. et al. 2015. *A simple and non-contact optical imaging probe for evaluation of corneal diseases*. Review of Scientific Instruments 86, 9 (September 2015), 093702. DOI= <http://doi.org/10.1063/1.4929684>
- [4] Vangindertael J. et al. 2018. *Topical Review: An introduction to optical super-resolution microscopy for the adventurous biologist*. Methods Appl. Fluoresc. 6, 2 (March 2018), 022003. DOI= <http://doi.org/10.1088/2050-6120/aaae0c>
- [5] Seah L. K et al. 2004. *Time-resolved imaging of latent fingerprints with nanosecond resolution*. Optics and Laser Technology, 36, 5 (July 2004), 371-376. DOI= <http://doi.org/10.1016/j.optlastec.2003.10.006>
- [6] Iwaniuk D., Rastogi P., and Hack E. 2011. *Correcting spherical aberrations induced by an unknown medium through determination of its refractive index and thickness*. Opt. Express 19, 20 (2011), 19407-19414 DOI= <http://doi.org/10.1364/OE.19.019407>
- [7] Murukeshan V. M., and Sujatha N. 2004. *Digital speckle pattern interferometry for deformation analysis of inner surfaces of cylindrical specimens*. Applied Optics, 43, 12 (April 2004) 2400-2408. DOI= <http://doi.org/10.1364/AO.43.002400>
- [8] Ehler M. 2013. *Modifications of iterative schemes used for curvature correction in noninvasive biomedical imaging*. J. of Biomedical Optics, 18, 10 (October 2013), 100503. DOI= <http://doi.org/10.1117/1.JBO.18.10.100503>
- [9] Pascolini D, Mariotti S. P. 2012. *Global data on visual impairment in the year 2010*. Br J Ophthalmol. 96, 5 (May 2012), 614-618. DOI= <http://doi.org/10.1136/bjophthalmol-2011-300539>
- [10] Salmon J.F. 1999. *Predisposing factors for chronic angle-closure glaucoma*. Prog. in Retinal and Eye Research 18, 1 (Jan 1999), 121-131. DOI= [http://doi.org/10.1016/S1350-9462\(98\)00007-X](http://doi.org/10.1016/S1350-9462(98)00007-X)

- [11] Hart W. M. 1992. Intraocular Pressure. *In: Adler's Physiology of the Eye*. F. H. Adler & W. M. Hart Ed, 9th ed. St. Louis: Mosby Year Book.
- [12] Castroviejo R. 1935. *Goniophotography: Photography of the Angle of the Anterior Chamber in Living Animals and Human Subjects*. American Journal of Ophthalmology, 18, 6(1935), 524-527. DOI= [http://doi.org/10.1016/S0002-9394\(35\)93547-4](http://doi.org/10.1016/S0002-9394(35)93547-4)
- [13] Baskaran M., Aung T., Friedman D. S., Tun T. A., and Perera S. A. 2012. *Comparison of EyeCam and anterior segment optical coherence tomography in detecting angle closure*. Acta Ophthalmologica, 90, 8 (December 2012), e621-e625. DOI= <http://doi.org/10.1111/j.1755-3768.2012.02510.x>
- [14] Shankar H., Taranath D., Santhirathelagan C. T., and Pesudovs K. 2008. *Anterior segment biometry with the Pentacam: Comprehensive assessment of repeatability of automated measurements*. Journal of Cataract & Refractive Surgery. 34, 1 (January 2008), 103–113 DOI= <http://doi.org/10.1016/j.jcrs.2007.09.013>
- [15] Pavlin C. J., Harasiewicz K., and Foster F. S. 1992. *Ultrasound biomicroscopy of anterior segment structures in normal and glaucomatous eyes*. Am J Ophthalmol, 113, 4 (April 1992), 381-389. DOI= [http://doi.org/10.1016/S0002-9394\(14\)76159-8](http://doi.org/10.1016/S0002-9394(14)76159-8)
- [16] Huang D., Swanson E. A., Lin C. P. et al. 1991. *Optical coherence tomography*, Science, 254, 5035 (November 1991), 1178-1181. DOI= <http://doi.org/10.1126/science.1957169>
- [17] Baskaran M., Perera S. A., Nongpiur M. E. et al. 2012. *Angle assessment by EyeCam, goniophotography, and gonioscopy*. Journal of glaucoma. 21, 7 (September 2012), 493-497. DOI= <http://doi.org/10.1097/IJG.0b013e3182183362>
- [18] Kagemann L., Wollstein G., Ishikawa H. et al. 2010. *Identification and Assessment of Schlemm's Canal by Spectral-Domain Optical Coherence Tomography*. Invest. Ophthalmol. Vis. Sci. 51, 8 (August 2010), 4054-4059. DOI= <http://doi.org/10.1167/iovs.09-4559>.
- [19] Santi P.A. 2011. *Light Sheet Fluorescence Microscopy: A Review*. J Histochem Cytochem. 59, 2 (February 2011), 129–138. DOI= <http://doi.org/10.1369/0022155410394857>
- [20] Baumgart E. and Kubitscheck U. 2012. *Scanned light sheet microscopy with confocal slit detection*. Opt. Express. 20, 19 (September 2012), 21805–14. DOI= <http://doi.org/10.1364/OE.20.021805>
- [21] Lee K-S. and Rolland J. P. 2008. *Bessel beam spectral-domain high-resolution optical coherence tomography with microoptic axicon providing extended focusing range*. Opt. Lett. 33, 15 (August 2008), 1696–1698. DOI= <http://doi.org/10.1364/OL.33.001696>
- [22] Olarte O E et al. 2012. *Image formation by linear and nonlinear digital scanned light-sheet fluorescence microscopy with Gaussian and Bessel beam profiles*. Biomed. Opt. Express. 3, 7 (July 2012), 1492–505. DOI= <http://doi.org/10.1364/BOE.3.001492>
- [23] Delori F. C., Webb R. H., and Sliney D. H. 2007. *Maximum permissible exposures for ocular safety (ANSI 2000), with emphasis on ophthalmic devices*. JOSA A 24, 5 (May 2007), 1250–1265. DOI= <http://doi.org/10.1364/JOSAA.24.001250>
- [24] Sliney D. et al. 2005. *Adjustment of guidelines for exposure of the eye to optical radiation from ocular instruments: statement from a task group of the International Commission on Non-Ionizing Radiation Protection (ICNIRP)*. Appl. Opt. 44, 11 (April 2005), 2162-2176. DOI= <http://doi.org/10.1364/AO.44.002162>
- [25] Gao L., Shao L., Chen B-C. and Betzig E. 2014. *3D live fluorescence imaging of cellular dynamics using Bessel beam plane illumination microscopy*. Nat. Protocols. 9, 5 (April 2014), 1083–1101. DOI= <http://doi.org/10.1038/nprot.2014.087>
- [26] Siegman A. E. 1986. *Lasers*. Mill Valley, CA: University Science Books.
- [27] Hong X. J. J., Shinoj V.K., Murukeshan V.M., Baskaran M., and Aung T. 2017. *Imaging of trabecular meshwork using Bessel–Gauss light sheet with fluorescence*. Laser Physics Letter 14, 3 (January 2017), 035602. DOI= <http://doi.org/10.1088/1612-202X/aa58b7>
- [28] Masihzadeh O. et al. 2013. *Direct trabecular meshwork imaging in porcine eyes through multiphoton gonioscopy*. J Biomed Opt. 18, 3 (March 2013), 036009. DOI= <http://doi.org/10.1117/1.JBO.18.3.036009>
- [29] Perincheri, S. M. et al. 2016. *High resolution iridocorneal angle imaging system by axicon lens assisted gonioscopy*. Sci. Rep. 6 (July 2016), 30844. DOI= <http://doi.org/10.1038/srep30844>

Semantic Segmentation of Colon Gland with Conditional Generative Adversarial Network

Liye Mei
Yunnan University
School of Information Science
and Engineering, Kunming,
Yunnan 650091, China
15972852508
liyemei@mail.ynu.edu.cn

Xiaopeng Guo^{*}
Yunnan University
School of Information Science
and Engineering, Kunming,
Yunnan 650091, China
18460894750
xiaopengguo@mail.ynu.edu.cn

Chaowei Cheng
Yunnan University
School of Information Science
and Engineering, Kunming,
Yunnan 650091, China
15927037450
1269678172@qq.com

ABSTRACT

Semantic segmentation of colon gland is notoriously challenging due to their complex texture, huge variation, and the scarcity of training data with accurate annotations. It is even hard for experts, let alone computer-aided diagnosis systems. Recently, some deep convolutional neural networks (DCNN) based methods have been introduced to tackle this problem, achieving much impressive performance. However, these methods always tend to miss segmented results for the important regions of colon gland or make a wrong segmenting decision. In this paper, we address the challenging problem by proposed a novel framework through conditional generative adversarial network. First, the generator in the framework is trained to learn a mapping from gland colon image to a confidence map indicating the probabilities of being a pixel of gland object. The discriminator is responsible to penalize the mismatch between colon gland image and the confidence map. This additional adversarial learning facilitates the generator to produce higher quality confidence map. Then we transform the confidence map into a binary image using a fixed threshold to fulfill the segmentation task. We implement extensive experiments on the public benchmark MICCAI gland 2015 dataset to verify the effectiveness of the proposed method. Results demonstrate that our method achieve a better segmentation result in terms of visual perception and two quantitative metrics, compared with other methods.

CCS Concepts

Computing methodologies → Artificial intelligence →
Computer vision → Computer vision representations →
Image representations

Keywords

Semantic segmentation; colon gland; conditional generative adversarial network; adversarial learning

1. INTRODUCTION

Permission to make digital or hard copies of all or part of this work for personal or classroom use is granted without fee provided that copies are not made or distributed for profit or commercial advantage and that copies bear this notice and the full citation on the first page. Copyrights for components of this work owned by others than ACM must be honored. Abstracting with credit is permitted. To copy otherwise, or republish, to post on servers or to redistribute to lists, requires prior specific permission and/or a fee. Request permissions from Permissions@acm.org.

ICBBB '19, January 7–9, 2019, Singapore, Singapore

© 2019 Association for Computing Machinery.

ACM ISBN 978-1-4503-6654-0/19/01...\$15.00

DOI: <https://doi.org/10.1145/3314367.3314370>

In this paper, we study the problem of semantic segmentation of colon gland where the goal is to predict a category label at each pixel in the colon gland images. The accurate segmentation results can assist pathologists to make diagnose whether the colon gland is benign or malignant. However, this is a challenge task due to two-fold reason. First, the colon gland images always have complex context and huge variation. Figure. 1 illustrates an example of different morphology for colon gland. Figure. 1(a) shows two benign cases while Figure. 1(b) gives two malignant cases. We can observe that both the benign and malignant cases reveal complex context. Also, the variation between benign and malignant cases is quite huge; Second, the colon gland images with accurate annotations are scarce, because of manually labelling a large-scale training dataset is labor-intensive and time-consuming.

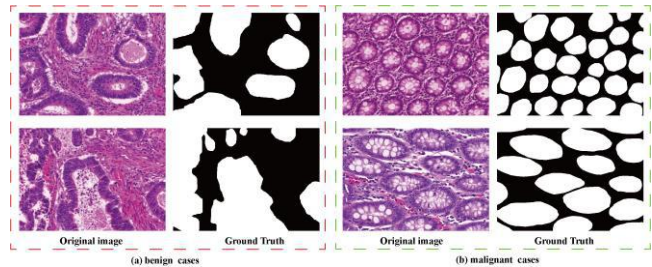


Figure 1. Different morphology of colon gland. The white regions of ground truth present different gland objects. Figure. 1(a) shows two benign cases while Figure. 1(b) gives two malignant cases

Recently, there are some attempts to address this challenging problem. These methods can be roughly classified into two groups: hand-crafted feature leaning based methods and deep-learning based methods. For the first group, some representative examples include structure-based method [1]-[2]; polar space random field-based method [3]; stochastic polygons-based method [4]. Though these methods achieved appealing segmentation performance, they harness the handed-crafted features to accomplish segmentation task, restricting segmentation effect because taking all the necessary factors into account for perfect design is almost impossible from a certain point of view.

With the great success of deep networks on 1000-way image classification [5], some deep leaning-based methods for segmentation task of have been proposed. Specifically, Ronneberger et al. introduced a U shape convolutional neural network to fulfill medical image segmentation (U-Net) [6]. Huang

^{*}corresponding author

et al. presented dense convolutional network [7], which has been impressive performance. Nevertheless, they always tend to miss segmented results for the important regions of colon gland or make a wrong segmenting decision.

Recently, the generative adversarial network (GAN) introduced by Goodfellow et al. [8] has acquired great success in generative modeling. Conceptually, it consists of a generator G and a discriminator D where G is in charge of capturing the potential data distribution while D attempt to distinguish a sample came from the training data rather than G. Later, Mirza et al. [9] expand the original GAN to the conditional case, i.e., conditional GAN (cGAN) where both G and D are conditioned on some additional information, such as class labels or data from other modalities. The authors argued that this conditional strategy can not only increase the stability during training but also improve the descriptive power of G. It has been widely used to some other tasks, such as image-to-image translation [10], image de-raining [11], CT denoising [12], just to name a few. Our work is also inspired by cGAN [9].

The main contributions of this work are listed as follows.

- (1) It proposes a novel framework through cGAN tailored for the semantic segmentation of colon gland. The generator learns a mapping from gland colon image to a confidence map. While the discriminator is to penalize the mismatch between colon gland image and the confidence map which, in turn, facilitates the generator to produce higher quality confidence map.
- (2) It harnesses a fixed threshold to transform the confidence map into a binary image to fulfill the segmentation task. This strategy is simple yet efficient.
- (3) It implements extensive experiments to verify the effectiveness of the proposed method. Results reveal that the proposed reaches a better segmentation results in terms of visual perception and two quantitative metrics.

the backbone adopted by many works. These methods achieved

2. THE PROPOSED METHOD

We detail the proposed method in this section. We start with the introduction of the cGAN-based segmentation architecture; then its objective is discussed; finally, we give the segmentation procedures.

2.1 Architecture

The overview of the architecture tailored for semantic segmentation of colon gland is illustrated in Figure. 2. Similar to the original GAN [8], the architecture consists of a generator G and a discriminator D. G is responsible for generating high-quality confidence map to indicate the score for each pixel belongs to gland objects, given a colon gland image as input; while D tries to distinguish the relationship between colon gland image and the ground truth or G-generated. The additional adversarial learning facilitates G to produce high quality confidence map. For simplicity, we denote the convolutional layer, BatchNorm layer, Deconvolutional layer as Conv, BN, Deconv, respectively. The numbers in the rectangle represent the kernel size, stride, and padding size of the Conv, respectively.

We can observe from Figure. 2(a) that G contains 16 blocks. G_1-G_3 are Conv-BN-ReLu blocks; G_4-G_14 are resnet blocks [13]; G_15-G_16 are Deconv-BN-ReLu blocks; G_17 is the Conv-Sigmoid block.

We leverage a 70×70 PatchGAN introduced by [10] as the discriminator D in this work. Generally speaking, it tries to distinguish each path with size of 70×70 in an image is real or fake. The discriminator convolves with image, and all the responses are averaged to generate the final output of D. Figure 2 (b) show the architecture of D.

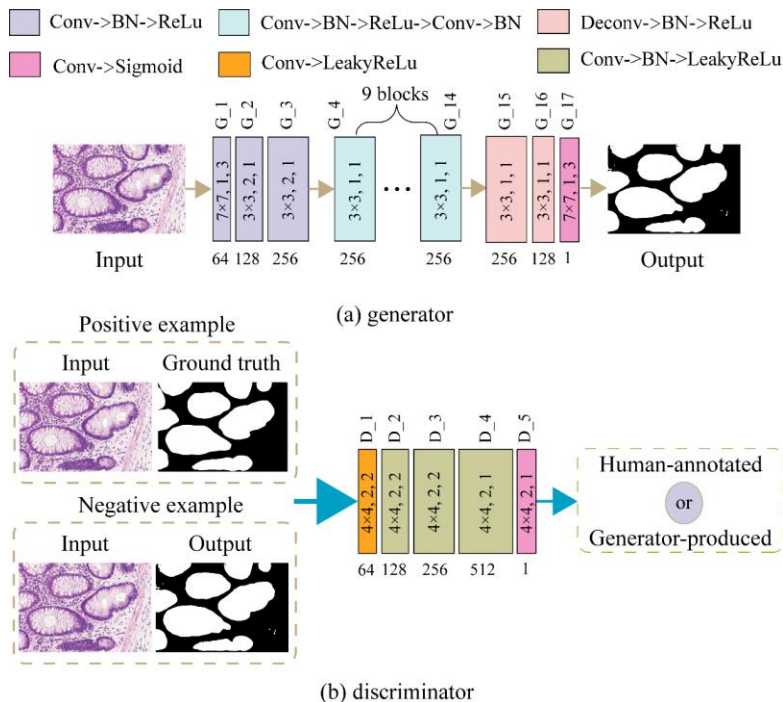


Figure 2. The overview of the proposed architecture. For each block, the numbers in the rectangle represent the kernel size, stride, and padding size of the Conv, respectively

2.2 Objective

Generator G learns a mapping from colon gland image \mathbf{x} to a confidence map \mathbf{y} , or $\mathbf{x} \mapsto \mathbf{y}$. G is trained to generate outputs that can confuse D while D tries to distinguish real images and G -generated images. This training procedure can be formulated as

$$L_{cGAN}(G, D) = \mathbb{E}_{\{x, y\} \sim P_{data}(x, y)} [\log D(x, y)] + \mathbb{E}_{\{x\} \sim P_{data}(x)} [\log(1 - D(x, G(x)))] \quad (1)$$

On the other hand, we also wish the output of G could reach the ground truth as much as possible. Hence, we employ the binary entropy loss towards this goal:

$$L_{BCE}(G) = \mathbb{E}_{\{x, y\} \sim P_{data}(x, y)} [-y \log(G(x)) - (1 - y) \log(1 - G(x))] \quad (2)$$

The final objective therefore is

$$G^* = \arg \min_G \max_D L_{cGAN}(G, D) + \lambda L_{BCE}(G) \quad (3)$$

Where λ controls the relative importance of the two terms. Experimentally, we set the λ to 80 throughout this work.

2.3 Segmentation Procedures

Once trained, we only harness the trained G to fulfill segmentation task. Given a colon gland image \mathbf{x} as input, the well-trained G outputs a confidence map \mathbf{y} with a range from 0 to 1 indicating the probability of being a pixel of gland object. The closer the score reach to 1, the more likely the corresponding pixel belongs to gland objects. To obtain the final binary segmentation result, the confidence map should be further processed. Specifically, we exploit a fixed threshold 0.5 to segment the confidence map to generate final binary segmented result \mathbf{m} . Mathematically, this process can be formulated as

$$\mathbf{m}_{i,j} = \begin{cases} 1, & \mathbf{y}_{i,j} \geq 0.5 \\ 0, & \text{otherwise} \end{cases} \quad (4)$$

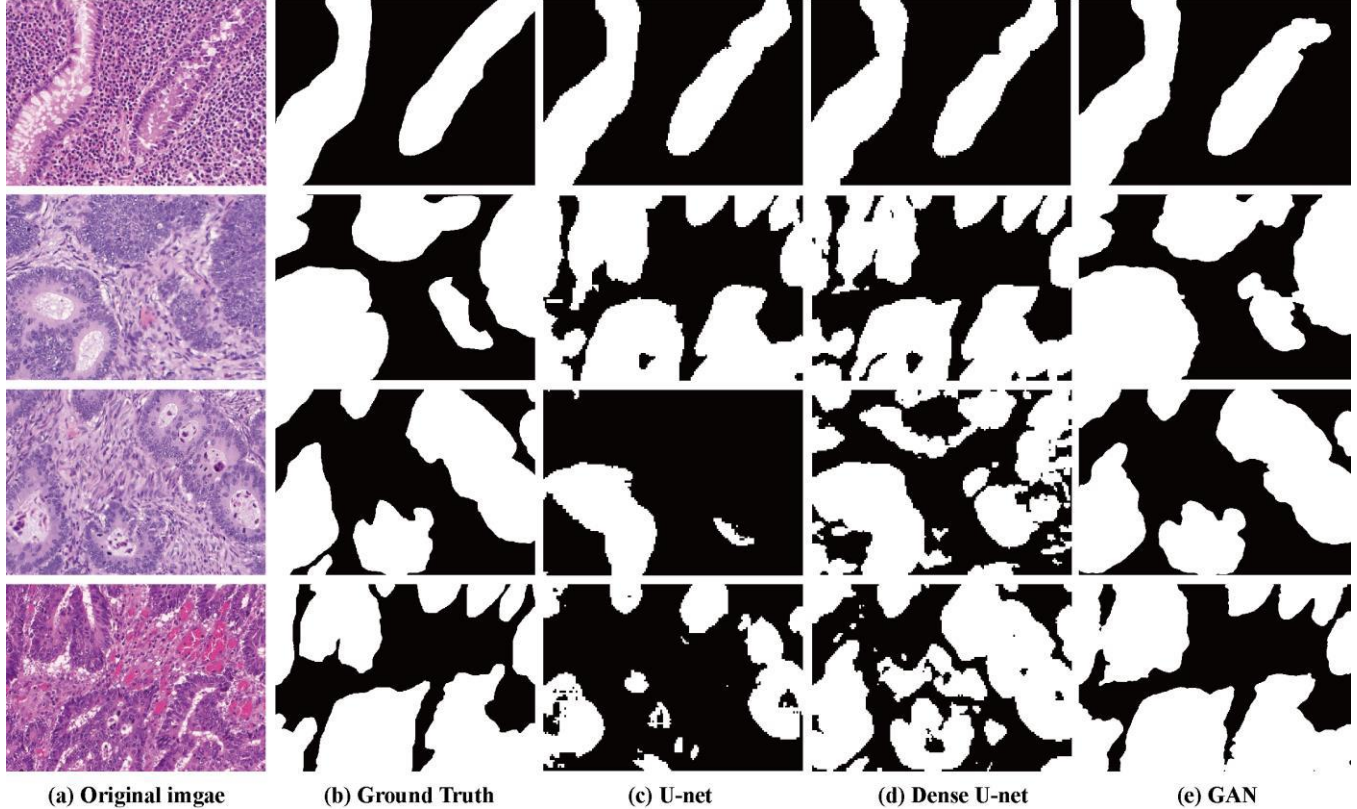


Figure 3. Four examples came from part A and the segmentation results generated by various methods

3. EXPERIMENTS AND DISCUSSION

3.1 Dataset Acquisition

We assess the proposed method on the public benchmark dataset of Gland Segmentation Challenge Contest in MICCAI 2015 [14]. The training dataset includes 85 images and the test dataset contains 80 images. The test dataset is further divided into two parts. The part A contains 60 test images while the part B includes 20 test images. Both the training and test images have the ground truth annotations provided by expert pathologists. We harness the original training dataset without any data augmentation transformations to train the model and evaluate our method on the test dataset.

3.2 Training Strategy

We implement our experiments in Pytorch [15]. Following [8], we train G and D alternately. Both G and D use Adam [16] solver with $\beta=0.5$. The learning rate remains a constant of 0.0002 throughout the learning process. We train the proposed framework from scratch and obtain the “optimal” model after 80 epochs through training dataset.

3.3 Visual Perception Assessment

We compare our method with two deep learning-based methods [6]-[7]. We first assess the visual perception of segmentation results. To have a fair and comprehensive comparison, we select four examples from test part A and test part B, respectively. Figure. 3 exhibits four examples came from part A and the segmentation results generated by various methods. We can observe that the segmentation results of our method are closest to ground truth, compared with other methods. All the gland regions almost have accurate segmentation results. Figure. 4 illustrates

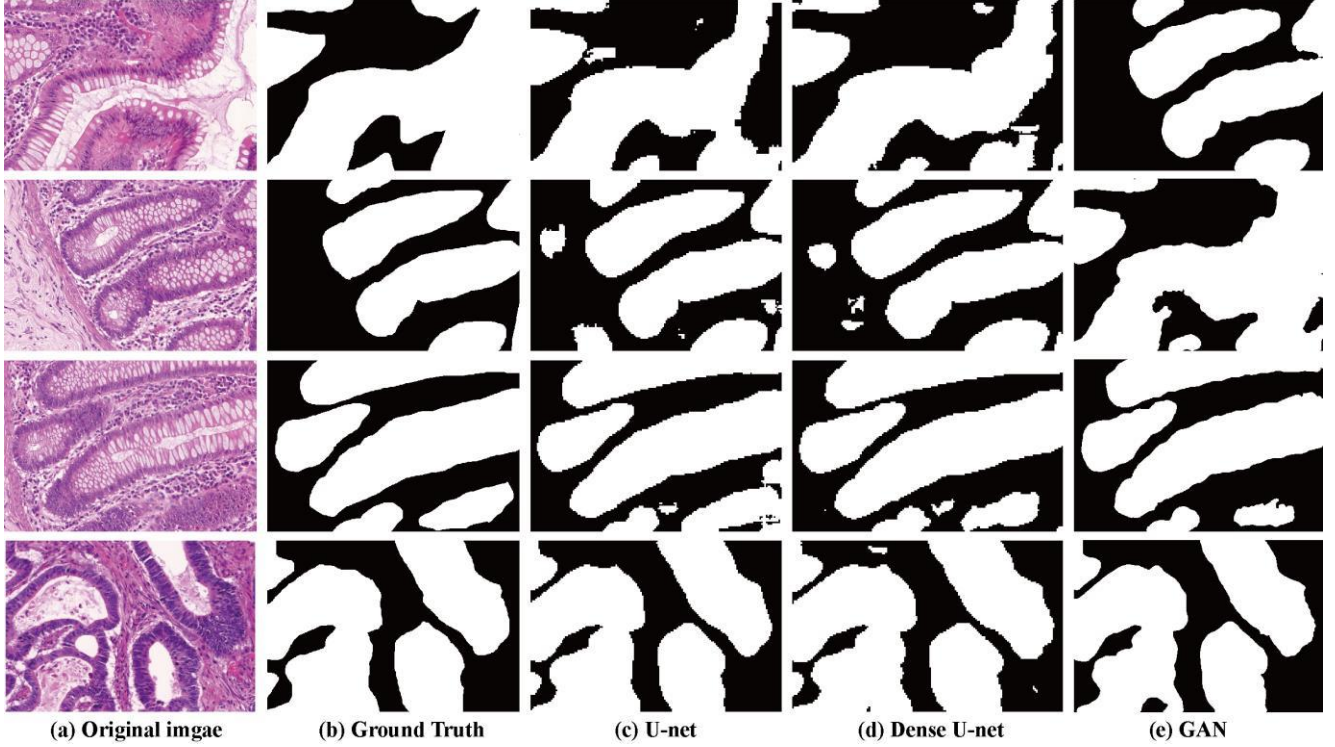


Figure 4. Four examples came from part B and the segmentation results generated by various methods

another four examples from part B. Similar to Figure. 3, our method also reveals good performance, leading to more accurate segmentation results. The eight examples above demonstrate that our method has a better visual perception of segmentation results.

3.4 Quantitative Comparison

We utilize two common metrics, the intersection over union (mIOU) [17] and dice coefficient to verify the proposed method. A brief introduction of the two metrics is presented as follows.

(i) Intersection over union (IOU) [17]

This metric is always utilized in the semantic segmentation task, comparing the global similarity between ground truth and prediction result. Its definition is

$$IOU(\mathbf{G}, \mathbf{P}) = \frac{|\mathbf{G} \cap \mathbf{P}|}{|\mathbf{G} \cup \mathbf{P}|} \quad (5)$$

where \mathbf{G} denotes the ground truth, \mathbf{P} is the prediction result. \cap , \cup represent the intersection and union between \mathbf{G} and \mathbf{P} , respectively.

(ii) dice coefficient

Similar to IOU, dice coefficient is another metric used in segmentation results assessment, which is formulated as

$$Dice(\mathbf{G}, \mathbf{O}) = \frac{2|\mathbf{G} \cap \mathbf{O}|}{|\mathbf{G}| + |\mathbf{O}|} \quad (6)$$

Note that for each metric, a higher value indicates a better segmentation result.

We calculate the mean IOU (mIOU) and mean Dice coefficient throughout the whole test dataset. Table. 1 list the mIOU and mean Dice scores of various methods.

We can observe that U-Net gives the lowest scores for test part A and test Part B in terms of mIOU and mean dice, whereas our method reaches the highest scores for test part A on both the metrics. Though our method achieves the second rank for test part B in terms of mean Dice, it presents the highest score on mIOU. To sum up, our method shows strong competitiveness in quantitative evaluation.

Table 1. The mIOU and mean Dice scores of various methods.

Approach	Test Part A		Test Part B	
	mIOU	mean Dice	mIOU	mean Dice
U-Net	0.7212	0.8241	0.7736	0.8650
Dense U-Net	0.7440	0.8445	0.7760	0.8695
GAN (ours)	0.8047	0.8866	0.7812	0.8678

Note: The best results for each metric are highlighted in bold.

4. CONCLUSION

In this paper, we proposed a novel framework via cGAN to accomplish the semantic segmentation of colon gland. The generator in the framework is trained to learn a mapping from gland colon image to a confidence map indicating the probabilities of being a pixel of gland object. While the discriminator penalizes the mismatch between colon gland image and the confidence map. This additional adversarial learning facilitates the generator to produce higher quality confidence map. Moreover, we transform the confidence map into a binary image using a fixed threshold to fulfill the segmentation task. Extensive experiments on the public benchmark dataset of MICCAI 2015 was implemented to verify the effectiveness of the proposed method. Results demonstrated that our method achieve a better

segmentation result in terms of visual perception and two quantitative metrics, compared with other methods. In the future work, we attempt to extend the proposed framework to other medical image segmentation task.

5 ACKNOWLEDGEMENTS

This work is supported by the innovative research program of Yunnan University (nos. YDY17111)

6 REFERENCES

- [1] Altunbay, D., Cigir, C., Sokmensuer, C., & Gunduz-Demir, C. (2010). Color graphs for automated cancer diagnosis and grading. *IEEE Transactions on Biomedical Engineering*, 57(3), 665.
- [2] Gunduz-Demir, C., Kandemir, M., Tosun, A. B., & Sokmensuer, C. (2010). Automatic segmentation of colon glands using object-graphs. *Medical Image Analysis*, 14(1), 1-12.
- [3] Fu, H., Qiu, G., Shu, J., & Ilyas, M. (2014). A novel polar space random field model for the detection of glandular structures. *IEEE Transactions on Medical Imaging*, 33(3), 764.
- [4] Sirinukunwattana, K., Snead, D. R. J., & Rajpoot, N. M. (2015). A stochastic polygons model for glandular structures in colon histology images. *IEEE Transactions on Medical Imaging*, 34(11), 2366-2378.
- [5] Krizhevsky, A., Sutskever, I., & Hinton, G. E. (2012). Imagenet classification with deep convolutional neural networks. In *Advances in neural information processing systems* (pp. 1097-1105).
- [6] Ronneberger, O., Fischer, P., & Brox, T. (2015). U-net: convolutional networks for biomedical image segmentation, 9351, 234-241.
- [7] Huang, G., Liu, Z., Laurens, V. D. M., & Weinberger, K. Q. (2016). Densely connected convolutional networks. 2261-2269.
- [8] Goodfellow, I. J., Pouget-Abadie, J., Mirza, M., Xu, B., Warde-Farley, D., & Ozair, S., et al. (2014). Generative adversarial nets. *International Conference on Neural Information Processing Systems (Vol.3, pp.2672-2680)*. MIT Press.
- [9] Mirza, M., & Osindero, S. (2014). Conditional generative adversarial nets. *Computer Science*, 2672-2680.
- [10] Isola, P., Zhu, J. Y., Zhou, T., & Efros, A. A. (2016). Image-to-image translation with conditional adversarial networks. 5967-5976.
- [11] Zhang, H., Sindagi, V., & Patel, V. M. (2017). Image de-raining using a conditional generative adversarial network.
- [12] Yi, X., & Babyn, P. (2017). Sharpness-aware low-dose ct denoising using conditional generative adversarial network. *Journal of Digital Imaging*, 1-15.
- [13] He, K., Zhang, X., Ren, S., & Sun, J. (2016). Deep residual learning for image recognition. In *Proceedings of the IEEE conference on computer vision and pattern recognition* (pp. 770-778).
- [14] Sirinukunwattana, K., Pluim, J. P., Chen, H., Qi, X., Heng, P. A., Guo, Y. B., ... & Bł̄̄m, A. (2017). Gland segmentation in colon histology images: The glas challenge contest. *Medical image analysis*, 35, 489-502.
- [15] Paszke, A., Gross, S., Chintala, S., Chanan, G., Yang, E., DeVito, Z., ... & Lerer, A. (2017). Automatic differentiation in pytorch.
- [16] Kingma, D., & Ba, J. (2014). Adam: a method for stochastic optimization. *Computer Science*.
- [17] Real, R., & Vargas, J. M. (1996). The probabilistic basis of jaccard's index of similarity. *Systematic Biology*, 45(3), 380-385.

Image Processing, Textural Feature Extraction and Transfer Learning based detection of Diabetic Retinopathy

Anjana Umopathy,
Anusha Sreenivasan,
Divya S. Nairy
PES University, Bangalore

S Natarajan
PES University, Bangalore
natarajan@pes.edu

B Narasinga Rao
PES University, Bangalore
narsingrao@outlook.com

ABSTRACT

Diabetic Retinopathy (DR) is one of the most common causes of blindness in adults. The need for automating the detection of DR arises from the deficiency of ophthalmologists in certain regions where screening is done, and this paper is aimed at mitigating this bottleneck. Images from publicly available datasets STARE, HRF, and MESSIDOR along with a novel dataset of images obtained from the Retina Institute of Karnataka are used for training the models. This paper proposes two methods to automate the detection. The first approach involves extracting features using retinal image processing and textural feature extraction, and uses a Decision Tree classifier to predict the presence of DR. The second approach applies transfer learning to detect DR in fundus images. The accuracies obtained by the two approaches are 94.4% and 88.8% respectively, which are competent to current automation methods. A comparison between these models is made. On consultation with Retina Institute of Karnataka, a web application which predicts the presence of DR that can be integrated into screening centres is made.

CCS Concepts

•Applied computing → Bioinformatics;

Keywords

Computer Aided Diagnosis; Biomedical Image Processing; Textural Feature Extraction; Transfer Learning

1. INTRODUCTION

Diabetic Retinopathy (DR) is caused by high blood sugar levels which affect blood vessels in the retina. It is predicted that the number of people suffering from DR would grow from 126.6 million in 2010 to 191 million by 2030[1]. DR is diagnosed by ophthalmologists through the analysis of retinal fundus images, which is exacting and time-consuming. Automating the detection of DR would reduce the burden on the ophthalmologists so that they can focus on the patients in need, and will allow more patients to be screened.

Permission to make digital or hard copies of all or part of this work for personal or classroom use is granted without fee provided that copies are not made or distributed for profit or commercial advantage and that copies bear this notice and the full citation on the first page. Copyrights for components of this work owned by others than ACM must be honored. Abstracting with credit is permitted. To copy otherwise, or republish, to post on servers or to redistribute to lists, requires prior specific permission and/or a fee. Request permissions from permissions@acm.org.

ICBBB '19, January 7–9, 2019, Singapore, Singapore

© 2019 ACM. ISBN 978-1-4503-6654-0/19/01...\$15.00

DOI: <https://doi.org/10.1145/3314367.3314376>

Some of the manifestations in the retinal fundus image from which the pathology can be detected are hard and soft exudates, red lesions, and venous loops. The feature extraction and classification approach in this paper focuses on the detection of exudates and red lesions as these are the most prominent signs of DR. In addition to these, it also uses the textural features extracted from the image to classify it. The transfer learning approach takes into account the features of the image that the deep learning model finds to be the most significant for classification, which is determined by the model after being trained with sufficient images. The doctors in Retina Institute of Karnataka [2] were consulted for this study, and based on their inputs, an end to end web application which predicts the presence of DR given a retinal fundus image, which can be integrated into screening centres was developed. Utilising the diagnosis predicted by the application, the medical practitioners in the screening clinics can accordingly refer the patients in need to ophthalmologists.

The rest of this paper is organised as follows: Section 2 highlights the previous research done on automating the detection of DR. Section 3 details the implementation of the proposed approaches for the detection of DR. Section 4 involves the results and discussion of the methods used. Section 5 holds the conclusion of this paper.

2. RELATED WORK

Previous research and work done on automating the detection of Diabetic Retinopathy are discussed below:

Grace and Kajamohideen[3] developed a Computer-Aided Diagnostic system to classify images with DR. Image processing techniques including colour space conversion, Kirsch's template and histogram equalization were employed to detect exudates present in the image. Seven morphological features were extracted from the processed image. These features were input to an RBF-kernel SVM classifier to predict the presence of DR. This method illustrated good performance, but was restricted to the identification of exudates. According to the Diabetic Retinopathy Disease Severity Scale and International Clinical Diabetic Retinopathy Disease Severity Scale, there are many cases in Nonproliferative DR where exudates are not present[4]. These cases will go undetected by this approach.

Pratt et al. [5] proposed a CNN approach to diagnose and classify the severity of DR. The severity classes include no DR, mild DR, moderate DR, severe DR and proliferative DR. Max pooling was performed using a kernel with size 3x3 and strides 2x2. The CNN was flattened into one dimension after the last convolutional block. Overfitting was avoided using class weights relative to the number of images in the respective class. Images input to the classifier were subjected to colour normalisation and resized into 512x512

pixels. The Kaggle dataset was used to test this system and it gave an accuracy of 75%.

On interacting with doctors from multiple eye hospitals, it was found that although much research has been done on automating the detection of common medical conditions, there is no software that is currently being used by clinics or hospitals to automate the detection of DR. This paper describes an approach that could serve as a tool which can be integrated into screening clinics.

3. MATERIALS AND METHODS

3.1 Data Collection

Anonymised retinal fundus images obtained from the Retina Institute of Karnataka were used, along with images from the publicly available STARE [6] dataset for the feature extraction and classification approach. For the Transfer Learning approach, images from STARE, HRF [7] and Messidor [8] datasets were used to train the model.

3.2 Feature Extraction and Classification Approach

The feature extraction approach involved the detection of the most common manifestations of DR - exudates and red lesions, in the fundus image. The areas of these manifestations along with the textural features of the image, were input to an Information Gain Decision Tree classifier to predict the presence of DR.

3.2.1 Exudates Detection

3.2.1.1 Image Preprocessing.

The retinal image was masked around the field of view (FOV) using Hough circle detection [9]. A good contrast between the exudates and the background, as well as between the optic disc and the background is provided by the green channel. Thus, the green channel was used for the exudates detection and for making the optic disc mask.

3.2.1.2 Optic Disc mask creation.

Contrast Limited Adaptive Histogram Equalization [10] (CLAHE) was applied to enhance the contrast of the green channel of the image. To the result of this step, 2-D first derivative of Gaussian Matched Filter with dynamic thresholds corresponding to the image was applied. The maximum intensity point in the filtered image was found. This point corresponds to the optic cup, which is the brightest region of the optic disc. Using the average cup to disc ratio and size of the retina, a mask of optic disc was created using the optic cup as center. Important stages involved in the creation of optic disc mask are shown in Figure 1: For the image shown in Figure 1(a), the resultant image formed by applying CLAHE to the inversion of its green channel is shown in Figure 1(b). Figure 1(c) is the filtered image and Figure 1(d) shows the optic disc mask.

3.2.1.3 Detection of Exudates.

Illumination Equalisation was applied to the preprocessed image to overcome uneven illumination of the images and to make all the images belong to approximately the same intensity range.

$$IE(Image) = Box51(Image) - 128 \quad (1)$$

where IE represents Illumination Equalisation and Box51 represents a Box filter of size 51 x 51

A 2-D first derivative of Gaussian Matched filter was used to convolve over the illumination equalised image. Optic disc was masked from the filtered image. This is illustrated in Figure 2. Figure 2(a) shows the Illumination equalised image. Figure 2(b)

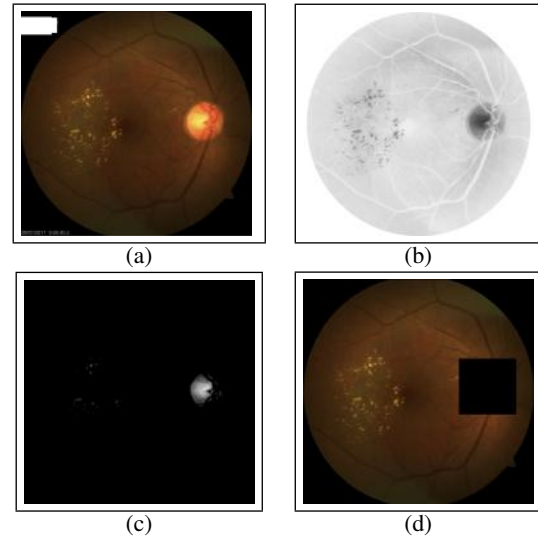


Figure 1: Optic Disc mask creation stages: For the image shown in (a) the resultant image formed by applying CLAHE to the inversion of its green channel is shown in (b). (c) is the filtered image and (d) shows the optic disc mask

shows the result of applying the exudates detection algorithm on Figure 1(a)

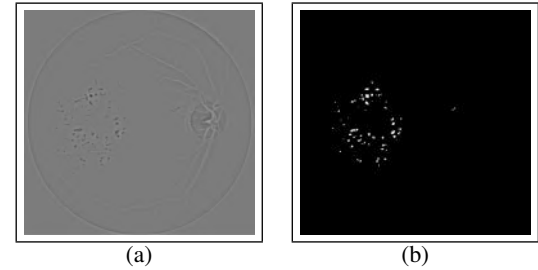


Figure 2: Exudates detection: (a) Illumination equalised image (b) Result of applying the exudates detection algorithm on Figure 1(a)

3.2.2 Red Lesions Detection

A good contrast between the red lesions and the background is provided by the green channel. To prevent the aberrant detection of bright regions (exudates and optic disc), a low intensity difference between them and the background is required, which is prominent in the red channel. To utilise the advantages of both the channels, the image formed by modifying the histogram of the green channel in accordance with that of the red channel was used. IE was employed to this image using Equation(1).

Simple image enhancement techniques like CLAHE and Contrast Stretching were used to enhance the contrast of the image while limiting the amplification of noise. This was followed by a 2-D Gaussian Matched Filter to match red lesion templates. The resulting image consisted of red lesions and blood vessels, which are similar in structure and colour, along with some noise. An opening morphological transformation with an elliptical kernel of size 7 was applied to the filtered image. Adaptive Gaussian Threshold-

ing, CLAHE and denoising were used on the filtered image to form the blood vessel mask. The blood vessel mask was applied to the morphologically transformed image to obtain the red lesions. The important stages in red lesions detection is illustrated in Figure 3: 3(a) is the original image, 3(b) is the histogram matched image, 3(c) is the filtered image 3(d) is the morphologically transformed image, 3(e) shows the blood vessel mask and 3(f) illustrates the red lesions detected.

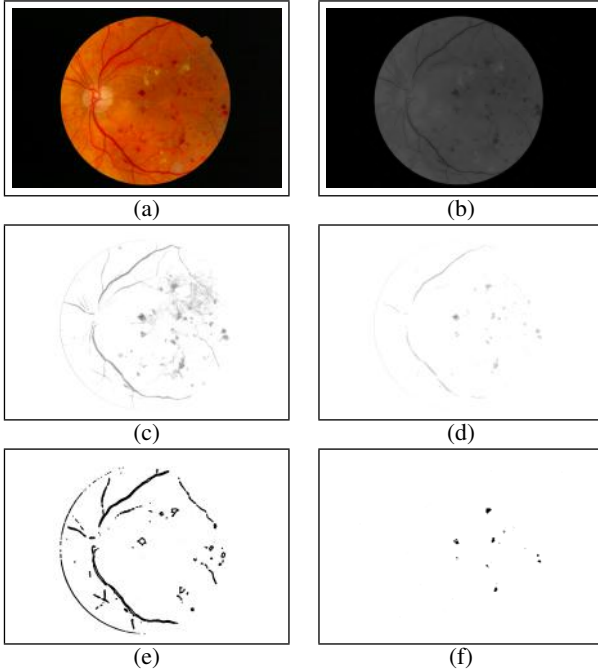


Figure 3: Important stages in red lesions detection: (a) Original image (b) Histogram matched image (c) Filtered image (d) Morphologically transformed image (e) Blood vessel mask (f) Red lesions detected

3.2.3 Textural Feature Extraction

Textural features [11] are quantifications of various textures perceived from an image. A grey level co-occurrence matrix (GLCM) was used for the calculation of the textural features of each image. To increase the accuracy of image classification and to make it less sensitive to the scale of each textural feature, the GLCM was normalised. 15 textural features were extracted, namely ASM, Energy, Dissimilarity, Entropy, Contrast, Correlation, Homogeneity, Sum of squares variance, Sum Average, Sum Variance, Sum Entropy, Difference Variance, Difference Entropy, Information Measure of Correlation - 1, and Information Measure of Correlation - 2, which are calculated using the formulae in Table 1.

3.2.4 Classification

The exudates area, red lesions area, and the 15 textural features extracted were input to Gini and Information Gain Decision Trees, Support Vector Machine with RBF Kernel and Linear Kernel and Feedforward Artificial Neural Network classifiers. The number of images of class DR was 89, while the number of images of class Normal (Healthy - No DR) was 25. To prevent class-bias and overfitting of the classifiers, stratified 5-fold cross validation was used. Table 2 shows the performance comparison of the classifiers. Since the Decision Tree with Entropy as the criterion for splitting had the

best cross validation accuracy and performance, it was the chosen as the final classifier for the feature extraction approach.

3.3 Transfer Learning

Transfer learning [12] was introduced to make machine learning systems leverage the knowledge learnt from the previous tasks for the current task. It has successfully been used to transfer knowledge and improve models from one domain with enough data to learn from, to a similar domain where not enough data is available. GoogleNet Inception-v3 [13], a deep Convolutional Neural Network (CNN) [14] with 22 layers was trained for the ImageNet challenge to classify 1,000,000 images into 1,000 classes. This pre-trained Inception-v3 deep CNN was used for image classification. The final layer of the CNN was re-trained to classify the images as DR and Normal. A total of 601 images labelled "Normal" and 761 images labelled "DR" from the online datasets HRF, STARE, and Messidor were used for training. An accuracy of 88.8% was obtained over the test dataset which was a combination of images provided by the Retina Institute of Karnataka along with images from the STARE dataset.

4. RESULTS AND DISCUSSION

The image processing, textural feature extraction and classification approach was developed using Open Source Computer Vision (OpenCV). This approach achieved an accuracy of 94.4% over a subset of the images in the STARE dataset, along with the dataset provided by the Retina Institute of Karnataka

TensorFlow was used to retrain the final layer of the pre-trained Inception-v3 deep CNN to classify the images as DR or Normal. Having an accuracy of 88.8% over the test dataset, the performance of this approach was slightly lower than the feature extraction approach.

To accommodate images from fundus cameras with varying focal length and images with varying illumination, the image processing method modifies all its images to match a baseline. During this process, some critical features of images with a different baseline may get obscured. This would reduce its performance with such images. However, it would perform very well with images having configurations similar to its baseline.

The transfer learning method uses a deep CNN which can capture all kinds of local and more abstract features of the image, and learns to adapt to different dataset configurations with increased range of datasets and images supplied for training the model, so it does better given a random image from any dataset or fundus camera, compared to the image processing method, but does not perform as well as the image processing method for images with a similar baseline.

The image processing method would be better suited for instances where the configuration of the images that will be input to it is known beforehand, and would perform well in screening clinics where the same fundus camera would be used to capture the retinal images. The transfer learning method would be of better use where the configuration of the image is not known, so it can be used in a website hosted on the internet for people to check the prediction of DR for a given retinal image from any dataset.

5. CONCLUSIONS

Two methods were used to detect the presence of DR in retinal fundus images. The first method employed image processing, textural feature extraction and classification using a decision tree with information gain classifier. The second method used Transfer Learning on the pre-trained GoogleNet Inception-v3 CNN. Both

Table 1: Textural Features Used

Texture Feature	Formula
ASM	$\sum_{i,j=0}^{levels-1} P_{i,j}^2$
Energy	\sqrt{ASM}
Dissimilarity	$\sum_{i,j=0}^{levels-1} P_{i,j} i-j $
Entropy	$-\sum_i \sum_j p(i,j) \log(p(i,j))$
Contrast	$\sum_{i,j=0}^{levels-1} P_{i,j}(i-j)^2$
Correlation	$\sum_{i,j=0}^{levels-1} P_{i,j} \left[\frac{(i-\mu_i)(j-\mu_j)}{\sqrt{(\sigma_i^2)(\sigma_j^2)}} \right]$
Homogeneity	$\sum_{i,j=0}^{levels-1} \frac{P_{i,j}}{1+(i-j)^2}$
Sum of squares variance	$\sum_i \sum_j (i-\mu)^2 p(i,j)$
Sum Average	$\sum_{i=2}^{2N_g} i p_{x+y}(i)$
Sum Variance	$\sum_{i=2}^{2N_g} (i-f_8)^2 p_{x+y}(i)$
Sum Entropy	$-\sum_{i=2}^{2N_g} p_{x+y}(i) \log\{p_{x+y}(i)\}$
Difference Variance	$\sum_{i=0}^{N_g-1} i^2 p_{x+y}(i)$
Difference Entropy	$-\sum_{i=0}^{N_g-1} p_{x-y}(i) \log\{p_{x-y}(i)\}$
Information Measure of Correlation - 1	$\frac{HXY - HXY1}{\max(HX, HY)}$, where $HXY1 = -\sum_i \sum_j p(i,j) \log\{p_x(i)p_y(j)\}$ and $HXY = -\sum_i \sum_j p(i,j) \log(p(i,j))$
Information Measure of Correlation - 2	$(1 - \exp[-2(HXY2 - HXY)])^{1/2}$, where $HXY2 = -\sum_i \sum_j p_x(i)p_y(j) \log\{p_x(i)p_y(j)\}$ and $HXY = -\sum_i \sum_j p(i,j) \log(p(i,j))$

Table 2: Classifier Comparison

Classifier	Mean Accuracy	Mean Precision	Mean Recall	F1 Score
Decision Tree (Gini)	0.849	0.919	0.836	0.876
Decision Tree (Information Gain)	0.944	0.926	0.953	0.939
SVM (RBF Kernel)	0.782	0.890	1	0.942
SVM (Linear Kernel)	0.765	0.893	0.944	0.917
Feedforward Artificial Neural Network	0.776	0.889	0.993	0.938
Logistic Regression	0.761	0.874	0.930	0.901

methods demonstrated good performance.

A web application was developed which would take as input a fundus image, and output the prediction of whether the image shows signs of DR or not. The screening clinics can integrate this tool with their systems so that the technician can refer the patients with the pathology to ophthalmologists.

The authors are currently collaborating with the doctors of Retina Institute of Karnataka to integrate the web application in diabetic screening centres.

6. ACKNOWLEDGMENTS

The authors thank Dr. Hemanth Murthy and Dr. Manjula V from Retina Institute of Karnataka, for their assistance in the detection of manifestations of DR, and for providing them with retinal images of patients to augment their dataset.

7. REFERENCES

- [1] Yingfeng Zheng, Mingguang He, and Nathan Congdon. The worldwide epidemic of diabetic retinopathy. *Indian journal of ophthalmology*, 60(5):428, 2012.
- [2] Retina institute of karnataka. <http://www.retinainstitute.org/>.
- [3] Annie Grace and S Kajamohideen. Diagnosis of diabetic retinopathy by extracting blood vessels and exudates using retinal color fundus images. 11:20–28, 01 2014.
- [4] Lihteh Wu, Priscilla Fernandez-Loaiza, Johanna Sauma, Erick Hernandez-Bogantes, and Marissé Masis. Classification of diabetic retinopathy and diabetic macular edema. *World journal of diabetes*, 4(6):290, 2013.
- [5] Harry Pratt, Frans Coenen, Deborah M. Broadbent, Simon P. Harding, and Yalin Zheng. Convolutional neural networks for diabetic retinopathy. *Procedia Computer Science*, 90:200 – 205, 2016. 20th Conference on Medical Image Understanding and Analysis (MIUA 2016).
- [6] AD Hoover, Valentina Kouznetsova, and Michael Goldbaum. Locating blood vessels in retinal images by piecewise threshold probing of a matched filter response. *IEEE Transactions on Medical imaging*, 19(3):203–210, 2000.
- [7] Attila Budai, Rüdiger Bock, Andreas Maier, Joachim Hornegger, and Georg Michelson. Robust vessel segmentation in fundus images. *International journal of biomedical imaging*, 2013, 2013.
- [8] Etienne Decencière, Xiwei Zhang, Guy Cazuguel, Bruno Lay, Béatrice Cochener, Caroline Trone, Philippe Gain, Richard Ordonez, Pascale Massin, Ali Erginay, Béatrice Charton, and Jean-Claude Klein. Feedback on a publicly distributed database: the messidor database. *Image Analysis & Stereology*, 33(3):231–234, August 2014.
- [9] Dana H Ballard. Generalizing the hough transform to detect arbitrary shapes. In *Readings in computer vision*, pages 714–725. Elsevier, 1987.
- [10] Stephen M Pizer, E Philip Amburn, John D Austin, Robert Cromartie, Ari Geselowitz, Trey Greer, Bart ter Haar Romeny, John B Zimmerman, and Karel Zuiderveld. Adaptive histogram equalization and its variations. *Computer vision, graphics, and image processing*, 39(3):355–368, 1987.
- [11] R. M. Haralick, K. Shanmugam, and I. Dinstein. Textural features for image classification. *IEEE Transactions on Systems, Man, and Cybernetics*, SMC-3(6):610–621, Nov 1973.
- [12] Lisa Torrey and Jude Shavlik. Transfer learning. *Handbook*

of Research on Machine Learning Applications and Trends: Algorithms, Methods, and Techniques, 1:242, 2009.

- [13] Christian Szegedy, Vincent Vanhoucke, Sergey Ioffe, Jon Shlens, and Zbigniew Wojna. Rethinking the inception architecture for computer vision. In *Proceedings of the IEEE Conference on Computer Vision and Pattern Recognition*, pages 2818–2826, 2016.
- [14] Alex Krizhevsky, Ilya Sutskever, and Geoffrey E Hinton. Imagenet classification with deep convolutional neural networks. In *Advances in neural information processing systems*, pages 1097–1105, 2012.

ICBBB 2019

Bioinformatics and Biosignal Analysis

Establishment of an Integrated Computational Workflow for Single Cell RNA-Seq Dataset

Miaomiao Jiang
School of Biological Science and
Medical Engineering, Southeast
University, Nanjing, China
86-18588964427
Cacti00@126.com

Qichao Yu
BGI-Shenzhen
Shenzhen, China
86-18576673283
yuqichao@genomics.cn

Jianming Xie [†]
School of Biological Science and
Medical Engineering, Southeast
University, Nanjing, China
86-025-83795174
xiejm@seu.edu.cn

Shiping Liu [†]
School of Biology and Biological
Engineering, South China University
of Technology, Guangzhou, China
86-13509653015
liushiping@genomics.cn

ABSTRACT

Single cell RNA-sequencing (scRNA-Seq) has emerged as a popular transcriptomic profiling approach to address long-standing questions on developmental biology and cancer biology. With the advent of increasing single-cell computational methods, it is not easy to determine which profiler to use. Here, we provide an integrated pipeline for both gene expression and genomic architecture analysis in single cells. Our pipeline reveals the global expression profile of the populations, and also identifies the changes in transcriptome/genome including alternative splicing (AS), single-nucleotide polymorphisms (SNPs), RNA editing and gene fusion.

CCS Concepts

Applied computing → Life and medical sciences → Bioinformatics

Applied computing → Life and medical sciences → Computational biology → Computational transcriptomics

Keywords

Single-cell RNA-Seq; Next-generation sequencing; Chronic lymphocytic leukemia

1. INTRODUCTION

Single cell RNA sequencing (scRNA-Seq) has been widely used in researches of various areas but not limited to tumorigenesis, neuroscience, metagenomics and evolution [1-3]. Although a numerous of pipelines have been published [4-6], few have introduced a series of toolkits inferring changes in genome from

Permission to make digital or hard copies of all or part of this work for personal or classroom use is granted without fee provided that copies are not made or distributed for profit or commercial advantage and that copies bear this notice and the full citation on the first page. Copyrights for components of this work owned by others than ACM must be honored. Abstracting with credit is permitted. To copy otherwise, or republish, to post on servers or to redistribute to lists, requires prior specific permission and/or a fee. Request permissions from Permissions@acm.org.

ICBBB '19, January 7–9, 2019, Singapore, Singapore

© 2019 Association for Computing Machinery.

ACM ISBN 978-1-4503-6654-0/19/01...\$15.00

DOI: <https://doi.org/10.1145/3314367.3314375>

RNA-Seq data. A typical scRNA-Seq pipeline focused on gene expression generally begins with quality control (QC) and read alignment, followed by quantification of gene expression levels. Softwares like FASTQC [7], Qualimap2 [8] and RSeQC [9] are commonly used for QC. Reads are mapped to genomic loci with tools such as HISAT [10] and STAR [11] and then normalized as TPM (Transcripts Per Million), FPKM (Fragments Per Kilobase of transcript per Million mapped reads), and RPM (Reads Per Million) using RSEM [12], HTSeq [13], WemIQ [14] etc. Afterwards, subpopulations are identified and characterized with RaceID3 [15], RCA [16] or other clustering algorithms. Furthermore, single cell sequencing data can shed lights on detailed trajectories of a biological process. For instance, methods like Monocle [17], Oscope [18] and TCM [19] can infer trajectories in cell differentiation.

In this study, we developed an efficient pipeline for full-length scRNA-Seq data analysis (shown in Figure 1), which meets the requirements of exploring of both expression patterns and structural features of a transcriptome. Starting from raw FASTQ files, the pipeline firstly applied quality control to the datasets, then mapped reads to the reference genome with STAR [11] and quantified the mRNA expression level using RSEM [12]. The landscape of gene expression were characterized mainly by Seurat [20]. Besides, changes in transcriptome including alternative splicing, SNPs, RNA editing, and gene fusion were assessed by appropriate tools.

2. MATERIALS AND METHODOLOGY

2.1 Preprocessing of scRNA-Seq Data

Raw sequencing data of chronic lymphocytic leukaemia (CLL) tumor cells [21] (renamed according to the sampling time) were downloaded from dbGAP on request. We assessed the read quality using FastQC (v0.11.5) [7] with default parameters. Cutadapt (v1.8) [22] was applied to the raw reads with parameter '-a GTCTCGTGGGCTCGG -A TCGTCGGCAGCGTC -mask-adapter --quality-base=64 --max-n=0.2'. Reads with adapter sequences or low-quality segments were removed from the downstream analysis. The high-quality reads were mapped to UCSC hg38 genome and transcriptome using STAR (v2.6.0c) [11]

[†] Corresponding author

using arguments ‘--genomeDir \$star_index_dir -twopassMode Basic -chimSegmentMin 12 --chimJunctionOverhangMin 12 --alignSJDBoverhangMin 10 --alignMatesGapMax 100000 --alignIntronMax 100000 --chimSegmentReadGapMax 3 --alignSJstitchMismatchNmax 5 -1 5 5 --outFilterMultimapNmax 10 --outSAMtype BAM SortedByCoordinate --outFilterType BySJout --outSAMstrandField intronMotif --quantMode TranscriptomeSAM’.

The output BAM files were sorted by reference coordinates and indexed with samtools (v1.5.0) [23]. We retained those single cells that yield more than five million mapped reads.

2.2 Expression Estimates

The TPMs for each gene/transcript was quantified by RSEM (v1.3.0) [12] and we limited the abundance estimation to known transcripts using “rsem-calculate-expression --alignments --no-bam-output --paired-end --single-cell-prior \$star_output_bam \$rsem_index_prefix”. Single-cell samples with distinct number of detected genes were considered as outliers and excluded.

Gene expression data of 49 CLL tumor cells were analyzed by Seurat (v2.3.2) [20] to identify subpopulations, where “bimod” test was used in the detection of marker genes in subpopulations. Subsequently, pathways of those differential expressed genes (DEGs) were enriched by clusterProfiler (v3.4.4) [24], with cutoff values of $p < 0.05$ and $q < 0.05$.

2.3 Alternative Splicing Detection

Splicing alterations were detected using junction reads from the output of aligner through Outrigger [25]. BAM files were firstly preprocessed by outrigger index. Then validation was done according to splice sites features by outrigger validate. While “percent spliced-in” (Psi/ Ψ) scores for skipped exon (SE) and mutually exclusive exon (MXE) events were estimated by outrigger psi. Subsequently, python package “anchor” [25] was applied to Psi matrix for feature identification, classifying alternative splicing events into included, excluded, bimodal, and multimodal according to psi distribution. Bimodal and multimodal AS events could be used for subpopulation identification with the help of their highly related genes. However, “anchor” was not included in the present pipeline on account of the vast majority of absent psi value in CLL dataset.

2.4 SNP Calling

SNPs were called following GATK workflow [26] using RNA-Seq data. We excluded SNP clusters or variants that were not passed the strand bias filter or read depth less than 20. The resulting callset in a single cell was combined using GATK toolkit “CombineVariants” [26] with the “-genotypeMergeOptions UNIQUIFY” option. Indels were removed by vcftools [27]. The remaining variants were annotated by Annovar [28], thus SNPs were defined as known SNPs (included in dbSNP [29]) and novel SNPs.

On the other hand, the coverage of variant sites was calculated by samtools [23] and finally integrated into the SNP matrix. We generate a binary matrix M for phylogenetic tree construction, where $M_{i,j}$ refers to genotype for variant site i in sample j . Mutations were removed when absent in less than 50% of cells, or observed in more than 80% of samples. SiFit [30] was employed for tumor phylogenetic inference under finite-sites models, taken M as the input. The SiFit method has taken the errors of single-cell sequencing into account and developed a heuristic search algorithm for phylogeny estimation

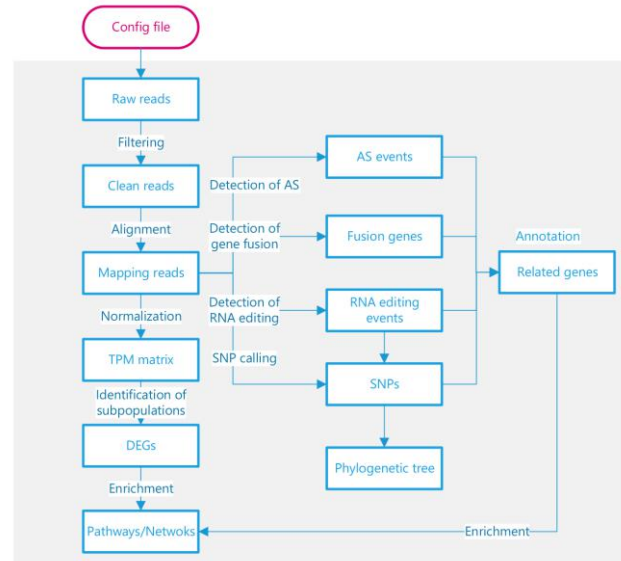


Figure 1. Overview of computational workflow for scRNA-Seq dataset

2.5 Detection of RNA Editing Events

We detected RNA editing sites using RED-ML [31] with commands “perl red_ML.v2.pl -rnabam \$BAM -reference \$GRCh38.primary.assembly.genome.fa -dbsnp dbsnp_151.hg38.vcf.gz -simpleRepeat simpleRepeat.bed -alu hg38.alu.bed”. Annotations were performed using Annovar [28] in editing sites with more than 20 supporting mutated reads. We then marked oncogenes and tumor suppressor genes using COSMIC database (release v84) [32].

2.6 Gene Fusion Detection

Fusion genes were predicted by STAR-Fusion (v1.4.0) [33] using BAM files from STAR aligner as inputs. Parameters “--FusionInspector inspect --FusionInspector validate --examine_coding_effect --extract_fusion_reads” were invoked for validation of fusion genes and exploration the impact of fusion events.

2.7 Availability

Codes and examples were provided online at <https://github.com/Cacti-Jiang/scICW>.

3. EXPERIMENT AND RESULT

3.1 Gene Expression Profiles of Single Cells

We download RNA-Seq data from dbGAP (phs001181.v1.p1). A total of 49 CLL tumor cells and 4 bulk samples were qualified for further analysis. The mean clean reads ranged from 5.43 Mb to 41.86 Mb in the single cell datasets. The mapping rate of most single cells (35/49) was over 75%, with more than 75% reads mapping to exonic regions. We filtered out genes with $TPM \leq 1$. Consequently, we obtained an average of 1430 and 22,540 genes for single cells and bulk samples respectively.

To assess the heterogeneity in tumor cells, a graph-based k Nearest-Neighbor method was employed for the identification of subpopulations. As presented in Figure 2A, CLL tumor cells sampling during 1982-2000 were divided into three groups. Group A mainly included cells from the early phase of observation (1982) or during recovery (1998). Most tumor cells sampled in the year

of progression made up of Group B. The majority of cells from 1995 were clustered into Group C, indicating a distinct expression

pattern in 1995.

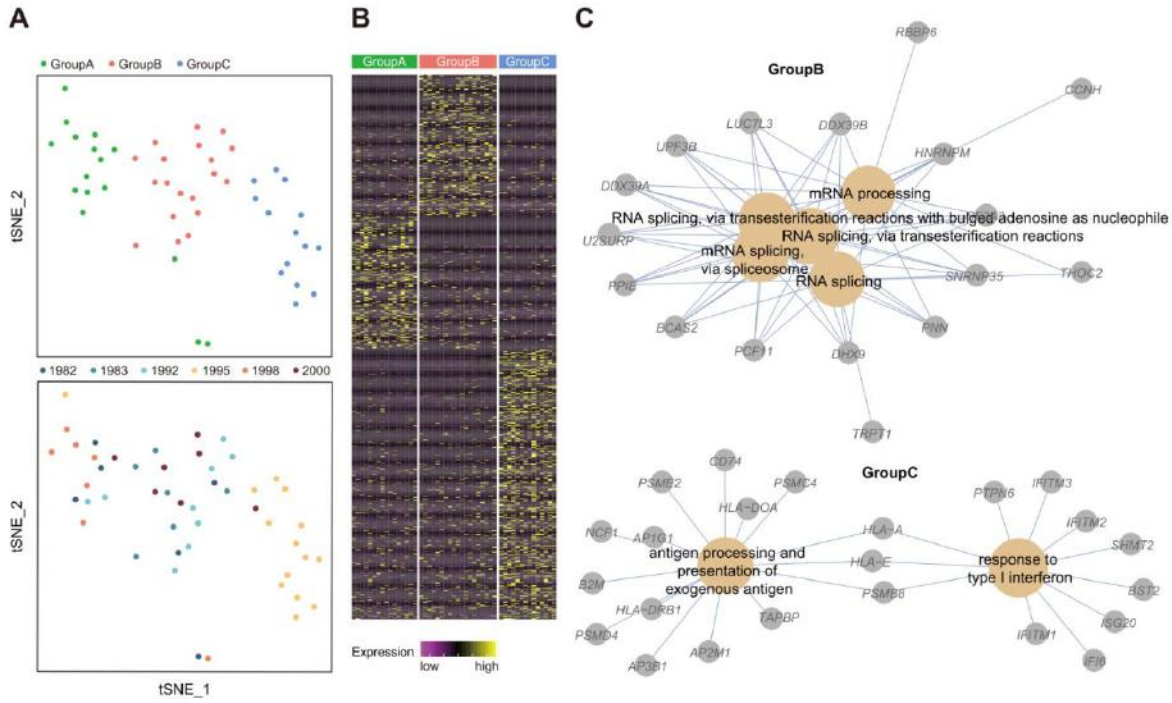


Figure 2. Gene expression profiles of 49 CLL tumor cells. (A) tSNE plot of CLL tumor cells. (B) Heat map of differentially expressed genes between subpopulations. (C) GO analysis for marker genes in Group B and Group C

Differential gene expression analysis was carried on the identified subpopulations, and 183, 196, 372 marker genes were obtained respectively (Figure 2B). *CCR6*, which is essential in the maturation and differentiation of antigen driven B-cells [34, 35], was upregulated in Group B. Immunosuppressive factor such as *TNFRSF14* [36, 37], *IL10RA* [38], *IL10RB* [39] were overexpressed in Group C. Gene ontology (GO) enrichment on DEGs shown in Figure 2C suggested a splicing activation in Group B. Meanwhile, cells in Group C presented the upregulation in “antigen processing and presentation of exogenous antigen” and “response to type I interferon” pathways, indicating that immune response is activated after cytotoxic therapy.

3.2 Characterization of Transcriptomic Architecture of a Single Cell

We further explored splicing alterations in the dataset. An average of 282 SE and MXE events were found, ranging from 23 to 487. Figure 3A illustrated that the number of AS events vary slightly from sampling time except 1998, which may be due to an improvement in the year. The frequency of AS events in different years was presented in Figure 3B, among which a vast majority of AS events were detected in a single cell. Bimodal exons constituted nearly a quarter of the AS events in the dataset, but it failed to aid in subpopulation classification due to excessive missing values.

SNPs calling from RNA-Seq data reflect changes on genomics to a certain extent. We ultimately obtained 200,910 SNPs from 49 CLL tumor cells. According to Figure 4A, over 80% SNPs were found in gene regions. SNPs in intron were the most common distribution in most years except 1995, which may be introduced by RNA editing. To further understand the effect of mutations,

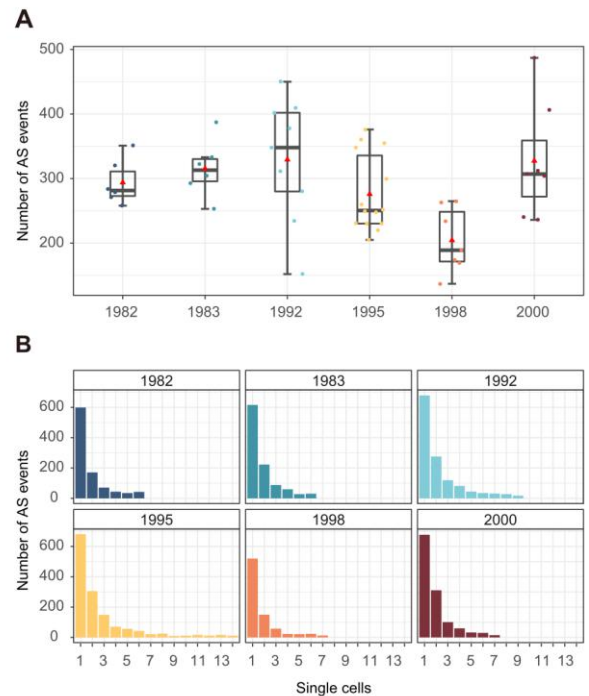


Figure 3. AS detection at the single cell level. (A) Boxplot showing AS events detected in single cells. (B) The frequency distribution of AS in cells sampled from different years. X-axis represents the number of single cells shared the same AS

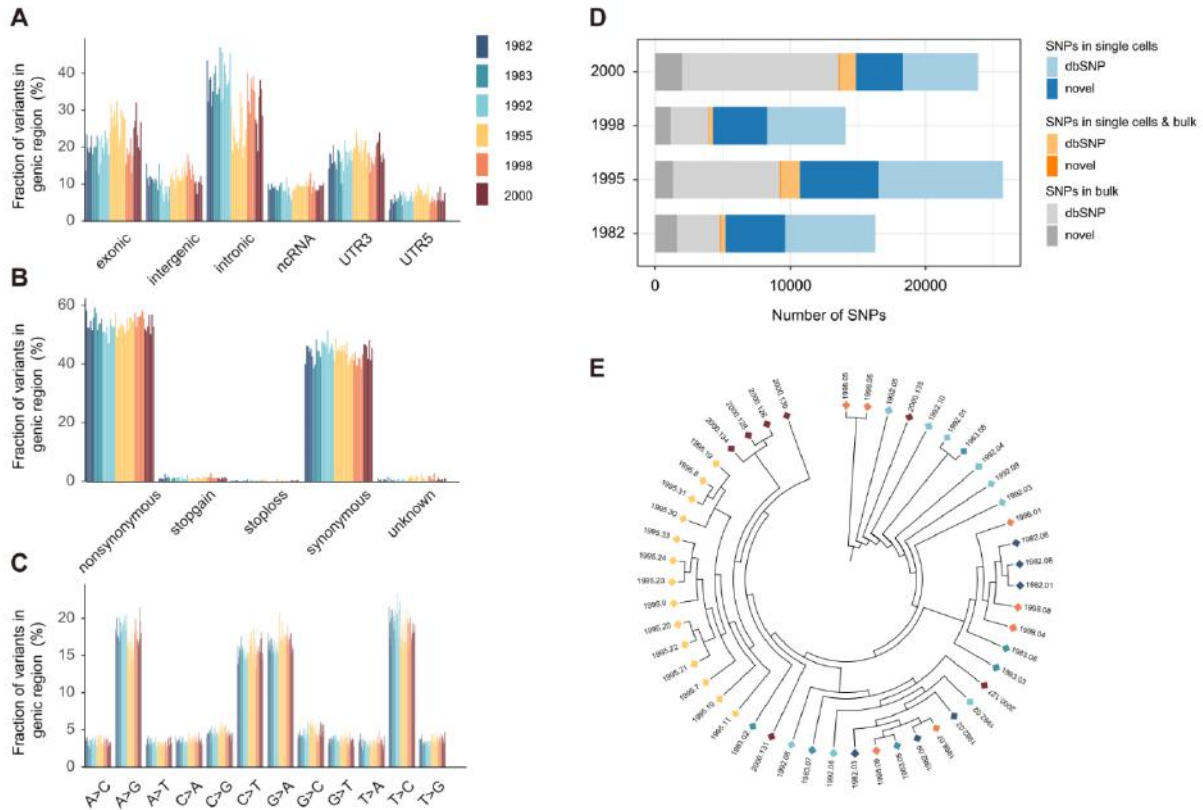


Figure 4. SNPs identified in single cells. The distribution of location (A), mutation type (B) and substitutions (C) of SNPs. (D) The percentages of SNPs shared between single cells and bulk samples. (E) Phylogenetic tree inferred from SNPs

variants in coding regions were assigned to nonsynonymous/synonymous SNPs. It can be seen from Figure 4B that more than half of the SNPs could modify the amino acid sequence of protein. Moreover, the most abundant types of RNA variants were A>G, T>G, C>T and G>A, among which A>G substitution was reported as the most frequently occurring RNA editing events as shown in Figure 4C. Surprisingly, single cells shared few SNPs with bulk populations, whereas variations in dbSNP comprised the majority (Figure 4D). Then we explored the effect of SNPs during tumor progression. Samples from 1995 were clustered together and resembled to a part of cells from 2000 in Figure 4E, suggesting a genomic distance in various cells.

Additionally, 111,558 RNA editing events in single cell dataset were detected in total, distinguishing editing sites from SNPs. As shown in Figure 5A, most RNA editing events occurred in intronic regions. Figure 5B indicated that the largest number of editing events/genes were identified in cells from the year 1995.

Gene fusion plays a crucial role in carcinogenesis so that a chimaera detection step was invoked in our pipeline. A small number of fusion genes were found, with the average number of 10 to 14 among different years (Figure 5C). A total of 479 chimaeras were detected in our single cell dataset, while 8 fusion genes were found in bulk populations. 57 fusion genes detected in more than 2 cells were listed in Figure 5D. It's worth noting that rearrangement between *MALATI* and *B2M*, which has not been reported previously in CLL, was detected in 5 cells (Figure 5E).

MALATI is an important long non-coding RNA (lncRNA) in tumor metastasis [40, 41], while *B2M* is reported as tumor suppressor gene in COSMIC database [32]. Therefore, we suppose that the *MALATI/B2M* fusion probably promotes tumor progression and metastasis.

4. CONCLUSION

In summary, we have presented an integrated pipeline for scRNA-Seq data analysis, which can be applied for either gene expression profiling exploration or detection of variants in genome based on RNA-Seq data. The pipeline is comprised of a variety of prevalent tools, which are suitable for researches on larger datasets. However, it is not applicable to studies using the unique molecular identifier (UMI)-tag-counting strategy, which fails to cover large segments of the gene body. While it is feasible to call SNPs using RNA-Seq data, the matched DNA-seq data are strongly recommended when calling variants such as SNPs and RNA editing sites.

Notably, coding in Perl, the pipeline is user-friendly. Researchers can easily adjust parameters in the config files to optimize the outputs. Indeed, our pipeline can be expediently reprogrammed with whichever toolkit the users preferred.

5. ACKNOWLEDGMENTS

The CLL dataset was provided by Zhikun Zhao. And We acknowledge Dr. Xiaoyun Huang and Dr. Ying Lei for comments on the manuscript.

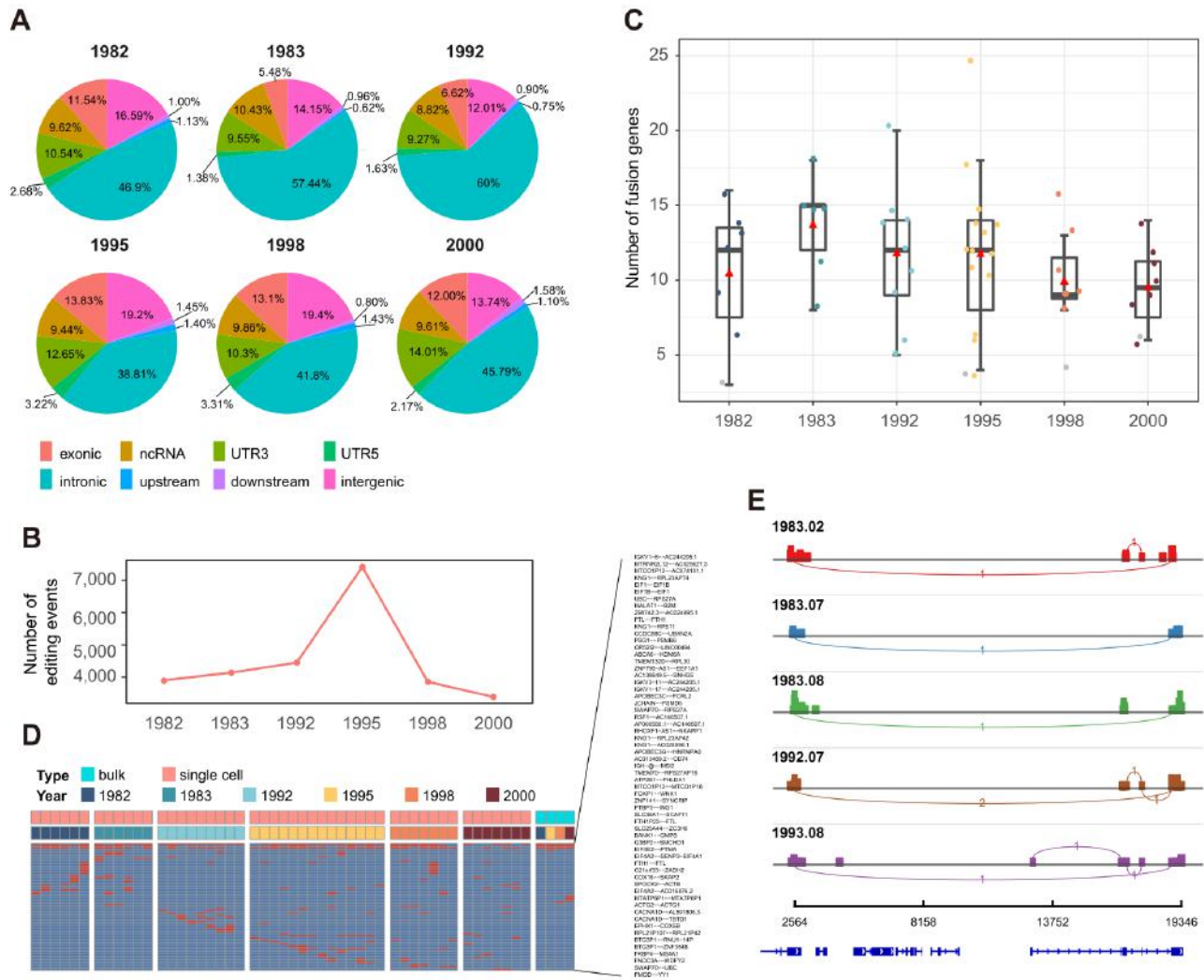


Figure 5. RNA editing and gene fusion detected in single cells. (A) The distribution of editing locus in different years. (B) The total RNA editing events in single cells. (C) The number of fusion genes in single cells. (D) Fusions observed in more than two single cells were displayed. (E) Sashimi plot of fusion gene *MALAT1/B2M* in 5 cells

6. REFERENCES

- [1] Pijuanasala, B., Guibentif, C. and Gütgens, B. 2018. Single-cell transcriptional profiling: a window into embryonic cell-type specification. *Nature Reviews Molecular Cell Biology*, 19(6).
- [2] Huang, X., Liu, S., Wu, L., et al. 2018. High Throughput Single Cell RNA Sequencing, Bioinformatics Analysis and Applications. Springer Singapore. 2018, 33-43.
- [3] Gawad, C., Koh, W. and Quake, S. R. 2016. Single-cell genome sequencing: current state of the science. *Nature Reviews Genetics*, 17(3), 175-188.
- [4] Guo, M., Hui, W., Steven, P. S., et al. 2015. SINCERA: A Pipeline for Single-Cell RNA-Seq Profiling Analysis. *PLoS Computational Biology*, 11(11), e1004575.
- [5] Torstenson, E. S., Li, B. and Li, C. 2013. ASAP: an environment for automated preprocessing of sequencing data. *Bmc Res Notes*, 6(1), 1-5.
- [6] McCarthy, D. J., Campbell, K. R., Lun, A. T. L., et al. 2017. Scater: pre-processing, quality control, normalization and visualization of single-cell RNA-seq data in R. *Bioinformatics*, 43(7), 1436-1449.
- [7] Andrews, S. 2010. FastQC. *A quality control tool for high throughput sequence data*
- [8] Okonechnikov, K., Conesa, A. and García-Alcalde, F. 2015. Qualimap 2: advanced multi-sample quality control for high-throughput sequencing data. *Bioinformatics*, 32(2), 292-294.
- [9] Wang, L., Wang, S. and Li, W. 2012. RSeQC: quality control of RNA-seq experiments. *Bioinformatics*, 28(16), 2184-2185.
- [10] Kim, D., Langmead, B. and Salzberg, S. L. 2015. HISAT: a fast spliced aligner with low memory requirements. *Nature methods*, 12(4), 357.
- [11] Dobin, A., Davis, C. A., Schlesinger, F., et al. 2013. STAR: ultrafast universal RNA-seq aligner. *Bioinformatics*, 29(1), 15-21.

- [12] Li, B. and Dewey, C. N. 2011. RSEM: accurate transcript quantification from RNA-Seq data with or without a reference genome. *BMC bioinformatics*, 12(1), 323.
- [13] Anders, S., Pyl, P. T. and Huber, W. 2015. HTSeq—a Python framework to work with high-throughput sequencing data. *Bioinformatics*, 31(2), 166-169.
- [14] Zhang, J., Kuo, C.-C. J. and Chen, L. 2014. WemIQ: an accurate and robust isoform quantification method for RNA-seq data. *Bioinformatics*, 31(6), 878-885.
- [15] Boisset, J.-C., Vivić J., Grün, D., et al. 2018. Mapping the physical network of cellular interactions. *Nature methods*, 1.
- [16] Li, H., Courtois, E. T., Sengupta, D., et al. 2017. Reference component analysis of single-cell transcriptomes elucidates cellular heterogeneity in human colorectal tumors. *Nature Genetics*, 49(5), 708-718.
- [17] Trapnell, C., Cacchiarelli, D. and Qiu, X. 2018. Monocle: Cell counting, differential expression, and trajectory analysis for single-cell RNA-Seq experiments.
- [18] Leng, N., Chu, L.-F., Barry, C., et al. 2015. Oscope identifies oscillatory genes in unsynchronized single-cell RNA-seq experiments. *Nature methods*, 12(10), 947.
- [19] Gong, W., Kwak, I.-Y., Koyano-Nakagawa, N., et al. 2018. TCM visualizes trajectories and cell populations from single cell data. *Nature communications*, 9(1), 2749.
- [20] Butler, A., Hoffman, P., Smibert, P., et al. 2018. Integrating single-cell transcriptomic data across different conditions, technologies, and species. *Nature Biotechnology*,
- [21] Zhao, Z., Goldin, L., Liu, S., et al. 2016. Evolution of multiple cell clones over a 29-year period of a CLL patient. *Nature communications*, 7, 13765.
- [22] Martin, M. 2011. Cutadapt removes adapter sequences from high-throughput sequencing reads. *EMBnet. journal*, 17(1), pp. 10-12.
- [23] Li, H., Handsaker, B., Wysoker, A., et al. 2009. The sequence alignment/map format and SAMtools. *Bioinformatics*, 25(16), 2078-2079.
- [24] Yu, G., Wang, L.-G., Han, Y., et al. 2012. clusterProfiler: an R package for comparing biological themes among gene clusters. *Omic: a journal of integrative biology*, 16(5), 284-287.
- [25] Song, Y., Botvinnik, O. B., Lovci, M. T., et al. 2017. Single-Cell Alternative Splicing Analysis with Expedition Reveals Splicing Dynamics during Neuron Differentiation. *Molecular Cell*, 67(1), 148-161.e145.
- [26] Van der Auwera, G. A., Carneiro, M. O., Hartl, C., et al. 2013. From FastQ data to high-confidence variant calls: the genome analysis toolkit best practices pipeline. *Current protocols in bioinformatics*, 43(1), 11.10. 11-11.10. 33.
- [27] Danecek, P., Auton, A., Abecasis, G., et al. 2011. The variant call format and VCFtools. *Bioinformatics*, 27(15), 2156-2158.
- [28] Wang, K., Li, M. and Hakonarson, H. 2010. ANNOVAR: functional annotation of genetic variants from high-throughput sequencing data. *Nucleic Acids Research*, 38(16), e164.
- [29] Sherry, S. T., Ward, M. H., Kholodov, M., et al. 2001. dbSNP: the NCBI database of genetic variation. *Nucleic Acids Research*, 29(1), 308.
- [30] Zafar, H., Tzen, A., Navin, N., et al. 2017. SiFit: inferring tumor trees from single-cell sequencing data under finite-sites models. *Genome biology*, 18(1), 178.
- [31] Xiong, H., Liu, D., Li, Q., et al. 2017. RED-ML: a novel, effective RNA editing detection method based on machine learning. *Gigascience*, 6(5), 1-8.
- [32] Forbes, S. A., Beare, D., Boutselakis, H., et al. 2017. COSMIC: somatic cancer genetics at high-resolution. *Nucleic Acids Research*, 45(D1), D777.
- [33] Haas, B., Dobin, A., Stransky, N., et al. 2017. STAR-Fusion: fast and accurate fusion transcript detection from RNA-Seq. *BioRxiv*, 120295.
- [34] Tsuruyama, T., Hiratsuka, T., Aini, W., et al. 2016. STAT5A Modulates Chemokine Receptor CCR6 Expression and Enhances Pre-B Cell Growth in a CCL20-Dependent Manner. *J Cell Biochem*, 117(11), 2630-2642.
- [35] Suan, D., Krautler, N. J., Maag, J. L. V., et al. 2017. CCR6 Defines Memory B Cell Precursors in Mouse and Human Germinal Centers, Revealing Light-Zone Location and Predominant Low Antigen Affinity. *Immunity*, 47(6), 1142-1153 e1144.
- [36] Zhao, Q., Zhang, G. L., Zhu, X., et al. 2017. The paradoxical changes of membrane and soluble herpes virus entry mediator in hepatocellular carcinoma patients. *J Gastroenterol Hepatol*, 32(8), 1520-1524.
- [37] Kotsiou, E., Okosun, J., Besley, C., et al. 2016. TNFRSF14 aberrations in follicular lymphoma increase clinically significant allogeneic T-cell responses. *Blood*, 128(1), 72-81.
- [38] Zadka, L., Kram, P., Kosciński, J., et al. 2017. Association Between Interleukin-10 Receptors and the CD45-Immunophenotype of Central Nervous System Tumors: A Preliminary Study. *Anticancer Res*, 37(10), 5777-5783.
- [39] Beguelin, W., Sawh, S., Chambwe, N., et al. 2015. IL10 receptor is a novel therapeutic target in DLBCLs. *Leukemia*, 29(8), 1684-1694.
- [40] Gutschner, T., Hämmerle, M. and Diederichs, S. 2013. MALAT1 — a paradigm for long noncoding RNA function in cancer. *Journal of Molecular Medicine*, 91(7), 791.
- [41] Gutschner, T., Hämmerle, M., Eißmann, M., et al. 2013. The non-coding RNA MALAT1 is a critical regulator of the metastasis phenotype of lung cancer cells. *Cancer Research*, 73(3), 1180-1189.

An Interactive Gameplay to Crowdsource Multiple Sequence Alignment of Genome Sequences: Genenigma

D. A. Meedeniya, S. A. P. A. Rukshan
Department of Computer Science and Engineering,
University of Moratuwa, Sri Lanka
{dulanim, amila.15}@cse.mrt.ac.lk

A. Welivita
École polytechnique fédérale de Lausanne, Lausanne,
Switzerland
kalpani.welivita@epfl.ch

ABSTRACT

Comparative genomics is a field of research that compares genomes of different organisms to identify common patterns. It is a powerful method used to identify the genetic diseases that cause mutations. Multiple Sequence Alignment (MSA) is an intermediate step in comparative genomics analysis that aligns three or more biological sequences of similar length. MSA is an NP-hard problem for which no efficient algorithm exists to perform this in a reasonable amount of time. However, humans across evolution have developed special intuition to identify visual patterns in short periods of time. Hence, a citizen science approach can be devised to solve the MSA problem by transforming it into a human computing game on creating visually similar patterns. In this paper, we introduce the mobile game “Genenigma”, which harnesses the human computing capability to align multiple sequences of genomes and use the results to help geneticists to understand the genetic code. The usability and performance scores of “Genenigma” predicts a larger user base than existing mobile games built for this purpose.

CCS Concepts

Applied computing → Life and medical sciences → Genomics → Computational genomics

Information systems → Information systems applications → Mobile information processing systems

Keywords

Comparative genomics; Multiple sequence alignment; Citizen science; Crowdsourcing; Gamification; Genenigma application

1. INTRODUCTION

Comparative genomics is a field of biological research where genomes of different species are compared to identify mutations that cause genetic diseases [1]. However, the NP hardness of multiple sequence alignment (MSA) problem, which is an intermediate step in comparative genomics analysis, poses significant challenges in this field.

Since the multiple sequences of DNA alignment require high computing capabilities [2], an alternative devises citizen science approaches can be used to solve the problem of MSA. Citizen

Permission to make digital or hard copies of all or part of this work for personal or classroom use is granted without fee provided that copies are not made or distributed for profit or commercial advantage and that copies bear this notice and the full citation on the first page. Copyrights for components of this work owned by others than ACM must be honored. Abstracting with credit is permitted. To copy otherwise, or republish, to post on servers or to redistribute to lists, requires prior specific permission and/or a fee. Request permissions from Permissions@acm.org.

ICBBB '19, January 7–9, 2019, Singapore, Singapore

© 2019 Association for Computing Machinery.

ACM ISBN 978-1-4503-6654-0/19/01...\$15.00

DOI: <https://doi.org/10.1145/3314367.3314374>

science is a contribution by the public to science and research by participating in crowdsourcing, data collection and analysis. By applying citizen science in genomic research, the general users can use their human computing ability to align sequences and contribute to solving the MSA problem. One such initiative is the development of human-computing games, where the players align multiple sequences under a given set of rules and constraints.

The number of smartphone users is estimated to grow from 2.1 billion in 2016 to around 2.5 billion in 2019. It has been observed that over 36% of the world's population is projected to use a smartphone by 2018, up from approximately 10% in 2011 [3]. Therefore, the smartphone can be considered as a suitable medium to reach a larger crowd. According to statistics, consumers spend more than 1 billion hours per month playing mobile games [4]. The time and effort spend on mobile games can be utilized productively for knowledge improvements of the users, while providing an entertainment factor. Thus, a problem can be converted to a mobile game that exploits the problem-solving capabilities of the general users. For example, mobile gaming applications can be built as a part of large-scale projects to collect data and analyze them with the use of crowd sourcing.

This paper introduces the human-computing mobile game, ‘Genenigma’ that solves the NP-hard computation problem of aligning multiple sequences of DNA. Genenigma is an easy to play game application with an underlying research purpose. DNA sequences are composed of four acids named Adenine (A), Cytosine (C), Guanine (G), and Thymine (T) [5].

```
ARMADILLO -----TGCTACTAATAT-----
COW          GCGTCTCTTT-----CTGCCCTGCAG
HORSE        GTCACAATTTAGGAAAGTCCCACTGGCCT
CAT          GTCACAGTTTAGGGGGTACTACTGGCAT
DOG          GTCACAATTTGGGGGATACTACTGGCAT
HEDGEHOG    GTCATAATTT-----GATTATATGGGCTT
MOUSE        GTCACAGTTTGGAGGATGTTACTGCACAT
RAT          GTCACAATTTGGAGGATGTTACTGGCAT
RABBIT       ATCACAATTTGGGGAACCCACTGGCAT
LEMUR        ATCACAA--TTGGGGG--TGCCACGGTCCCT
MOUSELEMUR  ATCACAG--TTGGGGGATGCCACTGGCCT
VERVET       GTCACAATTTGGGGGATGCTTCTGGCTC
MACAQUE      GTCACAATTTGGGGGATGCTTCTGGCTC
BABOON       GTCACAATTTGGGGGATGCTTCTGGCTC
```

Figure 1. Alignment of ACGT DNA sequences

Supplying these raw ACGT sequences (see Figure 1) to non-expert human users to be aligned is not effective. Instead, they are represented by four images that look like normal puzzle pieces and the entire alignment problem is represented as a puzzle game, which requires as much as similar pieces to be aligned under the same column. Additionally, Genenigma has a defined scoring system. Players can read the game rules and understand the scoring process. While playing the game they can use the clues that popup to improve their scores. If a player's score is higher than the available maximum score for a given alignment, those significant scores are stored for the use of geneticists. Geneticists can use this data to conduct research on genetic diseases such as cancers, heart and muscular and brain diseases that are involving the sensory system. The concept of this game is adapted from the

similar game “Phylo”, developed by Kawrykow et al. [6] in 2012. Our study explores the ways and aims to increase the usability of gamification. With the usability measures, it is expected to have a larger user base for Genenigma.

This paper is structured as follows. Section 2 describes the existing applications that use the concept of citizen science to process genomic and protein sequence data. Section 3 states the functional and non-functional requirements, the architecture and the scoring mechanism used in Genenigma. Specific implementation details of the game are presented in Section 4. Section 5 describes the testing procedure and the results in terms of the aspects; functionality, performance and usability. Section 6 concludes the paper indicating future possible extensions.

2. BACKGROUND

2.1 Human Computing Games

Different human computing games exist with an underlying research purpose and several of them use the concept of citizen science to solve problems in bioinformatics research. Phylo [6]-[8] and Bionigma [9], [10] are some of the existing such games. “Phylo” is developed by McGill University, Canada for DNA sequence alignment and it has been built as a web-based game. It is facilitated with both desktop and mobile application [8]. “Bionigma”, a collaborative game which is inspired by Phylo is developed for protein sequence alignment. It can be played on standalone PCs and supports different operating systems. This has been built using Unity game engine and contains attractive graphics. Both these games have their own scoring systems [9]. Even though web-based and PC versions of human computing games

are available for solving DNA and protein sequence alignment problems, they are not as popular as mobile games [11]-[13]. Although Phylo supports MSA of DNA, there is some negative user feedback, such as the inability to track user scores, not keeping the users logged in, difficulty to move puzzle pieces due to their small size and inability to zoom in and out [7].

There are different tools specifically developed for mobile game development. The Unity game engine, Corona SDK, Unreal engine, LibGDX, Flash and Action Script are some of them. LibGDX [14], [15] is a cross platform Java game development framework, which is capable of publishing games on Windows, Mac, Linux, Android, iOS, BlackBerry and HTML5, with the same code base. However, from the developer point of view, the lack of a visual editor is a limitation. Unity game engine [16] is also a cross platform game engine used primarily to develop both 3D and 2D video games for PCs, consoles and mobile devices. The benefit of using Unity over LibGDX is the visual editing for UIs and active community support. Popular 2D mobile games such as Angry Birds, Orio and Blind Forest have been developed using Unity. Since Unity 3D is a commercial product, it has been evolving and becoming easy to use. Thus, Unity3D has become a popular choice among modern day mobile game developers.

2.2 Multiple Sequence Alignment

Sequence alignment in bioinformatics is used to arrange the sequences of data such as DNA, protein in order to categorize similar regions based on the relationships among the sequences [17].

Table 1. Feature comparison of MSA approaches

Feature	Progressive approach	Iterative approach
Key idea	Mathematical process independent of the biological reality Heuristic method Starts with one sequence and progressively aligns the others Initially requires $n-1+n-2+n-3\dots n-n+1$ pairwise alignment	Realigns the sequences during multiple iterations of the process Iteratively realigns the initial sequences and adds new sequences to the growing MSA.
Alignment method	Let $x_1 \dots x_n$ be a sequence. Start with the most similar sequence. For each pair x_i, x_j , compute the pair-wise alignment - Align the new sequence with every previous sequence. - Create a distance matrix for each sequence pair. - Placing the sequences at the terminal nodes and create a phylogenetic “guide tree” from the matrices. - Determine the next sequence to be added to the alignment using the guide tree. - Preserve gaps. Merge the result to create MSA	Subgroups are selected based on the sequence relations on the guide tree/ random selection. Start with the pair-wise re-alignment of sequences within subgroups and then the re-alignment of the subgroups. -Compute the initial profile, by taking the highest scoring pair-wise alignment -Find the sequence, that is most similar and align with the profile; Repeat for all sequences in MSA -Obtain the convergence using an iterative process: for a given sequence x_i , align it against the profile of the other sequences to create new MSA
Plus points	A fast approach and efficient with large scale data A widely used method due to speed and accuracy	Optimization method
Uncertainty	MSA depends on the merging order Initial errors can propagate to the rest of the MSA. Not guarantee the optimal alignment. Can be a good or poor estimate Require user judgement for the reliability Low performance when the sequences are vaguely related	This can be resulted in local minima and can be slower, as it is inherited from optimization methods
Other facts	The initial decision is fixed Most successful implementation is Clustal Requires user input and skill	Use machine learning approaches such as genetic algorithms and Hidden Markov Models. Successful implementations are PRRP, MAFFT, MUSCLE

Genome sequences are analyzed to identify the functional regions including genes and regulatory regions in the sequences. There are two types of sequence alignments, (1) pair-wise alignment that

identifies similar regions between two biological sequences and (2) multiple sequence alignment (MSA) that considers more than two sequences of the same length. The goals of MSA can be identified

as: (1) summarize the sequence of data; (2) identify the variation among sequences; (3) use alignment model as a test hypothesis and (4) check whether a model reflects a known biological evidence [17][18]. MSA can be implemented using two main approaches, progressive and iterative. Table 1 states a comparison of these two approaches.

The progressive approach is a mathematical process that begins with one similar sequence and gradually align the other sequences. Progressive MSA is an efficient approach to align large scale sequences and a popular due to its speed and accuracy. However, this method does not ensure a globally optimal alignment as this is a heuristic method with a fixed initial decision and the errors can be propagated. Also, when the sequences are distantly related, this gives low performances.

Instead, the iterative approach re-aligns the initial sequences during the iterations of the process by adding new sequences to the growing MSA [17]. Here, the re-alignment of the sequence relations are made using guide tree and random selections. This is an optimal method that uses techniques such as genetic algorithms and Hidden Markov Models. There are several iterative methods such as PRRP, MAFFT, MUSCLE [19]. However, this process can be trapped in local minima and can be slower.

In order to fulfil the growing bioinformatics computational needs many techniques have been used in the literature, such as using GPUs with cloud computing [20], [21] and webservices [22] that enables high power computations. Alternatively, gamification together with crowdsourcing is a widely used method to acquire and analyze scientific data [12]. Based on the literature, human-computing systems are efficient in mobilizing general users and generating scientific data. Being a distributed production and problem-solving model in many domains, crowdsourcing gathers contributions from online communities [23].

Thus, we propose an approach for the MSA of a genome assembly using crowdsourcing with gamification. Our development of MSA is based on the progressive approach and use heuristics to get aligned the sequences. We have used the same concept as of Phylo, with more user friendly features and overcoming some of the limitations of Phylo game. We expect the proposed game to have a larger user base that will contribute to solving the problem of MSA in DNA sequences.

3. SYSTEM DESIGN

3.1 System Features

The main functional requirement of Genenigma is the ability to calculate the alignment score while the player is moving blocks. This requires an efficient score calculation algorithm that works in real-time. Section 4 describes the mechanism employed in Genenigma to calculate the alignment score. The system has functionalities to save the current level of the game and load the last saved level when the player continues playing. The non-functional requirements include real-time performance, ability to run on multiple mobile platforms, user friendly gaming interface and offline syncing of data. Also, the system should not crash or hang, other than due to an operating system or device fault.

Figure 2 shows the use cases view of the game application. Initially a new player must register for the system. Once the login

is successful, the user can start playing. When the player completes a level, his progress, alignments and scores are saved in a remote database. If the mobile device is not connected to the internet, it temporarily saves this data to a local database and later synchronizes with the main server. This data is made accessible for geneticists and other researchers as well. Once a player quits the game, his level is also saved and resumed when he returns.

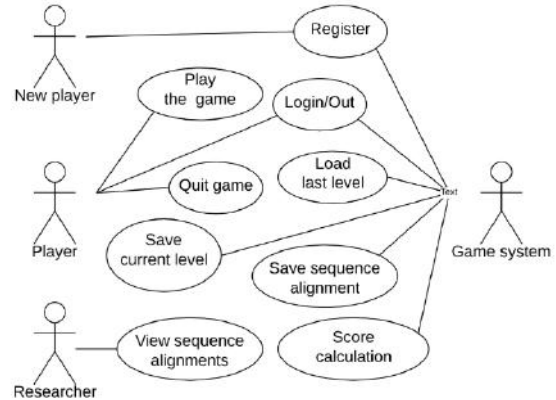


Figure 2. Usecase view of Genenigma

3.2 System Architecture

Figure 3 shows the component level architecture diagram of the system followed by descriptions of each component.

3.2.1 User-Interface

The user interface (UI) of the system is the touch sensitive display of the mobile device that the player holds. The main user inputs are a tap (touch), double tap, drag and drop, and slide. Tap on buttons will navigate to the corresponding menus, start/quit/save a game etc. A player can move puzzle pieces on the game board by dragging and dropping. A player can slide the background to view longer puzzle sequences. The outputs are perceived by the player in terms of audio, visual and haptic interactions happening between the player and the mobile device. Player activities and game responses are displayed visually on the device screen. Players hear background music and sense vibratory reactions when puzzle pieces collide with one another.

3.2.2 Game Runtime Environment

The player inputs are handled by the input handler. Responses to those inputs will map to one of the outputs described above after going through processing. Game data is stored in the application itself or in a backend database. Details of user accounts are stored in a remote database. The resource manager manages the memory and CPU processing to ensure efficient performance.

3.2.3 Game Logic

This component handles all the logic related to the game play. Calculating and updating the alignment score in real-time with each player movement is its main function. It has a script engine which consists of scripts attached to each game object in the core. The physics engine contains the logic to move the puzzle pieces and handle collisions. The movements are depicted as naturally as possible so that it never bores the player.

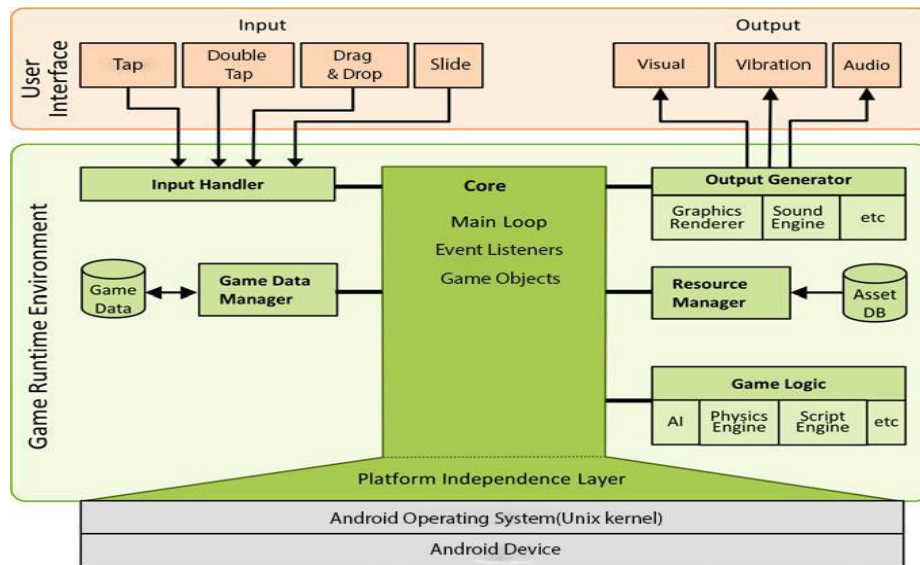


Figure 3. The component level architecture of the Genenigma system

3.2.4 Core Module

The Core module contains the game loop, event listeners and game objects. When a player drags and drops a puzzle piece, it executes the same code inside the loop that contains the logic for score calculation. This happens continuously until the player reaches or exceeds the available maximum score for that level. Then the player is re-directed to the next level where the score is re-calculated. The puzzle piece is game objects inside the core which listen to drag and drop events. A trigger ‘onEndDrag’ is set in each puzzle piece to notify the scoring functions to update the score each time a player releases a given piece.

3.3 Logical View of the System

Figure 4 shows the class interactions of the application. The class ‘BuildAncestorAndScore’ calculate the alignment score and building ancestor sequences. ‘AddSprites’ class loads new puzzle sequences to the game. All the classes named ‘UpdateX..XX’ listen to updates of the score and sub components of the score and refresh the visual score boards accordingly.

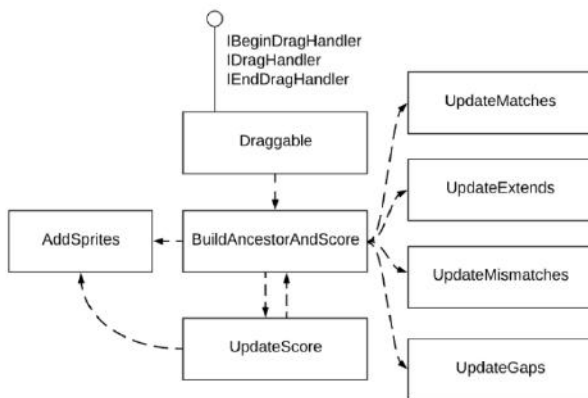


Figure 4. Logical design view of Genenigma

3.4 Process View of the System

Each sequence consists of four different puzzle pieces, which represent nucleotides A, C, G and T. Puzzle pieces can be moved (dragged and dropped) horizontally, swapping of pieces is not

allowed, however. After each player movement, the score is calculated as follows.

Consider the comparison of two sequences,

- Matches: If two similar puzzle pieces from two sequences occupy the same position in the horizontal axis, then the player earns +1.
- Mismatches: If two different puzzle pieces from two sequences occupy the same position in the horizontal axis, then the player earns -1 or -2.
- Gaps: If there exists a gap between two puzzle pieces in the same sequence, then the player earns -4 irrespective of the gap size.
- Extends: Each additional free space in a gap is considered as an extend and the player earns -1 per each extends.

Figure 5 shows the alignment of two sequences with matches, mismatches, gaps and extends. When this is applied to multiple sequences that form a phylogenetic tree, this sequence comparison needs to be done for all pairs of sequences in the alignment.



Figure 5. An alignment of two sequences

Figure 6 shows two separate phylogenetic trees and the green arrows show the pairs of sequences compared in it. Ancestor sequences are not shown in the diagram. For example, the first two sequences generate an ancestor sequence and it is compared with the third sequence.



Figure 6. Comparing sequences in two Phylogenetic trees

This is carried out iteratively until all given sequences in the phylogenetic tree are compared and the final score is calculated. This process is illustrated in Figure 7.

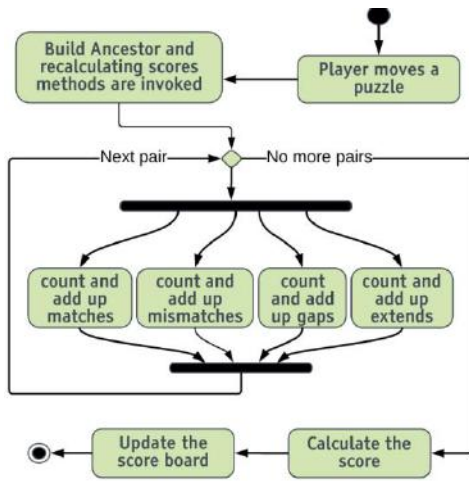


Figure 7. Activity diagram for score calculation

3.5 Data View of the System

Genenigma mobile application is designed by following the data-driven design principles in which game content such as sprites, textures and sounds are separated from the code. This separates game design from implementation and enables code reuse. In addition, the system uses a backend NoSQL database to store sequence alignment data, user account details and the current level and the current score at the time of quitting. It also uses a local embedded database to temporarily store results when network connectivity is not available. Once the connectivity is back, the system syncs this data with the backend server database and frees-up the device space. Figure 8 shows the structure of the NoSQL database the game uses. Data is saved in the database in JSON (Java Script Object Notation) format. A separate data management layer handles saving, retrieval and transfer of data.

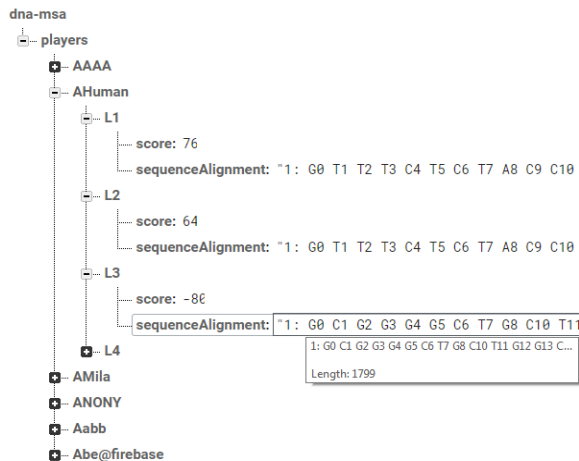


Figure 8. Database structure of Genenigma system

4. SYSTEM METHODOLOGY

4.1 Implementation Procedure

The application is developed using C# scripts. Unity Editor 2017.3 is used as the game engine. It is where all the scenes, menus and UIs reside. Graddle in JDK 1.8.0_101 and Android SDK 3.1.1 are used to build the application for Android mobile platform. To create graphics rich UIs, Adobe Photoshop CS6 is used. Firebase, a cloud-hosted real-time NoSQL database is used to save game scores and sequence alignments of a given player. Firebase is used, since it can persist data locally even when the device is not connected to the internet. This avoids the complexity of maintaining two databases, a local and a backend server database to maintain responsiveness while the user is offline. When the device is connected to the internet again, Firebase synchronizes all the local updates with the cloud database, automatically merging any conflicts. DC Free (Database Control Free) [24], which is a free asset available in Unity asset store is used to manage user accounts and authenticate users.

4.2 Score Calculation

It is important to measure the quality of MSA. The main techniques that can be used to measure the alignment accuracy are (1) Sum-of-pairs score (SPS) and (2) total-column score (TCS) [19]. SPS is the sum of all pair-wise induced alignment scores.

According to the literature, since the well-defined algorithms and better approximations are expensive to use for score calculations, we have used a simple scoring method similar to the scoring mechanism given in Phylo application. We have customized the existing scoring mechanism to make the game easier to play, increase the speed with a minor accuracy loss. For example, the value deducted from the final score due to the subsequent mismatches, extends and gaps, is reduced to avoid the score being rapidly reduced only after a few movements of play. In sequence alignments, some mismatches happen due to complementary pairs of nucleotides in DNA sequences and they are considered as key and lock pairs in biology [25]. For a better alignment, it is suitable to deduct a lower value from the score for a mismatch occurring due to a complementary pair of nucleotides than for a mismatch occurring due to a non-complementary pair. When a mismatch occurs, better alignment scores can be obtained by using a scoring matrix derived from statistical analysis of DNA data.

The pseudo-code of the main algorithm, which calculates the score for a given alignment is indicated in Figure 9. Each bold coloured method calculates its sub-score component according to the rules described in Section 3.5). This calculation is performed in each time a player changes the position of a puzzle piece. For this, the position of the puzzle piece and its attached tags are used.

```

Integer totalScore ← 0
for each (related pair of sequences and its
ancestor sequence in the dictionary) {
//calculating matches
Integer matches ← CalMatches (firstSeq,
secondSeq, AncestorSeq);

//calculating mismatches
Integer mismatches ← CalMismatches
(firstSeq, secondSeq);

//calculating gaps and gap extends
Integer gapsAndExtends ← CalGapsAndExtends
(firstSeq, secondSeq);

//calculating the total score for the
comparison
totalScore ← totalScore + matches -
mismatches - gapsAndExtends [0] -
gapsAndExtends [1];
}

```

Figure 9. Pseudo-code for score calculation

4.3 Genenigma User Interfaces

Figure 10 shows the main user interfaces of the game. The application starts with the login interface. The main menu appears once a player is successfully authenticated. There is a user instruction interface that describes how the game is played and how the score is calculated. Figure 10 (a) shows the interface that prompts the user to select a set of puzzle pieces. One set consists of four differently coloured puzzle pieces that represent ACGT nucleotides in a DNA sequence. The use of different coloured sets breaks the monotony and improves the player experience. Figure 10 (b) shows a snapshot of the game in play mode. It shows the score, the number of matches, mismatches, gaps and extends and the phylogenetic tree formed by the sequences. Images are included in the phylogenetic tree to show the organisms to whom the DNA sequences belong to. The puzzle pieces are draggable and longer sequences can be discovered by sliding the device screen. Figure 10 (c) shows the level completion interface which is prompted when the player completes all the stages in a level.

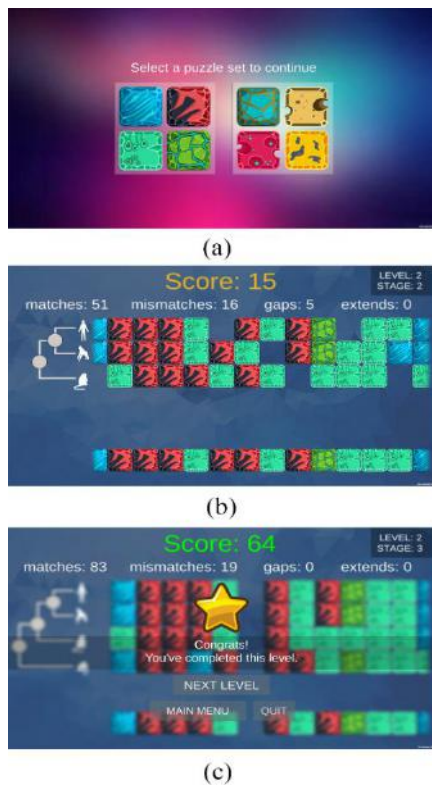


Figure 10. (a) Puzzle piece set selection, (b) Snapshot of the game play, (c) Interface prompted at level completion

We have improved the GUI of Genenigma, compared to Phylo. The UIs are made similar to the current puzzle games including high quality graphics, animations and sounds. Phylo contains much simpler and monotonous user interfaces having single coloured puzzle pieces and fewer animations. Genenigma also prompts pop up scores indicating whether the player movement is good or bad, while Phylo does not have this feature.

5. TESTING AND ANALYSIS

Genenigma [26] runs on the Unity Editor. For testing purposes, the game was built for Android OS and tested using a Samsung Note5 mobile device having the specifications indicated in Table 2. The performance and the usability aspects of the game were tested and compared with those of Phylo.

Table 2. Specifications of Samsung Galaxy Note5 model

Category	Specification
Operating System	Android 5.1.1 Lollipop, TouchWiz
Display	5.7-inch QHD (2560x1440, 518 ppi) Super AMOLED
Processor	Exynos 7420 octa-core (2.1GHz quad + 1.5GHz quad)
Storage	32GB
RAM	4GB (LPDDR4)

5.1 Performance Evaluation

Performance and usability are two important aspects of mobile games. Mobile devices have less computing power and memory capacity than personal computers. Therefore, it is important to devise mechanisms to reduce the consumption of power and memory. At the same time, mobile games should be user-friendly and appeal to the user. However, there is often a trade-off between these two aspects. Samsung's Smart Manager widget was used to monitor the speed and the memory usage of both Phylo and Genenigma. At the time of this evaluation McGill University has also upgraded Phylo using the Unity game engine. Thus, we have compared the two games that run on Unity, which is a fairer comparison. Table 3 shows the obtained performance measures.

Table 3. Performance comparison of Phylo and Genenigma

Feature	Phylo	Genenigma
Storage	61.73MB	71.1MB
RAM (Avg)	181.3MB	196.32MB
CPU usage	Negligible (0.0%)	Negligible (0.0%)
Data usage	Depends	Depends

When compared to Phylo, Genenigma consumes 15% more storage space and 8% more RAM. This is because Genenigma uses large and colourful images that are attractive to the users and easily touchable while Phylo has simple and small single coloured puzzle pieces that are less appealing and harder to touch. Thus, compared to the benefits gained in terms of usability, the higher usage of memory in Genenigma can be considered insignificant. Also, once the installation is complete, no static memory is consumed by Genenigma. Therefore, consumption of ~10MB more of RAM at the installation can be considered acceptable.

Each puzzle piece is an image and the memory usage is approximate to a number of images multiplied by the image size. The memory usage can be reduced by destroying game objects after each level that will release the used memory. Popup score animations are also game objects. These animations are also destroyed in the background. The player is unaware of all these functions happening in real-time at the back-end and is provided with a smooth and appealing game flow.

5.2 Feature Comparison

Genenigma gaming application has considered design constraints of crowdsourcing to find optimal evolutionary scenarios for genome transformations for the genome evolution with duplicate genes. Although, there are many MSA tools, it is identified that none of the tools are accurate for any data set and the tool selection is based on their popularity. Table 4 shows the feature comparison of this application with Phylo, which is an existing application that transforms an MSA problem into a set of puzzles with the intention of accuracy improvement of the comparison of DNA data.

Table 4. Feature comparison of Phylo and Genenigma

Property	Phylo [6][12]	Genenigma Tool
General features	Entertaining game No standard score to estimate the alignment quality Use a simple structure to guide the participants	Both general and expert users can play Attractive with high quality graphics, animations and sounds.
Task difficulty	Identify the useful features that predict - The difficulty level of the puzzle - Improvements of computer-generated alignment - The number of solutions needs to improve an MSA	Identify player strategies to solve the game by recording every move Adjusting difficulty levels of the game based on the player's skill level: longer and balanced trees are assigned to high levels.
Task aggregation	Describe the pipeline filtering and solution assemble Measure the improvements Estimate the efficiency Support the scientific interpretability of the data.	Includes a pop-up score prompt, that hints at the likelihood of the player's move that can increase the score, leading to produce high quality alignments with a minimum error. Consists with a leaderboard that shows the high scores for each level in the game, its sequence alignment, and the player. Thus, interested users can take the current best alignment (high-score), by giving their sequences as a level.
User profiling	Analyze individual player performance Characterize the performance of different level players. Regular players perform well on difficult puzzles by progressively identifying good alignments	Keep track of user profile data for performance measures Record all the sequence alignments corresponding to a player and identify top players according to the scores.
Prior knowledge	Anyone can use the game without a prior training or knowledge in biology	Alignment accuracy is independent of general and expert users

5.3 Usability Testing

The System Usability Scale (SUS) [27] was used to measure the usability of Genenigma. It consists of a 10-item questionnaire with five response options for respondents; from strongly agree to strongly disagree. This questionnaire was shared among a sample of undergraduate and postgraduate students, and the responses were collected separately. The Results of the responses were plotted in Figure 11.

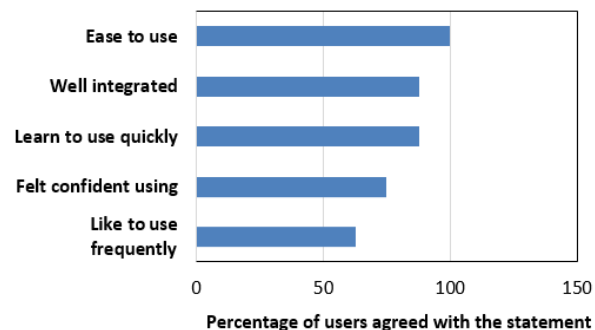


Figure 11. N-gram options vs. percentage users

All the players in the sample have agreed with the ease of the game. This is due to the easy navigation, familiar game objects (puzzles) and the supplied tutorial on score calculation. Next identical high percentile is reported for well-integrated and learn to use quickly items. This is because; score board and game play, stages and levels have been integrated well.

Once a player plays the first few introductory levels, then the player becomes familiar with the game. The item "Like to use" has a value of 63%, because the MSA game is simple and different than existing puzzle type mobile games. Since the purpose of this game is not completely entertainment, Genenigma has a level of complexity inherited by long gene sequences

6. CONCLUSION

This paper describes the design and implementation of a human computing game, Genenigma, which provides successful means of solving the multiple sequence alignment problem making use of the concept of citizen science. This tool considers the design constraints of the crowdsourcing game to find optimal evolutionary scenarios for genome transformations for the genome evolution with duplicate genes. The calculation of the alignment score in Genenigma is similar to the game "Phylo", which is a popular mobile game for aligning DNA sequences. According to the usability evaluation scores, Genenigma shows better improvement due to its user-friendliness, graphics rich interface, animations and sounds, and hence is expected to reach a larger community. Also this paper has considered optimization techniques for memory usage and process speed up.

As future enhancements, this game can be extended to compare multiple protein sequences. Efficient and effective methods for genome evolution with duplicate genes can be identified. A game needs to have an essence of excitement and curiosity for it to be more interesting. The strategies to solve the game by players can be identified by tracing user movements in the game play. The difficulty levels of the game can be adjusted based on the skill level of the players. This game currently contains only a few levels. But more challenging levels can be added including timeouts and accomplishments, which may add more anxious and excitement to the game, making it more interesting to play. The user performances can be measured by keeping track of profile data. Moreover, as the game reaches a large user base, the stored sequence alignments in the remote database will be made available for the access of researchers through a public website. Further, the design constraints of the game can be enhanced to get an optimal evolutionary scenario for genome transformations.

7. ACKNOWLEDGMENTS

The author acknowledges the support received from the Senate Research Committee Grant SRC/LT/2017/11, University of Moratuwa, Sri Lanka to conduct this research.

8. REFERENCES

- [1] Jordan, D. M., et al. 2015. Identification of cis-suppression of human disease mutations by comparative genomics. *Nature*. 524, (June 2015). 225–229. DOI= <http://dx.doi.org/10.1038/nature14497>
- [2] Zou, Q., Hu, Q., Guo, M., and Wang, G. 2015. HALign: Fast multiple similar DNA/RNA sequence alignment based on the centre star strategy. *Bioinformatics*. 31, 15 (Aug. 2015). 2475–2481. DOI= <https://doi.org/10.1093/bioinformatics/btv177>
- [3] The Statistics Portal. 2018. Number of smartphone users worldwide from 2014 to 2020. (May 2018). Retrieved from <https://www.statista.com>
- [4] Verto Analytics. 2018. How Big Is the Mobile Games Market?. (May 2018). Retrieved from <https://www.vertoanalytics.com/big-mobile-games-market/>
- [5] Egholm, M., Nielsen, P. E., Buchardt, O., and Berg, R. H. 1992. Recognition of Guanine and Adenine in DNA by Cytosine and Thymine Containing Peptide Nucleic Acids (PNA). *Journal of the American Chemical Society* 1992. 114, 24 (Nov, 1992). 9677–9678. DOI= <https://doi.org/10.1021/ja00050a068>
- [6] Kawrykow, A., et al. 2012. Phylo: A Citizen Science Approach for Improving Multiple Sequence Alignment. *PLoS One*. 7, 3: e31362 (Mar. 2012). 1-9. DOI= <https://doi.org/10.1371/journal.pone.0031362>
- [7] Phylo. 2018. Phylo DNA Puzzle. (April, 2018). Retrieved from <https://phylo.cs.mcgill.ca/>
- [8] Kwak, et al. 2013. Open-Phylo: a customizable crowd computing platform for multiple sequence alignment. *Genome Biology*. 14: R116 (Dec. 2013). 1-11. DOI = <http://doi.org/10.1186/gb-2013-14-10-r116>
- [9] Göbel, S. 2016. Serious Games Application Examples. Därner, R., Göbel, S., Effelsberg, W., Wiemeyer, J. Ed. *Serious Games*. Springer, Cham, (Aug. 2016). 319-405. DOI https://doi.org/10.1007/978-3-319-40612-1_12
- [10] Hess, M., Wiemeyer, J., Hamacher, K., and Goesele, M. 2014. Serious Games for Solving Protein Sequence Alignments - Combining Citizen Science and Gaming. Göbel, S., Wiemeyer, J. Ed. *Games for Training, Education, Health and Sports*. GameDays 2014. LNCS, 8395 (2014). Springer, Cham. 175-185. DOI= https://doi.org/10.1007/978-3-319-05972-3_18
- [11] Burnett, S., Furlong, M., Melvin, P. G., and Singiser, R. 2016. Games that Enlist Collective Intelligence to Solve Complex Scientific Problems. *Journal of Microbiology & Biology Education*. 17, 1 (March 2016), 133-136. DOI = <http://doi.org/10.1128/jmbe.v17i1.983>
- [12] Singh, A., Ahsan, A., Blanchette, M., and Waldspühl, J. 2017. Lessons from an Online Massive Genomics Computer Game. In *Proceedings of the Fifth AAAI Conference on Human Computation and Crowdsourcing*. (Québec, Canada, October 24-26, 2017). AAAI Publications. 177-186.
- [13] Baaden, M., Delalande, O., Ferey, N., Pasquali, S., Waldspühl, J., and Taly, A. 2018. Ten simple rules to create a serious game. illustrated with examples from structural biology. *PLoS Comput Biol* 14, 3: e1005955 (Mar. 2018). DOI= <https://doi.org/10.1371/journal.pcbi.1005955>
- [14] Libgdx. 2018. Cross Platform game development. (April 2018). Retrieved from <https://libgdx.badlogicgames.com/>
- [15] Cook, M., Colton, S., Raad, A., and Gow, J. 2013. Mechanic miner: Reflection-driven game mechanic discovery and level design. Esparcia-Alcázar, A.I. Ed. *Applications of Evolutionary Computation*, 7835 (2013), LNCS, Springer, Berlin, Heidelberg. 284–293. DOI = https://doi.org/10.1007/978-3-642-37192-9_29
- [16] Unity game engine. 2018. The world’s leading content-creation engine. (April 2018). Retrieved from <https://unity3d.com/unity>
- [17] Gollery, M. 2004. *Bioinformatics: Sequence and Genome Analysis*. 2nd ed. Mount, D. W., Cold Spring Harbor, New York, (Oct. 2005). DOI= <http://doi.org/10.1373/clinchem.2005.053850>
- [18] Blanchette, M., et al. 2004. Aligning Multiple Genomic Sequences with the Threaded Blockset Aligner. *Genome Research*, 14, 4 (April 2004). 708–715. DOI= <http://doi.org/10.1101/gr.1933104>
- [19] Edgar, R. C. 2004. MUSCLE: multiple sequence alignment with high accuracy and high throughput. *Nucleic Acids Research*, 32, 5 (Mar. 2004), 1792–1797. DOI= <http://doi.org/10.1093/nar/gkh340>
- [20] Welivita, a., Perera, I., and Meedeniya, D. 2017. An Interactive Workflow Generator to Support Bioinformatics Analysis through GPU Acceleration. In *Proceedings of the international Conference on Bioinformatics and Biomedicine*. (Kansas City, MO, USA. Nov. 13-16, 2017). 457-462. DOI= <https://doi.org/10.1109/BIBM.2017.8217691>
- [21] Welivita, A., et al., Managing Complex Workflows in Bioinformatics: An Interactive Toolkit with GPU Acceleration. *IEEE Transactions on NanoBioscience*, 17, 3 (2018). 199-208. DOI= <https://doi.org/10.1109/TNB.2018.2837122>
- [22] Mallawaarachchi, V., et al. 2018. Efficient Bioinformatics Computations through GPU Accelerated Web Services. In *Proceedings of the 2nd International Conference on Algorithms, Computing and Systems* (Beijing, China. July 27 – 29, 2018). ACM, New York, NY. 94-98. DOI= <https://doi.org/10.1145/3242840.3242848>
- [23] Hewawalpita, S., Herath, S., Perera, I., and Meedeniya, D. 2018. Effective Learning Content Offering in MOOCs with Virtual Reality: An Exploratory Study on Learner Experience. *Journal of Universal Computer Science*, 24, 2 (Feb. 2018). 129-148.
- [24] Unity asset store. 2018. Database Control Free. (April. 2018). Retrieved from <https://assetstore.unity.com/>
- [25] Morrison, J. L., Breitling, R., Higham, D. J., and Gilbert, D. R. 2006. A lock-and-key model for protein–protein interaction. *Bioinformatics*. 22, 16 (Jun 2006), 2212-2019. DOI= <https://doi.org/10.1093/bioinformatics/btl338>
- [26] Genenigma app. 2018. Google drive repository. https://drive.google.com/file/d/1q5yts8HxBPT_Doly5NkRqMEXiB-0owlG/edit
- [27] Bangor, A., Kortum, P. T., and Miller, J. T. 2009. Determining what individual SUS scores mean: Adding an adjective rating scale. *Journal of Usability Studies*. 4, 3 (May 2009). 114-123.

A Hybrid Approach to Optimize the Number of Recombinations in Ancestral Recombination Graphs

Nguyen Thi Phuong Thao
Institute of Information Technology
Vietnam Academy of Science and Technology
+84-9-1621-8689
thaontp@ioit.ac.vn

Le Sy Vinh
University of Technology and Engineering
Vietnam National University, Hanoi
+84-9-0226-2444
vinhls@vnu.edu.vn

ABSTRACT

Building ancestral recombination graphs (ARG) with minimum number of recombination events for large datasets is a challenging problem. We have proposed ARG4WG and REARG heuristic algorithm for constructing ARGs with thousands of whole genome sequences. However, these algorithms do not result in ARGs with minimal number of recombination events. In this work, we propose GAMARG algorithm, an improvement of ARG4WG, to optimize the number of recombination events in ARG building process. Experiment with different datasets showed that GAMARG algorithm outperforms other heuristic algorithms in building ARGs for large datasets. It also is much better than other heuristic algorithms and comparable to exhaustive search methods for small datasets.

CCS Concepts

Applied computing → Life and medical sciences → Bioinformatics

Keywords

Ancestral recombination graphs; Minimal ARG; Minimum number of recombinations; Recombination breakpoint

1. INTRODUCTION

Ancestral recombination graph (ARG) plays a central role in the analysis of within-species genetic variations [1]. The relationships between current species and common ancestors can be described by coalescence, mutation and recombination events in the ARG (Figure 1). Looking backward in time, the coalescence events merge two identical sequences to one; the mutation events make change in a site of the sequence; the recombination events break one sequence to two subsequences that then make change in the genetic information of the next generations. So the mutation and recombination events are important factors in consideration when building ARGs.

Approaches have been proposed to infer ARGs. Most of methods use the infinite-sites assumption that does not allow back and recurrent mutation in a single site. Thus, they try to build ARGs

with the minimum number of recombination events. This is proved an NP-hard problem [2].

Several methods have been proposed to construct ARGs with optimal number of recombination events (called minimal ARGs) for small datasets. Song et al. [3] built minimal ARGs by scanning all possible ways and selecting the best way to move trees for each marker from left to right along the sequence to optimize the number of recombination events. Given a number of recombination events, Lyngsø et al. [4] tried to construct an ARG using a branch and bound algorithm. If it is impossible to have an ARG, the number of recombination events is increased by one. The process is continued until an ARG is constructed. All these exhaustive search methods have very high computational complexity. They are just able to work with up to dozens of short sequences.

To deal with larger datasets, other heuristic methods have been proposed. In spite of focusing on building minimal ARGs, they try to build plausible ARGs. Margarita proposed by Minichiello and Durbin [5] can handle a thousand sequences with hundreds of markers; ARG4WG of our group [6] can handle thousands of whole human genomes. The longest shared ends criterion in building ARGs allows ARG4WG to work on large datasets with less number of recombination events than Margarita. Our experiments showed that ARG4WG is able to build ARG with fewer number of recombination events than Margarita but still does not reach the minimal ARGs.

To build large ARGs with minimum number of recombination events, we evaluated the effect of different factors on reducing the number of recombination events in ARG building process for genome-wide and suggested a new design of ARG4WG, called REARG [7]. Specifically, we combined some other factors such as similarity between sequences and the length of sequences into REARG. This strategy enables REARG to build ARGs with a smaller number of recombination events in comparison to ARG4WG. However, REARG still is not as good as other exhaustive search methods.

As the longest shared ends criterion does not result in the minimum number of recombination events (Figure 2b), we should combine ARG4WG with other optimal criteria to reduce the recombination events. Notably, the four-gamete test [8] is the key idea leading to various methods either to find the lower bound of the number of recombination events or to construct explicitly minimum recombination ARG. In this work, we propose GAMARG method to build large ARGs with the minimum number of recombination events. Our experiments on different datasets showed that GAMARG algorithm is able to handle thousands sequences with tens of thousands of markers, and also could reach the minimum recombination ARGs.

Permission to make digital or hard copies of all or part of this work for personal or classroom use is granted without fee provided that copies are not made or distributed for profit or commercial advantage and that copies bear this notice and the full citation on the first page. Copyrights for components of this work owned by others than ACM must be honored. Abstracting with credit is permitted. To copy otherwise, or republish, to post on servers or to redistribute to lists, requires prior specific permission and/or a fee. Request permissions from Permissions@acm.org.

ICBBB '19, January 7–9, 2019, Singapore, Singapore

© 2019 Association for Computing Machinery.

ACM ISBN 978-1-4503-6654-0/19/01\$15.00

DOI: <https://doi.org/10.1145/3314367.3314385>

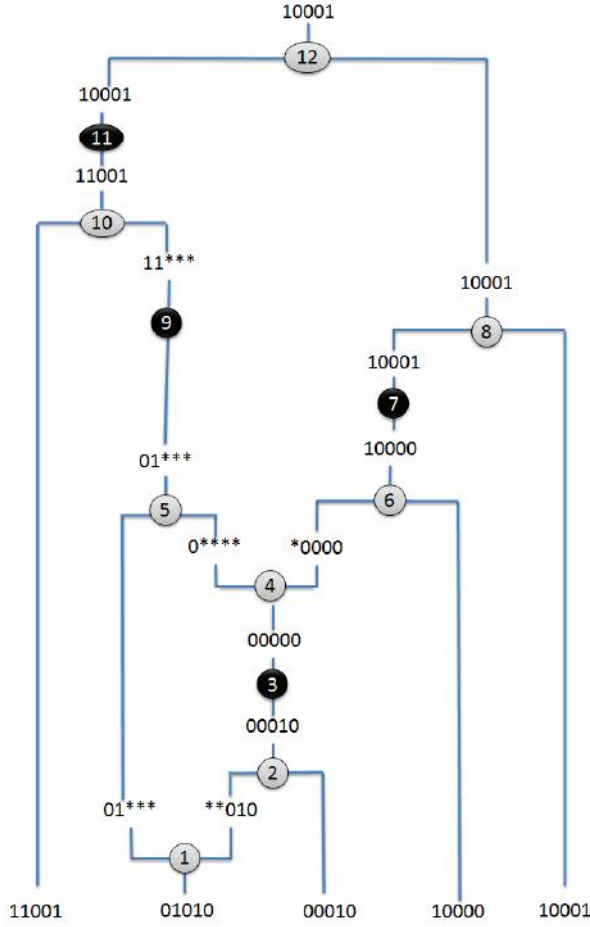


Figure 1. An example of an ARG for 5 sequences of length 5

The paper is organized as follows. In section II, we introduce the ARG building problem. Some problems in choosing the breakpoint position in recombination step of four-gamete test method and ARG4WG algorithm that directly affect to the number of recombination events in ARG building process are pointed out in section III. The GAMARG algorithm will also be proposed in this section. The performance of our algorithm in comparison to other heuristics and exhaustive search methods is discussed in section IV. Finally, we conclude our work and suggest some future works.

2. ARG BUILDING PROBLEM

Given a set $D = \{S_1, \dots, S_N\}$ of N input sequences (haplotypes), S_x has m markers, $1 \leq x \leq N$; $S_x[i]$ denotes site i of S_x that has the value of either 0 (one of the SNP alleles), or 1 (another allele), $1 \leq i \leq m$. The ARG building problem is to construct the relationships between sequences in D through three events: coalescence, mutation, and recombination. The coalescence events merge two identical sequences to one. The mutation event makes change in a site of the sequence. The recombination event breaks one sequence to two subsequences, one subsequence contains the prefix of the sequence and one contains the suffix of the sequence. Our task is to build an ARG with the minimum number of recombination events under the infinite-sites assumption.

Consider a data set $D(5) = \{S_1, S_2, S_3, S_4, S_5\}$ of 5 sequences with 5 sites as below:

	1	2	3	4	5
S_1	1	1	0	0	1
S_2	0	1	0	1	0
S_3	0	0	0	1	0
S_4	1	0	0	0	0
S_5	1	0	0	0	1

Figure 1 is an example of an ARG building process for $D(5)$. An ARG with 12 events (numbered from 1 to 12 in circles) is built backward in time, starting from the input data, until a single common ancestor (10001) is reached. A "*" at a site denotes a non-ancestral material. 3 different evolutionary events are performed in the building process. A recombination event as in the state 1 breaks a sequence 01010 into two sub-sequences: 01*** contains the prefix and **010 contains the suffix of the sequence 01010. A coalescence event as in the state 2 combines two sequences **010 and 00010 into one sequence 00010. A mutation event as in the state 3 changes a mutated site 4 from 1 to 0.

3. METHOD

3.1 Four-Gamete Test

Under the infinite-site assumption, we called two sites i and j incompatible if they contain all four gametic types 00, 01, 10, 11 [3]. There will be at least one recombination event between two incompatible sites i and j . The exhaustive methods aim to find out the optimal breakpoints, that is, the smallest number of recombination events, to break all these incompatible sites.

Let $FreqGamete_{i,j} = \{freq00_{i,j}, freq01_{i,j}, freq10_{i,j}, freq11_{i,j}\}$ be the frequencies of gametic types 00, 01, 10, 11 occurring between sites i and site j , respectively.

In the data set $D(5)$, there are three pairs of incompatible sites: site 1 and site 2; site 2 and site 4; site 2 and site 5. The frequencies of 4 gametic types are $FreqGamete_{1,2} = \{1,1,2,1\}$; $FreqGamete_{2,4} = \{2,1,1,1\}$; $FreqGamete_{2,5} = \{2,1,1,1\}$, respectively. In this case, at least two recombination events must be happened in the evolutionary history of the sequences. Figure 1 is a minimal ARG with two recombination events representing the evolutionary history of data set $D(5)$.

We observed that there are three gametic types having frequency 1. So breaking one of these gametic types between these sites will give us better solution. For example, performing a recombination between site 1 and site 2 on one of three sequences S_1, S_2, S_3 will break this pair of incompatible sites. However, as $freq10_{1,2}$ equals 2, so if we perform a recombination between site 1 and site 2 on one of two sequences S_4, S_5 , we just reduce the frequency of occurrence of gametic type 10 by one and we do not break this pair of incompatible sites. In this case, we need one more recombination event to break this pair of incompatible sites (Figure 2a).

3.2 ARG4WG Algorithm

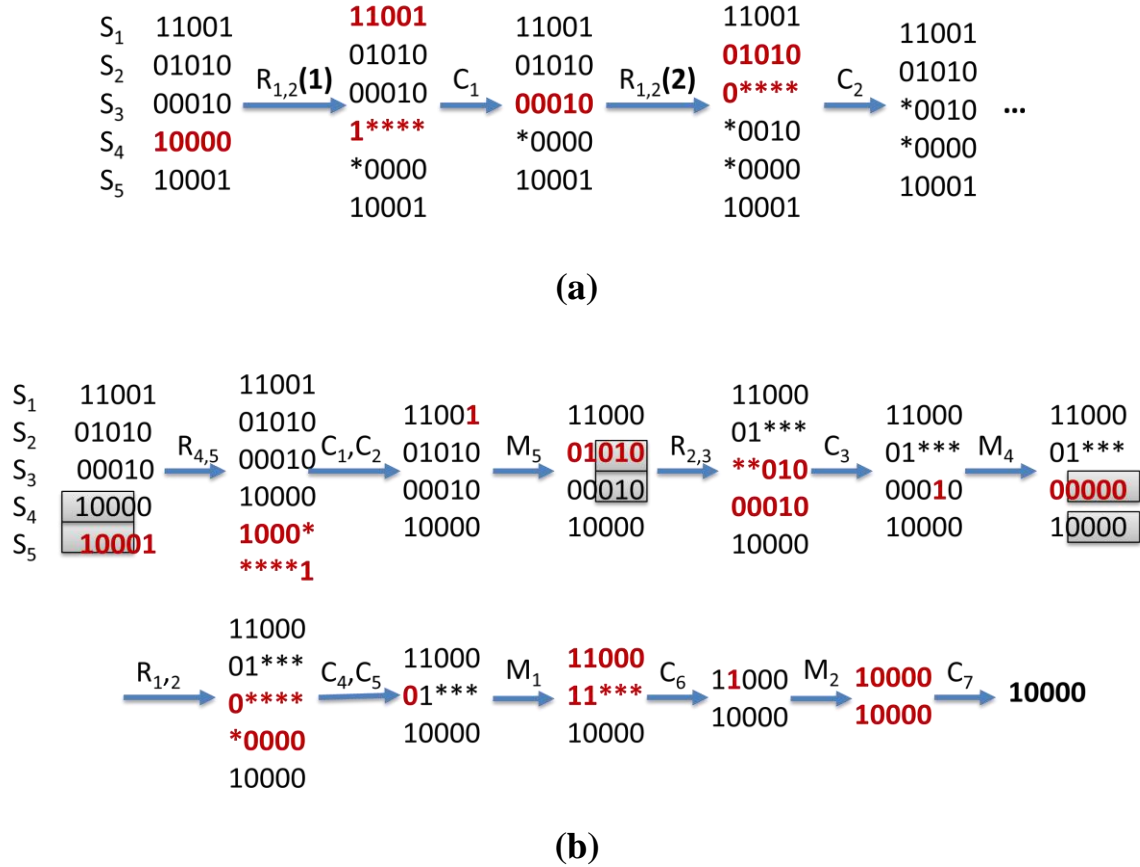


Figure 2. ARG building process for data set $D=\{S_1, S_2, S_3, S_4, S_5\}$ (a) based on four gametic tests and (b) in ARG4WG algorithm $\xrightarrow{R_{i,j}}$ denotes a recombination event between site i and site j ; $\xrightarrow{C_x}$ denotes x th coalescence event; $\xrightarrow{M_i}$ denotes a mutation event at site i . (a) The ARG building process started by choosing S_4 to do a recombination event between site 1 and site 2 ($R_{1,2}(1)$). As $freq_{01_{1,2}} = 2$, this recombination event help to reduce the frequency of gametic type 01 between site 1 and site 2 by one and $Freq_{Gamete_{1,2}} = \{1,1,1,1\}$ on the next generation. So we need to do one more recombination event between those sites ($R_{1,2}(2)$) to break this pair of incompatible sites. So this choice (and also the same with S_5) will waste two recombination events while choosing S_1, S_2, S_3 (that all have the frequency of occurrence of gametic type equal 1) to break between those sites just waste one recombination events. (b) The longest shared end is detected between S_4 and S_5 (covered by rectangles), a recombination event between site 4 and site 5 is putted on S_4 (or S_5) to produce 2 subsequences. By this way, ARG4WG always need 3 recombination events to build ARGs for this data set.

Working backward in time, ARG4WG first performs all possible coalescence and mutation events. The algorithm then searches for a pair of sequences that have the longest shared ends, that is, the longest match in term of ancestral material from the left or the right of two sequences. A recombination is performed on a sequence to break a sequence into two subsequences. A subsequence containing the longest shared region will be coalesced with the remaining sequence right after the recombination step.

The longest shared ends strategy helps ARG4WG to work with thousands of whole genome sequences. It aims to build plausible ARGs and cannot give us the minimal ARGs. Figure 2b illustrates briefly the way ARG4WG works with data set $D(5)$. As we see, in this case, ARG4WG always performs recombination on S_4 or S_5 first. This choice does not give us the optimal solution and require at least 3 recombination events to build an ARG.

3.3 GAMARG Algorithm

We propose GAMARG algorithm that combines the four-gamete test constraint with the longest shared ends strategy in ARG4WG to optimize the number of recombination events in ARG building process.

As using four-gamete test to build minimal ARG is not possible for large datasets. From the observation described in Section 3.1, we propose a simplification of the four-gamete test by considering only pairs of incompatible sites having frequency 1 for at least one gametic type. This assumption guarantees that we always break at least one pair of incompatible sites when performing a recombination between a pair of incompatible sites i and j .

Let δ be a size of sliding window that we will scan to find all pairs of incompatible sites in this region. In particular, we scan through all markers. For each marker i ($0 \leq i < m$), we will scan to find all pairs of incompatible sites in a range $[i, i + \delta]$.

Let $S_x(i,j)$ be a sequence containing a gametic type with frequency 1 at a pair of incompatible sites i and j ($0 \leq i < m, j - i \leq \delta$). That is, $S_x(i,j)$ satisfies the following conditions:

$$\{ \text{freq}00_{i,j} > 0 \text{ and } \text{freq}01_{i,j} > 0 \text{ and } \text{freq}10_{i,j} > 0 \text{ and } \text{freq}11_{i,j} > 0 \\ \{ \text{freq}00_{i,j} = 1 \text{ or } \text{freq}01_{i,j} = 1 \text{ or } \text{freq}10_{i,j} = 1 \text{ or } \text{freq}11_{i,j} = 1$$

We use the same definitions as in [1]:

- $S_x[i]$ matches $S_y[i]$ if $S_x[i] = S_y[i]$ or $S_x[i] = *$ or $S_y[i] = *$.
- $(S_x, S_y)\{d, l\}$ is a shared end pair of sequence S_x and sequence S_y with the maximal matching length l from the left ($d = \text{left}$) or from the right ($d = \text{right}$).
- $(S_x, S_y)\{d, l\}$ exists if and only if there are at least one marker i in matching region that $S_x[i] = S_y[i] \neq *$.

For a shared end pair $(S_x, S_y)\{d, l\}$, following the longest shared end strategy, the breakpoint is specified between:

- l and $l + 1$ where $d = \text{left}$ and $S_x[i]$ match $S_y[i]$ for all $l \leq i \leq l + 1$ and $S_x[l + 1] \neq S_y[l + 1]$.
- $l - 1$ and l where $d = \text{right}$ and $S_x[i]$ match $S_y[i]$ for all $l - 1 \leq i \leq l$ and $S_x[l - 1] \neq S_y[l - 1]$.

Given a candidate sequence $S_x(i,j)$, we need to find the best breakpoint in range $[i,j]$. We once again tackle this problem by using the longest shared end strategy. We find out the longest shared end between this sequence and all other sequences. If there exists a sequence S_z that a shared end pair $(S_x, S_z)\{d, l\}$ satisfies $i \leq l \leq j$, then S_x will be broken at marker l as mentioned above. If no shared end pair in range $[i,j]$ exists, the breakpoint is chosen randomly between site i and $i + 1$ or between site $j - 1$ and j .

GAMARG algorithm: The GAMARG algorithm starts from time $t = 1$. The set of sequences at time t is denoted as D_t ($D_1 = D$). For each D_t , the candidate lists for coalescence, mutation and recombination events are constructed as the following:

- Coalescence list **C**: For a shared end pair $(S_x, S_y)\{d, l\}$ of sequences S_x and S_y , if $l = m$, then $(S_x, S_y)\{d, l\}$ is added into the coalescence list.
- Mutation list **M**: For a marker i ($1 \leq i \leq m$), if $S_x[i] = 1$ and $\forall S_y \in D_t \setminus \{S_x\}: S_y[i] \neq 1$ or $S_x[i] = 0$ and $\forall S_y \in D_t \setminus \{S_x\}: S_y[i] \neq 0$, then $S_x[i]$ is added into mutation list.
- Gamete list **G**: For a pair of incompatible sites (i,j) ($0 \leq i < m, j - i \leq \delta$), if exist a sequence S_x that contains a gametic type with frequency 1, then $S_x(i,j)$ is added into gamete list.
- Shared-end list **S**: For a shared end pair $(S_x, S_y)\{d, l\}$ of sequences S_x and S_y , if $0 < l < m$, $(S_x, S_y)\{d, l\}$ is added into the recombination list.

When one of three events occurs, the next sequence set D_{t+1} is created from the current sequence set D_t as described below and four candidate lists are updated.

- If a coalescent event occurs between two sequences S_x and S_y , two sequences S_x and S_y are merged into a common ancestor S' :

$$D_{t+1} = (D_t \setminus \{S_x, S_y\}) \cup \{S'\}.$$

- If a mutation event occurs on a sequence S , a new sequence S'

is created from sequence S with the mutation:

$$D_{t+1} = (D_t \setminus \{S\}) \cup \{S'\}.$$

- If a recombination occurs on a sequence $S_x(i,j)$, a breakpoint is put in $[i,j]$. Two new subsequences S_{x1} and S_{x2} are created from sequence S_x :

$$D_{t+1} = (D_t \setminus \{S_x\}) \cup \{S_{x1}, S_{x2}\}$$

- If a recombination occurs on a shared end pair $(S_x, S_y)\{d, l\}$, pick a sequence having less ancestral material in its shared end part to do recombination. Assuming S_x is chosen, sequence S_x will be broken into two new subsequences S_{x1} and S_{x2} :

$$D_{t+1} = (D_t \setminus \{S_x\}) \cup \{S_{x1}, S_{x2}\}$$

The GAMARG algorithm

Input: A set of N sequences with m markers (snps)

Output: An ARG containing coalescence, mutation and recombination events among sequences.

- **Step 1:** If Coalescence list **C** is not empty, do all possible coalescence events.
- **Step 2:** If Mutation list **M** is not empty, do all possible mutation events then go to Step 1. If no mutation possible, go to Step 3.
- **Step 3:** If Gamete list **G** is not empty, do a recombination then go to Step 1.
- **Step 4:** If Shared-end list **S** is not empty, do a recombination followed by a coalescence. Go to Step 1.
- **Step 5:** Repeat Step 1, Step 2 and Step 3, Step 4 until a single common ancestor is reached.

Candidates from four lists are selected as the following:

- The candidate from the coalescence list or the mutation list to perform coalescence or mutation is taken randomly.
- In the Gamete list, if a candidate sequence $S_x(i,j)$ having the shortest distance from site i to site j , that is, $(j - i)$ has the smallest value, S_x is the first priority to perform recombination. If there is more than one candidate having the same shortest distance, we will choose one randomly.
- In the Shared-end list, the pair of sequences with the longest shared end in term of ancestral material will be the first choice for recombination. If there is more than one candidate having the same longest shared end, one is picked randomly.

The random choices in GAMARG algorithm result in different ARGs for different runs.

4. EXPERIMENTS AND RESULTS

To evaluate the performance of GAMARG, we conducted experiments on different datasets. First, we measured GAMARG, Margarita, ARG4WG, REARG, and exhaustive algorithms on Kreitman's dataset [9] that included 11 sequences of length 43. This small dataset is a benchmark used in evaluating the performance of many algorithms either to find lower bound of recombination or to build minimal ARGs.

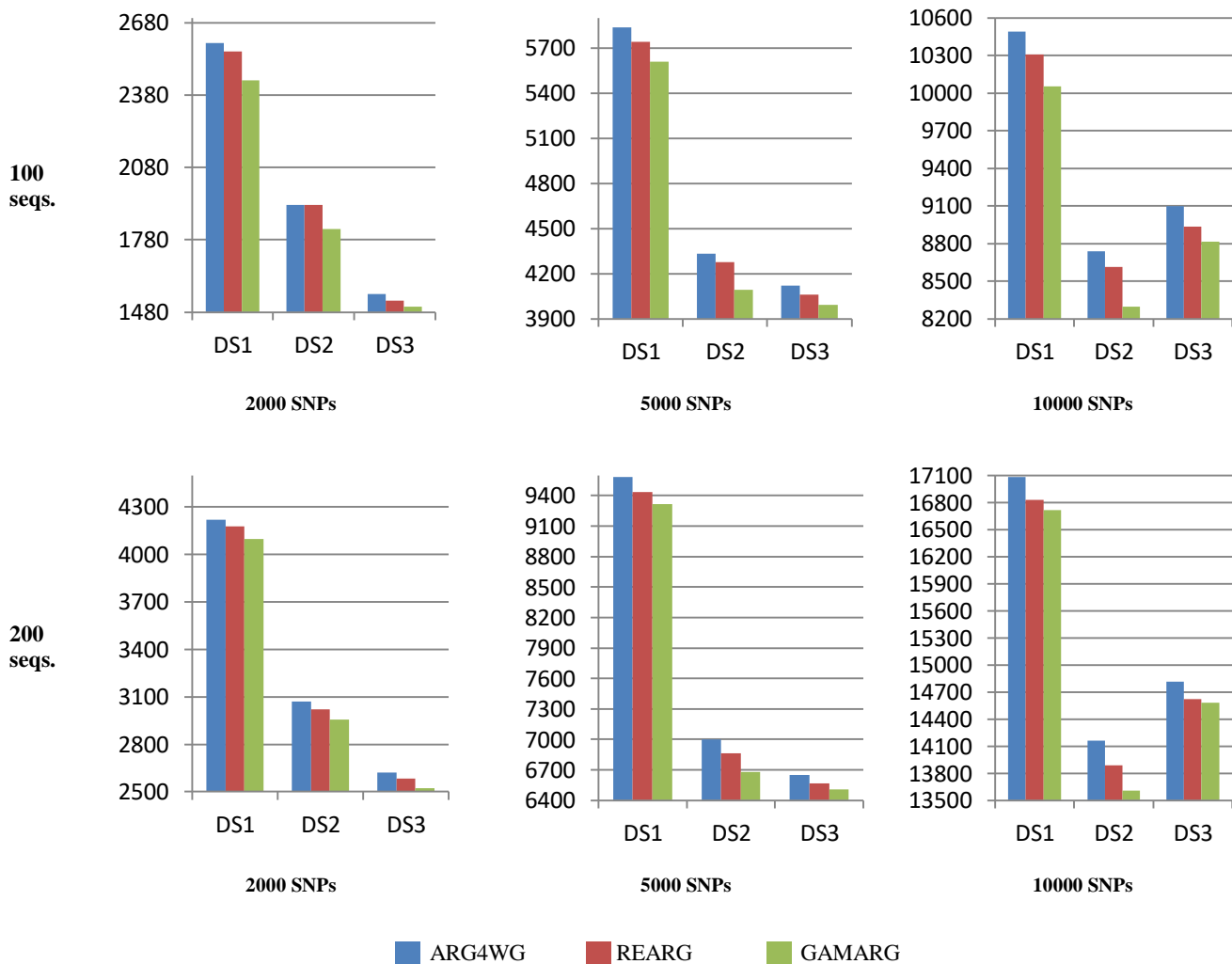


Figure 3. The smallest number of recombination events found by 3 algorithms for 100 and 200 haplotypes with 2000, 5000, and 10000 SNPs of DS1, DS2, and DS3

Second, we tested all 4 above algorithms on two simulation datasets: SDS1 included 50 sequences of length 54 and SDS2 included 75 sequences of length 45 that were public at <https://people.eecs.berkeley.edu/~yssl/lu.html>.

Third, we examined GAMARG algorithm on the datasets used in [7] that extracted from the 1000 Genomes Project [10]. Note that experiment results from [7] showed that Margarita was not stable and needed a huge number of recombination events to build an ARG for these datasets. We compared GAMARG with ARG4WG and REARG in terms of the number of recombination events and the runtime. We could not perform exhaustive search methods as they were not applicable for these large datasets.

REARG has three versions called REARG_SIM, REARG_LEN, REARG_COM. The output of REARG is the best output from all these versions.

4.1 Kreitman’s Dataset

1000 ARGs were built by each algorithm and we recorded the ARG having the smallest number of recombination events. ARG4WG and REARG got ARG with **10** recombination events as their best results. Margarita could build an ARG with **8** recombination events. The GAMARG could generate different ARGs with **7** recombination events using $18 \leq \delta < 43$. This result is the optimal solution as is also found by exhaustive search methods [3], [4]. This result shows that GAMARG is as good as exhaustive searches for small datasets. Moreover, it takes only 8 seconds to build 1000 ARGs (i.e., as fast as ARG4WG).

4.2 Simulation Datasets

10000 ARGs were built by each algorithm on each dataset and we recorded the ARG having the smallest number of recombination events. We ran GAMARG with different δ and we had best results

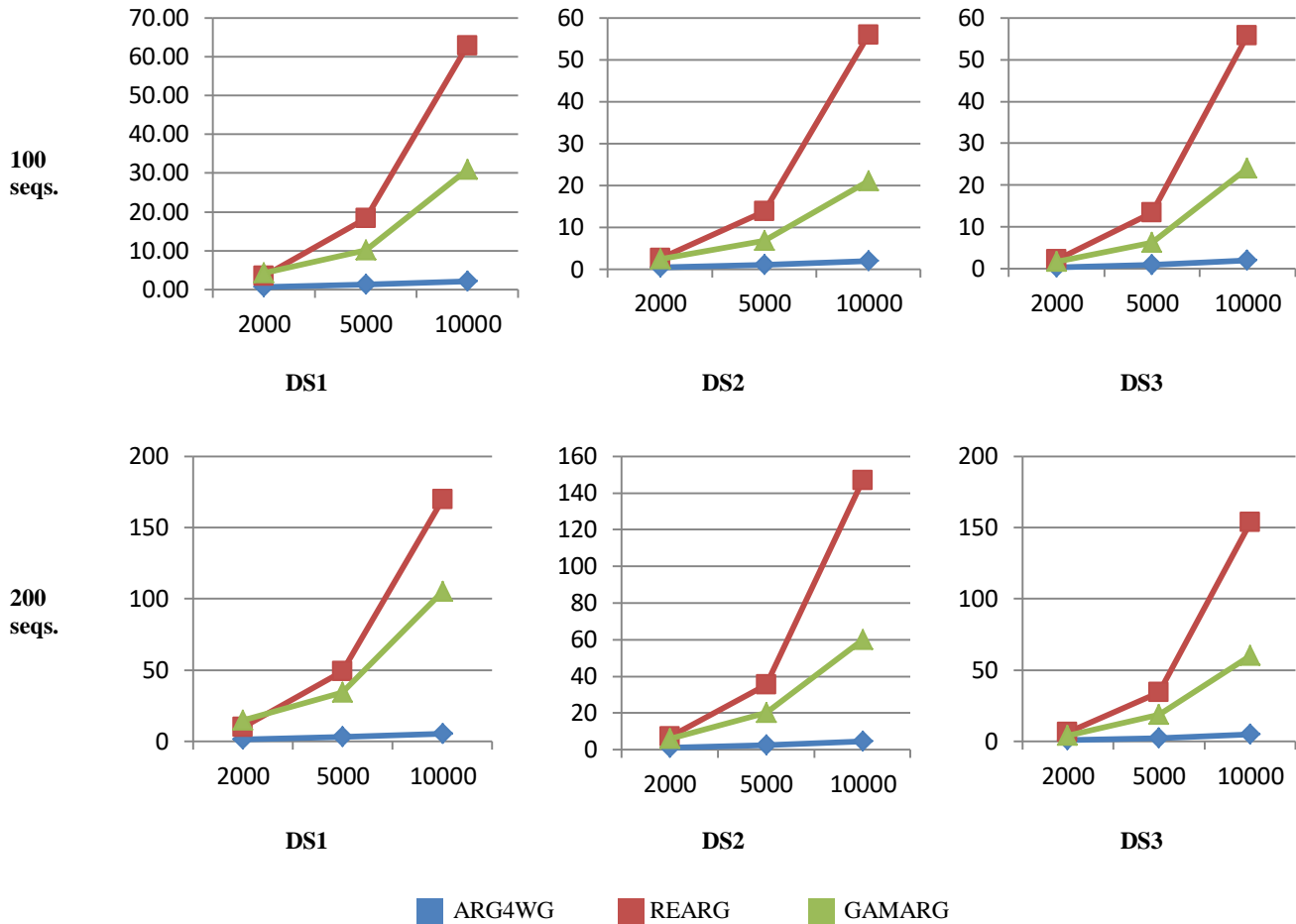


Figure 4. Average of runtimes (second) of ARG4WG, REARG, and GAMARG for 100 and 200 haplotypes with 2000, 5000, and 10000 SNPs of DS1, DS2, and DS3 datasets

with $29 \leq \delta < 54$ for SDS1 and $11 \leq \delta < 45$ for SDS2. The results of all algorithms are described in Table 1.

The experiment results show that GAMARG can reach to minimal ARGs for SDS1 and only one recombination more than the optimal solutions for SDS2. The results of Margarita, ARG4WG, and REARG are very far from the optimal solutions.

Table 1. The results from different algorithms on simulated datasets

	SDS1	SDS2
Minimal ARG	10	12
Margarita	14	18
ARG4WG	17	18
REARG	17	20
GAMARG	10	13

4.3 Datasets from the 1000 Genomes Project

We compared the runtime and the number of recombination events on 18 datasets of 100, 200 haplotypes with 2000, 5000, 10000 SNPs extracted from 3 different regions (i.e. DS1, DS2, DS3) of Chromosome 1 from the 1000 Genomes Project.

As in [7], on each data set, 1000 ARGs were built by each algorithm and the ARG with the smallest number of recombination events was recorded. In these tests, we ran GAMARG using $\delta = 5$.

Experiment results (see Figure 3) show that GAMARG algorithm produces ARGs with much smaller number of recombination events in comparison to that of ARG4WG and REARG in all tests. The outperformance of GAMARG in comparison to other algorithms is clearly significant for 100 sequences. For larger datasets with more sequences, the diversity of the data increases. Thus, there are many incompatible sites, however, only few of many of them might satisfy the constraint that at least one gametic type having frequency 1. In this case, the advantage of GAMARG over ARG4WG and REARG is not very significant.

The average running times to build an ARG by each algorithm were calculated for each test. As shown in Figure

4, for 2000 SNPs, there are not much different in the running times between algorithms. For longer sequences (i.e., 5000 and 10000 SNPs), GAMARG is slower than ARG4WG but faster than REARG.

4.4 Discussion

Four-gamete test is the well-known technique in computing the minimal recombination ARG for small datasets. The longest shared end strategy in ARG4WG algorithm is very effective for large datasets. The combination of them in GAMARG algorithm allows it not only to work with thousands sequences with tens of thousands of SNP markers but also to find minimal recombination ARGs.

The results on small datasets indicate that both ARG4WG and REARG algorithms are not suitable for small datasets. The longest shared segment strategy of Margarita has obtained the better results than ARG4WG and REARG for small datasets. However, this strategy causes Margarita much more recombination events and runtime than ARG4WG and REARG for medium or large datasets [6], [7].

The proposed GAMARG algorithm performs well in all cases, not only for small datasets but also for large datasets. However, we need to investigate the best choice for δ parameter more. For small datasets, it is not a problem because GAMARG requires only small time to build thousands ARGs.

For human genome data set, we examined GAMARG with different values for δ (i.e., 5, 10, 15, 20, 25, and 30) on different datasets with different sizes. 5000 ARGs were built and ARG with the smallest number of recombination events was recorded on each dataset. The results show that GAMARG produces similar results while δ has one of values 5, 10, 15 for 500 SNPs. However, for longer sequences (i.e., 1000 and 2000 SNPs), the algorithm works best in term of number of recombination events with $\delta = 5$.

5. CONCLUSION

Constructing minimal ARGs from large datasets is still an open problem. ARG4WG algorithm can build ARG for thousands of whole genome sequences, however, it is not designed to construct minimal ARGs. In this work, we propose GAMARG algorithm that combines four-gamete test with the longest shared end strategy in recombination step to optimize the number of recombination events in ARG building process. The GAMARG algorithm infers ARGs with smaller number of recombination events than all other heuristic methods. Specially, the GAMARG algorithm can competitive with exhaustive search methods as it can find minimal ARGs for small datasets in very little time.

In the future, we will consider more about methods to calculate the haplotype blocks to have a better estimation for parameter δ .

6. ACKNOWLEDGMENTS

We thank Centre for Informatics Computing (VAST) for allowing us to use their HPC. This research is supported by Vietnam Academy of Science and Technology (ĐLTE00.01/19-20).

7. REFERENCES

- [1] M. Arenas, "The importance and application of the ancestral recombination graph," *Front. Genet.*, vol. 4, p. 206, 2013.
- [2] L. Wang, K. Zhang, and L. Zhang, "Perfect phylogenetic networks with recombination," *J. Comput. Biol.*, vol. 8, no. 1, pp. 69–78, 2001.
- [3] Y. S. Song and J. Hein, "Constructing minimal ancestral recombination graphs," *J. Comput. Biol.*, vol. 12, no. 2, pp. 147–169, 2005.
- [4] R. B. Lyngsø, Y. S. Song, and J. Hein, "Minimum recombination histories by branch and bound," in *International Workshop on Algorithms in Bioinformatics*, 2005, pp. 239–250.
- [5] M. J. Minichiello and R. Durbin, "Mapping trait loci by use of inferred ancestral recombination graphs," *Am. J. Hum. Genet.*, vol. 79, no. 5, pp. 910–922, 2006.
- [6] T. T. P. Nguyen, V. S. Le, H. B. Ho, and Q. S. Le, "Building ancestral recombination graphs for whole genomes," *IEEE/ACM Trans. Comput. Biol. Bioinforma.*, vol. 14, no. 2, pp. 478–483, 2017.
- [7] T. T. P. Nguyen and V. S. Le, "Building minimum recombination ancestral recombination graphs for whole genomes," in *2017 4th NAFOSTED Conference on Information and Computer Science, NICS 2017 - Proceedings*, 2017, vol. 2017–Janua, pp. 248–253.
- [8] R. R. Hudson and N. L. Kaplan, "Statistical properties of the number of recombination events in the history of a sample of DNA sequences," *Genetics*, vol. 111, no. 1, pp. 147–164, 1985.
- [9] M. Kreitman, "Nucleotide polymorphism at the alcohol dehydrogenase locus of *Drosophila melanogaster*," *Nature*, vol. 304, no. 5925, p. 412, 1983.
- [10] 1000 Genomes Project Consortium and others, "A map of human genome variation from population-scale sequencing," *Nature*, vol. 467, no. 7319, p. 1061, 2010.

CNN-SVR for CRISPR-Cpf1 Guide RNA Activity Prediction with Data Augmentation

Guishan Zhang
School of Electronics and Information Technology
Sun Yat-sen University
Guangzhou, China
zhanggsh7@mail2.sysu.edu.cn

Xianhua Dai
School of Electronics and Information Technology
Sun Yat-sen University
Guangzhou, China
issdxh@mail.sysu.edu.cn

ABSTRACT

CRISPR from *Prevotella* and *Francisella* 1 (Cpf1), a RNA-guided DNA endonuclease that belongs to a novel class II CRISPR system, has recently become a popular tool for genome editing. How to improve the on-target efficiency and specificity of this system is an important and challenging problem. This paper presents a method for CRISPR-Cpf1 guide RNA activity prediction. Convolutional Neural Network (CNN) and support vector regression (SVR) are combined for this purpose. In the proposed framework, single-base substitution mutation data augmentation technique is applied to generate guide RNAs with indel frequencies, thus increasing the labeled data. In the hybrid CNN-SVR model, CNN works as a trainable feature extractor and SVR performs as the regression operator. Specifically, a merged CNN-based regression model is used to pre-train the model for predicting Cpf1 activity based on target sequence composition. Considering the chromatin accessibility information, the SVR is used to generate the predictions. Experiments on the commonly datasets show that our algorithm outperforms the available state-of-the-art tools.

CCS Concepts

Applied computing → Life and medical sciences → Bioinformatics

Keywords

CRISPR-Cpf1; data augmentation; convolutional neural network (CNN); support vector regression (SVR); on-target

1. INTRODUCTION

Clustered regularly interspaced short palindromic repeats (CRISPR) from *Prevotella* and *Francisella* 1 (Cpf1) is an effector endonuclease of the class II CRISPR-Cas gene editing system [1, 2]. CRISPR-Cpf1 differs from Cas9 in several ways: cleavage with 5' overhangs, a shorter guide RNA (gRNA), and a longer distance between the seed sequence and cleavage site [3]. Previous studies demonstrated that CRISPR-Cas based genome editing may introduce off-target effects which can lead to a significant level of non-specific editing at other unplanned

Permission to make digital or hard copies of all or part of this work for personal or classroom use is granted without fee provided that copies are not made or distributed for profit or commercial advantage and that copies bear this notice and the full citation on the first page. Copyrights for components of this work owned by others than ACM must be honored. Abstracting with credit is permitted. To copy otherwise, or republish, to post on servers or to redistribute to lists, requires prior specific permission and/or a fee. Request permissions from Permissions@acm.org.

ICBBB '19, January 7–9, 2019, Singapore, Singapore

© 2019 Association for Computing Machinery.

ACM ISBN 978-1-4503-6654-0/19/01...\$15.00

DOI: <https://doi.org/10.1145/3314367.3314383>

genome loci [4]. Therefore, the efficacy of the CRISPR-Cpf1 gRNA needs to be carefully studied.

An increasing number of studies have reported on prediction of CRISPR single guide RNA on-target knockout efficacy based machine learning, such as L1-regularized linear regression [5], L1/L2-regularized linear regression [5], random forest [6, 7], support vector machine (SVM) [7, 8], gradient boosted regression trees [5, 9-11], logistic regression classifier (CINDEL)[2]. A benchmark study demonstrated that machine learning based tools generally perform better performance than traditional alignment-based methods (CasFinder [12], etc.). However, the conventional machine learning techniques were limited in their ability to process the raw data. Further, a major limitation of these methods is that they rely on laborious manual feature engineering. Additionally, the prediction results mainly depend on the feature extraction. Therefore, machine learning system requires considerable domain expertise to design the feature extractor [13].

Guide RNA activity prediction in CRISPR-Cas system based on deep learning techniques can effectively resolve the problems mentioned above. Deep learning allows computational models that are consist of multiple processing layers to learn representations of features with multiple levels of abstraction [13]. More importantly, deep learning methods require very little engineering by hand. The layers of features are learned from data by a general-purpose learning procedure instead of designing by human engineers. Some successful deep learning based models have been provided for solving the challenges of evaluating CRISPR-Cas system guide RNA activity. For example, Chuai et al. proposed DeepCRISPR tool for single guide RNA (sgRNA) on-target and off-target site prediction based deep learning. It has been shown that data augmentation technique to generate novel sgRNAs with meaningful labels, thus indeed improving the prediction performance and making the training model robust [14]. Kim et al. proposed convolutional neural networks (CNN) incorporated chromatin accessibility for CRISPR-Cpf1 gRNA activity prediction [9]. In their research, the training dataset used in the study is relatively small (n=15, 000). Notably, compared with Cas9, the available information about Cpf1 is relatively limited.

In this paper, we introduce a hybrid CNN-SVR model for CRISPR-Cpf1 gRNA activity evaluation with data augmentation. The key idea of our method is to train a specialized CNN to extract robust target sequence composition features and provide them to SVR regression operator. First, we investigate data augmentation technique named single-base substitution mutation for CRISPR-Cpf1 gRNA training datasets. Considering that one base mismatch in the PAM-distal region of the gRNA has little influence on the indel frequency. We amplified the training dataset by changing one base of gRNA at position 5 in the promiscuous region (at positions 19-23 from PAM), and the indel

frequency keeps consistent with the original gRNA. After data augmentation, we get 60,000 training data with indel frequency. Second, we merge two independent sub-networks to pre-train the parameters of the model, and then use the element-wise multiplication operator by considering chromatin accessibility feature. Finally, the SVR procedure is performed to predict the gRNA indel frequency. Experiments show that the proposed model can give good gRNA activity prediction compared with other state-of-the-art algorithms.

2. PROPOSED FRAMEWORK

2.1 Single-base Substitution Mutation Data Augmentation

The CNN model relies on large amounts of the training data. In order to combat overfitting, we used a specific data augmentation method to add sample replicas with indel frequency preservation. Previous studies have shown that the PAM-distal region has a high tolerance for mismatches [15, 16]. Specifically, Kim et al. proposed that promiscuous region, at position 19-23 from PAM, one base mismatch only slightly decreased the indel frequencies. Inspired by this research, single-base substitution mutation was performed to make data augmentation. Considering that gRNAs with one mismatch in the promiscuous region has little effect on cleavage efficacy, we extended the raw datasets by changing the fifth position base in promiscuous region into three new gRNAs, meanwhile, the indel frequencies of the augmented gRNAs are consistent with the original gRNA. Consequently, a 34-nt guide sequence can be expanded to 4 gRNAs with the same indel frequency (Figure 1). By adopting single-base substitution mutation data augmentation technique, data set HT1-1(n=15,000) was extended to 60,000 non-redundant gRNAs with biologically meaningful indel frequencies.

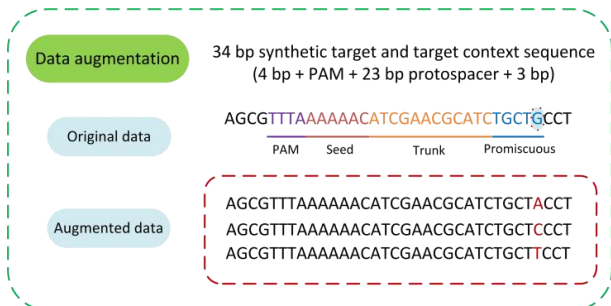


Figure 1. Illustration of the single-base substitution mutation data augmentation procedure

2.2 One-hot Encoding for gRNA Sequence

We formulated one-hot encoding to encode the gRNA sequence. The nucleotide sequence is represented by four channels: A-channel, C-channel, G-channel and T-channel. For example, for A-channel, the presence of the nucleotide A at a particular base pair position is denoted by 1, while the absence of A is denoted by 0. Similarly, C-channel, G-channel and T-channel were represented in the same way. As a result, we obtained a four-binary-channel representation of each gRNA. Figure 2 shows an example of the one-hot encoding representation schema of the gRNA sequence.

2.3 CNN Feature Extraction

A convolutional neural network (CNN) is a feed-forward artificial neural network [13]. It is a multi-layer neural network with a deep supervised learning architecture. CNN integrates feature learning

and regression into the optimization progress. The CNN procedure mainly consists of two parts: an automatic feature extractor and a trainable classifier. The automatic feature extractor contains convolution layers and pooling layers. Backpropagation algorithm usually used to train the convolution kernels and the weights of the last output layer.

	A	G	C	T	A	G	C	C	C	G	A	A	G	T	A	C	A	G	
A	1	0	0	0	0	1	0	0	0	0	0	1	1	0	0	1	0	1	0
C	0	0	1	0	0	0	0	1	1	1	0	0	0	0	0	0	1	0	0
G	0	1	0	0	0	0	1	1	0	0	0	1	0	0	1	0	0	0	1
T	0	0	0	1	1	0	0	0	0	0	0	0	0	0	1	0	0	0	0

Figure 2. One-hot encoding schema for the gRNA. The gRNA sequence is denoted by four channels: A-channel, C-channel, G-channel, and T-channel

In our study, we build our merge CNN-based network with pre-training based fine-tune for CRISPR-Cpf1 gRNA on-target prediction. Our merged CNN model mainly following the three-stage designs, such as convolutional layers, pooling layers and fully connected layers with modifications, including batch normalization [17] rectified linear unit (ReLU) [18], and dropout, to prevent overfitting. The structure of the sub-network is shown in Figure 3 for on-target prediction. The inputs of the CNN are the gRNA regional information data. We used 3 convolution layers for feature extraction. Each convolutional layer is followed by batch normalization and a ReLU activation function. Batch normalization can deal with both the overfitting and underfitting problem in a robust way. Also, we utilized average pooling layer to reduce the dimension of the input. Moreover, we employ dropout regularization technique with a 0.3 dropout rate to combat overfitting. Subsequently, we added 3 dense layers to collect knowledge of the network and keep the remaining feature maps unchanged [19].

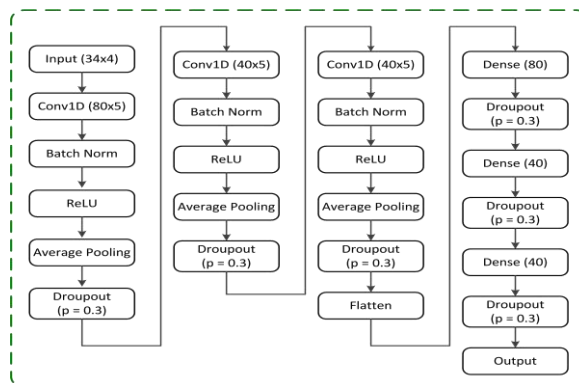


Figure 3. Block of the sub-network for feature extraction

2.4 Support Vector Regression

Support vector regression (SVR) aims at minimizing the generalization error bound to improve generalized performance [20]. The main idea of SVR is based on the computation of a linear regression function in a high dimensional feature space where the input data are mapped via a nonlinear function [20, 21]. Supposing a training set $D = \{(x_1, y_1), (x_2, y_2), \dots, (x_m, y_m)\} \in \mathfrak{X} \times \mathfrak{R}$, where \mathfrak{X} denotes the space of the input patterns. ε -SV regression tries to find a function $f(x)$ that has at most ε deviation from the actually obtained targets y_i for all the training data. The objective function is:

$$\min_{\omega, b} \frac{1}{2} \|\omega\|^2 + C \sum_{i=1}^m l_{\varepsilon}(f(x_i) - y_i) \quad (1)$$

where C is the regularization constant, ε -insensitive loss function l_ε described by

$$l_\varepsilon(p) = \begin{cases} 0, & \text{if } \|p\| \leq \varepsilon \\ |p| - \varepsilon, & \text{otherwise} \end{cases} \quad (2)$$

Analogously to the ‘‘soft margin’’ loss which was used in SVM, by introducing slack variables ξ_i and $\hat{\xi}_i$, then the corresponding objective function is:

$$\min_{\omega, b, \zeta, \hat{\zeta}, \xi, \hat{\xi}} \frac{1}{2} \|\omega\|^2 + C \sum_{i=1}^m l_\varepsilon(\xi_i + \hat{\xi}_i) \quad (3)$$

s.t.

$$\begin{aligned} f(x_i) - y_i &\leq \varepsilon + \xi_i \\ y_i - f(x_i) &\leq \varepsilon + \hat{\xi}_i \\ \xi_i &\geq 0, \hat{\xi}_i \geq 0, i = 1, 2, \dots, m \end{aligned} \quad (4)$$

The corresponding Lagrangian is:

$$\begin{aligned} L(\omega, b, \zeta, \hat{\zeta}, \xi_i, \hat{\xi}_i, \mu, \hat{\mu}) \\ = \frac{1}{2} \|\omega\|^2 + C \sum_{i=1}^m (\xi_i + \hat{\xi}_i) - \sum_{i=1}^m \mu_i \xi_i - \sum_{i=1}^m \hat{\mu}_i \hat{\xi}_i \\ + \sum_{i=1}^m \zeta_i (f(x_i) - y_i - \varepsilon - \xi_i) + \sum_{i=1}^m \hat{\zeta}_i (y_i - f(x_i) - \varepsilon - \hat{\xi}_i) \end{aligned} \quad (5)$$

Here L is the Lagrangian and $\zeta, \hat{\zeta}, \mu, \hat{\mu}$ are Lagrange multipliers. By solving the dual optimization problem, the result of SVR may be written as

$$f(x) = \sum_{i=1}^m (\hat{\zeta}_i - \zeta_i) x_i^T x + b \quad (6)$$

Consider the map $\Phi: \mathcal{X} \rightarrow \mathcal{F}$, training patterns of x_i are mapped into some feature space \mathcal{F} . And the SVR can be written as

$$f(x) = \sum_{i=1}^m (\hat{\zeta}_i - \zeta_i) \kappa(x, x_i) + b \quad (7)$$

where $\kappa(x, x_i) = \phi(x_i)^T \phi(x_j)$ is a kernel function.

2.5 Hybrid CNN-SVR Model

In the CNN network, the input of the activation function is the summation of linear combination of the outputs from previous hidden layer with trainable weights and the corresponding bias. The outputs of the last layer are the estimated probabilities for the inputs. In general, the output probability is calculated by an activation function. Compared with simple linear combination, SVR performs better in handling high dimension regression problem. The combination of CNN-SVR network can combine their virtues and make them complement each other to improve the prediction.

Inspired by this, we use SVR regression operator to replace the final layer in CNN model. The proposed CRISPR-Cpf1 guide RNA activity prediction system was designed to integrate the CNN and SVR regression operator. Specifically, first, the encoded augmented on target gRNA data are sent to the input layer, and the original merged CNN with the output layer is trained until the training process converges. Second, the SVR with Radial Basis Function (RBF) kernel replaces the CNN linear output layer. The SVR operator takes the outputs from the hidden layer as a new feature vector for training. After being well trained, the SVR performs the regression task and makes indel frequency prediction for gRNAs with such automatically extracted features.

2.6 Overview of Hybrid CNN-SVR with Data Augmentation Procedure

We introduce a hybrid CNN-SVR model for CRISPR-Cpf1 gRNA activity prediction with single-base substitution mutation data augmentation. As shown in Figure 4, the main idea of our hybrid CNN-SVR algorithm is described as follows: (1) Single-base substitution mutation data augmentation procedure was performed

to magnify the training data size. (2) The 1-by-34 target sequence (4 bp + PAM + 23 bp protospacer + 3 bp) was converted to 4-by-34 binary vectors using one-hot encoding. (3) Two independent sub-nets based CNN with the same structure were joined by ‘‘concatenate’’ operator. The structure of the sub-net was described in ‘‘CNN feature extraction’’ section. (4) Two sub-nets based CNN were concatenated to pre-train the model using augmented data. And the goal of pre-train is to minimize the mean square error loss of the loss function. The pre-trained model parameters were saved to further fine tune the model. (5) We loaded the trained model weights parameters and fixed the corresponding layers. The chromatin accessibility information was incorporated to fine-tune the model. (6) The SVR operator was performed to get the regression score for CRISPR-Cpf1 indel frequency prediction.

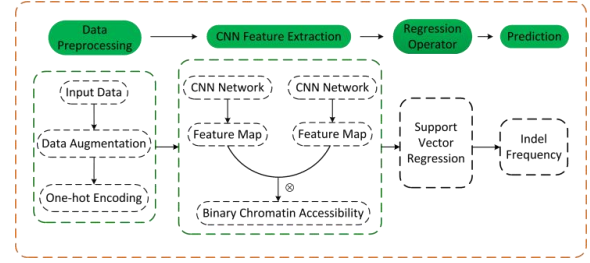


Figure 4. CRISPR-Cpf1 gRNA activity prediction schema based on hybrid CNN-SVR combining data augmentation

3. EXPERIMENTS

To evaluate the feasibility of the hybrid CNN-SVR model with data augmentation for CRISPR-Cpf1 gRNA activity prediction, we conducted experiments on the public datasets. We implemented our algorithms using Keras and Tensorflow, running on Intel Core i7 CPU at 3.6 GHz with 16 GB RAM and NVIDIA 8 GB GTX 1080 GPU. The optimized parameters are tuned automatically under the Adam optimizer. We empirically demonstrate the hybrid CNN-SVR’s effectiveness on several commonly datasets and compare with the state-of-the-art architectures. Spearman correlation coefficient was used to quantitatively validate the performance of the proposed algorithm.

3.1 Data Resources

We used the public dataset available in [9], namely HT 1 and HT 2, and HT 3, which contain target sequence compositions and the corresponding indel frequencies. The HT 1 and HT 2 datasets consist of 16,292 and 2,963 unique guide sequences in HEK293T cells, respectively. HT1 dataset was randomly split into data set HT 1-1 (n=15,000) and HT 1-2 (n=1,292). Single-base substitution mutation technique is used to increase the sample size of HT 1-1 dataset, this augmentation resulted into 60,000 non-redundant gRNAs with indel frequencies for training process. The above mentioned datasets have no available chromatin accessibility information. Data sets HEK-lenti (n=148), HEK-plasmid (n=55), and HCT-plasmid (n=66) contained the guide RNA sequences, chromatin accessibility information, and the corresponding indel frequencies. They were prepared at endogenous sites from HEK293T and HCT116 cell lines. The binary chromatin accessibility information for the cell lines were obtained from the Encyclopedia of DNA elements. The DNase I hypersensitive sites are labeled as ‘‘1’’ while the others are labeled as ‘‘0’’.

3.2 Epigenetic Features

Locus accessibility of the gRNA was important for determining the gRNA activity [22]. Specifically, the chromatin accessibility

can affect the efficiency of Cas9 mediated indel formation [22]. In eukaryotes, chromosomal DNA is packaged into a regularly repeating chain of nucleosomes. The chromosomal will prevent DNase I from nicking DNA sequence, which result in the preferential sensitivity of the accessible nucleosome free regions to DNase I cleavage. DNase I-hypersensitive sites (DHSs) are usually used to determine chromatin accessibility [23]. Kim et al. proposed that considering the chromatin accessibility information contributed to good-performing for CRISPR-Cpf1 guide RNA activity prediction. Enlightened by these, we incorporated chromatin accessibility expecting to get a better performance.

3.3 Training Hybrid CNN-SVR

We trained the proposed model in two main steps. First, pre-train of the entire architecture. Second, fine-tune with endogenous target data considering chromatin accessibility, which contribute to the improvement of the prediction.

3.3.1 Pre-Training

We used augmented HT 1-1 data set as training dataset, HT 1-2 as validation data set. The first input of hybrid CNN-SVR is the augmented 34-bp gRNA sequences with PAM. We use the grid search from the scikit-learn python machine learning library to tune the hyperparameters. The proposed model was wrapped with the KerasRegressor class. To use the wrapper, we first defined a function that creates the proposed model, then passed this function to the “build_fn” argument when constructing the KerasRegressor class. We optimized the mean squared error loss function using the Adam optimizer [24]. Hyperparameter optimization experiments were performed sequentially as follows: batch size (chosen from [64, 128, 150, 256, 300, 512, 1024]) and number of epochs (chosen from [10, 20, 40, 60, 80, 100, 200]), learning rate (chosen from [0.001, 0.01, 0.02, 0.03, 0.04, 0.05, 0.06, 0.07, 0.08, 0.09, 0.1, 0.2, 0.3]), neuron activation function (chosen from [‘hard_sigmoid’, ‘softplus’, ‘softsign’, ‘relu’, ‘tanh’, ‘sigmoid’, ‘linear’]), network weight initialization (chosen from [‘he_normal’, ‘he_uniform’, ‘glorot_uniform’, ‘glorot_normal’, ‘zero’, ‘normal’, ‘uniform’, ‘lecun_uniform’]), dropout regularization (chosen from [0.0, 0.1, 0.2, 0.3, 0.4, 0.5, 0.6, 0.7, 0.8, 0.9]). After that, hyperparameter of the number of epochs was re-tuned by optimizing the loss function. Hyperparameter optimization experiments were carried out by threefold cross-validation.

3.3.2 Fine-Tuning of Hybrid CNN-SVR Model

We next generated a hybrid CNN-SVR for gRNA on-target knockout efficacy prediction, comprising two parts. Taking chromatin accessibility into consideration, we added a chromatin accessibility layer before the SVR regression output layer. During the fine-tuning, we used the pre-trained network weights, only updating those of the last three layers.

3.4 Experimental Results

In order to quantitatively verify the superiority of the proposed hybrid CNN-SVR model with data augmentation, we compare its performance with DeepCpf1 network, and the conventional machine learning based methods, such as L1 regression, L2 regression, L1/L2 regression, gradient boosted regression, and CINDEL. Performance comparison experiments were trained on augmented HT1-1 dataset (n=60,000 with indel frequencies at independent target sequences), for 3 independent test data sets (HT 1-2, HT 2, HT 3), the Spearman correlation coefficient between measured indel frequencies and predicted Cpf1 activity scores are shown in Table 1. These results indicated that hybrid

CNN-SVR generally outperformed the conventional machine learning based algorithms and Seq-deepCpf1 for prediction of CRISPR-Cpf1 gRNA activity based on target sequence composition.

Table 1. Comparisons of testing results on HT 1-2, HT 2, HT 3 datasets

Model	HT 1-2	HT 2	HT 3
L1 regression [5]	0.75	0.73	0.57
L2 regression [5]	0.75	0.73	0.56
L1L2 regression [5]	0.75	0.73	0.57
BoostedRT [11]	0.74	0.74	0.53
CINDEL [2]	0.64	0.64	0.50
Seq-deepCpf1 [9]	0.76	0.75	0.58
CNN-SVR	0.77	0.76	0.57

Consider the chromatin accessibility may improve the prediction of Cpf1 activities at endogenous target site. HEK-lenti dataset was used to fine-tune the parameters of the proposed hybrid CNN-SVR model. HEK-plasmid (n=55) and HCT-plasmid (n=66) data sets were used for testing. Table 2 lists the Spearman correlations between measured indel frequencies and predicted activity scores comparison of hybrid CNN-SVR with other prediction models in HEK293T cells and HCT116 cell. Of the note that “+CA” means incorporating chromatin accessibility. Without considering the chromatin accessibility, we noticed that Spearman correlation of CNN-SVR method reached 0.73 and 0.57 on the HEK-plasmid and HCT-plasmid data sets. Combining the chromatin accessibility, compared with other models, CNN-SVR showed better performance, achieving Spearman correlations of 0.90 and 0.76, respectively. Notably, the chromatin accessibility information contributes to the prediction of Cpf1 activities at endogenous target sites.

Table 2. Spearman correlation results of CNN-SVR and other models on HEK-plasmid and HCT-plasmid data sets

Model	HEK-plasmid	HCT-plasmid
L1 regression [5]	0.67	0.56
L1 regression + CA [5]	0.77	0.64
L2 regression [5]	0.67	0.55
L2 regression + CA [5]	0.76	0.63
L1L2 regression [5]	0.67	0.55
L1L2 regression + CA [5]	0.77	0.64
BoostedRT [11]	0.69	0.56
BoostedRT + CA [11]	0.70	0.62
CINDEL[2]	0.55	0.42
CINDEL + CA [2]	0.63	0.50
Seq-deepCpf1 [9]	0.69	0.57
DeepCpf1 + CA [9]	0.87	0.77
CNN-SVR	0.73	0.57
CNN-SVR + CA	0.90	0.76

4. CONCLUSION

In this study, we present hybrid CNN-SVR with data augmentation, an efficient and extendable method for CRISPR-Cpf1 gRNA activity prediction. Compared with machine learning based models, such as L1 regression, L2 regression, L1/L2 regression, gradient boosted regression, and CINDEL, and the deep learning based DeepCpf1 method, experimental results indicate that leveraging single-base substitution mutation augmented labeled gRNA sequences as well as CNN-SVR based model contributes to efficiently learn gRNA representations and boost the prediction performance. The experimental results on the benchmark HEK-plasmid dataset demonstrate the power of our

hybrid CNN-SVR model for evaluating the activity of CRISPR-Cpf1 gRNA. Additionally, the proposed method automates the feature identification for gRNA design, which facilitating interpretation and optimized CRISPR on-target design. For future work, the hybrid CNN-SVR based CRISPR-Cpf1 gRNA activity evaluating precision will be further increased by using a larger dataset considering more epigenetic features.

5. ACKNOWLEDGMENTS

This work was supported by the National Natural Science Foundation of China (Grant No. 61872396).

6. REFERENCES

- [1] Zetsche, B., Heidenreich, M., Mohanraju, P., Fedorova, I., Kneppers, J., DeGennaro, E.M., Winblad, N., Choudhury, S.R., Abudayyeh, O.O., Gootenberg, J.S., Wu, W.Y., Scott, D.A., Severinov, K., van der Oost, J. and Zhang, F. 2017. Multiplex gene editing by CRISPR-Cpf1 using a single crRNA array. *Nat. Biotechnol.* 35, 31-34. DOI=10.1038/nbt.3737.
- [2] Kim, H.K., Song, M., Lee, J., Menon, A.V., Jung, S., Kang, Y.M., Choi, J.W., Woo, E., Koh, H.C., Nam, J.W. and Kim, H. 2017. In vivo high-throughput profiling of CRISPR-Cpf1 activity. *Nat Methods* 14, 153-159. DOI=10.1038/nmeth.4104.
- [3] Zetsche, B., Gootenberg, J.S., Abudayyeh, O.O., Slaymaker, I.M., Makarova, K.S., Essletzbichler, P., Volz, S.E., Joung, J., van der Oost, J., Regev, A., Koonin, E.V. and Zhang, F. 2015. Cpf1 is a single RNA-guided endonuclease of a class 2 CRISPR-Cas system. *Cell* 163, 759-771. DOI=10.1016/j.cell.2015.09.038.
- [4] Hsu, P.D., Scott, D.A., Weinstein, J.A., Ran, F.A., Konermann, S., Agarwala, V., Li, Y., Fine, E.J., Wu, X., Shalem, O., Cradick, T.J., Marraffini, L.A., Bao, G. and Zhang, F. 2013. DNA targeting specificity of RNA-guided Cas9 nucleases. *Nat. Biotechnol.* 31, 827-832. DOI=10.1038/nbt.2647.
- [5] Kuan, P.F., Powers, S., He, S., Li, K., Zhao, X. and Huang, B. 2017. A systematic evaluation of nucleotide properties for CRISPR sgRNA design. *BMC Bioinformatics* 18, 297. DOI=10.1186/s12859-017-1697-6.
- [6] Xie, S., Shen, B., Zhang, C., Huang, X. and Zhang, Y. 2014. sgRNAs9: a software package for designing CRISPR sgRNA and evaluating potential off-target cleavage sites. *Plos One* 9, e100448. DOI=doi:10.1371/journal.pone.0100448.
- [7] Erard, N., Knott, S.R.V. and Hannon, G.J. 2017. A CRISPR Resource for Individual, Combinatorial, or Multiplexed Gene Knockout. *Molecular Cell.* 67, 348. DOI=10.1016/j.molcel.2017.06.030
- [8] Ma, J., Köster, J., Qin, Q., Hu, S., Li, W., Chen, C., Cao, Q., Wang, J., Mei, S. and Liu, Q. 2016. CRISPR-DO for genome-wide CRISPR design and optimization. *Bioinformatics* 32, 3336-3338. DOI=10.1093/bioinformatics/btw476
- [9] Kim, H.K., Min, S., Song, M., Jung, S., Choi, J.W., Kim, Y., Lee, S., Yoon, S. and Kim, H.H. 2018. Deep learning improves prediction of CRISPR-Cpf1 guide RNA activity. *Nat. Biotechnol.* 36, 239-241. DOI=10.1038/nbt.4061.
- [10] Kescu, C., Arslan, S., Singh, R., Thorpe, J. and Adli, M. 2014. Genome-wide analysis reveals characteristics of off-target sites bound by the Cas9 endonuclease. *Nat. Biotechnol.* 32, 677-683. DOI= 10.1038/nbt.2916
- [11] Doench, J.G., Fusi, N., Sullender, M., Hegde, M., Vaimberg, E.W., Donovan, K.F., Smith, I., Tothova, Z., Wilen, C., Orchard, R., Virgin, H.W., Listgarten, J. and Root, D.E. 2016. Optimized sgRNA design to maximize activity and minimize off-target effects of CRISPR-Cas9. *Nat. Biotechnol.* 34, 184-191. DOI=10.1038/nbt.3437.
- [12] Aach, J., Mali, P. and Church, G.M. 2014. CasFinder: Flexible algorithm for identifying specific Cas9 targets in genomes. *Biorxiv.* DOI= 10.1101/005074
- [13] LeCun, Y., Bengio, Y. and Hinton, G. 2015. Deep learning. *Nature* 521, 436-444. DOI=10.1038/nature14539.
- [14] Chuai, G., Ma, H., Yan, J., Chen, M., Hong, N., Xue, D., Zhou, C., Zhu, C., Chen, K., Duan, B., Gu, F., Qu, S., Huang, D., Wei, J. and Liu, Q. 2018. DeepCRISPR: optimized CRISPR guide RNA design by deep learning. *Genome Biol* 19, DOI=80.10.1186/s13059-018-1459-4.
- [15] Kim, D., Kim, J., Hur, J.K., Been, K.W., Yoon, S.H. and Kim, J.S. 2016. Genome-wide analysis reveals specificities of Cpf1 endonucleases in human cells. *Nat. Biotechnol.* 34, 863-868. DOI=10.1038/nbt.3609.
- [16] Kleinstiver, B.P., Tsai, S.Q., Prew, M.S., Nguyen, N.T., Welch, M.M., Lopez, J.M., Mccaw, Z.R., Aryee, M.J. and Joung, J.K. 2016. Genome-wide specificities of CRISPR-Cas Cpf1 nucleases in human cells. *Nat. Biotechnol.* 34, 869-874. DOI= 10.1038/nbt.3620
- [17] Ioffe, S. and Szegedy, C. 2015. Batch Normalization: Accelerating Deep Network Training by Reducing Internal Covariate Shift. 448-456
- [18] Nair, V. and Hinton, G.E. 2010. *in International Conference on International Conference on Machine Learning*, 807-814
- [19] Huang, G., Liu, Z., Laurens, V.D.M. and Weinberger, K.Q. 2016. Densely Connected Convolutional Networks. 2261-2269. DOI=10.1109/CVPR.2017.243
- [20] Drucker, H., Burges, C.J., Kaufman, L., Smola, A.J. and Vapnik, V. 1997. *in Advances in neural information processing systems*, 155-161.
- [21] Basak, D., Pal, S. and Patranabis, D.C. 2007. Support vector regression. *Neural Information Processing-Letters and Reviews* 11, 203-224
- [22] Chari, R., Mali, P., Moosburner, M. and Church, G.M. 2015. Unraveling CRISPR-Cas9 genome engineering parameters via a library-on-library approach. *Nat Methods* 12, 823-826. DOI=10.1038/nmeth.3473.
- [23] Liu, Y., Fu, L., Kaufmann, K., Chen, D. and Chen, M. 2018. A practical guide for DNase-seq data analysis: from data management to common applications. *Brief Bioinform* DOI=10.1093/bib/bby057.10.1093/bib/bby057.
- [24] Kingma, D. and Ba, J. 2014. Adam: A Method for Stochastic Optimization. *Computer Science*

Extraction of Respiration from PPG Signals Using Hilbert Vibration Decomposition

Hemant Sharma

Department of Electronics & Communication Engineering
National Institute of Technology Rourkela
Rourkela-769008, India
sharmah@nitrrkl.ac.in

ABSTRACT

A new approach using the Hilbert vibration decomposition (HVD) for extracting the respiration from the photoplethysmographic (PPG) signal is proposed. It is suggested that the largest energy component of the PPG signal acquired using the HVD is analogous to the respiratory signal. The proposed PPG-derived respiration (PDR) technique is examined over the Capnabase and MIMIC datasets by evaluating the correlation and respiratory rate errors calculated between the derived and reference respiratory rates (RRs). Upon comparing the performance of the proposed approach with the existing techniques, the proposed approach is seen to be yielding better correlation and smaller errors in the RRs computed from the PDR and recorded respiration signals on both the datasets. The experimental analysis suggests that the proposed technique can be employed for efficacious computation of the respiration from the PPG signal. Efficient and reliable extraction of the respiratory signal from PPG will help in the improvement of low-cost and less discomfort mobile-based healthcare systems.

CCS Concepts

Applied computing → Health informatics

Keywords

PPG; Respiration; HVD; Respiratory rate

1. INTRODUCTION

The photoplethysmographic (PPG) signal is a preferable physiological signal for the development of mobile-based healthcare systems due to feasibility, mobility, comfortableness, and cost of the PPG device [1]. The PPG signals are primarily used for non-invasive measurement of blood oxygen saturation, but they can also be used for computing of many health parameters such as the respiratory rate (RR), heart rate (HR), and blood pressure (BP) [1]. The HR measurement using the PPG signal recorded from the wrist is very popular for monitoring of exercise in the sports.

Many algorithms have been developed by the researchers to extract RR using the PPG signals [1-8]. These techniques can be

Permission to make digital or hard copies of all or part of this work for personal or classroom use is granted without fee provided that copies are not made or distributed for profit or commercial advantage and that copies bear this notice and the full citation on the first page. Copyrights for components of this work owned by others than ACM must be honored. Abstracting with credit is permitted. To copy otherwise, or republish, to post on servers or to redistribute to lists, requires prior specific permission and/or a fee. Request permissions from Permissions@acm.org.

ICBBB '19, January 7–9, 2019, Singapore, Singapore

© 2019 Association for Computing Machinery.

ACM ISBN 978-1-4503-6654-0/19/01...\$15.00

DOI: <https://doi.org/10.1145/3314367.3314369>

categorized mainly into two classes: PPG pulse morphology-

based approaches [2-4] and filtering based approaches [1], [5-8]. Addison *et al.* [2] explained that the respiratory process influences the PPG signal mainly in following ways: baseline modulation, PPG pulse amplitude modulation, and modulation of pulse frequency. Based on these variations, Karlen *et al.* computed RR by fusing three respiratory rates (RRs) each estimated from three different changes in PPG due to the respiratory process [3]. Lazaro *et al.* proposed an algorithm to obtain RR by tracking variation in the width of PPG pulse caused by the respiration [4]. In [3-4], detection of the fiducial points in PPG (such as pulse peak, pulse apex, onset and end points) is needed for the RR estimation. These fiducial points are much responsive to the noise and movement artifacts [1]. The time-varying correlogram spectral density (CSD) of the PPG signal is also investigated for tracking the respiratory frequency peak in the spectrum [7]. However, most of these techniques are validated on a small dataset extracted either from the Capnabase database [9] or their personal database [5].

Further, Nakajima *et al.* derived RR and HR using the PPG based on a band-pass filter with a predefined frequency band [5]. The drawback of this approach is that if RR lies outside the predefined frequency band than the estimation of RR may be erroneous. The use of the wavelet functions for the RR estimation from PPG is exploited in [6]. In the wavelet-based techniques, a suitable choice of mother wavelet and levels of the decomposition is required for better results. The empirical mode decomposition (EMD) which is a data-driven technique is also employed to get the respiratory-related information from the PPG signal [8]. However, the EMD based approach suffers from mode mixing problem [1]. Recently, the ensemble empirical mode decomposition (EEMD) is used to process the PPG signal for deriving HR and RR [1]. The EEMD, however, resolved the hassle of mode mixing in EMD but it created a new one that accepts the residuary noise in the signal reconstruction.

Recently, the Hilbert vibration decomposition (HVD) is seen to be emerging as a popular tool to investigate the non-stationary signals [10]. The HVD technique has been applied to many biomedical signal processing applications including baseline wander removal of ECG [11] and computation of respiration from the electrocardiogram (ECG) signal [12]. The HVD decomposes the given signal into various mono-components of gradually changing amplitudes and frequencies. The first component of HVD corresponds to the varying largest energy component, and the residual signal comprises details of the smaller energy components in the input [10]. In this paper, a new approach based on the HVD is suggested for deriving the respiration from the PPG signal. It is hypothesized that the respiratory component in PPG has a significant portion of the overall energy of the PPG signal. The proposed hypothesis is supported by the fact that the

respiratory process affects the PPG characteristics (including the pulse amplitude and baseline of the PPG signal) significantly [3]. Consequently, these substantial magnitude variations can be separated in the largest component of PPG acquired through the HVD for an accurate estimation of the respiration.

2. MATERIALS AND METHODS

2.1 Data

The proposed PDR approach is tested on the Capnabase [9] and MIMIC [13] databases which are publically available. The Capnabase database consists of 42 concurrently acquired ECG, PPG and respiration signals with each of 8 minutes in duration from 29 children and 13 adults at a sampling rate of 300 Hz [9]. The recorded respiratory signal is used to compare the PDR signal and, therefore, it is denoted as the reference respiration. The recordings are segmented into equal length epochs of duration 30 seconds (s). For experimental use, a total of 605 epochs are extracted from the PPG recordings and used for the performance evaluation of the proposed technique.

On the other hand, the MIMIC database includes 72 simultaneous recorded BP, ECG, PPG, and respiratory signals at a rate of 125 Hz [13]. In 72 records, some of the records do not have either PPG or respiration or both. However, in this study, simultaneously recorded PPG and respiratory signals are required for the experimental analysis. Therefore, in the remaining records which have both the PPG and respiratory signals, a total of 2300 epochs (which are visually uncorrupted) of duration 30s each are selected for the experimental use.

2.2 Proposed Methodology

The HVD decomposes a given multicomponent non-stationary signal into various mono-components of slowly varying amplitudes and frequencies [10]. The first component of the decomposition represents the varying largest amplitude, and therefore this component is denoted as the dominant one in the input signal. The residual part is a mixture of other lower amplitude signals. The HVD is an iterative technique where extraction of each component consists of mainly three stages [11]: (i) computation of the instantaneous frequency (IF) of largest amplitude component, (ii) computation of the instantaneous amplitude of largest component, and (iii) subtraction of the estimated mono-component in the input signal to get the residual. Hence, the decomposition of a given signal $x(t)$ by applying the HVD technique can be represented as [10]

$$x(t) = \sum_k a_k(t) \cos\left(\int \omega_k(t) dt\right), \quad (1)$$

where $a_k(t)$ and $\omega_k(t)$ denote the envelope and the IF of k^{th} component, respectively. The HVD technique uses the analytical signal depiction of the input signal to compute the amplitude envelope and IF of the dominant component in the composite [10]. In the HVD based signal decomposition, the component $x_k(t)$ corresponds to higher energy as compared to the component $x_l(t)$ for $l > k$.

Upon decomposing the PPG signal $x(t)$ using the HVD, the component acquired in the first iteration of decomposition consonant with the largest energy component in PPG. In this study, it is hypothesized that the respiratory component in PPG has a substantial amount of the overall energy of the PPG. This essentially signifies that the largest energy component acquired

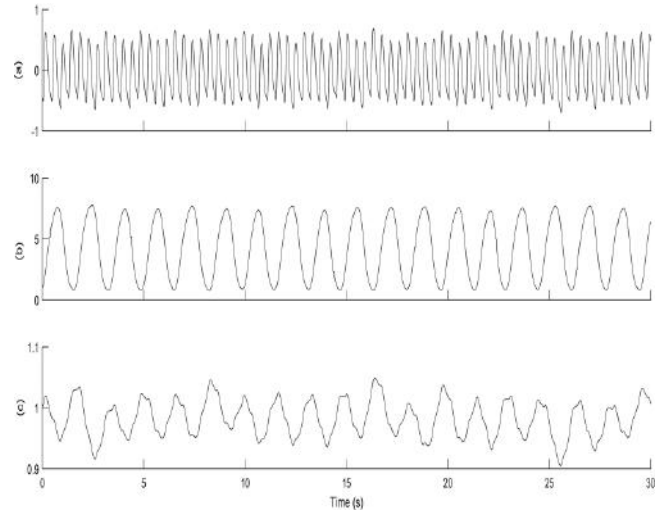


Figure 1. PPG signal decomposition using HVD method. (a) PPG signal, (b) reference (recorded) respiration, and (c) largest energy component (or first component) of the PPG decomposition using HVD

from PPG by applying the HVD method will be analogous to the respiration of the subject. Mathematically, the largest energy component $x_1(t)$ is expressed using (1) as [11]

$$x_1(t) = a_1(t) \cos\left(\int \omega_1(t) dt\right) \quad (2)$$

The signal $x_1(t)$, when plotted against time, shows cyclic variations closely resembling the reference respiration as illustrated in Figure 1. In Figure 1, it can be observed that the largest component of PPG matches the reference respiration. Next, the signal $x_1(t)$ is filtered through a band-pass filter (0.08 – 0.8 Hz) to remove the components other than the respiratory range. In this paper, the resultant output of the filter itself is denoted as the PPG derived respiration (PDR) signal. The PDR signal computed through the proposed approach is symbolized as R_{HVD} for further use.

It can also be highlighted here that if the respiratory component in the PPG has smaller energy than that of the other components in the PPG signal, the largest component of HVD may not resemble the reference respiration. The large signal DC offset is the required condition aimed at the HVD based adaptive non-stationary respiration filtering [10]. In the cases of a small respiratory component in the PPG, the required condition can be simply achieved by adding to the initial signal a constant value larger than the peak value.

2.3 Performance Measures

The proposed approach is evaluated by comparing the PDR with the recorded (reference) respiration by means of the correlation and errors in RRs. The Pearson's correlation coefficient (PCC) is computed here to measure the similarity among the PDR and reference respiratory signals. The error between RRs calculated from the PDR and reference signals is evaluated using the mean absolute error (MAE), percentage error (PE) and root mean square error (RMSE) defined as

$$MAE = \frac{1}{N} \sum_{n=1}^N |d(n) - r(n)|, \quad (3)$$

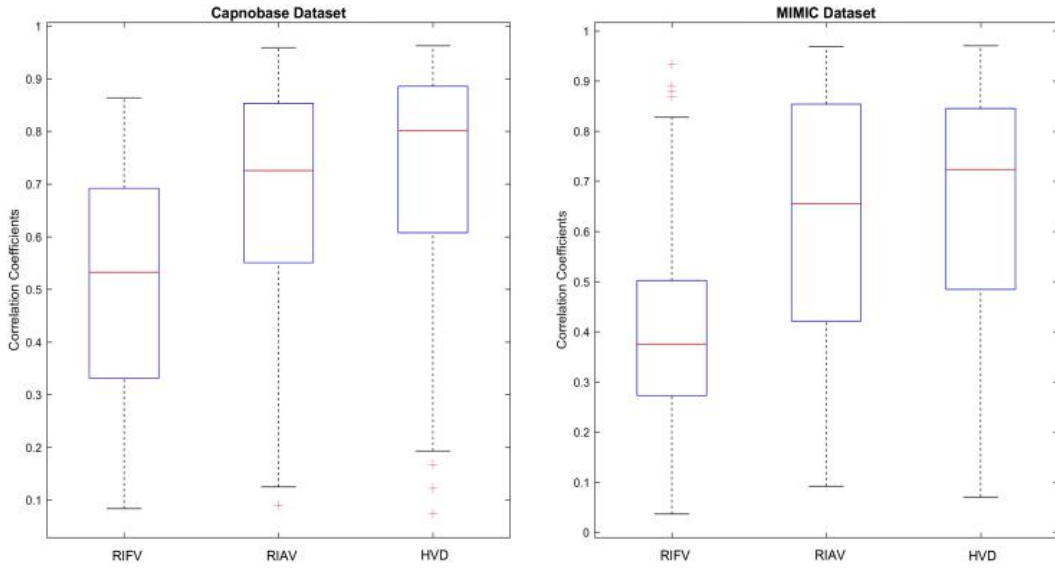


Figure 2. Box-whisker plots of correlation coefficient computed between the derived and reference respiration signals using the Capnabase (left) and MIMIC (right) datasets (RIFV: respiratory induced frequency variation approach, RIAV: respiratory induced amplitude variation approach, and HVD: proposed approach)

$$PE = \frac{1}{N} \sum_{n=1}^N \frac{|d(n) - r(n)|}{r(n)} \times 100 \%, \quad (4)$$

$$RMSE = \sqrt{\frac{1}{N} \sum_{n=1}^N [d(n) - r(n)]^2}, \quad (5)$$

where, N is the total number of epochs in a recording, $d(n)$ and $r(n)$ denote the RRs in breaths per minute (bpm) calculated from the PDR and reference respiration signals, respectively, for n^{th} epoch.

Here, $d(n)$ for n^{th} epoch is calculated using the fast Fourier transform method. In the PDR signal spectrum, the dominant frequency (f_r) in the respiration frequency band (0.08 – 0.8 Hz, i.e., 4.8 – 48 bpm) is determined, and then it is converted to RR which is defined in [1] as

$$d(n) = f_r * 60 \text{ (breaths/min)} \quad (6)$$

The RR of the reference respiration ($r(n)$) for n^{th} epoch is calculated using the similar process as described above.

3. EXPERIMENTAL RESULTS

The proposed approach is validated over a larger number of epochs of duration 30s each extracted from two well-known independent databases, namely the Capnabase and the MIMIC. The performance of the proposed PDR approach is compared with two state-of-art PDR methods based on the respiratory-induced amplitude variation (RIAV) [3] and respiratory-induced frequency variation (RIFV) [3]. Here, the PDR signal obtained using the RIAV and RIFV methods are denoted as R_{RIAV} and R_{RIFV} , respectively. Additionally, some other existing PDR techniques are also compared with the proposed technique based on the RMSE values.

Box-whiskers plots of correlation computed among the derived and reference signals for different PDR techniques are depicted in

Table 1. Comparisons of proposed PDR approach with some existing techniques using the Capnabase dataset (Parameters are shown as median values (1st quartile, 3rd quartile))

PDR Methods	MAE (bpm)	PE (%)	RMSE (bpm)
R_{RIFV}	2.5 (0.4, 4.5)	23.3 (2.7, 38.3)	4.8 (1.1, 7.5)
R_{RIAV}	1.9 (0.3, 3.9)	14.6 (2.6, 30.8)	3.3 (0.9, 6.3)
R_{HVD}	0.97 (0.2, 3.3)	8.8 (0.4, 26.5)	1.4 (0.3, 5.5)

Figure 2. Using the Capnabase dataset, the median values of the correlation coefficient for different PDR techniques are obtained as: $R_{RIFV} = 0.53$, $R_{RIAV} = 0.73$, and $R_{HVD} = 0.80$, and, using the MIMIC dataset, the median values of correlation are computed as: $R_{RIFV} = 0.38$, $R_{RIAV} = 0.66$, and $R_{HVD} = 0.73$. In the statistical test, Friedman test found a significant difference between the correlation values computed for different PDR techniques using both the datasets for a value of $p < 0.001$. As shown in Figure 2, the higher values of correlation are obtained for the proposed technique in both the datasets as compared to RIFV and RIAV techniques which shows the better resemblance between R_{HVD} and the reference respiration.

Other performance measures computed for different PDR technique using the Capnabase and MIMIC datasets are shown in Table 1 and Table 2, respectively. In the CapnoBase dataset, the proposed approach is observed to be providing the lower values (median) of MAE, PE, and RMSE as 0.97 bpm, 8.8%, and 1.4 bpm, respectively, then that of the two existing techniques. Contrarily, in the MIMIC dataset, the proposed technique outperformed the two well-known existing methods by achieving the lower values of MAE, PE, and RMSE as 1.8 bpm, 12.8%, and

Table 2. Comparisons of proposed PDR approach with some existing techniques using the MIMIC dataset (Parameters are shown as median values (1st quartile, 3rd quartile)

PDR Methods	MAE (bpm)	PE (%)	RMSE (bpm)
R_{RIFV}	6.5 (3.8, 8.9)	39.6 (28.1, 65.8)	8.1 (6.1, 10)
R_{RIAV}	2.2 (1.1, 4.4)	15.1 (6.3, 32)	3.6 (2.2, 6.3)
R_{HVD}	1.8 (0.9, 3.4)	12.8 (7.1, 20.4)	3.1 (1.4, 5.9)

3.1 bpm, respectively. These above results demonstrate that the proposed technique can be used for accurate monitoring of RRs in the patients with dissimilar problems.

Additionally, the Bland-Altman plot is also studied to assess the agreement between two variables. This plot investigates the limit of agreement (LOA) between two variables which is defined using the mean and standard deviation (SD) of difference as [mean - 1.96SD, mean + 1.96SD] for 95% confidence range [14]. Thus, to measure the agreement between derived and reference RRs, the Bland-Altman plots for the estimated RRs using the proposed approach over the Capnabase and MIMIC datasets are shown in Figure 3. In Figure 3, the values of LOA for the Capnabase and MIMIC datasets are obtained as [-9.83, 7.94] and [-7.38, 10.75], respectively. Upon analysing the respiratory rate errors, the performance of proposed approach is found to be satisfactory as it provides a good agreement in the RRs computed from derived and reference respiration signals for both the datasets used in this work.

4. DISCUSSION

This study aimed to develop an effective approach for non-invasive monitoring of the respiration from the PPG signal. The proposed work used the HVD method for decomposition of the PPG signal into various mono-components with gradually changing amplitudes and frequencies. As the respiratory process causes substantial variations in the PPG signal characteristics, the respiratory component in PPG can be assumed to be having a significant fraction of the overall energy of the input signal. This assumption, in turn, leads to develop a simple but effective approach for estimating the respiration from the largest energy component of the PPG signal obtained using the HVD method. The proposed approach is validated comparatively over a larger dataset obtained from the patients suffered from dissimilar problems. Results demonstrated that the proposed technique provides more accurate and reliable results than the existing methods.

Comparison of the proposed approach with some recently developed PDR algorithms based on the RMSE value is also presented in Table 3. Table 3 shows that the proposed PDR approach delivers a better estimation of the RR than the existing methods by attaining a lower value of RMSE as 1.4 bpm on the Capnabase dataset. In the comparison, the CSD based technique in [7] showed the lower value of RMSE than that obtained for the proposed technique. This lower value of RMSE is obtained due to longer data length (epoch length was taken as 120s) selected to validate the PDR technique. It is also mentioned in [7] that the performance of the algorithm degrades as the epoch length decreases. Since the shorter duration epochs are more suitable for clinical applications and therefore, in the current study, the proposed technique is validated over shorter data length segments of the PPG signal. Also, unlike to the EEMD based algorithm where many intrinsic mode functions (IMFs) are used to determine RR [1], the proposed PDR approach requires the largest energy component (which is obtained in the first iteration of

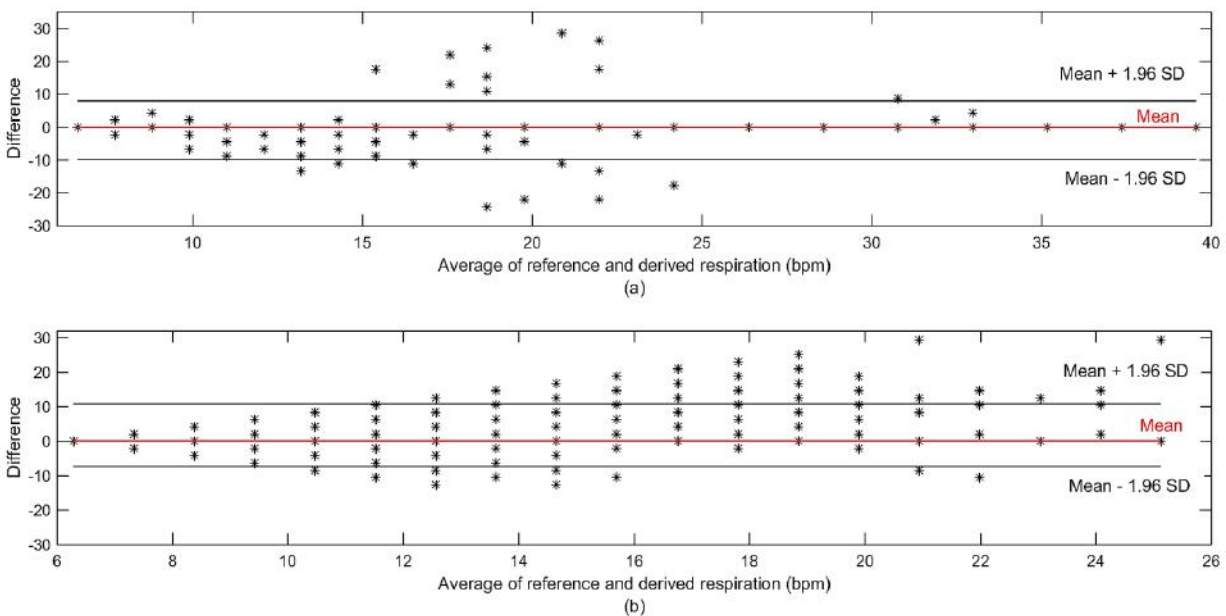


Figure 3. The Bland-Altman plot for the proposed technique showing the LOA between the reference and derived RRs for both the Capnabase and MIMIC datasets. (a) Capnabase dataset and (b) MIMIC dataset

Table 3. Comparison of the proposed PDR approach with some other existing methods over the Capnabase dataset based on median (1st quartile, 3rd quartile) values

PDR Methods	RMSE (bpm)	Epoch Length (s)
Proposed Approach	1.39 (0.3, 5.5)	30
EEMD-PCA [1]	2.77 (0.50, 5.9)	30
Smart Fusion [3]	1.56 (0.60, 3.15)	32
CSD [7]	0.95 (0.27, 6.20)	120
PSD [7]	3.18 (1.20, 11.3)	120
EMD [8]	3.5 (1.1, 11)	60

decomposition) alone to obtain the respiration. This, in turn, reduces the computational cost of the PDR approach which is an important factor considered in the development of mobile-based healthcare systems. In contrast to RIFV and RIAV, the proposed approach reduces the need for the detection of fiducial points (e.g., pulse peak positions) in the PPG which is an extra (but important) step required in the RIFV and RIA

It may so happen that the respiratory component in the PPG signal doesn't appear to be the largest energy component. Then, the first component obtained from the PPG decomposition using the HVD may not resemble the reference respiration. The large signal DC offset is the required condition aimed at the HVD based adaptive non-stationary respiration filtering [10]. In the cases of a small respiratory component in the PPG, the required condition can be simply achieved by adding to the initial signal a constant value larger than the peak value. This solution for the HVD based PDR approach in the case of a small respiratory component in the PPG further strengthens the reliability of the proposed technique for obtaining the respiration under diverse conditions. However, if the muscles noise or artifacts lie in the respiratory band and are of significant magnitude in the PPG signal, then the proposed HVD based scheme may provide erroneous results in the respiration estimation.

It can also be mentioned here that the recordings of both the datasets used here are recorded from different subjects suffering from unlike problems. Nevertheless, the HVD based approach not only shown a better resemblance with the reference respiration but also provided a good agreement in RRs computed from RHVD and the reference respiration. This essentially means that the performance of the proposed approach is not dependent on the type of dataset.

5. CONCLUSION

This paper presents a new approach using the HVD for extracting the respiration from the PPG signal. It is shown that the respiratory component in PPG can be separated in the largest energy component of PPG decomposition using the HVD method. In the experiments, the proposed PDR approach is applied to the Capnabase and MIMIC datasets. The proposed approach is found to be performing better than the available PDR techniques in the literature by attaining a greater value of the correlation among the PDR and reference signals, and the smaller values of errors in RRs calculated among the PDR and reference respiration. Results

prove that the proposed approach can be utilized for deriving the respiration from the PPG signal.

6. REFERENCES

- [1] Motin M. A., Karmakar C., and Palaniswami M. 2017. Ensemble empirical mode decomposition with principal component analysis: a novel approach for extracting respiratory rate and heart rate from photoplethysmographic signal. *IEEE J. Biomed. Health Inform.* 99, 766-774.
- [2] Addison P. S., Watson J. N., Mestek M. L., and Mecca R. S. 2012. Developing an algorithm for pulse oximetry derived respiratory rate (RRoxi): a healthy volunteer study. *J. Clin. Monitor. Comput.* 26, 45-51.
- [3] Karlen W., Raman S., Ansermino J. M., and Dumont G. A. 2013. Multiparameter respiratory rate estimation from the photoplethysmogram. *IEEE Trans. Biomed. Eng.* 60, 1946-1953.
- [4] Lázaro J., Gil E., Bailón R., Mincholé A., and Laguna P. 2013. Deriving respiration from photoplethysmographic pulse width. *Med. Biol. Eng. Comput.* 51, 233-242.
- [5] Nakajima K., Tamura T., and Miike H. 1996. Monitoring of heart and respiratory rates by photoplethysmography using a digital filtering technique. *Med. Eng. Phys.* 18, 365-372.
- [6] Leonard P., Grubb N. R., Addison P. S., Clifton D., and Watson J. N. 2004. An algorithm for the detection of individual breaths from the pulse oximeter waveform. *J Clin. Monitor Comput.* 18, 309-312.
- [7] Garde A., Karlen W., Ansermino J. M., and Dumont G. A. 2014. Estimating Respiratory and Heart Rates from the Correntropy Spectral Density of the Photoplethysmogram. *PLoS ONE.* 9, 1-11.
- [8] Garde A., Karlen W., DehKordi P., Ansermino J., and Dumont G. 2013. Empirical mode decomposition for respiratory and heart rate estimation from the photoplethysmogram. In *Computing in Cardiology Conference (2013)*. 799-802.
- [9] Karlen W., Turner M., Cooke E., Dumont G., and Ansermino J. 2010. CapnoBase: Signal database and tools to collect, share and annotate respiratory signals. In *Annual Meeting of the Society for Technology in Anesthesia (STA) (West Palm Beach 2010)*, 25.
- [10] Feldman M. 2006. Time-varying vibration decomposition and analysis based on the Hilbert transform. *J. Sound Vib.* 295, 518 - 530.
- [11] Sharma H. and Sharma K. K. 2015. Baseline wander removal of ECG signals using Hilbert vibration decomposition. *Electron. Lett.* 51, 447-449.
- [12] Sharma H. and Sharma K. K. 2018. ECG-derived respiration based on iterative Hilbert transform and Hilbert vibration decomposition. *Australas. Phys. Eng. Sci. Med.* 41, 429-443.
- [13] Moody G. B., and Mark R. G. 1996. A database to support development and evaluation of intelligent intensive care monitoring. In *Computing in Cardiology Conference (1996)*. 657-660.
- [14] Bland J. M. and Altman D. 1986. Statistical methods for assessing agreement between two methods of clinical measurement. *The Lancet.* 327 (8476), 307-310.

ICBBB 2019

Biological Systems Modeling and Simulation

Calcium Signaling and Finite Element Technique

Devanshi D. Dave
Department of Mathematics,
School of Technology, Pandit Deendayal Petroleum
University, Gujarat, India
ddave1822@gmail.com

Brajesh Kumar Jha
Department of Mathematics,
School of Technology, Pandit Deendayal Petroleum
University, Gujarat, India
brajeshjha2881@gmail.com

ABSTRACT

In this paper, we describe the calcium signaling phenomena using finite element method in a typical neuron cell. Neuron being the fundamental cell of the brain has many important roles to perform. The approximated geometry of the neuron is considered to approximate the calcium flow in it. Calcium is considered to be the important second messenger which helps in maintaining plethora of functions like synaptogenesis, proliferation, cell differentiation, etc. The level of the cell calcium is maintained by several important physiological parameters of the calcium toolkit like buffers, endoplasmic reticulum, mitochondria, voltage gated calcium channel, etc. Here, we have considered the cytoplasmic calcium binding buffers in knowing its effect on cytosolic calcium concentration. Exogenous buffers EGTA and BAPTA are considered here. Mathematical model involving two-dimensional partial differential equation is used to delineate the calcium diffusion in presence of calcium binding buffers. Appropriate boundary conditions matching with the physiology of the brain are incorporated. To obtain the desired results finite element technique is used. Discretization and further refinement of the mesh is done to obtain more better approximation of the calcium flow. The results obtained here clearly show the significant impact of buffers on calcium diffusion.

CCS Concepts

Computing methodologies → Modeling and simulation → Model development and analysis → Model verification and validation

Keywords

Calcium signaling; EGTA, BAPTA; Finite element technique

1. INTRODUCTION

Computational biology has emerged as an amalgamative research interest now-a-days. The combination of biology and computational tools helps in unrevealing many physiological facts. Computational tools comprises of mathematical models and innovative soft computing skills. Keeping in mind this background, in this paper, we have estimated the calcium flow in neuron cell. Neurons are the basic building blocks of the central nervous system which maintains the brain equilibrium with the

Permission to make digital or hard copies of all or part of this work for personal or classroom use is granted without fee provided that copies are not made or distributed for profit or commercial advantage and that copies bear this notice and the full citation on the first page. Copyrights for components of this work owned by others than ACM must be honored. Abstracting with credit is permitted. To copy otherwise, or republish, to post on servers or to redistribute to lists, requires prior specific permission and/or a fee. Request permissions from Permissions@acm.org.

ICBBB '19, January 7–9, 2019, Singapore, Singapore

© 2019 Association for Computing Machinery.

ACM ISBN 978-1-4503-6654-0/19/01...\$15.00

DOI: <https://doi.org/10.1145/3314367.3314377>

help of other cells like astrocytes, oligodendrocytes, microglia, etc. [1],[2],[3]. The fundamental function of a typical neuronal cell is to process and further transfer the set of information. Hence, the signaling pathways of calcium in neurons play a crucial role in maintaining cell balance. Calcium is ubiquitously known as the second messenger.[4] Out of three different types of second messenger calcium comes under the hydrophilic category which consists of the messengers that are situated at the cytosolic level. Being a second messenger, it handles variety of physiological functions like cell differentiation, synaptogenesis, proliferation, exocytosis, fertilization, depolarization, gene expression, energy production, etc.[3]. Hence, the level of calcium inside the neurons and in brain has great impact; the alterations in which would cause devastating neuronal disorders like Alzheimer's disease, Parkinson's disease, epilepsy and so on.[5]-[8] The cell calcium at cytoplasmic level is mainly maintained by calcium binding buffers.[9] Other than cytoplasmic calcium buffers, voltage gated calcium channel, endoplasmic reticulum, mitochondria, several pumps and exchangers have their role in maintaining the cell calcium.[4] As suggested by the name, buffers bind with the calcium at the peripheral level and thus the level of the calcium is maintained. It has been estimated that around 99 % of the calcium gets processed at the source and the rest passes through sink by certain physiological phenomena.[10] Endoplasmic reticulum and mitochondria are the small entities which are present inside the cell and maintain the cytoplasmic calcium levels. On the other hand, calcium channels and the calcium exchangers help in maintaining it by working simultaneously between plasma membrane and the cytosol. Thus, adequate and normal amount of calcium in cells helps in knowing spatial as well as temporal spread of calcium which further leads to normal calcium signaling cascades.

From the literature survey, it has been found that various analytical and numerical methods are incorporated by the researchers to study the calcium concentration distribution in presence of different physiological parameters in cells like neurons, astrocytes, myocytes, oocytes, etc. Finite element method has been employed by the researchers for one and two dimensional calcium diffusion problems. Naik and Pardasani have used voltage gated calcium channels, RyR and buffers to know their impact on calcium reaction diffusion using finite element method.[11], Panday and Pardasani delineated calcium concentration distribution in presence of sodium calcium exchanger in oocytes.[12] Also, one dimensional unsteady state for calcium diffusion has been solved using variational-Ritz approach by Tewari and Pardasani.[13] Jha et al. have used finite element method to portray the calcium diffusion in astrocytes in presence of various physiological parameters.[14] Jha and Adlakha studied calcium diffusion in dendritic spines using finite element method in presence of excess buffers.[15] Also, Kotwani and Adlakha used finite element method to show the significance of buffers, source amplitude and source geometry on spatial and temporal calcium concentration distribution.[16] All the authors

have considered the regular geometry to obtain the calcium flow. No attempts have been made in the past to delineate calcium concentration distribution for irregular shaped geometry of the neuron cell having sole as well as multiple calcium entries.

Keeping in mind the above physiological facts and the literature survey, in this paper we have computationally estimated the calcium concentration distribution in neuronal cells in presence of exogenous calcium binding buffers EGTA and BAPTA. The two-dimensional computational model and the technique used to obtain the desired results are shown in the next sections followed by results and discussion.

2. MATHEMATICAL FORMULATION

The two dimensional calcium diffusion model can be represented with the help of partial differential equation which can be stated as,[17]

$$\frac{\partial C}{\partial t} = D_{Ca_x} \frac{\partial^2 C}{\partial x^2} + D_{Ca_y} \frac{\partial^2 C}{\partial y^2} - f(x, y, C)$$

where $f(x,y,c)$ is the additional physiological phenomena like calcium buffering, flux through voltage channels, exchange through certain exchangers and so on.

In our case, the term $f(x,y,c)$ consists of the physiological phenomena of calcium buffering. The spatial and temporal spread of the calcium highly depends on the binding affinity and amount of buffer. Here, we have considered two exogenous buffers namely EGTA and BAPTA to estimate the calcium flow. Mathematically calcium buffering phenomena can be described as[18],[19]



Using Fickian law, the resulting differential equations can be stated as [19],[17],[20]

$$\frac{\partial [Ca^{2+}]}{\partial t} = D_{Ca} \left(\frac{\partial^2 [Ca^{2+}]}{\partial x^2} + \frac{\partial^2 [Ca^{2+}]}{\partial y^2} \right) + \sum_j R_j$$

$$\frac{\partial [B_j]}{\partial t} = D_{B_j} \left(\frac{\partial^2 [B_j]}{\partial x^2} + \frac{\partial^2 [B_j]}{\partial y^2} \right) + R_j$$

$$\frac{\partial [CaB_j]}{\partial t} = D_{CaB_j} \left(\frac{\partial^2 [CaB_j]}{\partial x^2} + \frac{\partial^2 [CaB_j]}{\partial y^2} \right) - R_j$$

where

$$R_j = -k_j^+ [B_j] [Ca^{2+}] + k_j^- [CaB_j]$$

$D_{Ca}, D_{B_j}, D_{CaB_j}$ denotes diffusion coefficients for calcium, buffer and calcium bound buffers respectively. k_j^+, k_j^- are the association and the dissociation rates for buffer 'j' respectively.

Thus, substituting the reaction term in the computational model, we have our problem model to process for numerical technique. Hence the two-dimensional model is described as,

$$\frac{\partial c}{\partial t} = D_x \frac{\partial^2 c}{\partial x^2} + D_y \frac{\partial^2 c}{\partial y^2} - k_m^+ [B]_\infty (c - c_\infty)$$

Further the boundary conditions are incorporated such that the physiological facts are not affected. Physiologically, the

background concentration of $[Ca^{2+}]$ is considered $0.1 \mu M$. Single and multiple fluxes of calcium are designed to estimate the actual flux conditions. It is stated as:

$$-D_{Ca} \frac{\partial u}{\partial x} = \sigma_{Ca}$$

This mathematical model is further treated with finite element technique to obtain the results.

3. FINITE ELEMENT TECHNIQUE

Basically finite element technique is used to obtain the solution for domains having complex geometries. Hence, here we have incorporated it to get the approximated calcium concentration distribution in neuronal cells. The geometry of a typical neuronal cell is designed as a domain which is further discretized into number of elements. On comparing the results obtained, it has been found that refined mesh yields better approximation. Thus, the finite element process is described as:

3.1 Approximated Geometry of the Cell-Domain Description

Figure 1 shows the domain of a typical neuronal cell. A typical neuronal cell geometry is taken as a domain, which consists of dendrites, soma, axon and axon terminals. Being computational study, only 6 dendrites and 5 axon terminals are assumed. The next step is to incorporate the physiological boundary condition

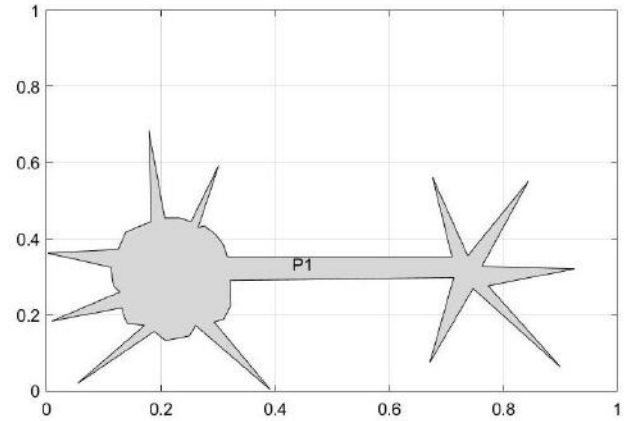
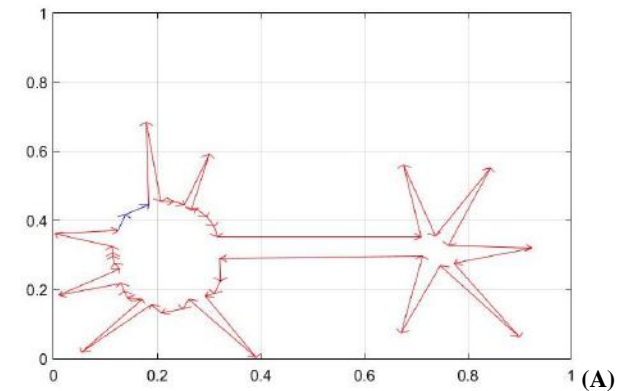


Figure 1. Approximated geometry of a typical neuron cell

3.2 Boundary conditions



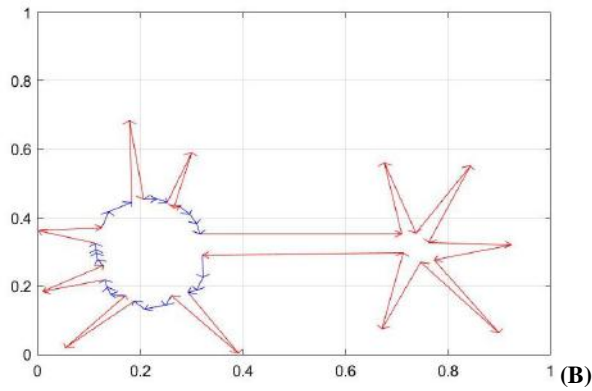


Figure 2. Physiological condition of calcium flux incorporated on the cell: A) Sole flux B) Multiple fluxes

The calcium from the plasma membrane enters in the cytoplasm of the neuronal cells. Here we have considered sole and multiples fluxes to obtain a better view about the calcium distribution. Figure 2 shows the incorporated boundary condition on the domain of the cell, which matches with actual physiology of the cell.

3.3 Discretization of the Domain

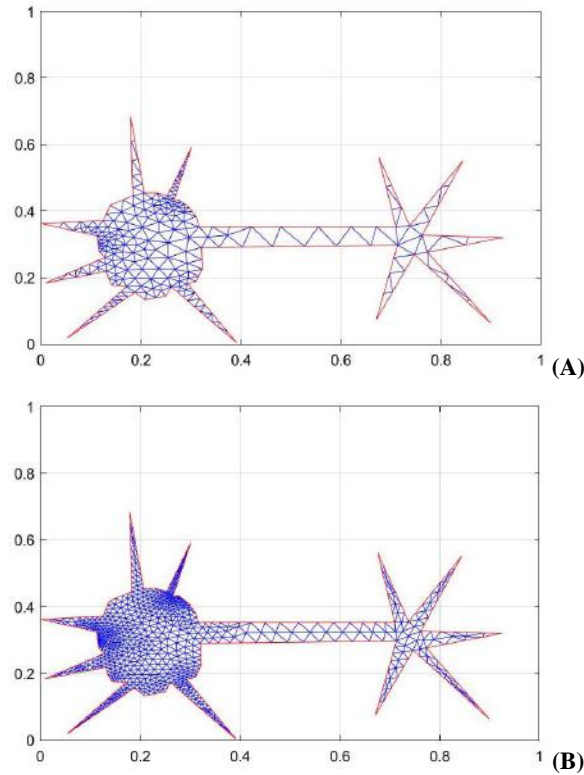


Figure 3. Meshing of the domain: A) Initial mesh B) Refined mesh

Figure 3 shows the discretization of the neuronal cell having initial and refined mesh. The initial mesh consists of 278 nodes and 382 triangular elements whereas refined mesh consists of 937 nodes and 1528 elements. Further refinement yield to increase in elements but no significant and noteworthy changes in the approximate solution is found. Hence we have not considered that results. Also, the results obtained for the initial mesh are not discussed, as we have a better approximation of calcium flow with

us. Next section shows the calcium concentration distribution in presence of EGTA and BAPTA in a typical neuronal cell having sole and multiple calcium fluxes.

4. RESULTS AND DISCUSSION

In this section, the obtained results are discussed. The values of all the physiological parameters are stated in Table 1 or mentioned when necessary.

Table 1. Values of physiological parameters[21],[10]

	Parameter	Values
D	Diffusion Coefficient	200-300 $\mu\text{m}^2\text{s}^{-1}$
k_+	Buffer Association Rate	1.6-600 $\mu\text{m}^{-1}\text{s}^{-1}$
$[B]_\infty$	Buffer Concentration	10-350 μM
$[Ca^{2+}]_\infty$	Background Calcium Conc.	0.1 μM

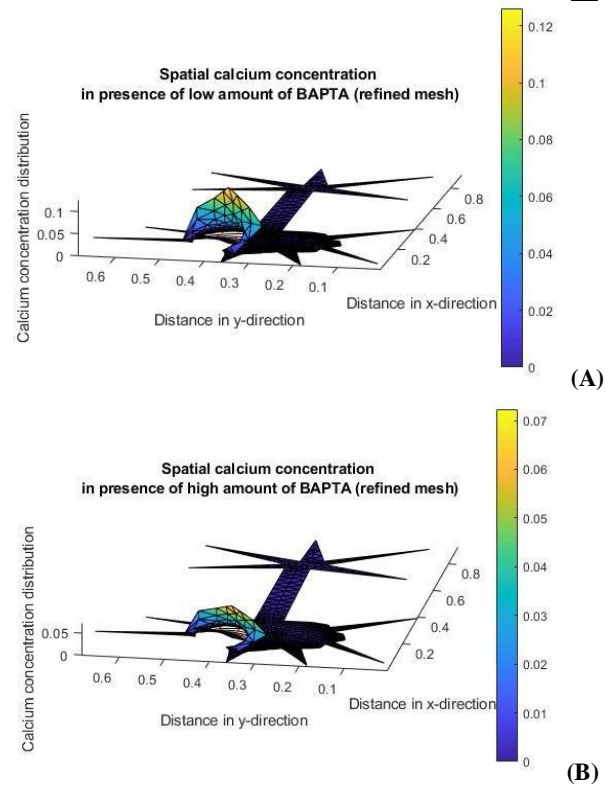


Figure 4. Spatial calcium concentration distribution in presence of BAPTA having sole fluxes: A) Low amount B) High amount

Figure 4 shows the spatial calcium concentration distribution in presence of sole flux of BAPTA. Here, the results are obtained for the refined mesh only, as it yields better approximation. The amount of the buffer considered and the buffer affinity for BAPTA are mentioned in Table 1. To know impact of calcium binding buffers on the cytosolic calcium, we have considered two cases having negligible and immense amount of BAPTA. As expected, it has been found that the amount of the buffer has noteworthy impact on the cytosolic calcium concentration distribution. It can be seen from the plots for the low and high amount of buffer that the plot having negligible amount of buffer have higher calcium as compared to the one having higher amount

of BAPTA. Thus, the results obtained here are in harmony with the physiological fact. Further, to get more realistic output, calcium flux is considered from multiple boundaries. The results for the multiple calcium flux are shown in Figure 5. The values of the physiological parameters are same as considered before. The change in the geometry of the cell due to it clearly shows the significant impact of the multiple calcium fluxes. Also, it can be observed that the amount of buffer greatly affects the spatial distribution of calcium concentration distribution.

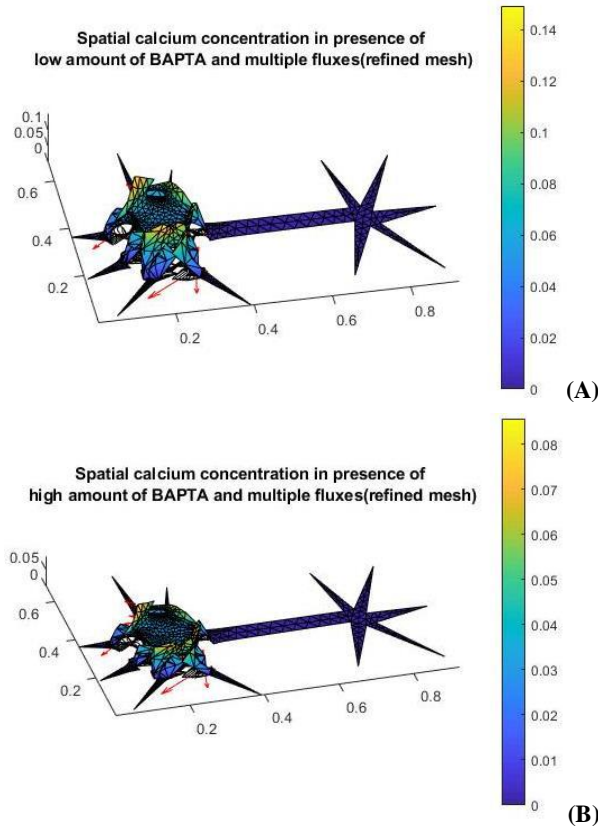


Figure 5. Spatial calcium concentration distribution in presence of BAPTA having multiple fluxes: A) Low amount B) High amount

Similarly, the results are obtained for EGTA. Figure 6 and Figure 7 shows the spatial calcium concentration distribution in presence of EGTA having single and multiple boundary conditions. The values of the physiological parameters are stated in Table 1. Here also, the results are obtained for refined mesh only. Figure 6 shows the calcium diffusion for sole flux having low and high amount of buffer whereas, Figure 7 shows it for the multiple calcium entries. It is known that the buffer present at the peripheral region binds with the calcium, resulting into calcium bound buffers and thus the cell level in the cytoplasm is altered, i.e. more the calcium, lower is the calcium level and vice-versa. From the graphs it is clearly seen that the amount of buffers is directly related to the two dimensional spatial spread of the calcium. The decrease in amount of buffer which further result into excess amount of calcium may lead to neurodegenerativity and the cell death cascades due to the toxicity rendered by cell calcium.

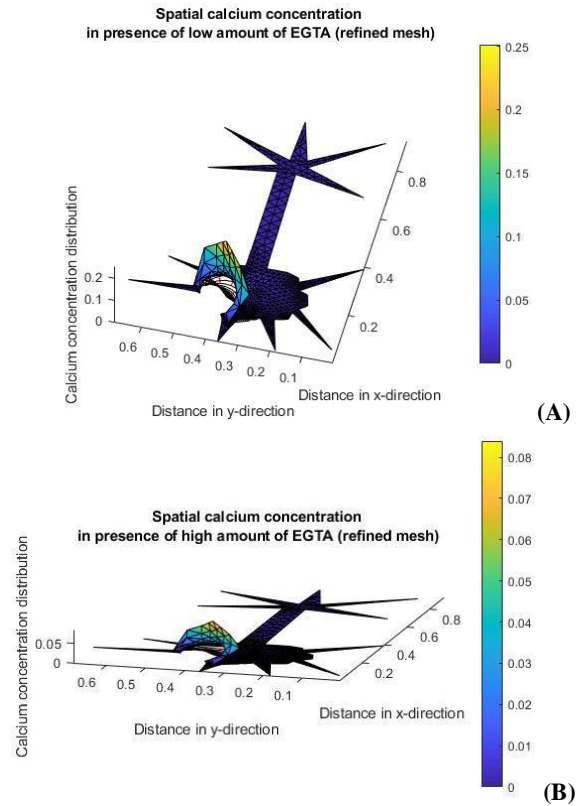


Figure 6. Spatial calcium concentration distribution in presence of EGTA having sole flux: A) Low amount B) High amount

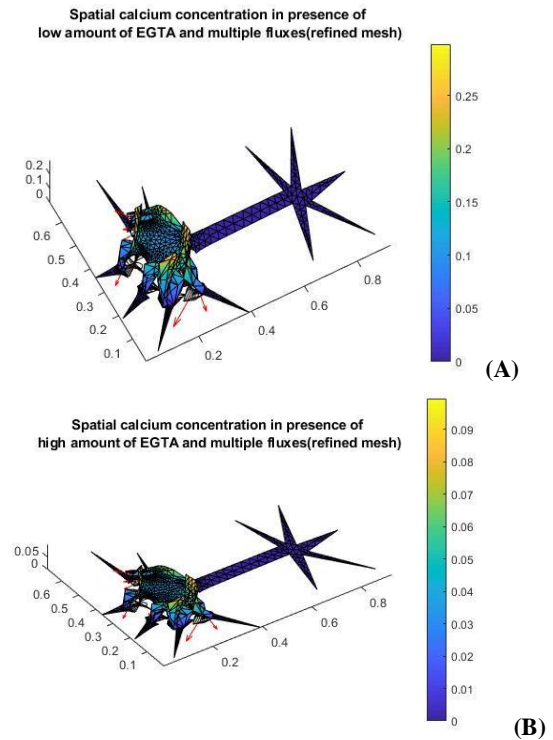


Figure 7. Spatial calcium concentration distribution in presence of EGTA having multiple fluxes: A) Low amount B) High amount

5. CONCLUSION

In this research article, we have considered two-dimensional partial differential diffusion equation to explicate calcium signaling pathways in presence of exogenous buffers named EGTA and BAPTA. The fundamental nature of the buffer is to lower down and maintain the cell calcium which is verified in this research article. The finite element technique is employed here to get the estimated results. The reason for employing to finite element technique is to get better approximate views about physiological phenomena. More realistic view is obtained with the help of multiple calcium fluxes and better approximation is generated due to refinement of the mesh. The results are obtained for low and high amount of EGTA and BAPTA which clearly shows the impact of buffers on cytosolic calcium concentration distribution. Also, multiple fluxes with high amount of buffer yield more realistic results. Thus, this research article explicates the normal cell signaling cascades of calcium. It can be concluded that the amount of buffer directly affects the calcium concentration. Hence it is essential for maintaining cell calcium; the alteration in which may lead to fatal neurodegenerative disease which can be further studied in higher dimensions.

6. REFERENCES

- [1] L. Squire, D. Berg, F. Bloom, S. du Lac, A. Ghosh, and N. Spitzer, *Fundamental Neuroscience*, Third. Elsevier, 2008.
- [2] B. Brawek and O. Garaschuk, "Microglial calcium signaling in the adult, aged and diseased brain," *Cell Calcium*, vol. 53, no. 3, pp. 159–169, 2013.
- [3] M. P. Mattson and S. L. Chan, "Neuronal and glial calcium signaling in Alzheimer's disease," *Cell Calcium*, vol. 34, pp. 385–397, 2003.
- [4] E. M. Kawamoto, C. Vivar, and S. Camandola, "Physiology and pathology of calcium signaling in the brain," *Front. Pharmacol.*, vol. 3, no. April, pp. 1–17, 2012.
- [5] S. Rajagopal and M. Ponnusamy, *Calcium Signaling: From Physiology to Diseases*. Springer Nature Singapore Pvt Ltd., 2017.
- [6] A. Demuro, I. Parker, and G. E. Stutzmann, "Calcium Signaling and Amyloid Toxicity in Alzheimer's Disease," *J. Biol. Chem.*, no. 6, pp. 1–14, 2010.
- [7] D. D. Dave and B. K. Jha, "Delineation of calcium diffusion in alzheimeric brain," *J. Mech. Med. Biol.*, vol. 18, no. 2, pp. 1–15, 2018.
- [8] B. K. Jha, H. Joshi, and D. Dave, "Portraying the Effect of Calcium-Binding Proteins on Cytosolic Calcium Concentration Distribution Fractionally in Nerve Cells," *Interdiscip. Sci. Comput. Life Sci.*, 2016.
- [9] B. Schwaller, "Cytosolic Ca²⁺ Buffers," *Cold Spring Harb. Perspect. Biol.*, pp. 1–20, 2010.
- [10] A. Jha, N. Adlakha, and B. K. Jha, "Finite element model to study effect of Na⁺-Ca²⁺ exchangers and source geometry on calcium dynamics in a neuron cell," *J. Mech. Med. Biol.*, vol. 16, no. 2, pp. 1–22, 2015.
- [11] P. A. Naik and K. R. Pardasani, "Finite element model to study calcium distribution in oocytes involving voltage gated Ca²⁺ channel, ryanodine receptor and buffers," *Alexandria J. Med.*, vol. 52, no. 1, pp. 43–49, 2016.
- [12] S. Panday and K. R. Pardasani, "Finite Element Model to Study Effect of Advection Diffusion and Na⁺ / Ca²⁺ Exchanger on Ca²⁺ Distribution in Oocytes," *J. Med. Imaging Heal. Informatics*, vol. 3, no. 3, pp. 374–379, 2013.
- [13] S. Tewari, "A Variational-Ritz Approach to Study Cytosolic Calcium Diffusion in Neuron Cells for a One-dimensional Unsteady State Case," *GAMS J. Math. Math. Biosci.*, vol. 2, no. December, pp. 1–10, 2009.
- [14] B. K. Jha, N. Adlakha, and M. N. Mehta, "Two-dimensional finite element model to study calcium distribution in astrocytes in presence of excess buffer," *Int. J. Biomath.*, vol. 7, no. 3, pp. 1–11, 2014.
- [15] A. Jha and N. Adlakha, "Finite element model to study the effect of exogenous buffer on calcium dynamics in dendritic spines," *Int. J. Model. Simulation, Sci. Comput.*, vol. 5, no. 2, pp. 1–12, 2014.
- [16] M. Kotwani, N. Adlakha, and M. N. Mehta, "Finite Element Model to Study the Effect of Buffers, Source Amplitude and Source Geometry on Spatio-Temporal Calcium Distribution in Fibroblast Cell," *J. Med. Imaging Heal. Informatics*, vol. 4, no. 6, pp. 840–847, 2014.
- [17] J. Crank, *The Mathematics of Diffusion*, Second. Clarendon Press Oxford, 1975.
- [18] G. D. Smith, "Analytical Steady-State Solution to the Rapid Buffering Approximation Near an Open Ca²⁺ Channel," *Biophys. J.*, vol. 71, pp. 3064–3072, 1996.
- [19] G. D. Smith, L. Dai, R. M. Miura, and A. Sherman, "Asymptotic Analysis of Buffered Calcium Diffusion near a Point Source," *SIAM J. APPL. MATH.*, vol. 61, no. 5, pp. 1816–1838, 2001.
- [20] J. Keener and J. Sneyd, *Mathematical Physiology*, Second. Springer US, 2009.
- [21] B. K. Jha, N. Adlakha, and M. Mehta, "Two-dimensional finite element model to study calcium distribution in astrocytes in presence of VGCC and excess buffer," *Int. J. Model. Simulation, Sci. Comput.*, vol. 4, no. 2, pp. 1250030–1–1250030–15, 2013.

A Fractional Mathematical Model to Study the Effect of Buffer on Calcium Distribution in Parkinson's Disease

Hardik Joshi
Department of Mathematics,
School of Technology
Pandit Deendayal Petroleum University
Gandhinagar, Gujarat, India
hardik.joshi8185@gmail.com

Brajesh Kumar Jha
Department of Mathematics,
School of Technology
Pandit Deendayal Petroleum University
Gandhinagar, Gujarat, India
brajeshjha2881@gmail.com

ABSTRACT

Calcium (Ca^{2+}) is a vital and very important cation for proper functioning of the nerve cells. There is abundant amount of Ca^{2+} in human nerve cells among them very few amount lies in the cytosol in the form of free Ca^{2+} . These free amounts of Ca^{2+} react with calbindin- $\text{D}_{28\text{k}}$ which works as buffer species and significantly lower down the intracellular Ca^{2+} concentration. Parkinson's disease is a brain disorder of the human nerve cells associated with alteration in Ca^{2+} signalling process. In present study an attempt has been made by considering fractional advection diffusion equation to study the effect of buffer on Ca^{2+} diffusion in Parkinsonic nerve cells. An appropriate initial and boundary condition is taken according to the physiology of the problem. Analytical solution is obtained corresponding to time fractional advection diffusion equation and space fractional advection diffusion equation. The obtained results are simulated in MATLAB and interpreted with the Ca^{2+} distribution in nerve cells.

CCS Concepts

Computing methodologies → Modeling and simulation → Model development and analysis → Model verification and validation

Keywords

Calcium diffusion; Buffer concentration; Fractional advection diffusion equation; Parkinson's disease; Caputo fractional derivative

1. INTRODUCTION

Ca^{2+} works as a second messenger in human nervous system and transmit the information in the form of signal transduction. Ca^{2+} signalling in the nerve cells has a complex biological process throughout the living life. The entire process of Ca^{2+} signalling is depends on various physiological parameters. Calbindin- $\text{D}_{28\text{k}}$ is a Ca^{2+} binding proteins to control the adequate amount of intracellular Ca^{2+} concentration in nerve cells [18]. Parkinson's disease is a chronic degenerative disease of central nervous system. The degeneration of dopamine neurons in the midparts of

the brain indicates the early symptoms of disease. Basically it is characterized by motor and non-motor symptoms. The motor symptoms include the shakiness in one or two hands, rigidity of muscles, inability to stand or walk and bradykinesia [2].

Jha et al. have studied the effect of buffer concentration on Ca^{2+} diffusion by using fractional modelling. They obtain the spatio-temporal profile of Ca^{2+} concentration for different amount of EGTA buffer. They observed that high amount of EGTA buffer gradually lower down the Ca^{2+} concentration. Finally they simulate the obtained results with the Parkinson's disease [12]. Joshi et al. have studied the effect of buffer concentration on Ca^{2+} diffusion in presence of mitochondria. They consider fractional diffusion equation and use the fractional integral transform to obtain the analytical solution. They observed that mitochondria play a significant impact on intracellular Ca^{2+} concentration. Also, they incorporated the obtained results with Parkinson's disease [13]. Dave and Jha have studied the effect of buffer concentration on Ca^{2+} diffusion in presence of voltage gated Ca^{2+} channel. They consider two dimensional advection diffusion equations to obtain the analytical solution. They observed that buffer concentration has lower down the Ca^{2+} concentration whereas voltage gated Ca^{2+} channel raise the Ca^{2+} concentration in the nerve cells. Lastly, they interpreted the obtained solution with the neurodegenerative disorder known as Alzheimer's disease [5]. Also, Dave and Jha have studied the effect of calmodulin on Ca^{2+} diffusion in view of normal and Alzheimeric human brain. They considered advection diffusion equation and solve using Laplace and similarity transformation. They obtained the distribution profile of Ca^{2+} concentration for normal and Alzheimeric brain [4]. Jha and Adlakhia have studied the effect of exogenous buffer on Ca^{2+} diffusion. They adopted finite element method to solve two dimensional diffusion equations. They obtained spatial distribution profile of Ca^{2+} concentration for different amount of EGTA buffer. They observed that exogenous buffer play significant role on Ca^{2+} diffusion process [7]. Naik and Pardasani have studied the effect of EGTA and BAPTA buffer on Ca^{2+} diffusion in presence of voltage gated Ca^{2+} channel and ryanodine receptor. They obtained numerical solution of two dimensional diffusion equations by finite element approach. They obtained the distribution profile of Ca^{2+} concentration for different amount of EGTA and BAPTA buffer [15]. Also, Jha et al. have studied the effect of EGTA and BAPTA buffer on Ca^{2+} diffusion. They considered advection diffusion equation and applied the finite volume method to obtain the distribution profile of Ca^{2+} concentration. They observed that both EGTA and BAPTA buffers have peculiar effect on Ca^{2+} diffusion [9]. From the literature survey, it is noticed that the effect of buffer on Ca^{2+} diffusion has been studied on various cells like neuron, astrocytes, fibroblast, myocytes, oocytes, etc. [6], [8], [10], [11], [14], [16], [20]. Also, it is observed that very less amount of work has been

Permission to make digital or hard copies of all or part of this work for personal or classroom use is granted without fee provided that copies are not made or distributed for profit or commercial advantage and that copies bear this notice and the full citation on the first page. Copyrights for components of this work owned by others than ACM must be honored. Abstracting with credit is permitted. To copy otherwise, or republish, to post on servers or to redistribute to lists, requires prior specific permission and/or a fee. Request permissions from Permissions@acm.org.

ICBBB '19, January 7–9, 2019, Singapore, Singapore

© 2019 Association for Computing Machinery.

ACM ISBN 978-1-4503-6654-0/19/01...\$15.00

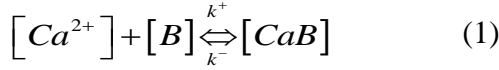
DOI: <https://doi.org/10.1145/3314367.3314378>

done by considering fractional modelling or in the view of neurological disorder.

In present study, the fractional advection diffusion model is incorporated by replacing the first order time derivative and second order space derivative in the classical advection diffusion equation by Caputo fractional derivative. Caputo fractional derivative is employed due to its non-local property and ability to deal with the integer order initial and boundary condition [1], [17].

2. MATHEMATICAL MODEL

The bidirectional reaction between Ca^{2+} and buffer is expressed as [10], [19]



The resulting partial differential equation is

$$\frac{\partial [Ca^{2+}]}{\partial t} = D_{Ca} \nabla^2 [Ca^{2+}] + \sum_j R_j \quad (2)$$

$$\frac{\partial [B]}{\partial t} = D_B \nabla^2 [B] + R_j \quad (3)$$

$$\frac{\partial [CaB]}{\partial t} = D_{CaB} \nabla^2 [CaB] - R_j \quad (4)$$

where reaction term R_j is in the terms of association and dissociation rate constant of buffer concentration of calbindin-D_{28k}.

$$R_j = -k^+ [B] [Ca^{2+}] + k^- [CaB] \quad (5)$$

D_{Ca} , D_B , D_{CaB} are diffusion coefficients of free Ca^{2+} , free buffer and Ca^{2+} bound buffers respectively. Then along with equation (1-5) the mathematical model can be frame as

$$\begin{aligned} \square_0 D_t^\alpha [Ca^{2+}] &= D_{Ca} \cdot \square_{-\infty} D_x^\beta [Ca^{2+}] - u D_x [Ca^{2+}] \\ &- k_j^+ [B]_\infty ([Ca^{2+}] - [Ca^{2+}]_\infty) \end{aligned} \quad (6)$$

where $\square_0 D_t^\alpha [Ca^{2+}]$ and $\square_{-\infty} D_x^\beta [Ca^{2+}]$ is the Caputo time fractional derivative of order α ($0 < \alpha \leq 1$) and Caputo space fractional derivative of order β ($1 < \beta \leq 2$) respectively.

Along with initial and boundary conditions as,

$$[Ca^{2+}](x, 0) = g(x), \quad [Ca^{2+}](\pm\infty, t) = 0 \quad (7)$$

The equation (6) can be rewritten as

$$\square_0 D_t^\alpha C = D_{Ca} \cdot \square_{-\infty} D_x^\beta C - u D_x C - aC + b \quad (8)$$

where $C = [Ca^{2+}]$, $a = k_j^+ [B]_\infty$ and $b = k_j^- [B]_\infty C_\infty$

Applying temporal fractional Laplace transform and spatial fractional Fourier transform technique on equation (8) and then by using equation (7), the solution of equation is obtained in terms of green function

$$\begin{aligned} G_{\alpha,\beta}(x,t) &= \frac{1}{2\pi} \int_{-\infty}^{\infty} e^{-ikx} E_\alpha \theta dk \\ &+ \frac{bt^\alpha}{2\pi} \int_{-\infty}^{\infty} e^{-ikx} E_{\alpha,\alpha+1} \theta dk \end{aligned} \quad (9)$$

where $\theta = \left\{ iuk + D_{Ca} (-ik)^\beta - a \right\} \cdot t^\alpha$,

$$E_\alpha(z) = \sum_{k=0}^{\infty} \frac{z^k}{\Gamma(\alpha k + 1)}, \quad R(\alpha) > 0, \quad \alpha, z \in \mathbb{C}$$

and

$$E_{\alpha,\beta}(z) = \sum_{k=0}^{\infty} \frac{z^k}{\Gamma(\alpha k + \beta)}, \quad R(\alpha), R(\beta) > 0, \\ \alpha, \beta, z \in \mathbb{C}$$

are the Mittag-Leffler function for one and two parameter [17].

The solution of time fractional advection diffusion equation can be obtained by varying fractional order α in equation (9) at $\beta=2$. Again by applying fractional integral transform, the solution of time fractional advection diffusion equation is

$$\begin{aligned} G_{\alpha,2}(x,t) &= \frac{1}{\pi \sqrt{2D_{Ca} t^\alpha}} \int_0^\infty e^{-\frac{x^2}{4D_{Ca} t^\alpha} - at^\alpha k} k^{-\frac{1}{2}} M_\alpha(k) \theta_1 dk \\ &+ \frac{bt^\alpha}{\pi \sqrt{2D_{Ca} t^\alpha}} \int_0^\infty e^{-\frac{x^2}{4D_{Ca} t^\alpha} - at^\alpha k} k^{-\frac{1}{2}} \phi(-\alpha, 1; -k) \theta_1 dk \end{aligned} \quad (10)$$

where $\theta_1 = \frac{\sin(x - kut^\alpha)}{(x - kut^\alpha)}$,

$$M_\alpha(z) = \sum_{k=0}^{\infty} \frac{(-1)^k z^k}{\Gamma(-\alpha k + (1-\alpha)) \cdot k!}, \quad 0 < \alpha < 1$$

and

$$\phi(\alpha, \beta; z) = \sum_{k=0}^{\infty} \frac{z^k}{\Gamma(\alpha k + \beta) \cdot k!}, \quad \alpha > -1, \beta \in \mathbb{C}$$

are the Mainardi function and Wright function [17].

The solution of space fractional advection diffusion equation can be obtained by varying fractional order β in equation (9) at $\alpha=1$. Again by applying fractional integral transform, the solution of space fractional advection diffusion equation in terms of stable distribution is [3]

$$\begin{aligned} G_{1,\beta}(x,t) &= \frac{e^{-at}}{(D_{Ca} t)^{\frac{1}{\beta}}} \theta_2 + \frac{bt}{(D_{Ca} t)^{\frac{1}{\beta}} \{\ln \theta_2 - at\}} \\ &\times \left[\left\{ \frac{e^{-at}}{(D_{Ca} t)^{\frac{1}{\beta}}} \theta_2 \right\} - 1 \right] \end{aligned} \quad (11)$$

where $\theta_2 = S \left(\frac{x-u}{(D_{Ca} t)^{\frac{1}{\beta}}} / \beta, 1, 1, u; 1 \right)$

3. RESULTS AND DISCUSSION

The numerical values to obtain the distribution profile of intracellular Ca^{2+} concentration is stated in Table 1. The

intracellular Ca^{2+} concentration is measured versus time and space by varying fractional order derivative.

Table 1. Numerical values of physiological parameters use [18], [11]

Symbol	Parameter	Value	Units
D_{Ca}	Diffusion coefficient of Ca^{2+}	200-300	$\mu\text{m}^2/\text{s}$
$[\text{B}]_{\infty}$	Buffer concentration of calbindin- $\text{D}_{28\text{k}}$	< 360	μM
$[\text{Ca}^{2+}]_{\infty}$	Background $[\text{Ca}^{2+}]$	0.1	μM
K_{D}	Dissociation constants of calbindin- $\text{D}_{28\text{k}}$	393	nM
k^+	Buffer association rate constant of calbindin- $\text{D}_{28\text{k}}$	75	$\mu\text{M}^{-1}\text{s}^{-1}$
k^-	Buffer dissociation rate constant of calbindin- $\text{D}_{28\text{k}}$	29.5	s^{-1}

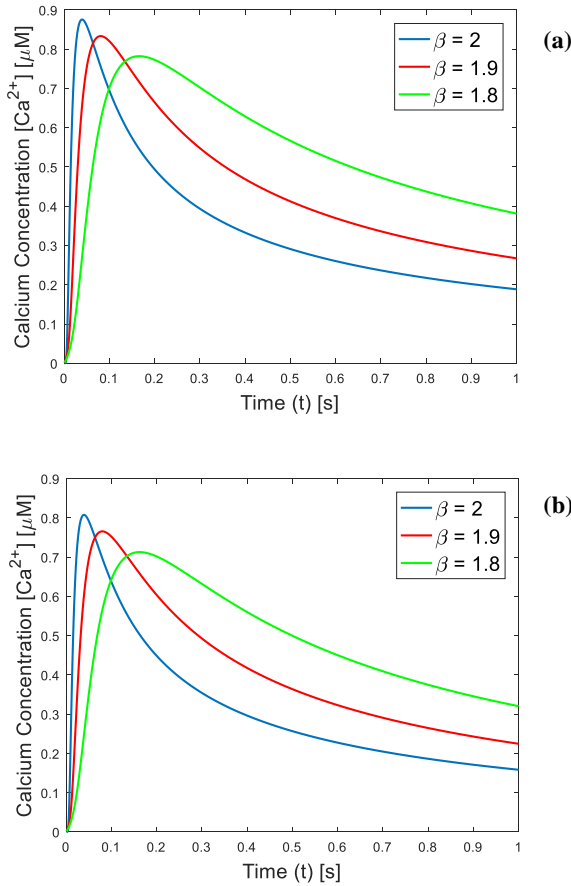


Figure 1. Temporal Ca^{2+} concentration profile at $\alpha=1$ for (a) Parkinsonic nerve cells (b) Normal nerve cells

Figure 1 shows the temporal profile of Ca^{2+} concentration at different value of space fractional derivative by keeping fix time derivative. The range of buffer concentration calbindin- $\text{D}_{28\text{k}}$ varies from 100 μM to 360 μM . Experimental evidence show that the low amount of calbindin- $\text{D}_{28\text{k}}$ is found in the person suffering from the Parkinson's disease [21]. So by keeping in mind, the

physiological amount of buffer concentration, we have taken into consideration 130 μM and 260 μM amount of buffer for Parkinsonic nerve cells and normal nerve cells respectively. The graphical results shows that the Ca^{2+} concentration profile for various values of space fractional derivative is high for lower amount of buffer concentration of calbindin- $\text{D}_{28\text{k}}$ (i.e. $[\text{B}]=130 \mu\text{M}$). For higher amount of calbindin- $\text{D}_{28\text{k}}$ (i.e. $[\text{B}]=260 \mu\text{M}$) in Figure 1b the entire profile of Ca^{2+} concentration significantly decreases. Physiologically it happens due to more amount of calbindin- $\text{D}_{28\text{k}}$ react with free Ca^{2+} ions and make a Ca^{2+} bound buffer.

Figure 2 shows the spatial profile of Ca^{2+} concentration at different value of space fractional derivative. The amount of buffer concentration of calbindin- $\text{D}_{28\text{k}}$ in Figure 2a and Figure 2b is same as Figure 1a and Figure 1b respectively. The graphical result shows that the peak in the profile of Ca^{2+} concentration is high for low amount of buffer concentration. It has been observed that by reducing the order of space fractional derivative the entire flow profile gradually decreases and finally attains the steady state level. The spatial distribution profile of Ca^{2+} concentration for $\beta=2$ and $\alpha=1$, i.e. corresponding to classical advection diffusion equation validate our obtained results to the previously reported results in the literature [4], [5], [9], [12].

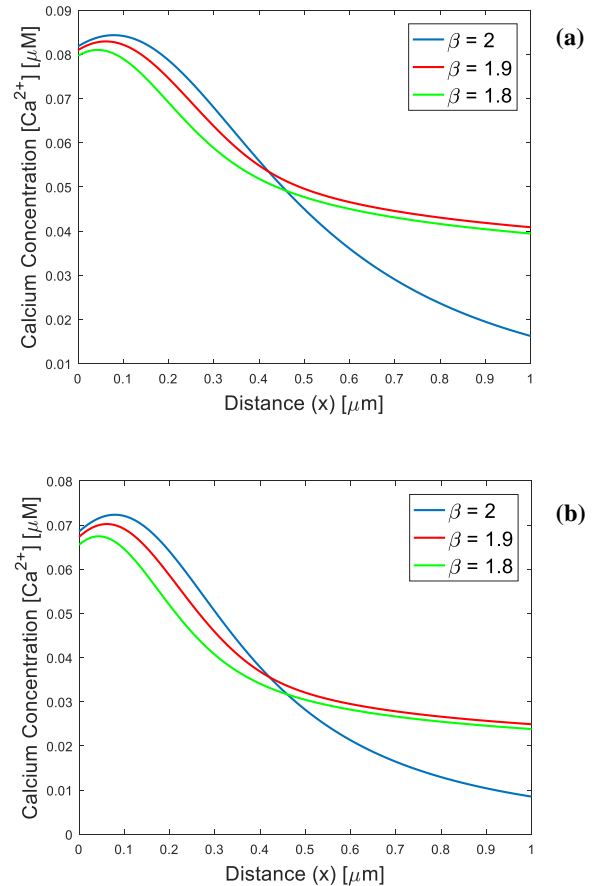


Figure 2. Spatial Ca^{2+} concentration profile at $\alpha=1$ for (a) Parkinsonic nerve cells (b) Normal nerve cells

Figure 3 shows the temporal profile of Ca^{2+} concentration for fractional order time derivative $\alpha=0.9$ and integer order space

derivative $\beta=2$. The effect of fractional advection diffusion is observed for low and high amount of calbindin- D_{28k} in Figure 3a and Figure 3b respectively. The higher amount of calbindin- D_{28k} reduces the intracellular Ca^{2+} concentration from $0.026 \mu M$ to $0.018 \mu M$.

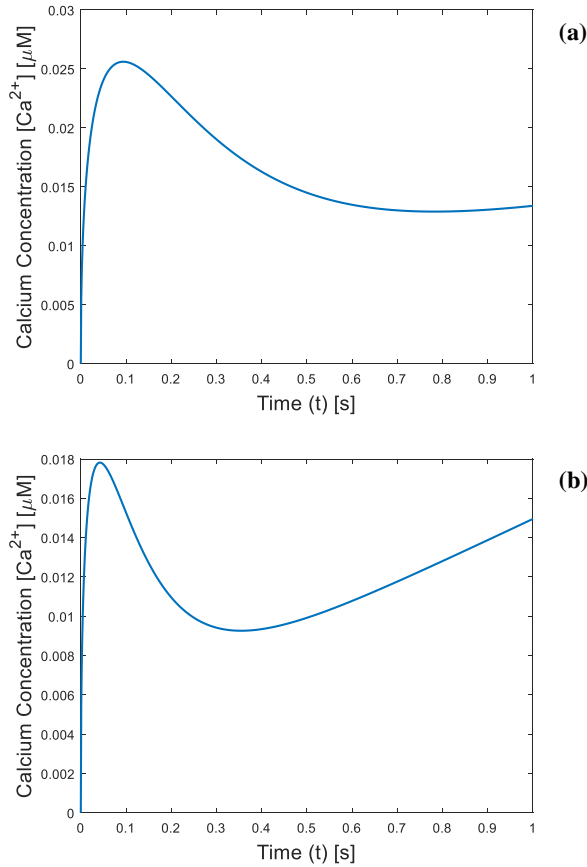


Figure 3. Temporal Ca^{2+} concentration profile at $\beta=2$ for (a) Parkinsonic nerve cells (b) Normal nerve cells

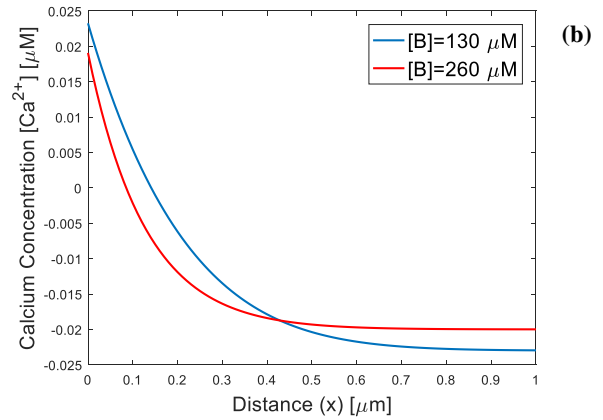
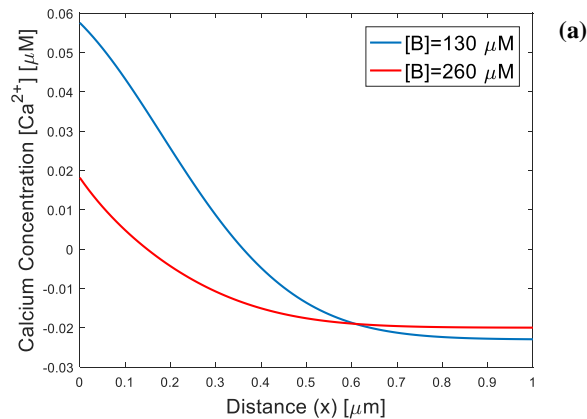


Figure 4. Spatial Ca^{2+} concentration profile at $\beta=2$ for (a) Parkinsonic nerve cells (b) Normal nerve cells

Figure 4 shows the spatial distribution profile of Ca^{2+} concentration for fractional order time derivative $\alpha=0.9$ and $\alpha=0.8$ for Figure 4a and Figure 4b respectively. The space order derivative is taken as integer order i.e. $\beta=2$. The effect of fractional advection diffusion is observed for $[B]=130 \mu M$ and $[B]=260 \mu M$ in both the cases. It is observed that flow profile is higher for low amount of calbindin- D_{28k} and lower for high amount or overexpression of calbindin- D_{28k} . The obtained results helps to identify when the nerve cells produce toxicity or apoptosis. Thus it reveals the beauty of fractional order modelling to study the complex behaviour of biomathematical problems.

4. CONCLUSION

In this paper, the effect of calbindin- D_{28k} is shown in presence and absence of advection flux. The mathematical model is framed in the form of fractional advection diffusion equation. The obtained results show the significant effect of buffer on calcium profile at high flux rate. The fractional advection diffusion model helps to reveal the inside mechanism to understand the physiological behaviour of normal and Parkinsonic nerve cells. Caputo fractional order derivative is a nonlocal operator so it gives the concise behaviour of the nerve cells. The obtained result is very interesting and helps the scientists by incorporating more physiological parameters in fractional advection diffusion model to reveal the entire molecular mechanism occurring in Parkinsonic brains.

5. REFERENCES

- [1] Agarwal, R., Jain S., and Agarwal R. P. 2018. Mathematical Modeling and Analysis of Dynamics of Cytosolic Calcium Ion in Astrocytes Using Fractional Calculus. *Journal of Fractional Calculus and Applications* 9(2):1–12.
- [2] Bezprozvanny, I. 2009. Calcium Signaling and Neurodegenerative Diseases. *Trends in Molecular Medicine* 15(3):89–100.
- [3] Borak, S., Wolfgang, H., and Rafal W. 2005. Stable Distributions. Pp. 21–44 in *Statistical Tools for Finance and Insurance*.
- [4] Dave, D. D. and Jha, B. K. 2018. Delineation of Calcium Diffusion in Alzheimeric Brain. *Journal of Mechanics in Medicine and Biology* 18(2):1–15.

- [5] Dave, D. D. and Jha, B. K. 2018. Modeling the Alterations in Calcium Homeostasis in the Presence of Protein and VGCC for Alzheimeric Cell. *Advances in Intelligent Systems and Computing* 584:181–89.
- [6] Jha, A. and Adlakha, N. 2014. Analytical Solution of Two Dimensional Unsteady State Problem of Calcium Diffusion in a Neuron Cell. *Journal of Medical Imaging and Health Informatics* 4(4):547–53.
- [7] Jha, A. and Adlakha, N.. 2014b. Finite Element Model to Study the Effect of Exogenous Buffer on Calcium Dynamics in Dendritic Spines. *International Journal of Modeling, Simulation, and Scientific Computing* 5(2):1–12.
- [8] Jha, A. and Adlakha, N. 2015. Two-Dimensional Finite Element Model to Study Unsteady State Ca^{2+} Diffusion in Neuron Involving ER LEAK and SERCA. *International Journal of Biomathematics* 8(1):1–14.
- [9] Jha, B. K., Adlakha, N. and Mehta, M. N. 2011. Finite Volume Model to Study the Effect of Buffer on Cytosolic Ca^{2+} + Advection Diffusion. *International Journal Of Mathematical, Computational, Physical, Electrical And Computer Engineering*. 5(3):248–51.
- [10] Jha, B. K., Adlakha N., and Mehta M. N. 2013. Two-Dimensional Finite Element Model To Study Calcium Distribution in Astrocytes in Presence of VGCC and Excess Buffer. *International Journal of Modeling, Simulation, and Scientific Computing* 4(2).
- [11] Jha, B. K., Adlakha N., and Mehta, M. N. 2014. Two-Dimensional Finite Element Model to Study Calcium Distribution in Astrocytes in Presence of Excess Buffer. *International Journal of Biomathematics* 7(3):1–11.
- [12] Jha, B. K., Joshi, H. and Dave, D. D. 2016. Portraying the Effect of Calcium-Binding Proteins on Cytosolic Calcium Concentration Distribution Fractionally in Nerve Cells. *Interdisciplinary Sciences, Computational Life Sciences*.
- [13] Joshi, H., Jha, B. K. and Dave, D. D. 2018. Mathematical Model to Study the Effect of Mitochondria on Ca^{2+} Diffusion in Parkinsonic Nerve Cells. P. 030013 in *AIP Conference Proceedings*, vol. 1975. American Institute of Physics.
- [14] Kotwani, M. and Adlakha, N. 2017. Modeling of Endoplasmic Reticulum and Plasma Membrane Ca^{2+} Uptake and Release Fluxes with Excess Buffer Approximation (EBA) in Fibroblast Cell. *International Journal of Computational Materials Science and Engineering* 06(01):1750004.
- [15] Naik, P. A. and Pardasani, K. R. 2016. Finite Element Model to Study Calcium Distribution in Oocytes Involving Voltage Gated Ca^{2+} Channel , Ryanodine Receptor and Buffers. *Alexandria Journal of Medicine* 52(MARCH):43–49.
- [16] Pathak, K. and Adlakha, N. 2016. Finite Element Model to Study Two Dimensional Unsteady State Calcium Distribution in Cardiac Myocytes. *Alexandria Journal of Medicine* 52(3):261–68.
- [17] Podlubny, I. 1999. *Fractional Differential Equations*. New York: Academic Press.
- [18] Schmidt, H. 2012. Three Functional Facets of Calbindin- D_{28k} . *Frontiers in Molecular Neuroscience* 5:25.
- [19] Smith, G. D., Dai L., Miura, R. M. and Sherman, A. 2001. Asymptotic Analysis of Buffered Calcium Diffusion near a Point Source. *Siam J. Appl Math*. 61(5):1816–38.
- [20] Tewari, S. G. and Pardasani, K. R. 2010. Finite Element Model to Study Two Dimensional Unsteady State Cytosolic Calcium Diffusion in Presence of Excess Buffers. *IAENG International Journal of Applied Mathematics* 40(3):261–68.
- [21] Yuan, H. H., Chen, R. J., Zhu, Y. H., Peng, C. L., and Zhu, X. R. 2012. The Neuroprotective Effect of Overexpression of Calbindin- D_{28k} in an Animal Model of Parkinson's Disease. *Molecular Neurobiology* 117–22.

Computational Modelling of Calcium Buffering in a Star Shaped Astrocyte

Amrita Jha

Department of Science and Humanities
Indus University,
Ahmedabad, Gujarat, India
tripathi.amrita28@gmail.com

Brajesh Kumar Jha

Department of Mathematics, School of Technology
Pandit Deendayal
Petroleum University
Gandhinagar, Gujarat, India
brajeshjha2881@gmail.com

ABSTRACT

Before last two decades, astrocytes were treated as supporting cells of neuron. Now it is regarded as important and strong participant in central nervous system. Astrocytes also play important role in many neuronal disorders like Alzheimer's, Parkinson's etc. Astrocytes release gliotransmitters like glutamate. Astrocytes take part in synapse in calcium dependent manner. However, it is not clear about the effect of astrocyte geometry on calcium distribution. In this study we present a geometry based mathematical model of an astrocytes. Mathematical model is developed in the form of reaction diffusion equation by considering the effect of endogenous and exogenous buffers on cytosolic calcium concentration. In present study it is concluded that the effect of geometry also visible and found significant on cytosolic calcium distribution in astrocytes.

CCS Concepts

Computing methodologies → Modeling and simulation → Model development and analysis → Model verification and validation

Keywords

Astrocytes; Calcium distribution; Astrocytes geometry; Computational modelling

1. INTRODUCTION

Since two decades, calcium signaling in central nervous system (CNS) has been associated with neuron only. Later on experimental observation gave importance to astrocytes and suggested that astrocytes are also involved in signaling process in CNS [27, 19]. Astrocytes are present in the brain around 10-15 times the number of neurons [13]. Astrocytes are electrically non-exitable cells as it does not generate action potential. Even though astrocytes play important role in calcium signalling and other brain function like synaptogenesis, cell differentiation, etc. [27, 19, 1, 4].

Free calcium ions (Ca^{2+}) are known as second messenger which

Permission to make digital or hard copies of all or part of this work for personal or classroom use is granted without fee provided that copies are not made or distributed for profit or commercial advantage and that copies bear this notice and the full citation on the first page. Copyrights for components of this work owned by others than ACM must be honored. Abstracting with credit is permitted. To copy otherwise, or republish, to post on servers or to redistribute to lists, requires prior specific permission and/or a fee. Request permissions from Permissions@acm.org.

ICBBB '19, January 7–9, 2019, Singapore, Singapore

© 2019 Association for Computing Machinery.

ACM ISBN 978-1-4503-6654-0/19/01...\$15.00

DOI: <https://doi.org/10.1145/3314367.3314379>

play important role in calcium signaling in nerve cells like neuron, astrocytes etc. [4, 28, 10]. Intracellular calcium signaling plays important role in synaptic activity. Astrocytes release gliotransmitters including glutamate, ATP or GABA in calcium dependent manner [5, 26]. High cytosolic calcium concentration leads to the release of gliotransmitters as well as responsible for the toxicity of cell death [10, 5, 26].

The calcium binding protein (Buffers) exists in the cytosol which binds with free calcium ions and thus reduces the cytosolic free calcium level [27, 14]. The effect of immobile buffers has been shown by the numbers of researchers in past experimentally as well as computationally [2, 6-9, 11, 12, 16-18, 20-25] for different nerve cells like neuron, astrocytes, oocytes, cardiac myocytes etc.

Earlier researchers have shown the effect of buffers on free calcium ions regular geometry in two dimensional like rectangular, circular etc. [22, 2, 17, 18, 20, 21, 7]. In this study a computational model is used to study the role of astrocytic geometry in regulating calcium distribution.

In literature, Jha et al. have studied the effect of immobile buffer on cytosolic calcium concentration in astrocytes [10]. Later on authors have extended the model by including voltage gated calcium channel [9] and endoplasmic reticulum [11]. Finite element method and finite volume method are employed to get the solution. Earlier authors have solution of advection diffusion using analytic solution [8]. Pathak and Adlakha have investigated about the effect of buffers and different intracellular flux on calcium distribution in cardiac myocytes [22, 23]. Kotwani and Adlakha have studied the effect of buffers and ER flux on calcium distribution in fibroblasts [16, 17]. Authors have studied the effect of fluxes with excess buffer approximation using source amplitude and source geometry. Bhargava and Pardasani have used Galerkin approach to study the calcium distribution in neuron. Later on Naik and Pardasani have extended the mathematical model and studied the effect of voltage gated channel and ryanodine receptor with excess buffer approximation [18]. Panday and Pardasani have used finite element method to study the mechanics of calcium regulation in oocytes [20, 21]. Authors have extended the mathematical model and investigated the effect of $\text{Na}^+/\text{Ca}^{2+}$ exchanger of Ca^{2+} distribution in oocytes. Jha et al. have studied the effect of buffer, ER fluxes and $\text{Na}^+/\text{Ca}^{2+}$ exchanger on cytosolic Ca^{2+} distribution in neuron [6, 7]. Authors have extended the mathematical model as well as the geometry of space and considered spine dendrite structure of neuron. Above and all, the authors have studied the effect of various parameters on cytosolic calcium distribution on different nerve cells. Many analytic and numerical methods have been employed to get the solution with regular geometry to approximate the shape of nerve cells. In 2017, Khalid et al. have studied the effect of ER on cytosolic calcium distribution in

astrocytes. The main motivation of this work is geometry based computational modeling of calcium distribution in astrocytes [15]. Authors have approximated the star shaped astrocyte using comsol interface. In present study, the geometry of astrocyte is plotted in MATLAB (Figure 2). The mathematical formulation and computational model implementation is given in next section.

2. COMPUTATIONAL MODEL IMPLEMENTATION

We have used a mathematical model in the form of reaction diffusion equation under physiology of astrocytes [10]. We have taken into account from the entry of free calcium ions in diffusion manner by mouth of the channel to react with buffers. The major significant difference between our implementation and model used by Jha et al, is the consideration of star shaped geometry of astrocytes. The mathematical model is solved using finite element method in MATLAB. In order to solve governing equation, we have used heat transfer in MATLAB.

3. MATHEMATICAL FORMULATION

To develop the mathematical model of calcium distribution in astrocytes, we have considered the law of conservation in differential form as shown in Figure 1 [10]

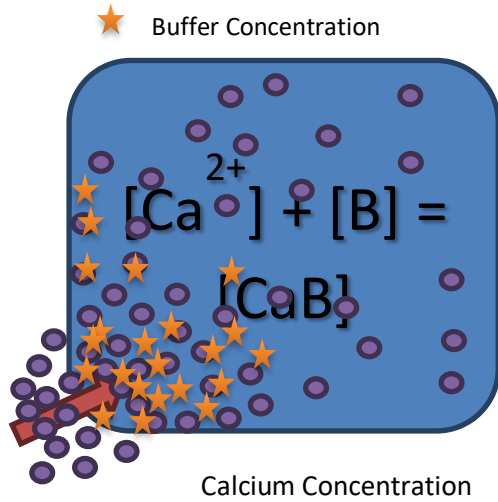


Figure 1. Spatial distribution of calcium concentration in astrocyte in presence of buffer [10]

$$\frac{\partial c}{\partial t} - \frac{\partial j}{\partial x} = f(x, t, C) \quad (1)$$

where c is the calcium concentration, j is the rate change of c across the boundaries, $f(x, t, C)$ is considered as reaction rate of calcium buffering inside the cytosol. The total diffusive flux is considered and given as

$$J(x, t) = -D_{Ca} \frac{\partial C(x, t)}{\partial x} \quad (2)$$

Using equation (1) and equation (2), two dimensional mathematical model is developed and given as

$$C' = \text{div}(D_{Ca} * \text{grad}(C)) + f(x, t, C) \quad (3)$$

To develop the mathematical term for calcium buffering in astrocyte, a reaction term is considered and shown in next subsection

3.1 Calcium Buffering

The free calcium ions in the cytosol bind with the buffers present in the peripheral region of the cytosol. There the reaction between buffers and calcium ions takes place which results in the calcium bound buffers.

Thus, the mathematical formulation for physiological phenomenon of calcium buffering is given as [24, 25, 3, 14]

$$[Ca^{2+}] + [B_j] = [CaB_j] \quad (4)$$

where $[B_j]$ and $[CaB_j]$ are free and bound buffer, respectively and j is an index over buffer species. The resulting partial differential equation in two dimensions using Fickian diffusion can be stated as [24, 25, 3, 14]

$$\frac{\partial C}{\partial t} = D_{Ca} \left(\frac{\partial^2 C}{\partial x^2} + \frac{\partial^2 C}{\partial y^2} \right) + \sum_j R_j + \sigma Ca \quad (5)$$

$$\text{where } R_j = -k_j^+ [B_j] [Ca^{2+}] + k_j^- [CaB_j]$$

In the above equation, D_{Ca} is the diffusion coefficient of free calcium, D_{B_j} is the diffusion coefficient of free buffer and D_{CaB_j} is the diffusion coefficient of calcium bound buffer. k_j^+ and k_j^- are association and dissociation rate constants for buffer j , respectively. For stationary immobile buffers, $D_{B_j} = D_{CaB_j} = 0$.

3.2 Finite Element Model

Finite element method is employed to solve the equation (3) using initial and boundary condition. Matlab pde tool is used to draw the structure of astrocyte. The whole area of astrocyte is discretized in 192 triangles consisting 129 nodes as shown in Figure 2.

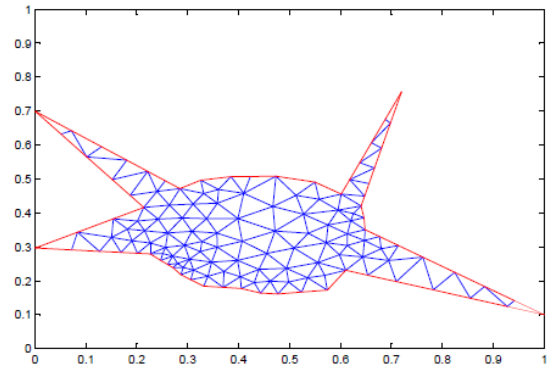


Figure 2. Finite element discretization of shape of astrocytes

4. RESULTS AND DISCUSSION

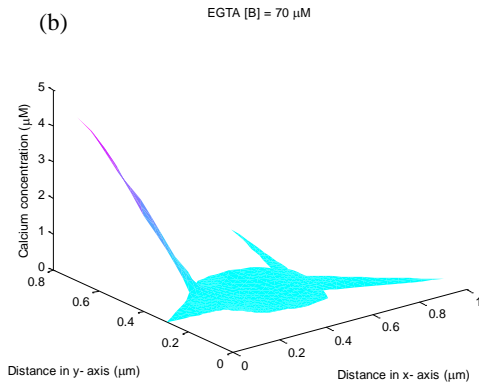
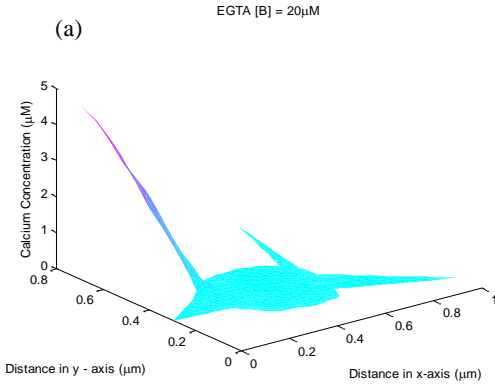


Figure 3. Spatial distribution of calcium concentration in astrocyte in presence of different amount of EGTA buffer

Figure 3 shows the spatial calcium concentration distribution in presence of the exogenous buffer. EGTA is considered to be the exogenous buffer having association rate of $1.6 \mu\text{M}$. Figure 3(a) shows the spatial diffusion in presence of $20 \mu\text{M}$ of EGTA, whereas Figure 3(b) shows the diffusion in presence of $70 \mu\text{M}$ of EGTA. As the association rate of EGTA is very low, i.e. $1.6 \mu\text{M}$, the significant difference due to the variable buffer concentration is not found. It is observed from Figure 2 that the diffusion starts from $0.445 \mu\text{M}$ and spreads gradually in both the directions and finally attains the background concentration.

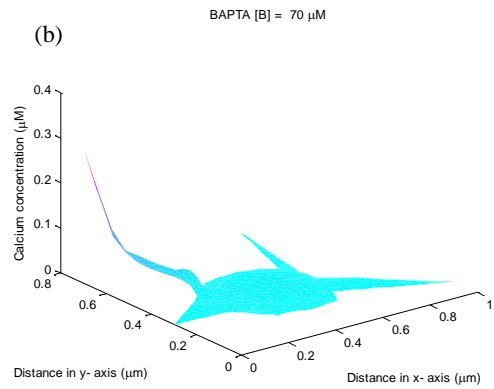
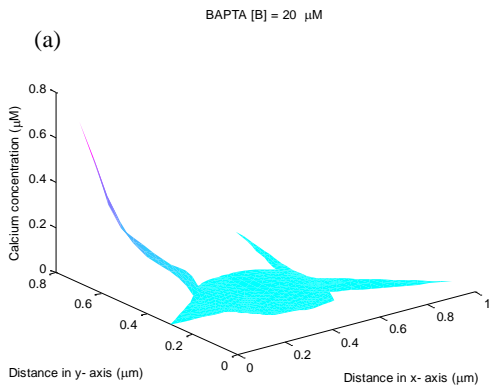


Figure 4. Spatial distribution of calcium concentration in astrocyte in presence of different amount of BAPTA buffer

Figure 4 depicts the calcium concentration distribution spatially in presence of BAPTA. The buffer association rate of BAPTA is $600 \mu\text{M}$. Figure 4(a) and Figure 4(b) shows the spatial distribution in presence of $20 \mu\text{M}$ and $70 \mu\text{M}$ of BAPTA respectively. The fundamental nature of the buffer is to lower down the calcium concentration. This fact can be clearly verified from both the figures. In Figure 4(a) the diffusion starts from $0.65 \mu\text{M}$ whereas in Figure 4(b) it starts from $0.25 \mu\text{M}$. The reason for the change at the mouth of the calcium channel is the high association rate of BAPTA and amount of it considered. The spread is observed to be in both the directions and it finally converges to the assumed background concentration, i.e. $0.1 \mu\text{M}$.

5. CONCLUSION

In this paper, a geometry based computational model is taken into consideration to visualize the calcium concentration distribution in presence of exogenous buffers, EGTA and BAPTA. To maintain the calcium concentration of the cell, buffers play an important role. The association rates of both the buffers have a vast change and hence the significant change can be seen. Graphically the diffusion is plotted spatially in presence of both the buffers and varying buffer concentrations. The nature of the buffer of maintaining the cellular calcium concentration can be visualized from both the figures. Also the geometry of the astrocytes and corresponding flow in it can be seen clearly from all the figures. Hence, the computational models play an important role in depicting the physiological process of calcium buffering. Further, more rigorous geometry can be formed in presence of various parameters to study the calcium diffusion.

6. REFERENCES

- [1] Arancio O. and Bezprozvanny I. 2017. Calcium hypothesis of Alzheimer's disease and brain aging: A framework for integrating new evidence into a comprehensive theory of pathogenesis. *Alzheimer's Dement.* 1-6.
- [2] Bhargava N. and Pardasani K.R. 2011. Galerkin approximation for the problem of calcium diffusion in neuron cell involving pump, leak and excess buffering approximation. *Appl. Math. Sci.* 5(55):27072720.
- [3] Crank J. 1975. *The Mathematics Of Diffusion*. Second. Clarendon Press Oxford.
- [4] Dupont G., Combettes L. and Leybaert L. 2007. Calcium dynamics: spatiotemporal organization from the subcellular to the organ level. *Int. Rev. Cytol.* 261: 193-245.

- [5] Fellin T., Pascual O., Gobbo S., Pozzan T., Haydon P. G. and Carmignoto G. 2004. Neuronal synchrony mediated by astrocytic glutamate through activation of extrasynaptic NMDA receptors. *Neuron* 43: 729-743.
- [6] Jha A., Adlakha N. and Jha B. K. 2015. Finite element model to study effect of $\text{Na}^+/\text{Ca}^{2+}$ exchangers and source geometry on calcium dynamics in a neuron cell. *J. Mech. Med. Biol.* 16(2):1-22.
- [7] Jha A. and Adlakha N. 2015. Two-dimensional finite element model to study unsteady state Ca^{2+} diffusion in neuron involving ER, LEAK and SERCA. *Int. J. Biomath.* 8(1):1-14.
- [8] Jha B. K., Adlakha N. and Mehta M. N. 2012. Analytic solution of two dimensional advection diffusion equation arising in cytosolic calcium concentration distribution. *Int. Math. Forum* 7(3): 135-144.
- [9] Jha B. K., Adlakha N. and Mehta M. N. 2013. Two-dimensional finite element model to study calcium distribution in astrocytes in presence of VGCC and excess buffer. *Int. J. Model. Simulation, Sci. Comput.* 4(2), 1-12.
- [10] Jha B. K., Adlakha N. and Mehta M. N. 2014. Two-dimensional finite element model to study calcium distribution in astrocytes in presence of excess buffer. *International Journal of Biomathematics* 7 (03), 1-11.
- [11] Jha B. K. and Jha A. 2015. Two dimensional finite volume model to study the effect of ER on cytosolic calcium distribution in astrocytes. *Procedia Comput. Sci.* 46:1285-1293.
- [12] Jha B. K., Joshi H. and Dave D. D. 2018. Portraying the effect of calcium-binding proteins on cytosolic calcium concentration distribution fractionally in nerve cells. *Interdiscip. Sci. Comput. Life Sci.* 10 (04), 674-685.
- [13] Kang M. and Othmer H. G. 2009. Spatiotemporal characteristics of calcium dynamics in astrocytes 19, 1–21.
- [14] Keener J. and Sneyd J. 2009. *Mathematical Physiology*. Second. Springer, US.
- [15] Khalid M. U., Tervonen A., Korkka I., Hyttinen J. and Lenk K. 2017. Geometry-based computational modeling of calcium signaling in an astrocyte. *IFMBE Proceedings* 65, 157-160.
- [16] Kotwani M. and Adlakha N. 2017. Modeling of endoplasmic reticulum and plasma membrane Ca^{2+} uptake and release fluxes with excess buffer approximation (EBA) in fibroblast cell. *Int. J. Comput. Mater. Sci. Eng.* 6(1):1-12.
- [17] Kotwani M., Adlakha N. and Mehta M. N. 2017. Finite element model to study the effect of buffers, source amplitude and source geometry on spatio-temporal calcium distribution in fibroblast cell. *J. Med. Imaging Heal. Informatics.* 4(6):840-847.
- [18] Naik P. A. and Pardasani K. R. 2016. Finite element model to study calcium distribution in oocytes involving voltage gated Ca^{2+} channel, ryanodine receptor and buffers. *Alexandria J. Med.* 52(1) 43-49.
- [19] Nedergaard M., Ransom B. and Goldman S. A. 2003. New Roles for astrocytes: Redefining the functional architecture of the Brain. *Trends Neurosci* 6, 523-530.
- [20] Panday S. and Pardasani K. R. 2013. Finite element model to study effect of advection diffusion and $\text{Na}^+/\text{Ca}^{2+}$ exchanger on Ca^{2+} distribution in oocytes. *J. Med. Imaging Heal. Informatics.* 3(3):374-379.
- [21] Panday S. and Pardasani K. R. 2014. Finite element model to study the mechanics of calcium regulation in oocyte. *J. Mech. Med. Biol.* 14(2)1-16.
- [22] Pathak K. and Adlakha N. 2015. Finite element model to study calcium signalling in cardiac myocytes involving pump, leak and excess buffer. *J. Med. Imaging Heal. Informatics.* 5:16.
- [23] Pathak K. and Adlakha N. 2016. Finite element model to study two dimensional unsteady state calcium distribution in cardiac myocytes. *Alexandria J. Med.* 52(3):261-268.
- [24] Smith G. D. 1996. Analytical steady-state solution to the rapid buffering approximation near an open Ca^{2+} channel. *Biophys. J.* 71:3064-3072.
- [25] Smith G. D., Dai L., Miura R. M. and Sherman A. 2001. Asymptotic analysis of buffered calcium diffusion near a point source. *SIAM J. Appl. Math.* 61(5):1816-1838.
- [26] Verkhratsky A. and Kettenmann H. 1996. Calcium signaling in glial cells. *Trends Neurosci.* 1: 346-352.
- [27] Volterra A. and Meldolesi J. 2005. Astrocytes, from brain glue to communication elements: the revolution continues. *Nat Rev. Neurosci* 6, 626-640.
- [28] Volman V., Ben-Jacob E. and Levine H. 2007. The astrocyte as a gatekeeper of synaptic information transfer. *Neur. Comput.* 19:303-326.

Stability of Mitotic Spindle Using Computational Mechanics

Andrii Iakovliev

School of Electronics and Computer Science. University of Southampton. University Road, Southampton, UK +44(0)7479045846

A.Iakovliev@soton.ac.uk

Srinandan Dasmahapatra

School of Electronics and Computer Science. University of Southampton. University Road, Southampton, UK +44(0)2380594503

sd@ecs.soton.ac.uk

Atul Bhaskar

Faculty of Engineering and the Environment. University of Southampton. University Road, Southampton, UK +44(0)2380593825

A.Bhaskar@soton.ac.uk

ABSTRACT

Fidelity of cell division depends on the ability of an internal cell structure called the mitotic spindle, to maintain the structural integrity of the cellular architecture despite being subject to high compressive loading. We propose a generic software tool called Spindle FEA that employs continuum mechanics and finite elements analysis (FEA) code Abaqus CAE to study the stability of mitotic spindles in various phases of mitosis. The proposed application has a modular structure which allows easy modification of any part of the analysis which is of particular importance considering that new knowledge of spindles is constantly emerging. Thanks to the highly optimised finite element solver used in Abaqus CAE, Spindle FEA is highly suitable for large multi-parametric studies which in turn may significantly benefit the planning of new experiments or identifying new key properties of the spindle. We also discuss the main physiological properties of spindles and show how they are modelled with the proposed technique as well as discuss all the essential analysis steps. We use Spindle FEA to study the buckling of a mitotic spindle in anaphase B to show how the additional stiffness of the lateral support of the spindle affects the left-right symmetry of cell division as well as to demonstrate the capacities of the proposed technique.

CCS Concepts

Applied computing → Life and medical sciences → Computational biology → Molecular structural biology

Applied computing → Physical sciences and engineering → Engineering → Computer-aided design

Keywords

Cell division; Mitotic spindle stability; Anaphase B

1. INTRODUCTION

The mitotic spindle is a cytoskeletal structure that plays a crucial role in cell division (mitosis) by generating forces needed to separate the chromosomes while preserving cell shape under

external loads and ensuring correct positioning of the nucleus. The structural performance of spindles is partially facilitated by their highly complex architecture that combines various proteins arranged in the form of microtubules (MTs), cross-linkers (connectors), protein motors, centrosomes (poles), chromosomes and others. Investigation of the arrangement, properties and interaction of these structural units is essential to understand the high load bearing capacity of the spindle and the consequent robustness of the biological functions that rely on its mechanical stability.

Many experimental [1–4] and theoretical studies [5–8] at various levels of spindle organisation and length scales address the questions of force generation, structural performance and stability of spindles. They include the near atomic level studies of MT connectors and motors [9], investigation of the structural properties of individual MTs [10–13] as well as analysis of MT organisation [1], coupling and positioning [6,14,15]. Studies of the spindle as a whole address spindle structure and orientation within the cell [2,16,17] and estimation of forces arising within the spindle as well as mechanisms of spindle formation [18].

The studies focused on creating some unified models of the spindle which incorporate the properties of each structural unit into a complete hierarchical model of the whole spindle are rather incomplete. One such generic model of the inter-polar bundle of MTs in the fission yeast cells is proposed by Ward et al. [2] and is based on the Langevin dynamics framework [19]. Other models aim at producing closed form analytical solutions or scaling laws to explain force generation and structural stability of the spindle under compression [7,8,20]. These studies are of particular interest to us as they lay the foundation for the understanding of the structural behaviour of the spindle as a whole and, to some extent, incorporate all its hierarchical complexity. Furthermore, they clearly make the case for the importance of structural models of the spindle as a whole in scaffolding biological mechanism. In addition to this, the global models of the spindle are mostly tailored to some specific cell types and/or particular phases of mitosis. Motivated by this, we propose an alternative approach to structural modelling of the spindle as a whole. Here, we lay the foundation for a generic computational framework based on continuum mechanics methods and the theory of elastic stability which deploys Abaqus CAE finite element analysis (FEA) code to studying structural response of spindles. The proposed framework is embedded in the developed application Spindle FEA [21] which is linked to Abaqus CAE code via an API and receives a list of spindle parameters from a user, generates a Finite Element (FE) model of a spindle and submits it to FEA solver for analysis. In this paper, we discuss a high-level architecture of the developed application, formulate essential assumptions and limitations, and employ Spindle FEA to study the elastic stability of the fission

Permission to make digital or hard copies of all or part of this work for personal or classroom use is granted without fee provided that copies are not made or distributed for profit or commercial advantage and that copies bear this notice and the full citation on the first page. Copyrights for components of this work owned by others than ACM must be honored. Abstracting with credit is permitted. To copy otherwise, or republish, to post on servers or to redistribute to lists, requires prior specific permission and/or a fee. Request permissions from Permissions@acm.org.

ICBBB '19, January 7–9, 2019, Singapore, Singapore

© 2019 Association for Computing Machinery.

ACM ISBN 978-1-4503-6654-0/19/01...\$15.00

DOI: <https://doi.org/10.1145/3314367.3314373>

yeast spindle in late anaphase B. Then we compare our results with those by Ward et al. [27] and discuss the applicability of the proposed framework. Our long-term goal is to create an open source modular platform that will be used and extended by the community of researchers and incorporate continuously emerging new knowledge about spindles.

We show that at the current development stage, Spindle FEA application based on the continuum mechanics framework is a highly customisable and versatile tool that can be tailored to model many structural aspects of mitotic spindles in various cell types.

2. ARCHITECTURE OF THE APPLICATION

The basic requirements that we pose to our application are the ability to model the hierarchical complexity of a mitotic spindle, applicability to various cell types and phases of mitosis, extensibility, and scalability & simplicity of use. We aim to develop a platform that can be used by researchers in the field and be extended by them to account for new experimental and theoretical findings as well as to give researchers a numerical tool that they can use to test various modelling assumptions.

The application is based on continuum mechanics discretised using a finite element (FE) method in quasi-static approximation. Continuum mechanics at a length scale of dozens of nanometres (length scale of an MT cross-section) has been successfully used before [6,15,22] demonstrating its applicability at such scales. In classical mechanics, finite element analysis (FEA) has long become a standard tool for computer-aided design and modelling of structures, especially when the geometry is complex and/or the boundary conditions are difficult for analytical treatment. The benefits of FEA are the high versatility of modelling, the applicability of the methods to virtually any structural mechanics problem and simplicity of its use. Therefore, at the current stage, in Spindle FEA we employ a highly optimised, efficient and reliable commercial FE solver such as Abaqus CAE. The reason for using this closed source solver is that it is one of the industry standards in FE analysis and also provides a convenient Python 2.7 API to control the solver. In the further releases we will aim to adjust the application to work with other open-source FE solvers but after their ability to deal with spindle stability problems is thoroughly tested.

Spindle geometry generation, material properties definition, FE meshing and model formulation is triggered in Spindle FEA and executed in Abaqus CAE. Such formulated problem is then wrapped in the form of a specific input file which is passed to the FE solver for analysis. The results of the calculations can be then extracted and visualised either in the Abaqus graphical user interface or using python data tools. In the basic use scenario, the user provides the essential model parameters in a single file “job.py” located at the root of application and executes a single command line command. The model generation and analysis are then done automatically. In such a way, altering the geometry of the spindle, and/or material properties of its parts and running multi-parameter studies is as easy as changing the appropriate parameters in “job.py” file. In the case of a more advanced use, new material models, geometric and/or material nonlinearities and new types of analysis can also be incorporated into the framework by modifying the existing modules or adding new ones.

The detailed interactive user manual for Spindle FEA explaining the steps needed to run the analysis as well as to introduce basic

configurational changes can be found within the Spindle FEA directory [21] by following the simple guide in “README.txt” file. Alternatively, the application directory can be downloaded or cloned from <https://git.soton.ac.uk/ai1v14/SpindleFEA.git> and the interactive documentation can also be accessed and cloned from <https://git.soton.ac.uk/ai1v14/SpindleFEA-docs.git>. A website with the interactive documentation as well as modelling examples is spindlefea.soton.ac.uk. The link to it will be added to a “README” file in <https://git.soton.ac.uk/ai1v14/SpindleFEA.git>

2.1 Main Assumptions

Some of the further discussed assumptions and limitations are inherited from the continuum mechanics and FEA, others come from the physics and biology of a mitotic spindle. Many of these assumptions are prone to changes as the understanding of the problem evolves and thus new material, geometry models, physical and physiological properties may be introduced by the users in the future.

We assume that all the structural parts of the spindle are solid and continuous bodies and that the atomic and molecular thermal fluctuations are neglected. As we are currently focused on the various scenarios in which a spindle becomes structurally unstable and buckles, only linear buckling is considered. At this stage we assume all spindle parts to be linearly elastic implying a linear stress-strain relationship defined by Hooke’s law also assuming all deflections and rotations to be small.

The mechanical model of MTs and connectors is an isotropic Bernoulli-Euler beam [23]. Although, several recent studies indicate that the orthotropic beam model for the MTs may be more realistic [10,13], we use the isotropic model due to its simplicity. Going beyond the assumptions of the models used in this paper – orthotropic models, geometric and material nonlinearities, as well as post-buckling analysis, may be also incorporated relatively easily as such problems are typically studied by FEA.

The implementation of the quasi-static assumption allows us to perform linear buckling analysis of the spindle without dealing with the complicated step-dependent nonlinear buckling analysis or dynamical analysis as done by Ward et al. [2]. The validity of the quasi-static assumption requires the slow evolution of the spindle in time. Thus, loads and deformations develop slowly and the forces are in equilibrium at each time snapshot of the mitosis which typically spans over time interval of dozens of minutes [2] and the each of the mitotic phases changes slowly over a duration of several minutes. Thus, we are able to neglect the time dependence of the problem and apply the linear theory of elastic stability.

Finally, in our use of finite element analysis we divide the spindle into a number of small sub-structures (finite elements) connected at nodes whose displacements are described by assumed shape functions used for the interpolation of the displacement field within each element; the shape being controlled by a set of relatively small number of generalised coordinates. These displacements are approximated by polynomial shape functions that satisfy variational constraints on the energy of the system. The matching of the displacements, strains, stresses, etc., between elements, is ensured by continuity conditions. In the case of linear buckling analysis, the FEA returns critical buckling loads of the structure and the associated instability shapes or modes.

2.2 Mitotic Spindle Structure

Consider the scheme of the mitotic spindle structure shown in Figure 1 (A). The red arrows indicate the direction of the loads generated by protein motors pushing against the antiparallel assembly of inter-polar MTs (ipMTs) indicated by purple and green lines. The purple lines indicate MTs growing from the left pole while the green ones indicate MTs growing from the right pole. A detailed view of the mid-zone and near-pole parts of the inter-polar assembly is shown in Figure 1 (B) and Figure 1 (C). The inter-polar MTs translate the forces generated by motor proteins to the centrosomes or poles indicated by two big blue circles in Figure 1 (A), causing the two poles to separate. The poles are supported inside the cell by a number of radially oriented astral MTs (aMTs) indicated by blue thick lines in Figure 1 (A). Astral MTs connect centrosomes to the membrane of the cell and experience forces transmitted by the poles as well as reaction forces from membrane resistance to expansion as indicated by blue arrows in Figure 1 (A). Furthermore, centrosomes are also connected to both halves of the chromosomes (orange bodies in Figure 1 (A)) by means of chromosomal MTs (chMTs) indicated by thin cyan lines. Thus, under the influence of protein motors the centrosomes move apart, pushing the membrane via the attached aMTs and pulling the chromosomes apart due to chMTs. The direction of the chromosome splitting loads is indicated with orange arrows. In the case of late anaphase B, chromosomes have been already split apart so we do not account for chromosome splitting forces.

Note that the actual spindle of a living cell contains hundreds of different MTs and other bodies. The scheme in Figure 1 (A), Figure 1 (B) and Figure 1 (C) is simplified to show only the high-level architecture of the spindle and thus emphasise the key structural elements modelled here. A photo of the actual spindle reconstructed from the electron microscopy was adapted from [17] and is shown in Figure 1 (D) to demonstrate how complex the actual spindle is. The white lines are the individual MTs and the black circles indicate the poles.

Following the scheme in Figure 1 (A) Spindle FEA generates a structure of a mitotic spindle depicted in Figure 2 (A). Here the centrosomes are indicated with the large red circles, the astral MTs and inter-polar MTs are represented by light-blue lines and the mid-zone where the MTs are connected by cross-linkers is shown in green. The detailed view of the mid-zone is shown in Figure 2 (B) depicting inter-polar MTs as well as connectors and motors. The zoomed view of a connector and an MT are shown in Figure 2 (C) and Figure 2 (D). The load P arising from motor push is shown with black arrows in Figure 2 (C). The centrosome with the radially oriented astral MTs is depicted in Figure 2 (E).

In the model presented here, we reduce the complex structural behaviour of the spindle to a problem of stability of equilibrium of the elastic system consisting of elastically coupled flexible bodies. The initial state of the system is taken to be in equilibrium. When loading is quasi-statically increased it reaches the critical point after which a pitch-fork bifurcation occurs, leading to symmetry breaking via buckling mode. We are interested in the onset of buckling and in the dependence of buckling loads and corresponding deformed configurations of the spindle on spindle parameters. Hence, in order to be able to study this problem, we first need to discuss the structure and mechanical behaviour of each individual part of a typical spindle.

2.3 Structure and Properties of a Microtubule

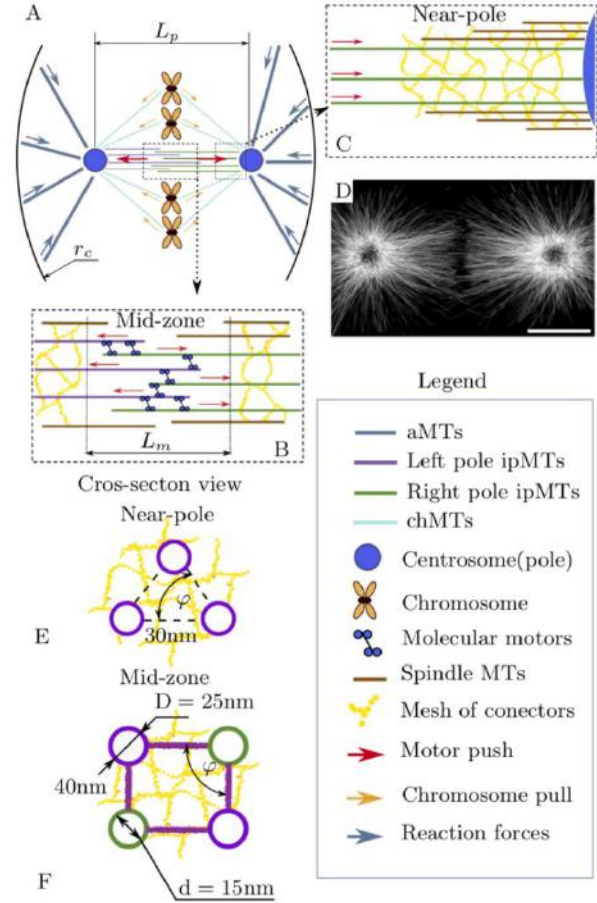


Figure 1. Mitotic spindle architecture at various hierarchical levels. Forces acting in spindle are shown in (A) along with the cell membrane, centrosomes, chromosomes, chromosome MTs (chMTs), astral MTs (aMTs) and inter-polar MTs (ipMTs).

The magnified view of the spindle mid-zone with protein motors and mesh of MT connectors reported in [17] are shown in (B). The inter-polar MTs along with the connector mesh near poles are shown in (C). Red arrows indicate the direction of protein motors push. The view of the spindle constructed from electron microscopy data is adapted from [15] and shown in (D) The cross-section of inter-polar MT bundles as reported in [27] near pole is shown in (E) while the cross-section of the inter-polar MT bundle in mid-zone as reported in [27] is shown in (F). The cross-section architecture was enriched by considering that inter-polar bundle is embedded in a mesh of connectors as reported in [17]. The motor proteins are omitted in (E) and (F) to simplify the scheme

Microtubules are hollow filaments with cylindrical cross-section [5,10,13]. The outer diameter of a typical MT is $D \approx 25$ nm while its inner diameter $d \approx 15$ nm as indicated in Figure 1 (F). The length of MTs varies depending on the cell type and is between 1 – 10 μm to 50 – 100 μm . Stiffness of MTs is derived from the characteristic length scale called persistence length which is measured in experiments [10], [23] and represents a ratio of MT bending stiffness κ to thermal noise $k_B T$ written as $l_p = \kappa/k_B T$; here κ is the bending moment per unit curvature response. The simplest mechanical model of an MT that has been often used in literature [6,15,22] is based on isotropic Bernoulli-

Euler beam. However, the values of persistence length measured in experiments [24,25] indicate that an orthotropic beam model with shear effects would more accurately capture the MT mechanics when MT length $L < 21 \mu\text{m}$ [10]. In the current study we restrain ourselves to the isotropic model with the orthotropic MT model to be incorporated in the near future.

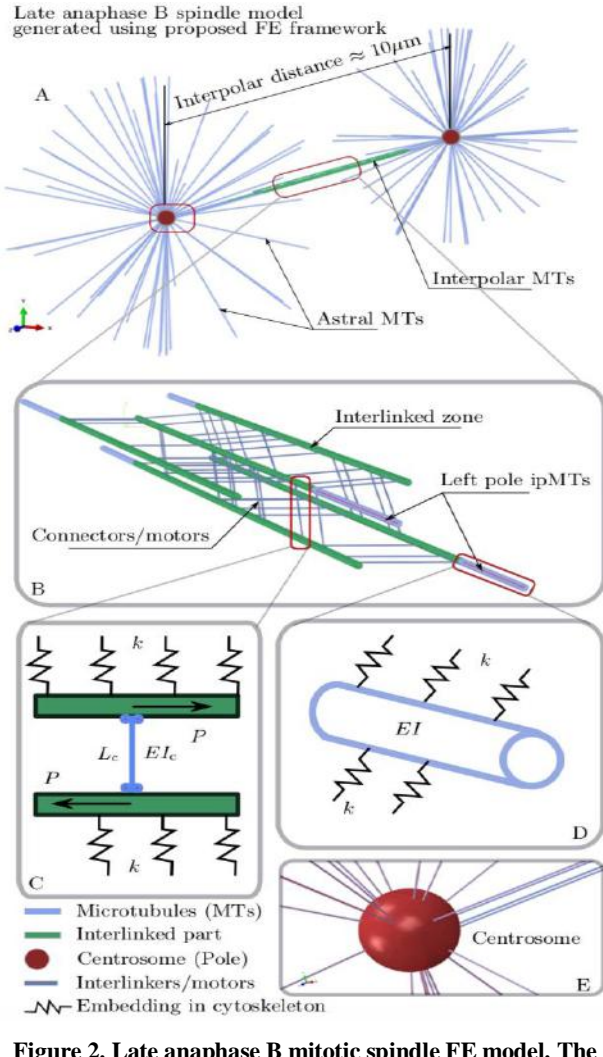


Figure 2. Late anaphase B mitotic spindle FE model. The generic architecture with centrosomes (red), inter-polar and astral MTs (blue) are shown in (A). The parts of the ipMTs interlinked by bridges and protein motors are green. The detailed view of the inter-polar zone is shown in (B). This blue links between MTs are MT connectors and motor proteins. The magnified view of a connector is shown in (C). Here, MTs are green and connector/motor is a blue link. When the motors walk in MTs they create two antiparallel loads P shown with arrows. The connector length is L_c and stiffness is EI_c . The MTs have stiffness EI and are also embedded in a highly chaotic mesh of cytoskeletal proteins. The effect of such embedding is modelled using distributed elastic springs k which are shown in (C) and (D). The detailed view of the centrosome with the radially extending astral MTs is shown in (E).

Typically, MTs that form a spindle are prone to large levels of compression due to forces generated by motor proteins that may destabilise them and cause buckling. In contrast to the typical

beam buckling, MTs retain a considerable level of initial load bearing capacity even when buckled [6,15]. This may be explained by the effect of a short wave-length buckling occurring thanks to the extra support that is provided by the cross-linkers. Furthermore, it has been shown that MTs in a living cell are also embedded in the mesh of connectors attaching them to the rest of the cytoskeleton and providing considerable lateral support [3] (see Figure 1 (B) and Figure 1 (C)) which also leads to the short-wave buckling mode.

We model MTs as long slender cylindrical elastic beams with circular cross-section as shown in Figure 1 (E) and Figure 1 (D). We employ the isotropic Bernoulli-Euler beam model. Every MT is defined by length L and cross-sectional stiffness EI as shown in Figure 2 (D). The MTs are embedded within the cytoskeleton by means of a dense network of protein connectors that we model using elastic springs k uniformly distributed along the MT contour as shown in Figure 2 (C) and Figure 2 (D).

Two types of MTs participate in a spindle, namely, inter-polar MTs in a pole-to-pole bundle which has length $\approx 10 \mu\text{m}$ in late anaphase B and astral MTs that extend from poles to the membrane and are $\approx 2 \mu\text{m}$ long. The locations of astral MTs are randomly generated on the centrosome sphere as shown in Figure 2 (A) and Figure 2 (E). The inter-polar bundle has a well-defined morphology presented in Figure 2 (B). The antiparallel alignment of MTs in a bundle implies that MTs do not span the entire inter-polar distance but grow towards each other from opposite poles and meet in the mid-zone where they are linked by cross-linkers and protein motors as shown in Figure 2 (A) and Figure 2 (B) as well as in Figure 1 (B) and Figure 1 (C). The cross-sectional assembly of ipMTs is defined by the inter MT distance δ and MT angle φ as shown in Figure 1 (E) and Figure 1 (F). For our modelling, we use values of δ and φ generated by the Gaussian distribution with mean and standard deviation taken from the spindle measurements performed by Ward et al. [2]. These parameters, as well as other model parameters, are given in Table 1 of Appendix A. The length of the inter-polar MTs is also picked from a Gaussian distribution defined by mean and standard deviation given in Table 1 of Appendix A. The inter-polar MTs grow from the centrosomes and thus are rigidly attached to them. In the model, it is represented by imposing continuity of displacements and rotations between the centrosomes and the ipMTs ends. The number of ipMTs in late anaphase B is between 5 and 6 [2].

2.4 Cross-Linkers and Protein Motors

Consider a zone of overlap in the inter-polar bundle where MTs are strongly cross-linked by actin-binding and kinesin proteins [3,26] as shown in Figure 1 (B). The protein motors push the antiparallel MTs into the opposite directions thus separating poles. Fidelity of this mechanism as well as structural integrity of the inter-polar bundle are crucial for mitosis and, thus, need to be accounted for by our modelling.

In the model both tubulin motors and other cross-linkers are regarded as thin 6 – 40 nm long struts randomly distributed along the mid-zone. Ward et al. [2] adopt from [26] the assumption that cross-linkers do not contribute to bending stiffness of the MT bundle. Yet, we assume that they have a finite but small thickness of $\approx 5 \text{ nm}$. This allows us to have the cross-linker radius as another arbitrarily small parameter which we believe would represent the actual physics of the connector more accurately. It was shown [9], [3] that connectors are well coupled to the adjacent MTs which allows us to assume continuity of

displacement and rotation between the adjacent nodes of the connector and the MT in the FE model. The estimated number of cross-linkers coupling inter-polar MTs varies in a wide range and they are randomly distributed along the MT length. The detailed scheme of the inter-polar bundle featuring dozens of connectors randomly distributed along five ipMTs is shown in Figure 2 (B). The detailed view of the connector linking two MTs is depicted in Figure 2 (C). The direction of force generated by the protein motor is shown with vectors \mathbf{P} and the connector length L_c as well as cross-sectional stiffness EI_c are indicated in the scheme.

Brangwynne et al. [15] have shown that individual microtubules bear up to 100 times larger compression loads in leaving cells. Also, in vivo buckling wavelengths of MTs appear much shorter than those predicted for isolated MTs [15,22]. It is argued that MTs in the cell are mechanically coupled not only to each other but also to the surrounding cytoskeleton by a mesh of cross-linkers which adds considerable stiffness to the MTs and contributes to short-wave buckling and to a dramatic increase in buckling loads compared to isolated MTs [3]. This network or mesh of proteins surrounding the MTs and linking them to the rest of the cytoskeleton has been observed using 3D reconstruction of electron microscopy data [3]. It was reported that this network has a chaotic morphology and can link 2, 3 or even 4 MTs at once which is shown in Figure 1 (B), Figure 1 (C), Figure 1 (E) and Figure 1 (F) with the help of yellow and orange dots.

We model the effect of the embedding of MTs into a cytoskeletal mesh by attaching an evenly distributed elastic springs k (stiffness per unit length) to the contours of MTs while the second ends of the springs are attached to some fixed points in space mimicking high rigidity of the cytoskeleton of the cell. Therefore, the distributed spring contributes to the stiffness of each individual MT. The proposed distributed springs are sketched in Figure 2 (C) and Figure 2 (D). We further omit displaying these springs to simplify the graphics.

2.5 Spindle Analysis Algorithm

The standard modelling case of a mitotic spindle employing Spindle FEA contains the following steps.

3. User specifies all the spindle analysis parameters in the "job.py" file located in the root of the application directory. The example of the user input data used in our modelling is shown in Table 1 of Appendix A and in the interactive user manual.
4. In "job.py" user may also specify the computation parameters such as number of CPUs requested, memory allocation and parallelisation algorithms.
5. The analysis may be run either from Abaqus graphical user interface or from command line. The "job.py" file is then submitted as an input file for the application.
6. The modelling starts by generating the geometry of individual parts of the spindle such as MTs, cross-linkers and centrosomes.
7. The material properties are then assigned to each part.
8. The parts are combined in the mitotic spindle assembly.
9. The connection properties between parts are specified.
10. The finite element mesh is generated on each part of the spindle.

11. The analysis input file is generated and submitted to the FE solver which formulates the generalised eigenvalue problem for the whole structure and works out the eigenvalues which represent the critical buckling loads and the eigenvectors that describe the buckling mode of the spindle.

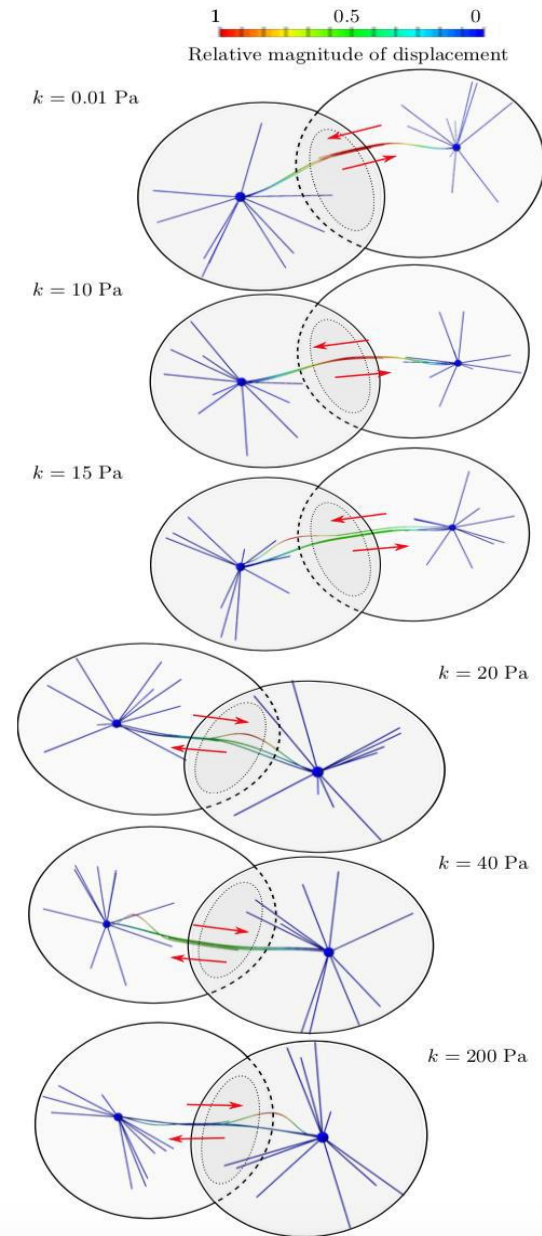


Figure 3. Buckling modes of late anaphase B mitotic spindle for various lateral support stiffness k . The colour code represents the non-dimensional relative displacement amplitude of the buckling mode with near-zero deflection being blue and the near-one deflection labelled with red colour

12. The analysis is terminated and the files with results "job.odb" and "job.dat" are written and can be manipulated with either from Abaqus GUI or directly executing python code.

3. STABILITY OF A MITOTIC SPINDLE IN ANAPHASE B

The stiffness added to the inter-polar MT bundle due to coupling with the rest of the cell cytoskeleton is challenging to measure in an experiment. Hence, we assume it as the governing parameter of our study and, thus, investigate how it affects the deformation profile of the late anaphase B spindle in buckling. We perform a parametric study of the dependence of the buckling and left-right symmetric properties of the spindle on the stiffness k of the embedding of the inter-polar MT bundle in the surrounding cytoskeleton. This is also a test case for the utility of our tool Spindle FEA. In contrast to [2] we consider not only the inter-polar MT bundle but also astral MTs which are attached to the centrosomes and to the cell membrane. Six cases defined by k being equal to 0.01 Pa, 10 Pa, 15 Pa, 20 Pa, 40 Pa and 200 Pa were considered.

The computed deformed configurations of the spindle are presented in Figure 3 for various values of lateral restoring force constant k . Each deformed configuration is characterised by the mode shape which is obtained from the eigenvector of the generalised eigenvalue problem constructed using the minimisation of the total potential energy according to the FE method. The eigenvector is determined up to an unknown scaling constant or amplitude of the buckling mode. Therefore, the analysis returns the shape of the deformation profile of the beam normalised to unity rather than the actual displacement in meters. The correspondent eigenvalue is, however, a physical critical buckling load in pN. It is essential to calculate the critical buckling loads of the spindle and the associated buckling modes as they give an estimate of the deformation pattern developing in a spindle should it be loaded to a particular critical load magnitude.

In Figure 3 a large relative displacement is indicated in red while the small relative displacement is shown in blue. The black circles represent the cell membrane which starts to split in the middle to form two new cells. The dotted ellipse shows the central plane of cell division with respect to which the division may be symmetric or asymmetric. The red arrows indicate the direction of the antiparallel push by protein motors.

From Figure 3, we observe that for $k = 0.01$ Pa the buckling mode of the inter-polar bundle resembles the Euler mode of the fixed-fixed beam-column [23] and also resembles the one reported in [2] for $k = 0$ Pa. In this case, the lateral reinforcement of the bundle is neglectfully small and the bundle forms an arc symmetric with respect to the central plane.

When $k = 10$ Pa, we see that the deformation profile starts to alter. The maximum displacement (shown in red) shifts slightly towards the left pole. As the support stiffness increases to $k = 15$ Pa we observe that the symmetric arc is no longer present. The high curvature zone indicated in red is now fully shifted to the left pole indicating the possibility of a violation of the division symmetry with respect to the central plane. In this case, the motor push may be unevenly distributed between the left and the right halves of the spindle. Also note, the local buckling of one or two MTs prevails over the global buckling mode of the whole spindle. When $k = 20$ Pa and then $k = 40$ Pa this effect becomes even more prominent clearly demonstrating asymmetric buckling with respect to the central plane. Furthermore, the wavelength of the buckling mode decreases with k . In the case of $k = 0.01$ Pa, the single arc extends over the whole bundle. However, for $k = 20$ Pa the arc spans roughly a half of the

bundle. When $k = 40$ Pa the arc is even shorter while the deformation of the whole bundle is strongly reduced. When $k = 200$ Pa the two arcs buckling mode is observed and the global mode of the whole bundle is mostly absent. This leads to the conclusion that the lateral support transforms the global long-wavelength buckling mode into the local short-wavelength buckling, thus enhancing the structural performance of the spindle. But on the other hand, the short-wavelength buckling mode is much more sensitive to the irregularities in the bundle geometry resulting in the effect of localisation of high relative displacement amplitudes towards either of the poles which presumably may affect the capacity of the cell to undergo symmetric division. Nevertheless, a cell still possesses a very reliable division mechanism which obviously should have some means of correcting the left-right symmetry breaking. This mechanism is not yet fully understood but we believe that the whole cell mechanical model may enrich our understanding of mitosis. We aim to create one such model in the future by extending the current application.

Interestingly, for $k = 200$ Pa, we have observed another type of mode which has not been reported before. For some bundle morphologies when the support stiffness is high it is energetically favourable not only to shorten the buckling wavelength but also to develop another type of deformation such as torsion. Such behaviour represents a bending-torsion deformation coupling and can be observed only in three-dimensional modes. The torsional part of the buckling mode arises from the rotation of the inter-polar bundle cross-section about the axis that goes through the shear centre of the cross-section. The actual three-dimensional view of such a mode along with its projections on xz and yz planes discarding the aMTs are shown in Figure 4 (A). The view on the inter-polar bundle from the xy plane is shown in Figure 4 (B). The direction of cross-section rotation is indicated by the grey arrow. Notice, that the inter-polar MTs deform in the helix-like fashion having both bending and torsion components to the deformation.

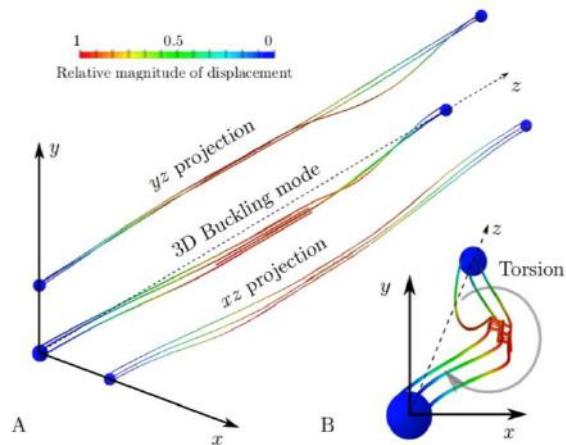


Figure 4. Three-dimensional buckling mode is depicted with its xz and yz projections in (A). The xy view of the buckling mode showing the inter-polar MT bundle cross-section rotation and the development of helical buckling shape due to torsion is shown in (B)

It should be also emphasised that due to the random positioning of MTs and cross-linkers mitotic spindles vary considerably in stiffness and structural morphology which, in turn, affect their critical loads and buckling mode shapes. The reported results are preliminary as many more computations are needed to gather

reliable statistics. Yet, the application testing and comparison of the modelling results with ones reported by Ward et al. [2] indicates the potential for our proposed method to address the complex questions of spindle structural performance and of cell mitosis as a whole.

4. CONCLUSIONS

In this paper, we have discussed a generic modular application focused on studying the structural stability of a mitotic spindle in cell division based on the continuum mechanics approach using finite element analysis. The application is created in Python 2.7 programming language and employs commercial FE code Abaqus CAE via Abaqus python API. The application can be easily applied to study various mitotic spindles provided that relevant experimental data is given. Large-scale parametric studies can be easily performed as the application uses a highly optimised FE solver that can be easily multithreaded. The application is easy to use as all the essential parameters need to be provided in a single file “job.py” and it can be also easily extended due to the module-based architecture. We have tested the application on the anaphase B spindle stability of the fission yeast cells and compared the buckling modes with ones reported in [2].

We have applied Spindle FEA to studying the effect of lateral reinforcement of the inter-polar MT bundle on the left-right symmetry of a mitotic spindle buckling. We have also reported a new type of buckling mode of the inter-polar MT bundle that can be observed only in 3D analysis and employs bending-torsion coupled deformation mechanism. Further testing and improving the application to facilitate user experience as well as to extend a range of application applicability is planned for the future work.

5. ACKNOWLEDGEMENTS

We would like to acknowledge Svitlana Braichenko and Lasse Wollatz for helpful discussions on developing the Spindle FEA application.

6. APPENDIX

6.1 Geometric and Physical Parameters of the Spindle

The geometric and physical parameters of the spindle employed in the study and supplied to “job.py” file located within the root directory of the application are presented in Table 1. The first column contains the explanation of the parameter, the second column contains name of the variable representing the parameter and the third column contains parameter values. The content of the “job.py” as well as the rules to modify it can be found in the interactive documentation to the Spindle FEA [21].

Table 1. Mitotic spindle parameters

Name	Name in “job.py”	Values
Spindle architecture		
Total spindle length [2]	-	14.3 μm
Cell radius [2]	-	1.6 \pm 1 μm
Inter-pole distance [2]	SpindleLength	10 μm
Length of interconnected zone [2]	-	2 μm
Microtubules		

MT inner diameter [10]	d	0.015 μm
MT outer diameter [10]	D	0.025 μm
Inter-polar MT length defined by Gaussian distribution	lengthInterval	$\sigma = 5 \mu\text{m}$, $\mu = 2 \mu\text{m}$
Astral MT length	aMTlength	2 μm
Number of ipMTs [2]	ipMTnumber	6
Number of aMTs	aMTnumbers	20
Distance between ipMTs, distribution fitted to [2]	separation	$\sigma = 0.029 \mu\text{m}$, $\mu = 0.04 \mu\text{m}$
Angle between ipMTs, distribution fitted to [2]	angle	$\sigma = 96.4^\circ$ $\mu = 11.1^\circ$
Elastic modulus of MTs [10]	ElasticModulus	1.5 $\times 10^9 \frac{\text{pN}}{\mu\text{m}^2}$
Assumed Poisson ratio of MT material for isotropic case	PoissonRatio	0.3
Centrosomes		
Centrosome radius	CentrosomeRadius	240 nm
Centrosome length	CentrosomeLength	480 nm
Elastic modulus of centrosome material	CentrosomeE	1.5 $\times 10^9 \frac{\text{pN}}{\mu\text{m}^2}$
Poisson ratio of centrosome material	CentrosomeNu	0.3
Connectors		
Connector radius	connectorRadius	5 nm
Connector length [27]	-	20 – 50 nm
Number of connectors per MT	Nconnectors	10
Elastic modulus of connector material	connectorE	1.5 $\times 10^9 \frac{\text{pN}}{\mu\text{m}^2}$
Poisson ratio of connector material	connectorNu	0.3
Other parameters		
Astral MT connecting spring stiffness	aMTspring	0 – 200 $\frac{\text{pN}}{\mu\text{m}^2}$
Inter-polar bundle supporting spring	groundSpring	0 – 200 $\frac{\text{pN}}{\mu\text{m}^2}$
Number of requested eigenvalues	NumberOfEigs	5

7. REFERENCES

- [1] Dogterom, M. and Surrey, T. 2013. Microtubule organization in vitro. *Current Opinion in Cell Biology*, **25**, 23–9. DOI=<https://doi.org/10.1016/j.ceb.2012.12.002>
- [2] Ward, J.J., Roque, H., Antony, C. and Nédélec, F. 2014. Mechanical design principles of a mitotic spindle. *ELife*, **3**, e03398. DOI=<https://doi.org/10.7554/eLife.03398>
- [3] Nixon, F.M., Gutiérrez-Caballero, C., Hood, F.E., Booth, D.G., Prior, I.A. and Royle, S.J. 2015. The mesh is a network of microtubule connectors that stabilizes individual kinetochore fibers of the mitotic spindle. *ELife*, **4**, 1–21. DOI=<https://doi.org/10.7554/eLife.07635>
- [4] Chaigne, A., Campillo, C., Voituriez, R., Gov, N.S., Sykes, C., Verlhac, M.-H. et al. 2016. F-actin mechanics control spindle centring in the mouse zygote. *Nature Communications*, **7**, 10253. DOI=<https://doi.org/10.1038/ncomms10253>
- [5] Kasas, S., Kis, A., Riederer, B.M., Forró, L., Dietler, G. and Catsicas, S. 2004. Mechanical Properties of Microtubules Explored Using the Finite Elements Method. *ChemPhysChem*, **5**, 252–7. DOI=<https://doi.org/10.1002/cphc.200300799>
- [6] Jin, M.Z. and Ru, C.Q. 2013. Localized buckling of a microtubule surrounded by randomly distributed cross linkers. *Physical Review E - Statistical, Nonlinear, and Soft Matter Physics*, **88**. DOI=<https://doi.org/10.1103/PhysRevE.88.012701>
- [7] Rubinstein, B., Larripa, K., Sommi, P. and Mogilner, A. 2009. The elasticity of motor–microtubule bundles and shape of the mitotic spindle. *Physical Biology*, **6**, 016005. DOI=<https://doi.org/10.1088/1478-3975/6/1/016005>
- [8] Malgaretti, P. and Muhuri, S. 2016. Mechanical stability of bipolar spindle assembly. *EPL (Europhysics Letters)*, **115**, 28001. DOI=<https://doi.org/10.1209/0295-5075/115/28001>
- [9] Kellogg, E.H., Howes, S., Ti, S.-C., Ramírez-Aportela, E., Kapoor, T.M., Chacón, P. et al. 2016. Near-atomic cryo-EM structure of PRC1 bound to the microtubule. *Proceedings of the National Academy of Sciences*, **113**, 9430–9439. DOI=<https://doi.org/10.1073/pnas.1609903113>
- [10] Pampaloni, F., Lattanzi, G., Jonas, A., Surrey, T., Frey, E. and Florin, E.-L. 2006. Thermal fluctuations of grafted microtubules provide evidence of a length-dependent persistence length. *Proceedings of the National Academy of Sciences*, **103**, 10248–10253. DOI=<https://doi.org/10.1073/pnas.0603931103>
- [11] Wang, C.Y., Ru, C.Q. and Mioduchowski, A. 2006. Orthotropic elastic shell model for buckling of microtubules. *Physical Review E*, **74**, 052901. DOI=<https://doi.org/10.1103/PhysRevE.74.052901>
- [12] Van den Heuvel, M.G.L., De Graaff, M.P. and Dekker, C. 2008. Microtubule curvatures under perpendicular electric forces reveal a low persistence length. *Proceedings of the National Academy of Sciences*, **105**, 7941–7946. DOI=<https://doi.org/10.1073/pnas.0704169105>
- [13] Liew, K.M., Xiang, P. and Sun, Y. 2011. A continuum mechanics framework and a constitutive model for predicting the orthotropic elastic properties of microtubules. *Composite Structures*, **93**, 1809–18. DOI=<https://doi.org/10.1016/j.compstruct.2011.01.017>
- [14] Soheilypour, M., Peyro, M., Peter, S.J. and Mofrad, M.R.K. 2015. Buckling behavior of individual and bundled microtubules. *Biophysical Journal*, **108**, 1718–1726. DOI=<https://doi.org/10.1016/j.bpj.2015.01.030>
- [15] Brangwynne, C.P., MacKintosh, F.C., Kumar, S., Geisse, N.A., Talbot, J., Mahadevan, L. et al. 2006. Microtubules can bear enhanced compressive loads in living cells because of lateral reinforcement. *Journal of Cell Biology*, **173**, 733–741. DOI=<https://doi.org/10.1083/jcb.200601060>
- [16] di Pietro, F., Echard, A. and Morin, X. 2016. Regulation of mitotic spindle orientation: an integrated view. *EMBO Reports*, **17**, 1106–30. DOI=<https://doi.org/10.15252/embr.201642292>
- [17] Müller-Reichert, T., Kiewisz, R. and Redemann, S. 2018. Mitotic spindles revisited – new insights from 3D electron microscopy. *Journal of Cell Science*, **131**, jcs211383. DOI=<https://doi.org/10.1242/jcs.211383>
- [18] Pavin, N. and Tolić, I.M. 2016. Self-Organization and Forces in the Mitotic Spindle. *Annual Review of Biophysics*, **45**, 279–98. DOI=<https://doi.org/10.1146/annurev-biophys-062215-010934>
- [19] Nedelec, F. and Foethke, D. 2007. Collective Langevin dynamics of flexible cytoskeletal fibers. *New Journal of Physics*, **9**. DOI=<https://doi.org/10.1088/1367-2630/9/11/427>
- [20] Jakobs, M., Franze, K. and Zemel, A. 2015. Force Generation by Molecular-Motor-Powered Microtubule Bundles; Implications for Neuronal Polarization and Growth. *Frontiers in Cellular Neuroscience*, **9**, 4413389–441. DOI=<https://doi.org/10.3389/fncel.2015.00441>
- [26] A. Iakovliev, *Spindle FEA*. University of Southampton. DOI=<https://doi.org/10.5258/SOTON/D0603>
- [22] Kabir, A.M.R., Inoue, D., Afrin, T., Mayama, H., Sada, K. and Kakugo, A. 2015. Buckling of Microtubules on a 2D Elastic Medium. *Scientific Reports*, **5**, 17222. DOI=<https://doi.org/10.1038/srep17222>
- [23] Timoshenko, S.P.S. and Gere, J.M.J. 2012. Theory of elastic stability [Internet]. Courier Corporation.
- [24] Gittes, F., Mickey, B., Nettleton, J. and Howard, J. 1993. Flexural rigidity of microtubules and actin filaments measured from thermal fluctuations in shape. *The Journal of Cell Biology*, **120**, 923–934. DOI=<https://doi.org/10.1083/jcb.120.4.923>
- [25] Janson, M.E. and Dogterom, M. 2004. A bending mode analysis for growing microtubules: evidence for a velocity-dependent rigidity. *Biophysical Journal*, **87**, 2723–2736. DOI=<https://doi.org/10.1529/biophysj.103.038877>
- [26] Claessens, M., Bathe, M., Frey, E. and Bausch, A.R. 2006. Actin-binding proteins sensitively mediate F-actin bundle stiffness. *Nature Materials*, **5**, 748–753. DOI=<https://doi.org/10.1038/nmat1718>
- [27] Subramanian, R., Wilson-Kubalek, E.M., Arthur, C.P., Bick, M.J., Campbell, E.A., Darst, S.A. et al. 2010. Insights into Antiparallel Microtubule Crosslinking by PRC1, a Conserved Nonmotor Microtubule Binding Protein. *Cell*, **142**, 433–43. DOI=<https://doi.org/10.1016/j.cell.2010.07.012>

ICBBB 2019

Bioscience and Biotechnology

Research on Response Surface Optimization of Culture Medium for Antibacterial Substances Produced by *Bacillus Amyloliquefaciens* GN59

Liu Yaping
¹Shandong Agricultural University,
Taian, China
²Qilu University of Technology
Jinan, China
86-18763803286
lyplyp_III@163.com

Zhao Bo
²Qilu University of
Technology, Jinan, China
86-13173059735
3181534367@qq.com

Emiliya Kalamiyets
³National Academy of Sciences
Belarus
86-0531-82605324
kolomiets@mbio.bas-net.by

Wu Peng*
¹Shandong Agricultural University, Taian, China
86-13954847828
wupengguai@163.com

Chu Jie*
²Qilu University of Technology, Jinan, China
86-13173025960
chujie6532@163.com

ABSTRACT

Single factor optimization experiment and response surface optimization experiment were designed to research the influence of different culture medium components to bacteriostatic active substances produced by *Bacillus amyloliquefaciens* GN59 strain, and a culture medium formula suitable for the GN59 strain to produce the bacteriostatic active substances was screened. In the single factor experiment, the optimal formula was: glucose 10.0 g/L, $K_2HPO_4 \cdot 3H_2O$ 1.2 g/L, KH_2PO_4 1.0 g/L, $(NH_4)_2SO_4$ 2.00 g/L, $Na_3C_6H_5O_7 \cdot 3H_2O$ 0.9 g/L, and $MgSO_4 \cdot 7H_2O$ 0.15 g/L, and the bacteriostatic activity was improved by 14.32% in comparison with that before optimization. In the response surface optimization experiment, the optimal culture medium components were glucose 6.15 g/L, $K_2HPO_4 \cdot 3H_2O$ 1.2 g/L, KH_2PO_4 1.0 g/L, $(NH_4)_2SO_4$ 2.50 g/L, $Na_3C_6H_5O_7 \cdot 3H_2O$ 1.01 g/L, and $MgSO_4 \cdot 7H_2O$ 0.15 g/L, the bacteriostatic activity was improved by 31.18% in comparison with that before optimization, and meanwhile, the product cost was lowered, and batch low-cost and efficient fermentation production of the *Bacillus amyloliquefaciens* GN59 strain was realized.

CCS Concepts

Applied computing → Life and medical sciences → Systems biology

Keywords

Bacillus amyloliquefaciens; Culture medium optimization; Bacteriostatic activity

1. INTRODUCTION

Permission to make digital or hard copies of all or part of this work for personal or classroom use is granted without fee provided that copies are not made or distributed for profit or commercial advantage and that copies bear this notice and the full citation on the first page. Copyrights for components of this work owned by others than ACM must be honored. Abstracting with credit is permitted. To copy otherwise, or republish, to post on servers or to redistribute to lists, requires prior specific permission and/or a fee. Request permissions from Permissions@acm.org.

ICBBB '19, January 7–9, 2019, Singapore, Singapore

© 2019 Association for Computing Machinery.

ACM ISBN 978-1-4503-6654-0/19/01...\$15.00

DOI: <https://doi.org/10.1145/3314367.3314368>

Since Johson et al. [1] published that bacillus has an effect of controlling plant diseases in 1945, relevant scientific researchers have made researches on it for many years. The researches show that bacillus is a kind of important biocontrol microbial resource [2-3], has the biocontrol effects of antagonism, bacteriolysis and the like, is wider in bacteriocidal spectrum of the antibacterial substances and high in stability [4], and has huge application potential in the aspects of food preservation, feed additives and biological medicine [5-6], etc. Researches on the bacteriostatic active substances of bacillus in China are relatively late and are not deep enough, and applications in the fields of feed, cultivation, medicine health care and food, etc. are less.

Bacillus amyloliquefaciens GN59 is a strain which is screened from collected samples of a poultry farm in the earlier stage by the laboratory and has pathogenic bacteria (*Escherichia coli*, *Salmonella*, *Staphylococcus*, etc.) inhibition activity. Shiwei et al. [7] found that *Bacillus amyloliquefaciens* had preservative and fresh-keeping effects for meat, and had a fine inhibiting effect for main pathogenic bacteria, *Pseudomonas* and *Listeria monocytogenes*. Liu Wenbo et al. [8] performed optimization on a carbon source and nitrogen source combined culture medium of *Bacillus amyloliquefaciens* HAB-7, so that the culture medium had a certain salt tolerance, and then a bacteriostatic effect for plant pathogenic fungi was improved. Han Yuzhu et al. [9] performed optimization on the fermentation and extraction conditions of *Bacillus amyloliquefaciens* H15 by taking common mould of corn as indicator bacteria, and proved that the activity of the antibacterial peptide obtained by hydrochloric acid and acetone extraction methods was the highest. Mariana et al. [10] inoculated *Bacillus* E164 strain on different medium, it showed different bacteriostatic activity to *Bipolaris sorokiniana*.

The researches showed that *Bacillus amyloliquefaciens* plays an inhibiting role on pathogenic bacteria, fungi and virus, etc. [11] in biological control application by producing active substances such as antibacterial protein or polypeptide. Biological control

¹ Biology Institute ,Qilu University of Technology (Shandong Academy of Sciences), Jinan 250103, China

² Institute of Microbiology, National Academy of Sciences, Belarus

* Corresponding author

has the advantages of high safety and pleiotropic effect [12], but the output and activity of the antibacterial active substances are affected by fermentation conditions[13]. For the same species of bacillus, but under the different culture medium, Landy medium can make Bacillus substills GEB3 and B2 strains to produce more output and activity of the antibacterial active substances [14-15]. This experiment mainly studied the response surface optimization of the culture medium of the bacillus amyloliquefaciens GN59 strain, and aims to increase active substances produced by the strain by reasonable design of the culture medium components, so as to provide reference for batch low-cost and efficient fermentation production of the bacillus amyloliquefaciens GN59 strain.

2. MATERIAL AND METHOD

2.1 Main Reagent and Instrument

LB nutrient agar medium, Bo Biotechnology Co. Ltd. in Qingdao Hi-tech Park; glucose, $K_2HPO_4 \cdot 3H_2O$, KH_2PO_4 and $Na_3C_6H_5O_7 \cdot 3H_2O$, Sinopharm Chemical Reagent Co. Ltd.; $(NH_4)_2SO_4$ and $MgSO_4 \cdot 7H_2O$, Beijing Yili Fine Chemical Co. Ltd.

Analytical balance METTLER TOLEDO; multiscan spectrum American DYNEX Spectra MR (used for testing absorbance); pH acidimeter SARTORLUS; autoclave; SGD-IV full-automatic reducing sugar tester, developed by Biology Institute of Shandong Academy of Sciences.

2.2 Tested Bacterium

Tested strain GN59 is a strain of bacillus amyloliquefaciens obtained by screening from collected samples of the poultry farm by the laboratory, the adopted culture medium is an LB culture medium: components (g/L) including 10.0 g of tryptone, 5.0 g of yeast extract powder, 10.0 g of sodium chloride, and 15.0 g of

agar, and pH being 7.0 ± 0.2 . The culture medium is preserved in a refrigerator of $4^\circ C$.

2.3 Preparation of Fermentation Supernatant

Operation is performed on an ultra-clean workbench, one loop of the GN50 strain preserved on the LB slant culture medium is scraped into 100mL of the LB liquid culture medium with an inoculating loop, a shaking table is arranged, and culture is performed for 15h at $30^\circ C$ and at rate of 180 r/min, so as to prepare a GN59 seed solution. The GN59 seed solution is inoculated into a fermentation culture medium according to the inoculation amount of 3%, constant-temperature shaking culture is performed for 15h ($30^\circ C$, 180 r/min), centrifugation is performed for 10min at the rate of 5000 r/min, the thallus is removed, and the supernate is collected and is filtered with a 0.22 μm membrane, so as to prepare a sterile fermentation broth, which is preserved in a refrigerator of $4^\circ C$ for later use.

2.4 Single Factor Optimization Experiment

The formula of the bacillus amyloliquefaciens GN59 reserved by the laboratory is: 20.0 g of glucose, 2.0 g of $K_2HPO_4 \cdot 3H_2O$, 3.0 g of KH_2PO_4 , 1.5 g of $(NH_4)_2SO_4$, 0.5 g of $Na_3C_6H_5O_7 \cdot 3H_2O$, and 0.1 g of $MgSO_4 \cdot 7H_2O$; pH is 7.0~7.2, industrial water is added to the volume of 1L, and sterilization is performed for 20min at 0.1MPa at $121^\circ C$.

Currently, according to the above-said culture medium, single factor optimization experiment * is performed on glucose, dipotassium phosphate, monopotassium phosphate, sodium citrate and magnesium sulfate respectively, and five different gradients are set for each factor, referring to table 1.

Table 1. Single factor optimization of GN59 medium

Factor	Level				
	1	2	3	4	5
Glucose	5	10	15	20	25
$K_2HPO_4 \cdot 3H_2O$	1	3	5	7	9
KH_2PO_4	0.5	1.0	2.0	3.0	4.0
$(NH_4)_2SO_4$	1.0	1.5	2.0	2.5	3.0
$Na_3C_6H_5O_7 \cdot 3H_2O$	0.3	0.5	0.7	0.9	1.1
$MgSO_4 \cdot 7H_2O$	0.05	0.10	0.15	0.20	0.25

*In each single factor, non-variable factors maintain the original formula.

2.5 Response Surface Optimization Experiment

According to the result of the single factor experiment, Design-Expert 8.0.6.1 is adopted for variance analysis, three factors which have the most significant influence on bacteriostatic activity are selected, and response surface experiments are designed for the three factor, wherein each group of experiment is repeated for three times.

2.6 Testing on Bacteriostatic Activity of Different Culture Media

A method of testing escherichia coli OD_{600} is adopted for the culture medium optimization experiment. The specific operation steps are as follows: on an ultra-clean workbench, adding 100 μL of escherichia coli liquid to each EP tube according to experiment dosage, centrifuging at a high speed for 1min, removing the supernatant and reserving the thallus, adding 1mL of fresh LB liquid culture medium, marking and adding 100 μL of sterile fermentation broth after culture medium optimization, and uniformly mixing. OD_{600} is tested respectively at the 0th hour and the 15th hour, and data are recorded. Each group of experiment is repeated for three times.

2.7 Verification Experiment

In order to further verify the research result of response surface analysis, the original formula and the formula after single factor optimization as well as condition parameters after response surface optimization are selected to perform verification experiment. Each group of formula is repeated for three times, and the experiment is performed according to the experiment steps of 1.6.

2.8 Statistic Analysis of Data

All experiments are repeated for three times, Excel software is adopted for plotting for data of the single factor experiment, and Design-Expert 8.0.6.1 software is adopted for the response surface experiment to perform experiment design, inter-class variance analysis (ANOVA) and data analysis.

3. RESULT AND ANALYSIS

3.1 Single Factor Optimization Experiment of *Bacillus Amyloliquefaciens* GN59

3.1.1 Influence of Glucose

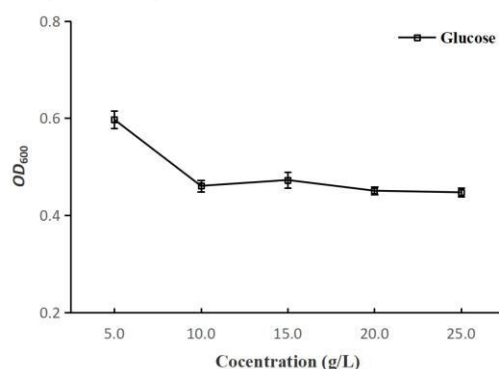


Figure 1. Effect of glucose on antifungal activity of *B. amyloliquefaciens* GN59

*Note: The lower the OD value is, the higher the bacteriostatic activity is, similarly hereafter.

As a carbon source, glucose provides a carbon skeleton of cells for the growth and metabolism of microorganism, and supplies energy required by vital movement of the cells. Tested OD_{600} data show that the bacteriostatic activity of the glucose is the strongest at the concentration of 10 g/L, referring to Figure 1. According to the experiment result, when the glucose concentration is higher than 10 g/L, the bacteriostatic activity does not have obvious change, proving that available carbon source of the bacillus amyloliquefaciens is about 10 g/L, and excessive carbon source cannot improve the bacteriostatic activity of the fermentation broth and may cause high cost. By comprehensive consideration, glucose with concentration of 10 g/L is selected as the optimal concentration for optimizing the culture medium.

3.1.2 Influence of $(NH_4)_2SO_4$

As an inorganic nitrogen source, $(NH_4)_2SO_4$ mainly provides element nitrogen needed by synthesis of amino acid, protein and nucleic acid, etc. Tested OD_{600} data show that the bacteriostatic effect of $(NH_4)_2SO_4$ is the optimal at the concentration of 2.0 g/L, referring to Figure 2. Carbon/nitrogen ratio (C/N) may affect the growth and propagation of microorganisms and the accumulation of metabolite, and in combination of this

experiment result, either too low or too high C/N has influence on the bacteriostatic activity of the bacillus amyloliquefaciens GN59, when C/N is too high, mass propagation of thalli is caused, and accumulation of bacteriostatic active products is less; and only when C/N is appropriate, the output of bacteriostatic active substances may be increased. According to the experiment result, $(NH_4)_2SO_4$ with concentration of 2.0 g/L is selected as the optimal concentration for optimizing the culture medium.

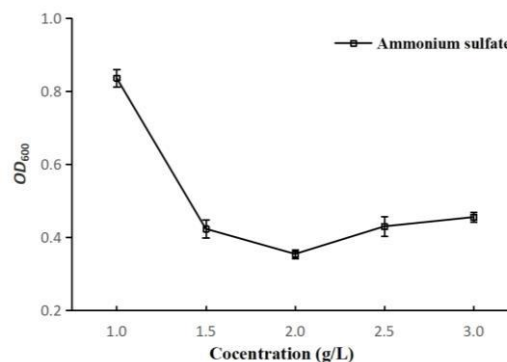


Figure 2. Effect of ammonium sulfate on antifungal activity of *B. amyloliquefaciens* GN59

3.1.3 Influences of $K_2HPO_4 \cdot 3H_2O$ and KH_2PO_4

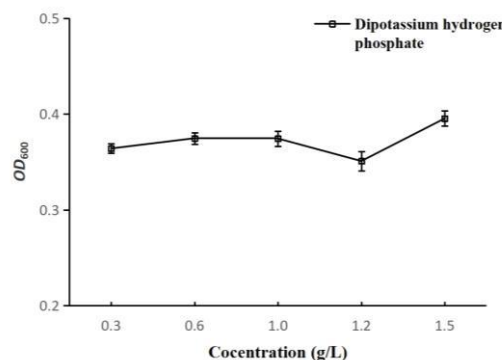


Figure 3. Effect of dipotassium hydrogen phosphate on antifungal activity of *B. amyloliquefaciens* GN59

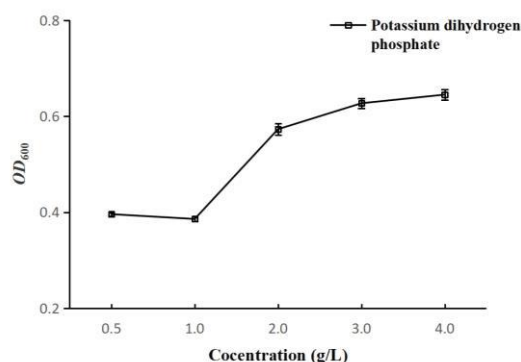


Figure 4. Effect of potassium dihydrogen phosphate on antifungal activity of *B. amyloliquefaciens* GN59

As pH buffering systems, $K_2HPO_4 \cdot 3H_2O$ and KH_2PO_4 can play an adjusting role in a certain pH scope, so as to meet growth and propagation of the microorganisms and produce metabolite.

Tested OD_{600} data show that the bacteriostatic effect of $K_2HPO_4 \cdot 3H_2O$ is the optimal at the concentration of 1.2 g/L, and the bacteriostatic effect of KH_2PO_4 is the optimal at the concentration of 1.0 g/L, referring to Figures 3 and 4. Suitable growth pH of the bacillus amyloliquefaciens GN59 is 6.8–7.2, and buffering systems of $K_2HPO_4 \cdot 3H_2O$ and KH_2PO_4 can play an adjusting role at the pH of 6.4–7.2. The $K_2HPO_4 \cdot 3H_2O$ solution is alkaline, the KH_2PO_4 solution is acidic, and when the two substances are mixed with equal dosage, pH is 6.8. According to the experiment result, when the two are combined to cause peracid, the bacteriostatic activity is reduced. By synthesis of the experiment result, when alkalinescent concentrations are selected, that is, $K_2HPO_4 \cdot 3H_2O$ concentration is 1.2 g/L and KH_2PO_4 concentration is 1.0g/L, the bacillus amyloliquefaciens GN59 is facilitated to produce bacteriostatic active substances.

3.1.4 Influences of $Na_3C_6H_5O_7 \cdot 3H_2O$ and Magnesium Sulfate

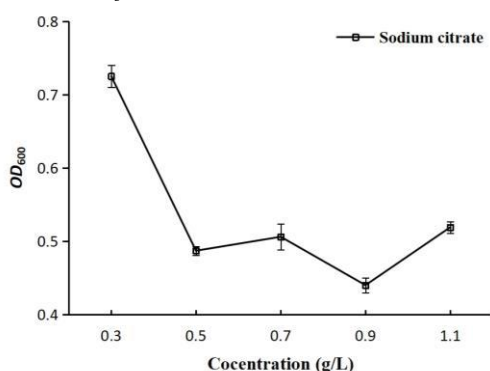


Figure 5. Effect of sodium citrate on antifungal activity of *B. amyloliquefaciens* GN59

$Na_3C_6H_5O_7 \cdot 3H_2O$ may be utilized by bacteria to decompose citrate to produce an alkali compound, and thus has good pH adjusting and buffering performances; $MgSO_4 \cdot 7H_2O$ is an activating agent of many enzymes, and is capable of promoting the metabolism of carbohydrates, synthesis of nucleic acid, and transformation of phosphate, etc., and Mg^{2+} is EMP and TCA paths and is an important enzyme activating agent for production of lysine. Tested OD_{600} data show that the bacteriostatic effect of $Na_3C_6H_5O_7 \cdot 3H_2O$ is the optimal at the concentration of 0.9 g/L, and the bacteriostatic effect of $MgSO_4 \cdot 7H_2O$ is the optimal at the concentration of 0.15 g/L, referring to Figures 5 and 6. According to the experiment result, growth and metabolism of the bacillus amyloliquefaciens GN59

may be affected due to lack of $Na_3C_6H_5O_7 \cdot 3H_2O$ and Mg^{2+} , resulting in reduction of bacteriostatic activity. By comprehensive consideration, $Na_3C_6H_5O_7 \cdot 3H_2O$ with concentration of 0.9 g/L and $MgSO_4 \cdot 7H_2O$ with concentration of 0.15 g/L are selected as the optimal concentration for optimizing the culture medium.

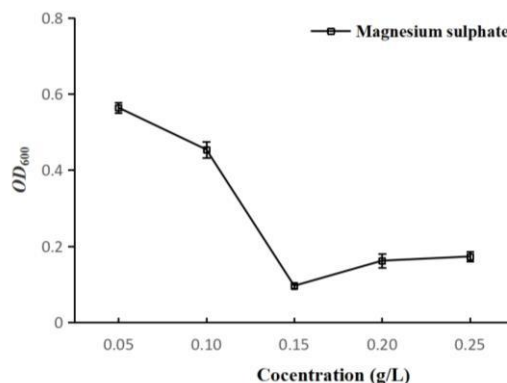


Figure 6. Effect of magnesium sulphate on antifungal activity of *B. amyloliquefaciens* GN59

3.2 Response Surface Optimization Experiment of Bacillus Amyloliquefaciens GN59

3.2.1 Establishment of Regression Model

According to the single factor experiment result, glucose, $(NH_4)_2SO_4$ and $Na_3C_6H_5O_7 \cdot 3H_2O$ are selected to perform response surface optimization experiment, and other factors of the culture medium select the optimal concentrations of single factors ($K_2HPO_4 \cdot 3H_2O$: 1.2 g/L, KH_2PO_4 : 1.0 g/L, $MgSO_4 \cdot 7H_2O$: 0.15 g/L). Design-Expert 8.0.6.1 is adopted for central combination experiment, and the experiment design and result are as shown in table 2. The regression equation of OD_{600} numerical value (Y) of the bacteriostatic activity experiment of the fermentation supernatant of the bacillus amyloliquefaciens GN59 to glucose (A), $(NH_4)_2SO_4$ (B) and $Na_3C_6H_5O_7 \cdot 3H_2O$ (C) is:

$$Y = 0.089 + 0.014A - 5.638 \times 10^{-3}B + 6.181 \times 10^{-3}C + 0.015AB - 2.250 \times 10^{-3}AC - 0.030BC + 0.018A^2 + 0.012B^2 + 0.030C^2.$$

Table 2. Response surface design matrix and experimental domain for the optimization of significant factors

Number	Factor			OD_{600}
	Glucose $g L^{-1}$	$(NH_4)_2SO_4$ $g L^{-1}$	$Na_3C_6H_5O_7 \cdot 3H_2O$ $g L^{-1}$	
High Level(+1)	15	2.5	1.2	
Middle level(0)	10	2.0	0.9	
Low level(-1)	5	1.5	0.6	
1	-1	-1	-1	0.139
2	+1	-1	-1	0.133

3	-1	+1	-1	0.122
4	+1	+1	-1	0.212
5	-1	-1	+1	0.204
6	+1	-1	+1	0.225
7	-1	+1	+1	0.104
8	+1	+1	+1	0.149
9	-1.68	0	0	0.111
10	+1.68	0	0	0.137
11	0	-1.68	0	0.095
12	0	+1.68	0	0.117
13	0	0	-1.68	0.154
14	0	0	+1.68	0.159
15	0	0	0	0.086
16	0	0	0	0.096
17	0	0	0	0.069
18	0	0	0	0.088
19	0	0	0	0.070
20	0	0	0	0.130

3.2.2 Variance Analysis of Regression Model

Quadratic polynomial model variance analysis (ANOVA) is performed according to variance data of the regression model, referring to table 3. In the regression model, $P=0.0188$, which is extremely significant; and in lack of fit, $P=0.2015$, which is not significant. The result shows that the regression model is better in degree of fitting, and the influence of unknown factors to the

result is small, which can well reflect the correlation between the OD_{600} numerical value of the bacteriostatic activity experiment of the fermentation supernatant of the bacillus amyloliquefaciens GN59 and glucose, $(NH_4)_2SO_4$ and $Na_3C_6H_5O_7 \cdot 3H_2O$. According to the significance testing result in variance analysis, in the model, C^2 is extremely significant, BC and A^2 are significant, and A, B, C, AB, AC and B^2 are not significant.

Table 3. ANOVA for the quadratic polynomial modal

Source	Sum of Squares	df	Mean Square	F	p-value
Model	0.030	9	3.309×10^{-3}	4.12	0.0188*
A	2.748×10^{-3}	1	2.748×10^{-3}	3.42	0.0940
B	4.341×10^{-4}	1	4.341×10^{-4}	0.54	0.4790
C	5.217×10^{-4}	1	5.217×10^{-4}	0.65	0.4389
AB	1.800×10^{-3}	1	1.800×10^{-3}	2.24	0.1652
AC	4.050×10^{-5}	1	4.050×10^{-5}	0.050	0.8268
BC	7.080×10^{-3}	1	7.080×10^{-3}	8.82	0.0141*
A^2	4.862×10^{-3}	1	4.862×10^{-3}	6.06	0.0336*
B^2	2.077×10^{-3}	1	2.077×10^{-3}	2.59	0.1388
C^2	0.013	1	0.013	16.00	0.0025**
Residual	8.029×10^{-3}	10	8.029×10^{-4}		
Lack of Fit	5.532×10^{-3}	5	1.106×10^{-3}	2.22	0.2015
Pure Error	2.497×10^{-3}	5	4.994×10^{-4}		

Note: * means significant different, $P < 0.05$; ** means extremely significant difference, $P < 0.01$.

3.2.3 Response Surface Analysis

Figures 7-9 are three-dimensional response surfaces and contour maps of influences of glucose (A), $(NH_4)_2SO_4$ (B) and $Na_3C_6H_5O_7 \cdot 3H_2O$ (C) on the OD_{600} numerical value of the

bacteriostatic activity experiment of the fermentation supernatant of the bacillus amyloliquefaciens GN59 under the conditions of constant $K_2HPO_4 \cdot 3H_2O$, KH_2PO_4 and $MgSO_4 \cdot 7H_2O$. By analyzing with Design-Expert 8.0.6.1

software, it is known that the optimal fermentation conditions for the bacillus amyloliquefaciens GN59 to produce bacteriostatic active substances are as follows: glucose 6.15 g/L, $(\text{NH}_4)_2\text{SO}_4$ 2.50 g/L, $\text{Na}_3\text{C}_6\text{H}_5\text{O}_7 \cdot 3\text{H}_2\text{O}$ 1.01 g/L. In such conditions, the OD_{600} numerical value of the bacteriostatic activity experiment is 0.0797.

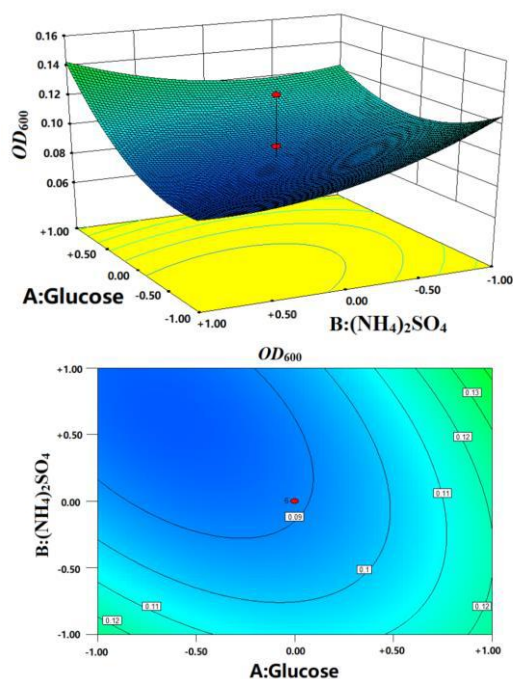


Figure 7. Three dimensional response surface and contour plots of the effect of glucose and ammonium sulfate on the antifungal activity of *B. amyloliquefaciens* GN59

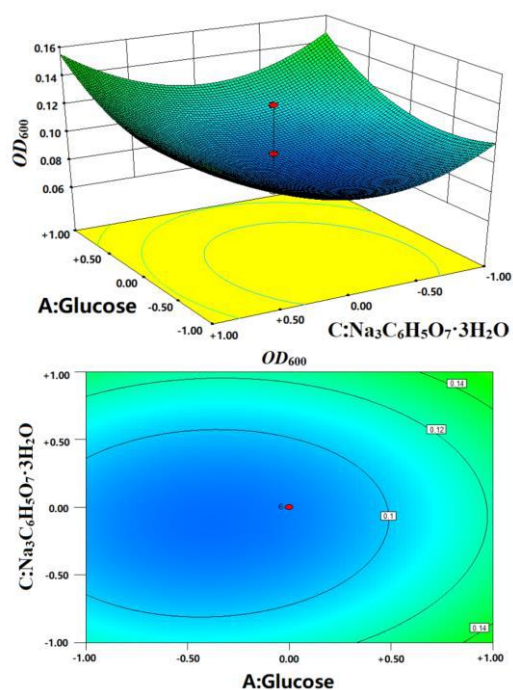


Figure 8. Three dimensional response surface and contour plots of the effect of glucose and sodium citrate on the antifungal activity of *B. amyloliquefaciens* GN59

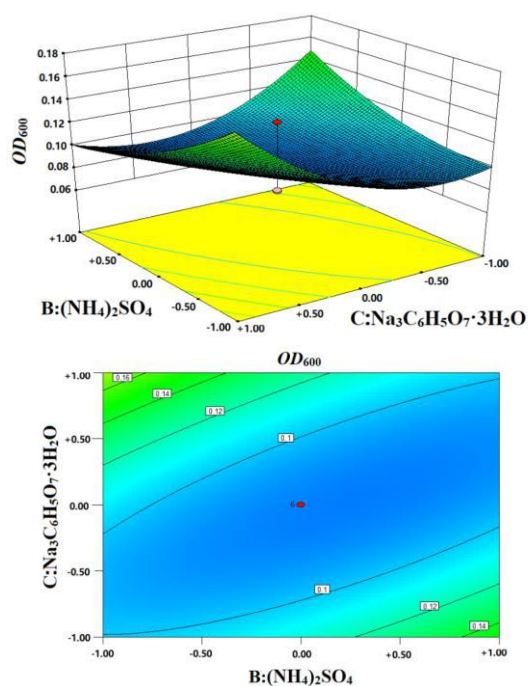


Figure 9. Three dimensional response surface and contour plots of the effect of ammonium sulfate and sodium citrate on the antifungal activity of *B. amyloliquefaciens* GN59

3.2.4 Verification Experiment of Response Surface Model

Based on the above-said experiment results, an original formula (glucose 20.0 g/L, $\text{K}_2\text{HPO}_4 \cdot 3\text{H}_2\text{O}$ 2.0 g/L, KH_2PO_4 3.0 g/L, $(\text{NH}_4)_2\text{SO}_4$ 1.5 g/L, $\text{Na}_3\text{C}_6\text{H}_5\text{O}_7 \cdot 3\text{H}_2\text{O}$ 0.5 g/L, $\text{MgSO}_4 \cdot 7\text{H}_2\text{O}$ 0.1 g/L), a single factor optimization formula (glucose 10.0 g/L, $\text{K}_2\text{HPO}_4 \cdot 3\text{H}_2\text{O}$ 1.2 g/L, KH_2PO_4 1.0 g/L, $(\text{NH}_4)_2\text{SO}_4$ 2.00 g/L, $\text{Na}_3\text{C}_6\text{H}_5\text{O}_7 \cdot 3\text{H}_2\text{O}$ 0.9 g/L, $\text{MgSO}_4 \cdot 7\text{H}_2\text{O}$ 0.15 g/L), a response surface optimization formula (glucose 6.15 g/L, $\text{K}_2\text{HPO}_4 \cdot 3\text{H}_2\text{O}$ 1.2 g/L, KH_2PO_4 1.0 g/L, $(\text{NH}_4)_2\text{SO}_4$ 2.50 g/L, $\text{Na}_3\text{C}_6\text{H}_5\text{O}_7 \cdot 3\text{H}_2\text{O}$ 1.01 g/L, $\text{MgSO}_4 \cdot 7\text{H}_2\text{O}$ 0.15 g/L) and a control group (only added with escherichia coli) are selected for verification experiment, and the experiment is repeated for three times. In such conditions, the OD_{600} average numerical values of the bacteriostatic activity experiment are respectively as follows: the original formula: 0.433, the single factor optimization formula: 0.371, the response surface optimization formula: 0.298, the control group: 0.709.

4. DISCUSSION

As a biocontrol microorganism, the metabolites of the bacillus amyloliquefaciens GN59 are affected by conditions of the culture medium, and increase of output of bacteriostatic active substances is of great importance to strengthening of bacteriostatic activity of the GN59 strain. Liu Jinglan et al.[16], by Plackett-Burman design and response surface experiment, optimized antibacterial components produced by fermentation of bacillus amyloliquefaciens CC09, the optimal culture medium composition is as follows: wheat flour 14.0 g/L, soybean cake meal 25.0 g/L, corn flour 8.0 g/L, MgSO_4 0.1 g/L, MnSO_4 2.5 mg/L, FeSO_4 0.8 mg/L, and the output is increased by 4.2 times in comparison with that before optimization.

In this research, culture medium composition of the bacillus amyloliquefaciens GN59 is optimized, single factor optimization and response surface optimization experiments are successively performed on totally five factors, including glucose, $K_2HPO_4 \cdot 3H_2O$, KH_2PO_4 , $Na_3C_6H_5O_7 \cdot 3H_2O$ and $MgSO_4 \cdot 7H_2O$, and the influences of culture media of different combinations on the metabolite of the bacillus amyloliquefaciens GN59 are verified. The verification experiment results show that by response surface optimization of the culture medium, in the same fermentation conditions, each single factor may affect the output of the metabolite of the bacillus amyloliquefaciens GN59, and after response surface optimization, in the formula conditions of glucose 6.15 g/L, $K_2HPO_4 \cdot 3H_2O$ 1.2 g/L, KH_2PO_4 1.0 g/L, $(NH_4)_2SO_4$ 2.50 g/L, $Na_3C_6H_5O_7 \cdot 3H_2O$ 1.01 g/L and $MgSO_4 \cdot 7H_2O$ 0.15 g/L, the antibacterial effect of the GN59 strain to escherichia coli is significantly increased, and the bacteriostatic activity is increased by 31.18% in comparison with that before optimization, proving that the content of bacteriostatic active substances in the fermentation metabolite is significantly increased.

The culture medium optimized by this research, by increasing the bacteriostatic metabolite of the GN59 strain, increasing the output of the bacteriostatic active substances by improving the original formula, and meanwhile reducing the use amount of fermentation raw materials, and lowering the production cost, provides reference for batch fermentation production of the bacillus amyloliquefaciens GN59 strain.

5. ACKNOWLEDGMENTS

The experiment was completed in Biology Institute, Qilu University of Technology (Shandong Academy of Sciences). Thanks to Chu Jie's support and guidance. This research was supported by the National Key Research and Development Plan (no. 2016YFE0111600) and the Collaborative Innovation Fund of Shandong Academy of Sciences (no. 2017CXY-17).

6. REFERENCE

- [1] Johnson F H, Campbell D H. 1945. The retardation of protein denaturation by hydrostatic pressure. *Journal of Cell Comp Physiol*, 26, 34-46.
- [2] YAN Wanrong, XIAO Min, CHEN Yuan, et al. 2018. Research Progress in Antimicrobial Lipopeptides of *Bacillus amyloliquefaciens*. *Northern Horticulture*, 07, 162-167.
- [3] CHEN X, Koumoutsi A, Scholz R, et al. 2007. Comparative analysis of the complete genome sequence of the plant growth-promoting bacterium *Bacillus amyloliquefaciens* FZB42. *Nature Biotechnology*, 25, 1007-1014.
- [4] ZHANG Xue, TAN Shiyao, QIAN Siriguleng, et al. 2018. Study on the Characteristics and Antibacterial Activity of *Bacillus amyloliquefaciens*. *China Animal Husbandry & Veterinary Medicine*, 45, 5, 1251-1257.
- [5] Haobin Zhao, Lu Yan, Xiaoguang Xu, et al. 2018. Potential of *Bacillus subtilis* lipopeptides in anti-cancer I: induction of apoptosis and paraptosis and inhibition of autophagy in K562 cells. *AMB Express*, 8, 1.
- [6] Mansour T., Abdullah, Nida Y., Ali, Patrice Suleman. 2008. Biological control of *Sclerotinia sclerotiorum* (Lib.) de Bary with *Trichoderma harzianum* and *Bacillus amyloliquefaciens*. *Crop Protection*, 27, 10.
- [7] SHI Wei, XIE Weitian, ZHANG Yan, et al. 2011. Preliminary research on effect of fermentation broth of *Bacillus amyloliquefaciens* on fresh-keeping of chilled meat. *China Brewing*, 30, 51-54.
- [8] LIU Wenbo, XIONG Yanhong, QIN Chunxiu, et al. 2017. Antifungal activity of *Bacillus amyloliquefaciens* HAB-7 and optimization of its culture medium. *China Plant Protection*, 37, 6, 5-13.
- [9] HAN Yuzhu, DENG Zhao, ZHANG Bao, et al. 2015. Optimization of Fermentation Conditions for Production of Antifungal Peptides by *Bacillus amyloliquefaciens* H15 and Comparison of Extraction Methods for Antifungal Peptides. *Food Science*, 36, 15, 135-141.
- [10] Mariana C M, Monique S G, José C G, et al. 2009. Antifungal activity of *Bacillus* sp. E164 against *Bipolaris sorokiniana*. *Biociencias*, 17, 1, 48-58.
- [11] Mercado B J, Rodriguez J D, Hervas A, et al. 2004. Suppression of *Verticillium wilt* in olive planting stocks by root-associated fluorescent *Pseudomonas* spp. *Biological Control*, 30, 2, 474-486.
- [12] Gabriele B, Christin Z, Jana L, et al. 2005. Impact of plant species and site on rhizosphere-associated fungi antagonistic to *Verticillium dahliae* kleb. *Applied And Environmental Microbiology*, 71, 8, 4203-4213.
- [13] Yoshida S, Hiradate S, Tsukamoto T, et al. 2001. Antimicrobial activity of culture filtrate of *Bacillus amyloliquefaciens* RC-2 isolated from mulberry leaves. *Biological Control*, 91, 2, 181-187.
- [14] GAO Xuewen, YAO Shiyi, Huong Pham, et al. 2003. Lipopeptide Antibiotics Produced by the Engineered Strain *Bacillus subtilis* GEB3 and Detection of Its Bioactivity. *Scientia Agricultural Sinica*, 36, 12, 1496-1501.
- [15] GAO Xuewen, YAO Shiyi, Huong Pham, et al. 2003. Inhibitive Substance Produced by *Bacillus subtilis* B2 Strain. *Chinese Journal of Biological Control*, 19, 4, 175-179.
- [16] LIU Jinglan, CAI Xunchao, XUE Yarong, et al. 2016. Optimization of Iturin A Synthesis by *Bacillus amyloliquefaciens* CC09 Using Response Surface Technique. *Chinese Journal of Biological Control*, 32, 2, 235-243.

Effectuated Brewing Time and Temperature of *Centella Asiatica* Tea on Antioxidant Activity and Consumer Acceptance

Rungnattakan Ploenkutham
Department of Food
Biotechnology, Faculty of
Biotechnology, Assumption
University, Bangkok, Thailand
Tel+662-3004553-60 to 3792
kelrnkp@gmail.com

Preeyapa Sripromma
Department of Food
Biotechnology, Faculty of
Biotechnology, Assumption
University, Bangkok, Thailand
Tel+662-3004553-60 to 3792

Suksan Amornraksa
King Mongkut's University of
Technology North Bangkok,
Bangkok Thailand, Tel +662745-
8584
suksuna@kmutnb.ac.th

Patchanee Yasurin
Department of Food
Biotechnology, Faculty of
Biotechnology, Assumption
University, Bangkok, Thailand
Tel+662-3004553-60 to 3792
patchaneeYsr@au.edu

Malinee Sririyanun
King Mongkut's University of
Technology North Bangkok,
Bangkok Thailand,
Tel +662555-2000
Macintous@gmail.com

Suvaluk Asavasanti
King Mongkut's University of
Technology Thonburi, Bangkok
Thailand
Tel +662470-9249
Savaluk.asa@kmutt.ac.th

Aussama Soontrunnarudrungsri
Department of Food Biotechnology,
Faculty of Biotechnology,
Assumption University, Bangkok, Thailand
Tel. 662-3004553-60 to 3792
aussamasnt@au.edu

ABSTRACT

Centella asiatica has known as medical plant that used for treating bruises and reducing swelling. From the previous research lately, it reported that *C.asiatica* has properties to improve memory recognition and promote healthy skin. *C.asiatica* is herbal plant that available in the market, it has been developed to enhance the amount of antioxidant. Therefore, this study was aimed to determine the most effective brewing process of *C.asiatica* tea and study the amount of antioxidant activities. The temperature was vary with 80 °C, 85 °C, and 90 °C and time was 2, 3, 4, and 5 minutes. The formation of consuming tea was determined by 30 target panelists. The result showed that there was no significant difference among all temperature and time that were determined. The best temperature and time for brewing is 80 °C at 5 minutes because it saves energy and can extract the highest amount of antioxidant from herbal tea.

CCS Concepts

Applied computing → Life and medical sciences → Computational biology

Permission to make digital or hard copies of all or part of this work for personal or classroom use is granted without fee provided that copies are not made or distributed for profit or commercial advantage and that copies bear this notice and the full citation on the first page. Copyrights for components of this work owned by others than ACM must be honored. Abstracting with credit is permitted. To copy otherwise, or republish, to post on servers or to redistribute to lists, requires prior specific permission and/or a fee. Request permissions from Permissions@acm.org.

ICBBB '19, January 7–9, 2019, Singapore, Singapore

© 2019 Association for Computing Machinery.

ACM ISBN 978-1-4503-6654-0/19/01...\$15.00

DOI: <https://doi.org/10.1145/3314367.3314371>

Keywords

Centella asiatica; Herbal tea; Antioxidant activity; Brewing tea

1. INTRODUCTION

World population right now is an increasing median age. Meaning, it is a shift in the distribution of a country's population towards old ages. There are two demographic effects that affecting the world population. First, increasing in longevity causes the average age of the population by increasing the numbers of elderly people. Another factor is decreasing in fertility which reducing the population of babies. (Brunborg H., 2012)[1] According to data from World Population Prospects in the 2015 Revision [2], they expect that between 2015 and 2030, the number of people in the world aged 60 years or over is predicted to grow by 56 percent from 901 million to 1.4 billion by 2050[2]. *Centella Asiatica* is a plant from India and Southeast Asia known as Asian medicine. It prefers in riverbank and humid area. It comes up with spherical shape of leave and has long stem. *Centella Asiatica* is a creeping annual herb with soft tender leaves. The roots and leaves develop from nodes. *Centella Asiatica* is a very popular herb in India for longevity and mental function. It is used to decrease fatigue and depression. It energizes the central nervous system. The plant is also useful in repairing skin and connective tissues. *Centella Asiatica* is used in Indian system of disease treatment as diuretic, nerve tonic, alternative, memory enhancer and blood purifier [3]. Chemically been identified leading to therapeutic properties. Asiatic acid, asiaticoside, and madecassoside form the major constituents responsible for pharmacological value apart from being rich in flavonoids and terpenoids. other volatile compounds was found to be in a prominent amount in the essential oil of *C. asiatica*

on analysis with gas chromatography-mass spectrometry (GC-MS). Chemically of *Centella asiatica* been identified and it had 3 major as main compounds that is asiatic acid, asiaticoside and madecassoside which responsible for pharmacological value and also rich in flavonoid and terpenoids [4]. Neuroprotection aspect of *C. asiatica* involves enzyme inhibition, prevention of amyloid plaque formation in Alzheimer's disease, dopamine neurotoxicity in Parkinson's disease, and reducing oxidative stress [5]. Brewing become importance factor in hot beverages especially coffee and tea. These beverages easily effect when use different condition for brewing. For example, For Arabica and Robusta Natural blend (espresso coffee), 92 °C was the optimal water temperature. For Robusta Torrefacto blend (espresso coffee) the overall acceptability might lead to the selection of 88 °C as the ideal water temperature[6]. Therefore, the aim of this project is to study the appropriate brewing condition for *Centella asiatica* tea.

2. MATERIALS AND METHODS

2.1 To Determine the Most Effective Brewing Condition of *Centella Asiatica* Tea

2.1.1 Procedure

Centella asiatica was prepared with tea process. The time and temperature brewing was varied which the time was used 2, 3, 4 and 5 minutes. The temperature was used 80 °C, 85 °C and 90 °C. Tea brewing was divided into 4 sets base on the time. Set 1, boiled water 150 ml will be prepared for 3 cups; the first tea bag was dropped at 90 °C for the first hot water and count the time for 5 minutes. After that, the second tea bag was dropped at 85 °C. The last tea bags of set one will be dropped at 80 °C. Serving temperature of tea was used between 65 – 75 °C. For other sets will be brewing as same as the set 1 respectively, that was 4, 3 and 2 minutes.

2.1.2 Sensory Analysis

There were 30 panelists that age between 50 – 75 years old participated in the test whose can be male or female. 2 grams of *Centella asiatica* dried leave was put in tea bag. Each panelist was received 50 ml of sample. The tea sample was served at room temperature. The herbal tea bag was shaking for 10 times before take out.

2.1.3 Chemical Analysis

The *Centella asiatica* tea was determined amount of antioxidant activities. The basic methods were used. The modified Folin-Ciocalteu method[7], DPPH radical scavenging[8] and Ferric reducing antioxidant potential assay[9] were used for evaluating antioxidant activity.

2.1.3.1 Antioxidant Activity by Determine Total Phenolic Content

The tea sample 20 µl of 10 mg/ml was mixed with 1.58 ml of distilled water and 100 µl Folin-Ciocalteu phenol reagent [7]. The samples were stood for 8 minutes 30 seconds at room temperature. Then, add 300 µl saturated sodium carbonate solution and incubated in dark place at room temperature for 30 minutes. After that, the test samples will be observed the optical density (OD) at 765 nm. The data was calculated as microgram garlic acid equivalent (µgGAE/ml). The experiment was done in triplicate[11].

2.1.3.2 Antioxidant Activity by DPPH Radical Scavenging Activity

DPPH radical scavenging activity assay[8]. This assay uses to show free radical scavenging activity between DPPH solvent (2, 2-diphenyl -1-picrylhydrazyl) and an antioxidant. Tea

sample 2 µl was mixed with 2 ml of methanol. Then, DPPH was mixed with 100 ml of methanol. After that, volume of DPPH reagent was varied with the volume of tea sample. The varied sample was leaved in the dark place for 30 minutes. The test samples was measured the optical density (OD) at 517 nm. The result will be expressed as percentage reduction of DPPH. All measurements should analyze in triplication and three replications

$$\% \text{ reduction of DPPH} = 100 \left(\frac{A_0 - A_c}{A_0} \right) \quad (1)$$

Where A_0 is the initial absorbance and A_c is the value for add sample concentration.

2.1.3.3 Antioxidant Activity by Ferric Reducing Antioxidant Potential Assay (FRAP)

The tea sample was used for 2 µl mixed with FRAP reagent[9] 1,000 µl, mix well. The mixture was kept in the dark place at room temperature for 30 minutes. After that, the mixture solution was measured the optical density (OD) at 593 nm. The value will be calculated as mmol Fe^{2+} /mg of sample. All measurements should analyze in triplication and three replications. FRAP reagent is mixture between sodium acetate buffer pH 3.6, Iron chloride and 2, 4, 6 tripyridyl-s-triazine.

2.1.4 Statistical Analysis

Data of survey information were processes using SAS version 9.4 (Copyright © [2017] SAS Institute Inc., Cary, NC, USA.), Factorial design with Randomized Complete Block Design (RCBD) was applied as experimental design. The data in this experiment was analyzed by using ANOVA (analysis of variance) and the multiple comparison Turkey to find the most effective factors to consumer ($p < 0.05$) The sensory testing was used about liking score with 9 point hedonic scale.

3. RESULT AND DISCUSSION

3.1 To Determine the Most Effective Brewing Process of *Centella Asiatica* Tea

3.1.1 Sensory Analysis

Table 1. Liking score of *Centella asiatica* tea in different conditions from 30 consumers in 10 attributes

Attribute	Time(minute)		
	2		
Temperature (°C)	80	85	90
Overall liking ^{ns}	7.0 ±0.9	6.7 ±1.3	6.4±1.2
Color ^{ns}	6.9 ±1.2	6.7 ±1.4	8.8±1.3
Green Aroma ^{ns}	6.8 ±1.0	6.7 ±1.1	6.1±1.4
Roast Aroma ^{ns}	6.6 ±1.0	6.6±1.2	5.8±1.3
Green Flavor ^{ns}	6.9±1.1	6.4±1.4	6.0±1.3
Roast Flavor ^{ns}	7.1±0.6	6.4±1.3	6.1±1.0
Sweetness ^{ns}	6.9±1.0	6.9±1.5	6.2±1.2
Bitterness ^{ns}	7.2±0.8	6.9±1.5	6.5±1.0
Green Aftertaste ^{ns}	7.0±0.9	6.6±1.4	6.9±0.9
Astringent ^{ns}	7.2±0.9	6.7±1.5	6.8±1.0
Attribute	Time(minute)		
	3		
Temperature (°C)	80	85	90
Overall liking ^{ns}	6.9±1.2	6.4±1.0	6.6 ± 1.0

Color ^{ns}	7.0±1.1	7.0±1.1	6.8 ±1.2
Green Aroma ^{ns}	7.0±1.1	6.9±1.0	6.4 ±1.1
Roast Aroma ^{ns}	6.8±1.3	6.0±0.9	6.5 ±0.8
Green Flavor ^{ns}	7.3±1.2	6.6±4.0	6.5 ±1.2
Roast Flavor ^{ns}	6.8±1.2	6.6±1.0	6.4 ±1.4
Sweetness ^{ns}	7.3±0.8	6.3±1.3	6.5 ±1.1
Bitterness ^{ns}	7.0±0.8	6.8±1.3	6.7 ±1.0
Green Aftertaste ^{ns}	7.3±0.6	6.8±1.1	7.1 ±0.8
Astringent ^{ns}	7.3±0.9	7.0±1.1	7.0 ±0.7
Attribute	Time(minute)		
	4		
Temperature (°C)	80	85	90
Overall liking ^{ns}	6.8±1.2	6.5 ±1.1	6.8 ±1.0
Color ^{ns}	6.9±1.3	7.0 ±1.0	7.0 ±1.0
Green Aroma ^{ns}	6.6±1.3	6.6 ±1.1	6.9 ±1.1
Roast Aroma ^{ns}	6.9±1.2	6.3 ±1.0	6.7 ±0.8
Green Flavor ^{ns}	6.4±1.1	6.4±1.1	6.5±1.1
Roast Flavor ^{ns}	6.4±1.0	6.4±1.0	6.6±1.3
Sweetness ^{ns}	6.6±1.3	6.6±1.3	6.6±1.2
Bitterness ^{ns}	6.6±1.4	6.6±1.4	6.9±1.2
Green Aftertaste ^{ns}	6.6±1.2	6.6±1.2	6.8±1.0
Astringent ^{ns}	6.8±1.4	6.8±1.4	6.9±1.0
Attribute	Time(minute)		
	5		
Temperature (°C)	80	85	90
Overall liking ^{ns}	6.6 ±1.4	6.7 ±1.1	2.4 ±1.1
Color ^{ns}	6.8 ±1.1	7.0 ±1.3	6.7 ±1.0
Green Aroma ^{ns}	6.6 ±1.1	6.9 ±1.2	6.7 ±1.0
Roast Aroma ^{ns}	6.3 ±1.2	6.6 ±1.0	6.6 ±0.8
Green Flavor ^{ns}	6.2±1.4	6.6±1.1	6.7±1.1
Roast Flavor ^{ns}	6.3±1.4	6.8±1.1	6.7±0.8
Sweetness ^{ns}	6.0±1.7	6.8±1.0	6.6±1.0
Bitterness ^{ns}	6.5±1.5	6.7±1.0	6.6±1.0
Green Aftertaste ^{ns}	6.5±1.5	6.8±0.9	6.6±1.2
Astringent ^{ns}	6.7±1.5	6.8±0.9	7.7±4.2

The result showed that there was no significant difference ($p>0.05$) in all time and temperature for brewing process (see Table 1). The highest mean score of brewing from overall liking is 80 °C with 2 minutes (7.0 ±0.9). From this testing can see that the liking score is decrease when they use more time for brewing the tea. Moreover, this condition also gets highest mean score in color (6.9 ±1.2), roasted flavor (7.1±0.6) and bitterness (7.2±0.8). But when the sample was brewed temperature at 80 °C with 3 minutes get more attributes than using 2 minutes for brewing that is green aroma (7.0 ± 1.1), green flavor (7.3±1.2), sweetness (7.3±0.8) and green aftertaste (7.3±0.6). Astringent give highest mean score (7.7±4.2) when brewed at 90 °C with 5 minutes. Heating can help in astringent,

focusing on tannin compound (give astringent feeling) which heating can reduce the level of tannin in winged bean. [11-13]. From other research said that green tea was brewed with water at 50 °C or 70 °C, the flavour intensity of seaweed did not change. But when brewing at 95 °C the intensity of seaweed flavour in the tea was lower than the intensity of tea brewed with 50 °C or 70 °C water. The intensity of straw-like flavour increased as the water temperature increased. [14]

3.1.2 Chemical Analysis

Herbs are rich in phenolic compounds which are active compound and act as antioxidant properties. *Centella asiatica* also has active compounds such as triterpenes [15] and polyphenols [16] which contains high total phenolic contents. There are no significant differently ($p>0.05$) in antioxidant activities (see Table 2). Total phenolic content was determined with standard garlic acid in term of µg/ml dried weight. The highest antioxidant activity represented by amount phenolic compound that is 2.5±1.8 µg/ml dried weights which use 85 °C with 5 minutes. This condition also gets highest in Ferric reducing antioxidant that is 2.5±1.8 mmol Fe²⁺. For DPPH assay is significantly different in all processes that the highest mean is 2.6±1.9 µg/ml which used 90 °C with 5 minutes. From the result can see that time to brewing is effect to the sample by let it extract with water or soaking for long time can get more antioxidant in total phenolic content, ferric reducing and DPPH. However, the result of commercial tea bag compared with tea bag that used in the experiment showed that there was the same. Brewing long time and high temperature can extract more antioxidant and intensity of tea [17]. For example, Brewing white tea at 98 °C for 7 min is the best condition to obtain a high content of antioxidant polyphenols and pleasant sensory properties. [18] Moreover, brewing time also important in tea infusion which brew tea for 3, 4 and 5 minutes get more antioxidant activity and phenolic content than brew tea for 1 minute. [19]

Table 2. Result of Total phenolic content, Ferric reducing antioxidant potential and DPPH radical scavenging of *Centella asiatica* tea from brewing different condition

Temperature (°C)	Time (min)	TPC ^{ns} µg/ml	FRAP ^{ns} mmol Fe ²⁺	DPPH ^{ns} µg/ml
80	2	1.4±0.9	1.4±1.0	0.1±0.0
80	3	1.0±0.3	1.0±0.3	0.2±0.0
80	4	1.3±0.2	1.3±0.2	0.2±0.1
80	5	2.2±2.3	2.2±2.3	0.6±0.1
85	2	1.5±0.3	1.5±0.3	0.4±2.5
85	3	1.3±0.3	1.3±0.4	0.2±0.0
85	4	1.6±0.3	1.6±0.3	0.2±0.0
85	5	2.5±1.8	2.5±1.8	1.8±0.5
90	2	1.2±1.1	1.2±1.1	0.3±0.1
90	3	1.1±0.2	1.2±0.2	0.5±0.2
90	4	1.6±0.6	1.7±0.6	0.8±0.4
90	5	2.2±0.6	2.1±0.6	2.6±1.9

4. CONCLUSION

Centella asiatica tea was developed to be functional herbal tea which improved for the people. Only *C. asiatica* tea can help to promote skin and improve memory and intelligence. The temperature and time for brewing tea do not affect the amount of antioxidant much so that the appropriate brewing temperature 80 °C and time for 5 minutes for brewing tea use less energy and get more intensity. This condition is not quite different in amount of antioxidant activity with 85 °C and time for 5 minutes.

5. ACKNOWLEDGE

The authors would like to thank National Research Council of Thailand (NRCT) for the financial support of this research. This work was financially supported by King Mongkut's University of Technology, North Bangkok (Research University Grant No. KMUTNB-61-GOV-01-55).

6. REFERENCE

- [1] Brunborg, H. Increasing life expectancy and the growing elderly population, 22, (2012)
- [2] United Nations, Department of Economic and Social Affairs, Population Division. World Population Ageing 2015
- [3] Sakshi Singh, *Centella asiatica* (L.): A Plant With Immense Medicinal Potential But Threatened, *International Journal of Pharmaceutical Sciences Review and Research*, 4, Issue 2, October 2010
- [4] Roy D. C., Barman S. K., Shaik M. M. *Centella asiatica*: Phytochemistry, pharmacology and traditional uses, 4, Pages 70-7, 2013
- [5] Orhan I. E. *Centella asiatica* (L.) Urban: From traditional medicine to modern medicine with neuroprotective potential. *Evid Based Complement Altern Med* (2012)
- [6] Susana Andueza , Laura Maeztu, Luc í Pascual, Carmen Ib áñez, M Paz de Pe ña. Influence of extraction temperature on the final quality of espresso coffee. *Journal of the Science of Food and Agriculture*, 83, Issue3, Pages 240-248 (2003)
- [7] Ragazzi, E.; Veronese, G. Quantitative analysis of phenolic compound after thin-layer chromatographic separation. *J. Chromatogr. A.* (1973)
- [8] Brand-Williams, W.; Cuvelier, ME.; Berset, C. Use of a free radical method to evaluate antioxidant activity. *LWT-Food Science and Technology.* (1995)
- [9] Benzie, I. F. and Strain, J. J. Ferric reducing/ antioxidant power assay: Direct measure of total antioxidant activity of biological fluids and modified version for simultaneous measurement of total antioxidant power and ascorbic acid concentration. *Methods Enzymol.* (1999)
- [10] Samtram S. Effect of heat treatments of antinutritional factors and quality of protein in winged bean. *Journal of the science of food and agriculture*, 39, 267-275 (1987)
- [11] Kesornbuakao & Yasuri.; The Development of *Centella asiatica* Extract-Loaded BSA Nanoparticles Production to Improve Bioavailability, *Orient. J. Chem.*, 32(5), 2425-2434 (2016)
- [12] Liang, Y., Zhang, L., & Lu, J. A study on chemical estimation of pu-erh tea quality. *Journal of the Science of Food and Agriculture*, 85, 381–390 (2005)
- [13] Zhang, J., Zhang, Z. Z., Zhou, Y. B., Ling, T. J., & Wan. Chinese dark teas: Postfermentation, chemistry and biological activities. *Food Research International* 53, 600-607 (2013)
- [14] J. Lee and D. H. Chambers, Sensory descriptive evaluation: brewing methods affect flavour of green tea, *Asian Journal Food and Agr-Industry*, 2, Issue 4, Pages 427-439 (2009)
- [15] Rattanakom, S.; Yasurin, P. Antibacterial activity, antioxidant activity and chemical profiling of *Centella asiatica* under different extraction solvents. *Orient. J. Chem* 31, page 2453-2459 (2015)
- [16] Zainol A, Hamid S, Yusof R, Muse. Antioxidative activity and total phenolic compounds of leaf, root and petiole of four accessions of *Centella asiatica* (L.) Urban. *Food Chemistry.* 81, 575-581(2003)
- [17] Leila N., et al., Effect of Different Brewing Times on Antioxidant Activity and Polyphenol Content of Loosely Packed and Bagged Black Teas (*Camellia sinensis* L.). 6, Issue 3, Pages 313-321 (2016)
- [18] S. Pérez-Burillo, R. Giménez, J.A. Rufián-Henares, S. Pastoriza. Effect of brewing time and temperature on antioxidant capacity and phenols of white tea: Relationship with sensory properties. *Food Chemistry*, 248, Pages 111-118, (2018)
- [19] Zeinab Nikniaz et al, Effect of different brewing times on antioxidant activity and polyphenol content of loosely packed and bagged black teas (*Camellia sinensis* L.), *Avicenna Journal of Phytomedicine*, Vol 6, No. 3, May-June (2016)

β -Cyclodextrin Inclusion Complex with Dimethyl[4-hydroxypiperidin-4-yl]Phosphonates as Green Plant Growth Stimulators

A. Ye. Malmakova,
V. K. Yu

Institute of Chemical Sciences
106, Walikhanov Str., Almaty, 050010,
Kazakhstan
+7 727 291 2464
malmakova@mail.ru,
yu_vk@mail.ru

N. U. Kystaubayeva,
A. G. Zazybin

Kazakh-British Technical University
59 Tole-bi street, Almaty,
050000, Kazakhstan
+7 727 2915784
k.nurjamal@mail.ru,
azazybin@mail.com

T. E. Li

Institute of Plant Biology and
Biotechnology
45, Timiryazev Str., Almaty
050040, Kazakhstan
+7 777 684 4924
tamaralee05@gmail.com

ABSTRACT

Herein we report on the synthesis of new dimethyl [1-(benzyl-, 2-phenylethyl-) 4-hydroxypiperidin-4-yl]phosphonates obtained by reacting 1-(benzyl- or 2-phenylethyl-)piperidone-4 with dimethylphosphite in presence of sodium methylate in hexane. NMR spectroscopy showed that the complexation of β -cyclodextrin (β -CD) (**host**) with the hydroxyphosphonate (**guest**) is accompanied by the entry of a hydrophobic aromatic fragment of the substrate molecule into the inner sphere of the host molecule. In addition, the supramolecular interaction of the hydrophilic part of the guest molecule with the outer surface of β -CD is shown. As a result, a 1:1 complex is formed. Dimethyl [1-(benzyl-, 2-phenylethyl-)4-hydroxypiperidin-4-yl]phosphonates showed perceptible stimulation of growth and development of stems and/or roots of spring wheat *Triticum aestivum* Kazakhstanskaya-10, Severyanka and Miras.

CCS Concepts

Applied computing \rightarrow Physical sciences and engineering \rightarrow Chemistry

Keywords

Design; Experimentation; Verification; dimethyl [1-(benzyl, 2-phenylethyl)-4-hydroxypiperidin-4-yl]phosphonates; β -CD inclusion complex: growth of stems and roots of spring wheat

1. INTRODUCTION

One of the most intensively developing areas of supramolecular chemistry is the preparation and study of inclusion complexes of biologically active compounds (BAC) with cyclodextrins (CD) [1-3]. It had been known that these complexes make it possible to regulate the solubility of BAC in water, reduce toxicity, permit the transfer of liquid substances to solid substances, and also increase

Permission to make digital or hard copies of all or part of this work for personal or classroom use is granted without fee provided that copies are not made or distributed for profit or commercial advantage and that copies bear this notice and the full citation on the first page. Copyrights for components of this work owned by others than ACM must be honored. Abstracting with credit is permitted. To copy otherwise, or republish, to post on servers or to redistribute to lists, requires prior specific permission and/or a fee. Request permissions from Permissions@acm.org.

ICBBB '19, January 7–9, 2019, Singapore, Singapore

© 2019 Association for Computing Machinery.

ACM ISBN 978-1-4503-6654-0/19/01...\$15.00

DOI: <https://doi.org/10.1145/3314367.3314381>

the stability of substances to oxidation and hydrolysis [4-6]. The choice of dimethyl[1-(benzyl- or 2-phenylethyl)-4-hydroxypiperidin-4-yl]phosphonates as a substrate for supramolecular self-assembly with β -CD is due to the fact that there were found promising biologically active compounds in a family of piperidine derivatives [7, 8] and piperidine hydroxyphosphonates [9,10]. The increased interest in CDs is due to their cyclic structure and the ability to form supramolecular host-guest inclusion complexes with a variety of hydrophobic substrates due to the internal cavity. The attractiveness of CD as host molecules is explained by their availability and non-toxicity [11]. In supramolecular chemistry, the determining role is played by the size and shape or geometric complementarity of the interacting components, therefore β -CD is chosen to obtain the inclusion complex with dimethyl[1-(benzyl-, 2-phenylethyl)-4-hydroxypiperidin-4-yl]phosphonates

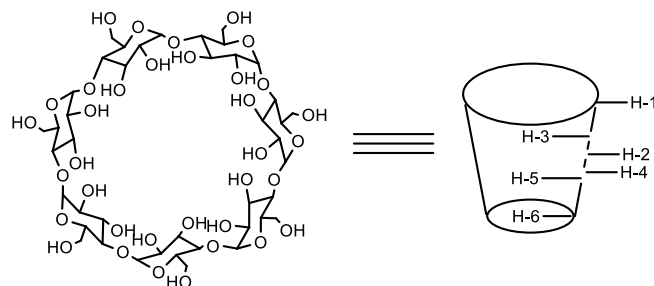


Figure 1. β -Cyclodextrin

Manuscript received on September 20, 2018. This work supported by Ministry of Education and Science of Republic of Kazakhstan under Grants AP05131025|GF5 and AP05131486|GF5.

A. E. Malmakova is with the Institute of Chemical Sciences named after A.B. Bekturov, Walikhanov Str., 106, Almaty 050010, Kazakhstan (e-mail: malmakova@mail.ru).

N. U. Kystaubayeva is with the Kazakh-British Technical University, 59 Tole-bi street, Almaty, 050000, Kazakhstan (e-mail: k.nurjamal@mail.ru).

V. K. Yu is with the Institute of Chemical Sciences named after A.B. Bekturov, Walikhanov Str., 106, Almaty 050010, Kazakhstan (e-mail: yu_vk@mail.ru).

A. G. Zazybin is with the Kazakh-British Technical University, 59 Tole-bi street, Almaty, 050000, Kazakhstan (e-mail: azazybin@yahoo.com).

T. E. Li is with the Institute of Plant Biology and Biotechnology, 45, Timiryazev Str., Almaty, 050040, Kazakhstan (tamaralee05@gmail.com).

2. SYNTHESIS OF DIMETHYL[1-(BENZYL-, 2-PHENYLETHYL-)-4-HYDROXYPIPERIDIN-4-YL]PHOSPHONATES

In the current work, dimethyl[1-(benzyl- or 2-phenylethyl)-4-hydroxypiperidin-4-yl]phosphonates and their supramolecular β -CD form were synthesized in order to investigate for all of them a plant growth stimulator and an immunocorrector activity. The structure of hydroxyphosphonates and complexes is established by NMR spectroscopy. The desired dimethyl[1-(benzyl- or 2-phenylethyl)-4-hydroxypiperidin-4-yl]phosphonates was prepared by reacting corresponding piperidone-4 with dimethyl phosphite in the presence of sodium methylate in 48% yield and 78% yield, respectively.

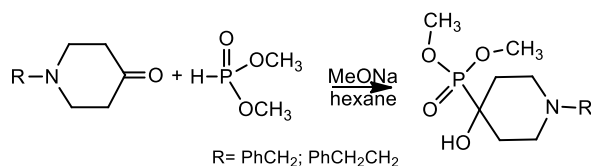


Figure 2. Synthesis of hydroxyphosphonates

Purification of the product was carried out by crystallization from hexane. Hydroxyphosphonates are crystalline substances with mp. 112-13 and 118-21 °C.

In the ¹H NMR spectrum (Table 1) of dimethyl[1-(2-phenylethyl)-4-hydroxypiperidin-4-yl] phosphonate, recorded in CDCl₃, strong-field multiplet signals are observed at 1.87-1.91 and 1.98-2.04 ppm corresponding to axial H^{3a,5a} and equatorial protons H^{3e,5e} of the piperidine ring. The multiplet signal in the form of an asymmetric triplet at 2.43-2.48 ppm. resonates the axial protons of the piperidine ring H^{2a,6a}. The remaining equatorial piperidine protons H^{2e,6e} and methylene protons H⁸ after superimposing signals appear as a multiplet in the area of 2.78-2.78 ppm. Multiplet in the area of 2.58-2.63 ppm. is attributed to the protons of the methylene bridge H⁷, singlets at 3.78 and 3.81 ppm. - to the hydrogen of the methoxy groups H¹⁷ and H²⁰, respectively. In the aromatic region of the spectrum, the multiplets at 7.18-7.20 and 7.25-7.29 ppm. correspond to the phenyl protons H^{11,12,13} and H^{10,14}. The hydroxyl proton H¹⁸ represents a broadened singlet at 3.94 ppm.

In the ¹³C NMR spectrum (Table 1), the piperidine ring signals are observed at 31.72 (C^{3,5}), 47.59 (C^{2,6}), and 69.38 (C⁴) ppm. When broadband proton decoupling is used, because of the conservation of spin-spin interactions of ¹³C-³¹P through one, two and three bonds, the singlet carbon signals are split into doublet ones with a consequent decrease in the value of J_{C-P} from the C⁴ atom to the carbon atoms C^{3,5} and C^{2,6}. Carbon atoms of methoxy groups C^{17,20} resonate at 53.75 ppm, methylene carbon atoms at 33.80 (C⁸) and 60.77 (C⁷) ppm. In the aromatic region, carbon signals of the phenyl substituent are observed at 126.12 (C¹²), 128.49 (C^{11,13}), 128.79 (C^{10,14}) and 140.47 (C⁹) ppm.

The structure of the compound was also confirmed by the two-dimensional NMR spectroscopy COZY (¹H-¹H) and HMQC (¹H-¹³C), which makes it possible to establish spin-spin interactions of a homonuclear and heteronuclear nature. The observed correlations in the molecule are presented in the Figure 3.

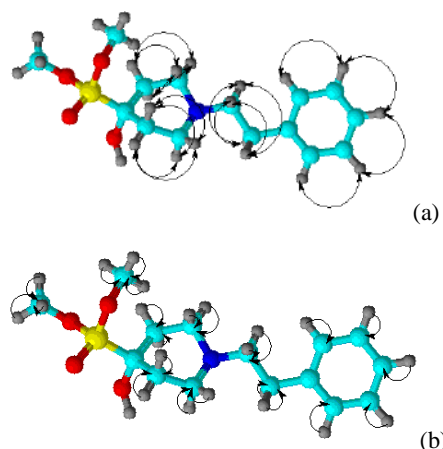


Figure 3. Correlations in COZY (a) and HMQC spectra (b)

In the ¹H-¹H COZY spectra of the compound, the spin-spin correlations through three bonds of protons belonging to neighboring methylene groups of the piperidine cycle and phenyl ring H^{3,5}-H^{2,6} (1.89, 2.05 and 2.08, 1.89; 1.99, 2.45 and 2.43, 2.00; 2.01, 2.79 and 2.00, 2.43; 2.43, 2.79 and 2.80, 2.47), H⁷-H^{2,6} (2.58, 2.78 and 2.78, 2.60) and H^{11,12,13}-H^{10,14} (7.19, 7.29 and 7.29, 7.19) are observed.

Heteronuclear interactions of protons with carbon atoms through a single bond were established using spectroscopy ¹H-¹³C HMQC for the following pairs: H^{3,5}-C^{3,5} (1.87, 31.71 and 2.00, 31.59), H^{2,6}-C^{2,6} (2.45, 47.62 and 2.79, 47.49), H⁸-C⁸ (2.83, 33.71), H⁷-C⁷ (2.57, 60.82), H^{17,20}-C^{17,20} (3.78, 53.78), H^{10,14}-C^{10,14} (7.19, 128.71), H^{11,12,13}-C^{11,12,13} (7.18, 126.17).

3. SYNTHESIS OF β -CD SUPRAMOLECULAR INCLUSION COMPLEX

A supramolecular inclusion complex is formed by mixing equimolecular amounts of ethanol solution of the corresponding hydroxyphosphonate with β -CD in water at room temperature, followed by evaporation of solvents at 50-55 °C.

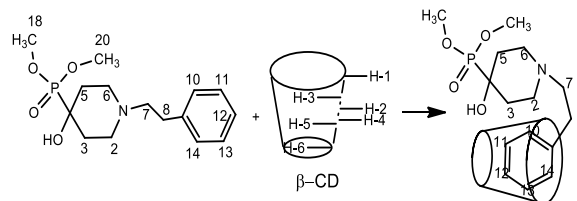


Figure 4. Formation of β -CD supramolecular inclusion complex with dimethyl[1-(2-phenylethyl)-4-hydroxypiperidin-4-yl]phosphonate

The investigation of supramolecular complexes via the NMR spectroscopy is based on the determination of the difference in the values of the chemical shifts ¹H and ¹³C of dimethyl[1-(2-phenylethyl)-4-hydroxypiperidin-4-yl]phosphonate, β -CD and complex. By the chemical shift values of internal or external protons of β -CD, it is possible to detect the formation of internal or external complexes, respectively. The change in chemical shifts of ¹H and ¹³C in the spectra of **guest** makes it possible to determine the direction of occurrence of the latter in the cavity of β -CD (**host**) [12, 13].

The comparison of ^1H NMR spectra of guest and the supramolecular complex recorded in D_2O shows that the protons H^{12} , $\text{H}^{11,13}$, and $\text{H}^{10,14}$ of the phenyl hydrophobic substituent, the piperidine protons $\text{H}^{3e,5e}$ and $\text{H}^{2a,6a}$, as well as methylene protons H^8 undergo the greatest screening due to the process of complexation of hydroxyphosphonate.

In the β -CD molecule, the maximum changes in the chemical shifts are observed for the proton H-3 host located in the internal hydrophobic cavity and the truncated cone of the proton H-4 located on the hydrophilic outer surface. It can be assumed that the greatest supramolecular interaction of “guest-host” molecules

is realized with the participation of the above protons during the formation of the inclusion complex according to the scheme:

Comparison of the integrated intensities of protons of β -CD and dimethyl[1-(2-phenylethyl)-4-hydroxypiperidin-4-yl]phosphonate in the complex indicates the formation of a supramolecular compound in which one molecule of the **host** belongs to one **guest** molecule.

A similar picture is observed in the NMR spectra of dimethyl[1-benzyl-4-hydroxypiperidin-4-yl]phosphonate, β -CD and their complex.

Table 1. The chemical shifts of ^1H and ^{13}C of phosphonate, β -CD (δ_0) and their complex (δ)

# H or C	Group CH_x	δ_0 , ppm		δ , ppm		$\Delta\delta = \delta - \delta_0$	
		^1H	^{13}C	^1H	^{13}C	^1H	^{13}C
dimethyl[1-(2-phenylethyl)-4-hydroxypiperidin-4-yl]phosphonate							
3 ^a ,5 ^a	CH_2	1.87-1.91	31.75	1.75-1.79	29.85	-0.12-(-0.12)	-1.65
3 ^e ,5 ^e		1.98-2.04		1.84-1.90		-0.14-(-0.14)	
2 ^a ,6 ^a	CH_2	2.43-2.48	47.59	2.24-2.38	46.64	-0.19-(-0.10)	-0.95
2 ^e ,6 ^e		2.78-2.81		2.78-2.80		0-(-0.10)	
4	>C<	-	69.38	-	68.52	-	-0.86
8	CH_2	2.78-2.81	33.80	2.66-2.68	32.04	-0.12-(-0.12)	-1.76
7	CH_2	2.58-2.63	60.77	2.53-2.55	59.88	-0.05-(-0.08)	-0.89
17	CH_3	3.78	53.75	3.70	54.44	-0.08	0.69
20	CH_3	3.81	53.75	3.72	54.44	-0.09	0.94
12	CH	7.18-7.20	126.12	7.04-7.05	126.56	-0.14-(-0.15)	0.44
11, 13	CH	7.18-7.20	128.49	7.04-7.05	128.44	-0.14-(-0.15)	-0.05
10, 14	CH	7.25-7.29	128.79	7.14-7.15	128.44	-0.11-(-0.14)	-0.35
9	>C<	-	140.47	-	139.35	-	-1.12
β -CD							
1	CH	4.87	102.43	4.89	102.11	0.02	-0.32
2	CH	3.45	72.87	3.48	72.00	0.03	-0.87
3	CH	3.77	73.54	3.70	73.32	-0.07	-0.22
4	CH	3.39	82.00	3.45	80.93	0.06	-1.07
5	CH	3.68	72.52	3.65	72.00	-0.03	-0.52
6	CH_2	3.68	60.40	3.68	59.88	-0.03	-0.52

In the β -CD molecule, the maximum changes in the chemical shifts are observed for the proton H-3 host located in the internal hydrophobic cavity and the truncated cone of the proton H-4 located on the hydrophilic outer surface. It can be assumed that the greatest supramolecular interaction of “guest-host” molecules is realized with the participation of the above protons during the formation of the inclusion complex according to the scheme:

Comparison of the integrated intensities of protons of β -CD and dimethyl[1-(2-phenylethyl)-4-hydroxypiperidin-4-yl]phosphonate in the complex indicates the formation of a supramolecular compound in which one molecule of the **host** belongs to one **guest** molecule.

A similar picture is observed in the NMR spectra of dimethyl[1-benzyl-4-hydroxypiperidin-4-yl]phosphonate, β -CD and their complex.

4. BIOSCREENING OF DIMETHYL[1-(BENZYL-, 2-PHENYLETHYL-)-4-HYDROXYPIPERIDIN-4-YL]PHOSPHONATES ON SAMPLES OF SPRING WHEAT

The studies were carried out on model samples of spring wheat *Triticum aestivum* *Kazakhstanskaya-10*, *Severyanka* and *Miras*. *Severyanka* and *Miras* are drought tolerant varieties, and the *Kazakhstanskaya-10* was studied as a standard. There was a significant stimulation of growth and development of wheat seedlings of all three tested varieties with both hydroxyphosphonates - stems by about 30%, roots by 20-30% (Tabl.2.)

Table 2. Biometric data of wheat of three varieties in the control and in the presence of SAV-2 and SAV-3; n = 15

Wheat	Kazakhstanskaya -10		Severyanka		Miras	
	Height, cm	Root length, cm	Height, cm	Root length, cm	Height, cm	Root length, cm
Control	15,82 ±1,45	7,25 ±1,45	15,67 ±1,62	7,42 ±1,34	14,93 ±1,25	7,21 ±1,36
SAV-2	15,44 ±1,72	9,28 ±1,59 (28% *)	15,58 ±1,15	10,5 ±1,55 (41% *)	14,79 ±0,77	9,5 ±1,86 (31% *)
SAV-3	18,27 ±0,8 (25% *)	9,97 ±0,81 (18% *)	16,77 ±1,64 (35% *)	9,08 ±2,24 (22% *)	16,12 ±1,16 (30% *)	7,29 ±2,21

Note: * - of stimulation

5. EXPERIMENTAL PART

IR spectra were recorded on a spectrometer «Nicolet 5700 FT-IR» in the tablet with KBr. NMR spectra of synthesized compounds were recorded at «JNM-ECA 400» («Jeol» company) spectrometer with an operating frequency of 399.78 MHz (^1H) and 100.53 MHz (^{13}C) on carbons in CDCl_3 or D_2O at 25°C . Monitoring of the reactions and the individual compounds were done by Thin Layer Chromatography (TLC) on Al_2O_3 . Separation and purification of the substances was performed using crystallization from hexane.

5.1 General Procedure

Dimethyl[1-(benzyl-, 2-phenylethyl)-4-hydroxy-piperidin-4-yl]phosphonate. To the cooled (10°C) stirred solution of 0.0246 mol of 1-(benzyl- or 2-phenethyl)piperidin-4-one and 0.0246 mol of dimethyl phosphite in 20 ml hexane 0.7 ml of the sodium methoxide solution was slowly added dropwise at such a rate that the temperature of the reaction mixture does not rise above 30°C . The reaction solution was stirred at room temperature for 4 h. In the process of the dropwise addition of CH_3ONa the precipitate formation was observed which then was filtered off, washed with hexane, and dried in a vacuum desiccator.

Yield 3.54 g (48.1%) of dimethyl[1-(2-phenylethyl)-4-hydroxypiperidin-4-yl]phosphonate as a white solid. T_{melt} $112-113^\circ\text{C}$. IR (KBr), cm^{-1} : 3368.4 (O-H); 2927.4 (C-H_{arom.}), 1652.7 (C-C_{arom.}), 1419.6 (C-N), 1156.7 (P-O), 1031.4 (P=O). Calculated for $\text{C}_{14}\text{H}_{22}\text{NO}_4\text{P}$, %: C, 56.18; H, 7.41; N, 4.68; O, 21.38; P, 10.35. Found, %: C, 56.03; H, 7.38; N, 4.90; P, 10.23.

Yield 6.04 g (78.2%) of dimethyl(1-benzyl)-4-hydroxy-piperidin-4-yl]phosphonate as a white solid. T_{melt} $118-121^\circ\text{C}$. IR (KBr), cm^{-1} : 3333.0 (O-H); 2928.5 (C-H_{arom.}), 1654.0 (C-C_{arom.}), 1454.0 (C-N), 1156.1 (P-O), 1033.5 (P=O). Calculated for $\text{C}_{15}\text{H}_{24}\text{NO}_4\text{P}$, %: C, 57.50; H, 7.72; N, 4.47; O, 20.43; P, 9.89. Found, %: C, 57.33; H, 7.48; N, 4.39; P, 10.03.

Complex of dimethyl[1-(benzyl-, 2-phenylethyl)-4-hydroxypiperidin-4-yl]phosphonate with β -CD. To a solution of 0.0015 mol of dimethyl[1-(benzyl-, 2-phenylethyl)-4-hydroxypiperidin-4-yl]phosphonate in 20 ml of ethanol with

stirring, add 1.7 g (0.0015 mol) of β -CD dissolved in 40 ml of distilled water. The mixture is placed in a drying oven ($50-55^\circ\text{C}$) for evaporation of ethanol and water.

Yield 2.10 g (97.8%) of complex of dimethyl 1-benzyl-4-hydroxypiperidin-4-yl]phosphonate with β -CD as a white powder melting with decomposition above 250°C . Calculated for $\text{C}_{56}\text{H}_{92}\text{NO}_{39}\text{P}$, %: C, 46.89; H, 6.47; N, 0.98; O, 43.51; P, 2.16. Found, %: C, 47.00; H, 6.56.

Yield 2.09 g (96.2%) of complex of dimethyl[1-(2-phenylethyl)-4-hydroxypiperidin-4-yl]phosphonate with β -CD as a white powder melting with decomposition above 250°C . Calculated for $\text{C}_{57}\text{H}_{94}\text{NO}_{39}\text{P}$, %: C, 47.27; H, 6.54; N, 0.97; O, 43.08; P, 2.14. Found, %: C, 47.13; H, 6.68.

6. CONCLUSION

Thus, there had been synthesized dimethyl[1-(benzyl-, 2-phenylethyl)-4-hydroxypiperidin-4-yl]phosphonates and their complexation behavior with β -CD was studied. The phosphonate molecules react by its hydrophobic part with the host hydrophobic surface, and the more hydrophilic part of guest molecule is located close to the external hydrophilic part of β -CD.

Bioscreening on seeds and seedlings of spring wheat of three varieties: *Kazakhstanskaya-10*, *Severyanka* and *Miras* showed significant stimulation of growth and development in presence of hydroxyphosphonates - stems by about 30% and roots by 20-30%.

7. ACKNOWLEDGMENTS

Our thanks to Ministry of Education and Science of the Kazakhstan for grants: AP05131025 and AP05131486.

8. REFERENCES

- Malenkovskaya, M.A., Vasyanina, L.K., Grachev, M.K. 2015. NMR Spectroscopy Study of Complex Formation between Dimeric Derivative of β -Cyclodextrine and Some Pharmacologically Important Compounds. *Russ. J. Gen. Chem.* 85, 7 (July 2015), 1681-1685. DOI=<https://link.springer.com/article/10.1134/S1070363215070191>.
- Orgovan, G., Kelemen, H., Noszal, B. 2016. Protonation and β -cyclodextrin complex formation equilibria of fluconazole. *J. Incl. Phenom. Macrocycl. Chem.* 84, 3 (Apr. 2016), 189-196. DOI=<https://hungary.pure.elsevier.com/hu/publications/protonation-and-%CE%B2-cyclodextrin-complex-formation-equilibria-of-fl>.
- Li, J., Zhang, S., Zhou, Y., Guan, S., Zhang, L. 2016. Inclusion complexes of fluconazole with β -cyclodextrin and 2-hydroxypropyl- β -cyclodextrin in aqueous solution: preparation, characterization and a structural insight. *J. Incl. Phenom. Macrocycl. Chem.* 84, 3 (Feb. 2016) 209-217, DOI=https://www.researchgate.net/publication/293045164_Inclusion_complexes_of_fluconazole_with_beta-cyclodextrin_and_2-hydroxypropyl-beta-cyclodextrin_in_aqueous_solution_Preparation_characterization_and_a_structural_insight.
- Yanga, R., Chena, J.-B., Dai, X.-Y., Huang, R., Xiao, C.-F., Gao, Zh.-Y., Yang, B., Yang, L.-J., Yan, S.-J., Zhang, H.-B., Qing, Ch., Lin, J. 2012. Inclusion complex of GA-13315 with cyclodextrins: Preparation, characterization, inclusion mode and properties. *Carbohydr. Polym.* 89, 1 (June 2012), 89-97. DOI=<https://www.ncbi.nlm.nih.gov/pubmed/24750608>.

- [5] Yuan, Ch., Jin, Zh., Xu, X. 2012. Inclusion complex of astaxanthin with hydroxypropyl- β -cyclodextrin: UV, FTIR, ^1H NMR and molecular modeling studies. *Carbohydr. Polym.* 89, 2 (June 2012), 492-496. DOI=<https://www.sciencedirect.com/science/article/pii/S0144861712002469?via%3Dihub>.
- [6] Dandawate, P.R., Vyas, A., Ahmad, A., Banerjee, S., Deshpande, J., Swamy, K.V., Jamadar, A., Dumhe-Klaire, A.K. Padhye, S., Sarkar, F.H. 2012. Inclusion Complex of Novel Curcumin Analogue CDF and β -Cyclodextrin (1:2) and Its Enhanced In Vivo Anticancer Activity Against Pancreatic Cancer. *Pharm. Res.* 29, 7 (July 2012) 1775-1786. DOI=<https://link.springer.com/article/10.1007/s11095-012-0700-1>.
- [7] Kemelbekov, U.S., Hagenbach, A., Lentz, D., Imachova, Sh.O., Pichkhadze, G.M., Rustembekov, Zh.I., Beketov, K.M., Praliev, K.D., Gabdulkhakov, A., Guskov, A., Saenger, W. 2010. Pharmacology and structures of the free base of the anaesthetic kazcaine and its complex with β -cyclodextrin. *J. Incl. Phenom. Macrocycl. Chem.* 68, 3 (December 2010) 323-330. DOI=<https://link.springer.com/article/10.1007/s10847-010-9791-7>.
- [8] Iskakova, T.K., Ibrayeva, S.S., Praliyev, K.D., Malmakova, A.Ye., Baktybaeva, L.K., Seilkhanov, T.M. 2014. Synthesis and Myelostimulatory Activity of 1-(2-Ethoxyethyl) piperidine Derivatives. In *Procedia Chemistry of XV International Scientific Conference "Chemistry and Chemical Engineering in XXI century" dedicated to Professor L.P. Kulyov (Russia, 10, 2014)*, 358-363. DOI=<https://www.sciencedirect.com/science/article/pii/S1876619614001053>.
- [9] Yu, V.K., Praliev, K.D. 1997. 1-(2-Ethoxyethyl)-4-(dimethoxyphosphoryl)-4-hydroxypiperidine which possesses plant growth stimulating activity. *Preliminary Pat. 5011 RK. Bul.№3*, (Aug. 1995).
- [10] Dzhiembraev, B.Zh. 2003. α -Oxy- and β -aminophosphonates of six-membered (N, O, S, Se) heterocycles. *Monograph*. (Kazakhstan, Almaty, 2003), 234 p.
- [11] Nguyen, T.A., Liu, B., Zhao, J., Thomas, D.S., Hook, J.M. 2013. An investigation into the supramolecular structure, solubility, stability and antioxidant activity of rutin/cyclodextrin inclusion complex. *Food Chem.* 136, 1 (Jan. 2013), 186-192. DOI=<https://www.ncbi.nlm.nih.gov/pubmed/23017411>.
- [12] Nowakowski, M., Ejchart, A. 2014. Complex formation of fenchone with α -cyclodextrin: NMR titrations. *J. Incl. Phenom. Macrocycl. Chem.* 79, 3 (Aug. 2014), 337-342. DOI=<https://link.springer.com/article/10.1007/s10847-013-0356-4>.
- [13] Maheshwari, A., Sharma, M., Sharma, D. 2013. Complexation of sodium picosulphate with beta cyclodextrin: NMR spectroscopic study in solution. *J. Incl. Phenom. Macrocycl. Chem.* 77, 1-4. (Dec. 2013), 337-342. DOI=https://www.researchgate.net/publication/257581749_Complexation_of_sodium_picosulphate_with_beta_cyclodextrin_NMR_spectroscopic_study_in_solution.

Antimicrobial Activity of Lichens-Associated Actinomycetes Strain LC-23

Agustina E. Susanti

Department of Biology
Faculty of Mathematics and Natural Science
Universitas Indonesia, Depok, 16424, Indonesia
+6221 786 3436
agustina.laz@gmail.com

W. Mangunwardoyo

Department of Biology, Faculty of Mathematics and
Natural Science
Universitas Indonesia, Depok, 16424, Indonesia
62- 7270163
wibowo.mangun@ui.ac.id

Shanti Ratnakomala

Research Center for Biotechnology, Indonesian Institute
of Sciences
Jl. Raya Bogor Km. 46, Cibinong 16911
+62 (021) 8754587
shanti_ratna01@yahoo.com

Puspita Lisdiyanti

Research Center for Biotechnology, Indonesian Institute
of Sciences
Jl. Raya Bogor Km. 46, Cibinong 16911
+62 (021) 8754587
puspita.lisdiyanti@bioteknologi.lipi.go.id

ABSTRACT

Actinomycetes known as the largest antibiotic producer that has a broad range habitat. Research has been done to find a new antibiotic from the various habitats of actinomycetes. Lichens was the symbiotic structure of alga and fungi known as the ecological niche of various kinds of microbes including actinomycetes. The aim of this study in deep of isolate strain LC-23 for production of antimicrobial, characterize the metabolite profile of the ethyl acetate extract and identification based on 16S rRNA gene sequence analysis. The result revealed actinomycetes from lichen, strain LC-23 showed potency against Gram positive bacteria. Ethyl acetate extract of the strain showed positive inhibition against *Staphylococcus aureus* BTCC B-611 and *Micrococcus luteus* BTCC B-552. Minimum Inhibitory Concentration (MIC) of extract LC-23 was less than 2.106 ppm. The ethyl acetate extract was subjected to fractionation and tested against the pathogenic microbes and showed inhibition activity in column 9 and 10, and specifically in column 7E to 7G for *Staphylococcus aureus* BTCC B-611 and 7E-7H for *Micrococcus luteus* BTCC B-552. The identification based on 16S rRNA gene sequence showed strain LC-23 was 98.51% similarity to *Streptomyces palmae* type strain. Neighbor-joining phylogenetic tree confirmed the relationships of this strain to other members of *Streptomyces* genera.

CCS Concepts

Applied computing → Life and medical sciences → Computational biology

Keywords

Actinomycetes; Antimicrobial; Identification 16S srRNA gene;

© 2019 Association for Computing Machinery. ACM acknowledges that this contribution was authored or co-authored by an employee, contractor or affiliate of a national government. As such, the Government retains a nonexclusive, royalty-free right to publish or reproduce this article, or to allow others to do so, for Government purposes only.

ICBBB '19, January 7–9, 2019, Singapore, Singapore

© 2019 Association for Computing Machinery.

ACM ISBN 978-1-4503-6654-0/19/01...\$15.00

DOI: <https://doi.org/10.1145/3314367.3314386>

Lichens.

1. INTRODUCTION

The pharmaceutical industry was an implication of the bioprospecting development in human's life. Exploration various organisms as the drug sources has been developed to all biological taxa including Prokaryotes [1]. Ability to produce secondary metabolite was the important roles of Prokaryotes for humans. One function of Prokaryote's metabolite was to inhibit the growth of pathogenic microbes. The discovery of new drugs in academics and laboratory level has traditionally been focused on the exploitation of actinomycetes and filamentous fungi [2].

Actinomycetes as the highest producer of antibiotics from Prokaryotes have been known for decades [3]. Two third or approximately 80% of the world's antibiotics including the most important in medical treatment produce by actinomycetes in the genus of *Streptomyces* and *Micromonospora* [4]. The specific potency of actinomycetes in pharmaceutical as anti-infection [5] and anticandidal [6].

The enchantment for actinomycetes also caused by the broad habitat of these filamentous bacteria. Actinomycetes are kind of microorganisms that has the widest distribution in nature [4]. It's broad habitat urged some research to find new compound through invention of ecological niches that still rare to be explored. Invention of new source of actinomycetes being a good choice for pharmaceutical development [7]. Some studies have been conducted to isolate actinomycetes from new sources; endosymbiont of plant species [8], extreme habitats [9,10], and symbiosis of microorganisms such as lichen [1,11]

One source that interesting to be explored is lichens. Lichens are the symbiotic of alga/cyanobacteria and fungi [11]. The structure of this organisms made it possible to produce thousands of bioactive compounds [7]. Lichens also being habitat for various bacteria, that the roles in lytic activity was important to produce bioactive compound such as hormones or antibiotics to fulfill nitrogen requirement [12].

The aim of this study was to analyze strain LC-23 isolated from Indonesian lichen growth on the bark of *Averrhoa carambola* for production of antimicrobial, characterize the metabolite profile of

the ethyl acetate extract and identification based on 16S rRNA gene sequence analysis.

2. MATERIAL AND METHODS

2.1 Microorganism Used

Strain LC-23 was isolated from Lichen grown on the bark of *Averrhoa carambola* plant. The strain is grown in ISP2 medium and maintained in glycerol suspensions (20%, v/v) at -80 °C [7,11]. The strain was deposited in Research Centre for Biotechnology, Cibinong West Java. *Bacillus subtilis* BTCC B-612, *Escherichia coli* BTCC B-614, *Candida albicans* BTCC Y-33, *Staphylococcus aureus* BTCC B-611, *Micrococcus luteus* BTCC B-552 were used as pathogenic microbial testing. The growth medium of the bacterial testing was Nutrient Broth while *Candida* was Potato Dextrose Broth. All the microbial testing was grown for 18-24 hours. Morphological characterization was conducted by using light microscope and Scanning Electron microscope.

2.2 Screening Antimicrobial Activity of Strain

The actinomycete pure strain on ISP-2 agar medium was screened by agar diffusion method to determined antimicrobial potency. The microbial that used as indicator for the testing consists of three Gram positives bacteria: *Bacillus subtilis* BTCC B-612, *Micrococcus luteus* BTCC B-552, *Streptococcus aureus* BTCC B-611; Gram negative bacteria *Escherichia coli* BTCC B-614; and fungi *Candida albicans* BTCC Y-33. The pure strain of actinomycete was taken with sterile straws and put on the surface of medium agar with the microbial testing, and incubated in optimum temperature of each microbial testing. The inhibition zone was measured [7].

2.3 Extraction and Metabolite Identification by Disc Diffusion Method

One loop of pure strain was cultured in 10 ml into of NL19 liquid medium for 4 days as pre-culture. It was then moved to 100 ml of liquid medium as main culture and incubated for another four days in baffle Erlenmeyer. The composition of NL19 liquid medium was 20 g/L soy flour, 20 g/L D-mannitol, and pH 7.2. The culture was then centrifuged at 9,000 rpm for 10 minutes to separate supernatant and sediment pellet. The supernatant was taken, and added by ethyl acetate in ratio 1:1, and incubated in shaker incubator for 1 hour. The upper layer was then evaporated and measured the dry mass of the extract [14]. The screening was done in paper disc diffusion method after diluted the dry extract by acetonitrile.

2.4 Determination of Minimum Inhibitory Concentration (MIC)

Determination of MIC values were carried out by serial dilution methods on 96 well microplate. The dilution method was conducted in this study (Figure 4) as follows: 150 µl of pathogen microbial testing culture was put to the wells column 1-3 of microplate, then the first row added with 130 µl of NB sterile medium and 20 µl of extract LC-23. This first row is 0× dilution. A 150 µl was then moved from the first row to the second row, and this second row is 2× dilution. The dilution was done until the last row, and the dilution times of extract was 4×, 8×, 16×, 32×, 64×, and 128×. If the extract can inhibit the growth of microbial testing, the well became clear after 24 hours incubation at 37 °C. While to observed the effect of acetone nitrile as extract solvent, second column was used, 130 µl sterile medium and 20 µl of acetonitrile was added to the first well of second column. A 150 µl was then moved from the first row to second row. The dilution

was done until the last row. As negative control, the well will be unclear after 24 hours incubation at 37 °C. As the positive control, streptomycin was used in third column with the same method. Minimal Inhibitory Concentration (MIC) were defined as the lowest concentration of the tested extract that visible growth of the test microorganism was not observed. Concentration value will be determined by measure the mass of dry extract compared to dilution numbers [6].

2.5 Fractionation Extract

Fractionation method was conducted to investigate which fraction has the activity. Fraction collector was used to separate the crude extract every 40 second in 20 µl, and used for bioassay using microplate. Bioassay was done to the fraction by added 150 µl of NB medium mixed by microbial tested to each well and incubated for a night 24 hours [6]. The plates were evaluated and documented.

2.6 Molecular Identification 16S rRNA

One loop of pure strain on ISP-2 agar medium was cultured into 5 ml of Tryptic Soy Broth (TSB) and incubated at 30 °C for 5 days at 200 rpm [13]. A 1 ml of culture was then put into microtube and centrifuged at 13,000 rpm for 5 minutes. The supernatant was thrown out, and the pellet was used for DNA extraction. The pellet was washed by TE-buffer then centrifuged at 13,000 rpm for 5 minutes, this step was done twice. A 300 µl of buffer extraction was added to lyse the pellet, then warm up in 60 °C bath for 10 minutes. The DNA solution was then kept in room temperature ±25 °C and added 150 µl of 5.2 M sodium acetate. The DNA solution was added by isopropanol with ratio 1:1, centrifuged at 13,000 for 10 minutes. The DNA pellet was washed by ethanol, dried, and dissolved by 50 µl TE buffer. The DNA was used for 16S rRNA gene amplification using forward primer 9F and reverse 1541R by the following procedure: Denaturation 96 °C for 5 minutes, followed by 30 cycles of denaturation 96 °C for 30 seconds, annealing at 55 °C for 30 seconds, extension at 72 °C for 7 minutes [14]. Visualization of PCR product was conducted on 1% agarose and the sequencing was conducted by First Base Sequencing Company. The sequencing product was then edited using Bioedit program and confirmed to Eztaxon. Phylogenetic tree construction was used MEGA 6.06 program, Neighbour Joining statistical method with the number of bootstrap replications was 1000 [15].

3. RESULT AND DISCUSSION

3.1 Characterization of Strain LC-23

Strain LC-23 was isolated from lichen on the stem surface of plant *Averrhoa carambola*. The isolate grew on HV agar media with nalidixic acid and cycloheximide after 14 days incubation in 30 °C. The colony color of strain LC-23 on HV agar was stone grey. The HV agar was a poor media with the main composition is humic acid. Nalidixic acid was added to prevent the growth of other bacteria and cycloheximide to prevent fungi. Purification process of the isolate was conducted on ISP2 agar medium. The color of strain LC-23 on ISP2 agar medium was white and has morphological characteristics of the genus *Streptomyces* which are chalky, heaped and folded colony with aerial and substrate mycelium possessed an earthy odor [17]. This isolate also produced yellow pigment and was able to change the medium color into yellowish (Figure 1).

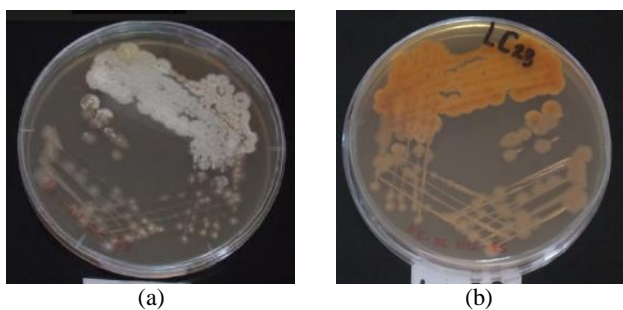


Figure 1. Isolate LC-23 (a) Top surface (b) Bottom surface in 9 cm diameter of Petri dish

3.2 Screening Antimicrobial Activity of Strain LC-23

The ability of strain LC-23 to inhibit Gram positive bacteria; *B. subtilis* BTCC B-612, *S. aureus* BTCC B-611, and *M. luteus* BTCC B-552. The strongest inhibition of LC-23 was against *M. luteus* (22.45-23 mm), followed by *S. aureus* (22.4-22.5 mm), and *B. subtilis* (15-21 mm) and did not show any activity against *E. coli* and *C. albicans* (Table 1).

Extract of LC-23 did not show any inhibition activity against *E. coli* that belongs to Gram-negative bacteria. Cell wall structure of Gram-negative bacteria more complex than Gram-positive in the term of protection. Prokaryotic Gram-positive and negative has cell wall as protector that consists of peptidoglycan. Peptidoglycan layer of Gram positive were thicker, meanwhile Gram-negative bacteria has thin layer, but protected by outer membrane consisting Lipopolysaccharide (LPS) protein and lipoprotein. This complexity caused the resistance of Gram-negative bacteria higher than Gram-positive bacteria. The tested microbes *C. albicans* was fungi that include as Eukaryote organism. This group structurally more complex than prokaryotes such as bacteria. Eukaryote has membrane-enclosed structures in the cytoplasm that affected the metabolism process of the cell to be more complex than prokaryotes. *C. albicans* could be more resistant to antimicrobial compound because it is extensively membrane system [18].

Table 1. Screening Antimicrobial Activity of Strain LC-23 (mm)

Repetition	<i>B. subtilis</i>	<i>S. aureus</i>	<i>M. luteus</i>	<i>E. coli</i>	<i>C. albicans</i>
I	21.00	22.50	22.45	-	-
II	15.00	22.50	23.00	-	-
III	17.65	22.40	23.00	-	-
Average	17.88	22.47	22.82		

Note: - (negative)

3.3 Metabolite Compound of Extract LC-23

The extraction process with NL19 liquid medium resulted yellow extract with dry extract obtained 25.8 mg or equal with 25,800 ppm. It was then diluted by 1 ml of acetonitrile to be used in screening process with disc diffusion method. The 20 µl of extract was dropped to paper disc, put in 2 layers of NA medium with bacterial testing or PDA medium with *C. albicans*, and incubated for 24 hours at 30°C. Extract of LC-23 was able to inhibit all the

Gram-positive bacteria tested. The largest inhibition zone was against *S. aureus*, followed by *M. luteus*.

The potency of antimicrobial according to Davis and Stout (1971) is as follows: about the diameter of inhibitory zone more than 20 mm (very strong), 10-20 mm (strong), 5-10 mm (medium), and less than 5 mm (weak). The extract showed very strong ability to inhibit the growth *M. luteus* (22.70 mm) and *S. aureus* (24.50 mm) [16,19]. While the inhibition activity of extract LC-23 against *B. subtilis* no longer appeared (Figure 2). This result possibly caused by different medium used by the strain to grow. The strain grows well on ISP2 agar which consist of yeast, malt, and glucose. While, for extraction, NL-19 liquid medium used consist of mannitol and soybean meal. The choice of the cultivation parameters is the critical point to the number of secondary metabolites produced by microorganisms. Small changes in the culture medium may not only impact the quantity of a certain compound but also the general metabolic profile of new natural product. It was also affected by variation of culture conditions, the influence of various stress conditions on secondary metabolite [20].

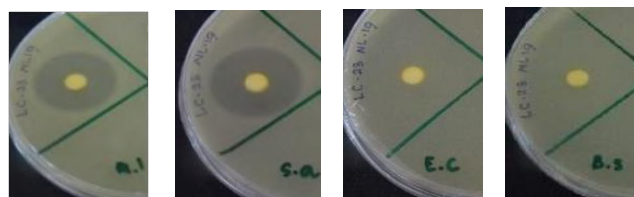


Figure 2. Screening antimicrobial activity of extract LC-23. (a) *Micrococcus luteus* BTCC B-552 (b) *Staphylococcus aureus* BTCC B-611 (c) *Escherichia coli* BTCC B-614 (d) *Bacillus subtilis* BTCC B-612

3.4 Minimal Inhibitory Concentration (MIC)

The MIC test of extract LC-23 showed that it was able to inhibit the growth of *S. aureus* and *M. luteus* until the last row (128×) dilution (Figure 3). However, *B. subtilis* BTCC B-612 and *E. coli* BTCC B-614 did not show an inhibitory activity. The result revealed that extract exhibited the strongest antimicrobial activity against *S. aureus* BTCC B-611 and *M. luteus* BTCC B-552 with concentration less than 2.016 ppm (Table 2).

Table 2. Screening Antimicrobial Activity of Strain LC-23 (mm)

Extract	Concentration	<i>B. subtilis</i>	<i>S. aureus</i>	<i>M. luteus</i>	<i>E. coli</i>
LC-23	258 ppm	-	<2.016 ppm	<2.016 ppm	-

Acetone nitrile seems has an effect to inhibit *M. luteus* BTCC B-552 until second well and *S. aureus* BTCC B-611. However, the negative control did not show inhibitory activity in third well for *M. luteus* BTCC B-552 and the second well for *S. aureus* BTCC B-611 (Figure 3), so extract with activity in this dilution number and so on could still contain active compound [21]. Ability of the extract has more impact to inhibit the growth of tested microbes and the solvent did not impact significantly.

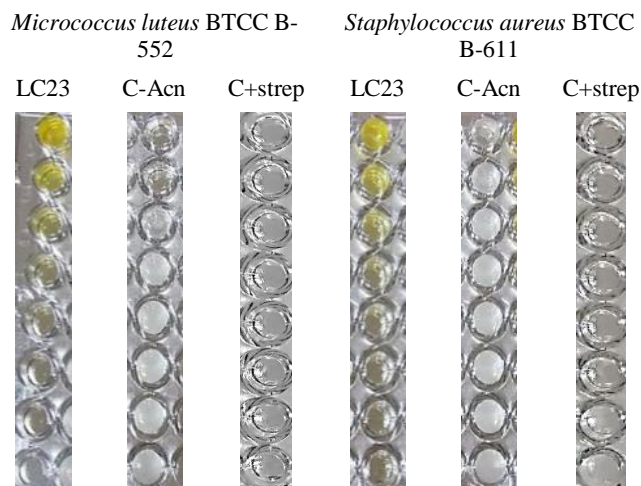


Figure 3. Minimal Inhibitory Concentration (MIC) of extract LC-23 against *Micrococcus luteus* and *Staphylococcus aureus*

3.5 Fractionation of Extract LC-23

Fractionation conducted of the crude extract, with the product collected in 96- well microtiter plate. The retention time used in this process was 40 seconds. Bioassay of the fraction conducted to the fraction product against *S. aureus* BTCC B-611 and *M. luteus* BTCC B-552 to find the specific well that has antimicrobial activity against the tested microorganism based on retention time. The use of *S. aureus* and *M. luteus* for screening based on the screening and MIC result. The growth of both bacteria was inhibited by extract LC-23.

Screening for antimicrobial activity of fractionation product showed that fraction in column 9 and 10 has positive activity against all tested bacteria. Specifically, to *S. aureus* fraction in column 7E to 7G showed positive inhibitory activity (Figure 4). While for *M. luteus*, fraction in column 7E to 7H showed positive inhibitory activity. According to the retention time of fractionation process, the effective compound fraction around 35'33'' until 37'33'' (well 7E-7H) and 46'00'' until 53'33'' (well 9A-10H). Mass spectrum of the fractionation compound in the certain well need to be checked to find the specific character of compound in hole 7E to 7H of the fractionation product of extract LC-23.

	1	2	3	4	5	6	7	8	9	10	11	12
A	○	○	○	○	○	○	○	○	+	+	○	○
B	○	○	○	○	○	○	○	○	+	+	○	○
C	○	○	○	○	○	○	○	○	+	+	○	○
D	○	○	○	○	○	○	○	○	+	+	○	○
E	○	○	○	○	○	○	+	○	+	+	○	○
F	○	○	○	○	○	○	+	○	+	+	○	○
G	○	○	○	○	○	○	+	○	+	+	○	○
H	○	○	○	○	○	○	+	○	+	+	○	○

Micrococcus luteus (a)

	1	2	3	4	5	6	7	8	9	10	11	12
A	○	○	○	○	○	○	○	○	+	+	○	○
B	○	○	○	○	○	○	○	○	+	+	○	○
C	○	○	○	○	○	○	○	○	+	+	○	○
D	○	○	○	○	○	○	○	○	+	+	○	○
E	○	○	○	○	○	○	○	○	+	+	○	○
F	○	○	○	○	○	○	○	○	+	+	○	○
G	○	○	○	○	○	○	○	○	+	+	○	○
H	○	○	○	○	○	○	○	○	+	+	○	○

Staphylococcus aureus (b)

Note: + (Inhibited)

Figure 4. Screening of fractionation product against tested microbials; (a) *Micrococcus luteus* BTCC B-552 (b) *Staphylococcus aureus* BTCC B-611

3.6 Molecular Identification

Polymerase Chain Reaction (PCR) and sequencing of the DNA extract was conducted for the sequence analysis of 16S rRNA gene. The 16S rRNA gene sequence of the strain was confirmed to data base of GenBank/DDBJ/EMBL and showed that the closest species of LC-23 was *Streptomyces palmae* with the similarity 98.51% where there was 21 base different over 1408 bp. The closest similarity value was followed by *Streptomyces misionensis* (98.44%) *Streptomyces matensis* (98.43%), and *Streptomyces althoticus* (98.43%). Sequence similarity with other *Streptomyces* members were lower than 98.4%.

Strain LC-23 showed some different characteristic to *S. palmae* that isolated from oil palm rhizosphere soil [16]. Strain LC-23 did not show any inhibition activity against *Candida* which reportedly possessed by *S. palmae*. This isolate also is able to produce pigment that changed the color of ISP2 medium into yellowish, while *S. palmae* did not change the color of ISP2 to ISP5 media. The SEM observation also revealed that the strain is differ from *S. palmae* (Figure 5). *Streptomyces palmae* formed compact spiral with a *spirales* type morphology. It is aerial and substrate mycelia were formed without fragmentation [16]. Strain LC-23 has rod shape, with filamentous septae and formed branch to made network of the mycelium.

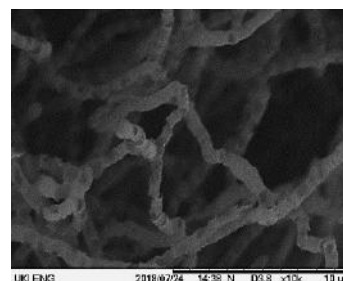


Figure 5. Scanning Electron Microscopy Strain LC-23 (10000 X)

The phylogenetic tree based on Kimura algorithm method showed that strain LC-23 formed a distinct phyletic line to type strain of the closest species of *Streptomyces* member with bootstrap value under 70 % (Figure 6). According to the tree, the closest species to LC-23 was *Streptomyces wuyuanensis* with the similarity value 98.23%. It formed a different cluster both to *S. palmae* and *S. wuyuanensis*. This result explained that strain LC-23 was member of *Streptomyces* genera but does not belong to any species.

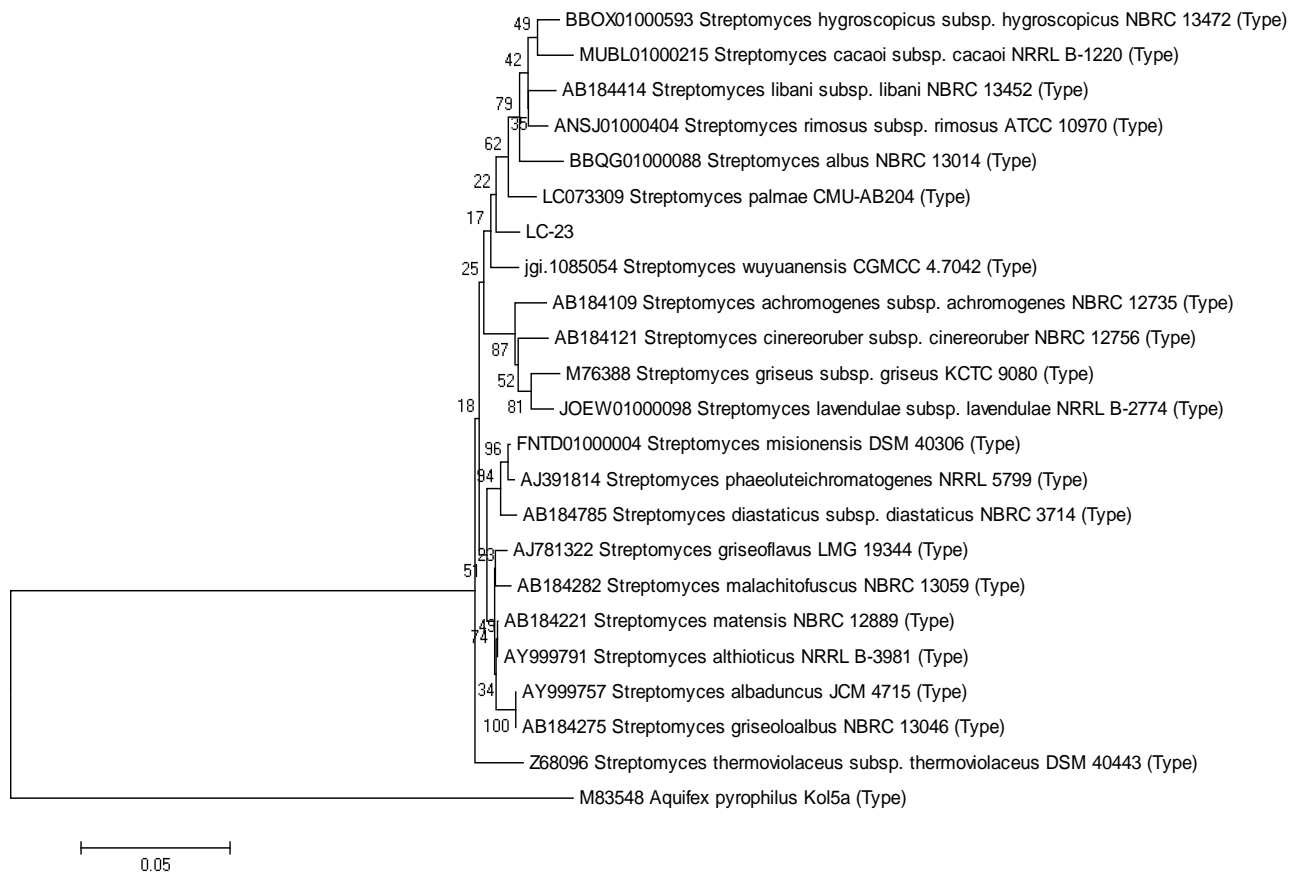


Figure 6. Phylogenetic position of LC-23 based on 16S rRNA gene sequencing compare to type strains in the Family *Streptomycetaceae*

4. ACKNOWLEDGMENTS

The author is grateful to Indonesia Endowment Fund for Education (LPDP RI) for the scholarship and support to this research and Research Centre for Biotechnology, Indonesian Institute of Sciences where the research conducted.

5. REFERENCES

- [1] Parrot D, Antony-Babu S, Intertaglia L, Grube M, Tomasi S and Suzuki M T 2015 Litoral lichens as a novel source of potentially bioactive Actinobacteria. *Scientific Report* **5**: 1-14.
- [2] Genniloud O, Gonzales I, Salazar O, Martin J, Tormo J R and Vicente F 2011 Current Approaches to Exploit Actinomycetes as a Source of Novel Natural Products. *Journal Industries Microbiol Biotechnol* **38**: 375-389.
- [3] Berdy J 2012 Thoughts and facts about antibiotics: Where we are now and where we are heading. *The Journal of Antibiotics* **65**: 325--395.
- [4] Kumar N, Singh R K, Mishra S K, Singh A K and Pachouri U C 2010 Isolation and screening of soil actinomycetes as source of antibiotic Active Against Bacteria. *International Journal of Microbiology Research* **2**: 12-16.
- [5] Abdelmohsen U R, Piementel-Elardo S M, Hanora A, Radwan M, Abou-El-Ela S H, Ahmed S, and Hentschel U 2010 Isolation, Phylogenetic Analysis and Anti-infective Activity Screening of Marine Sponge-Associated Actinomycetes *Marine Drugs* **8**: 399-412.
- [6] Charausova I, Steinmetz H, Medo J, Javorekova S and Wink J 2016 Characterization of Antimycin-Producing Streptomycete Strain VY46 Isolated from Slovak Soil. *Brazilian Archives of Biology and Technology* **59**: 1-8.
- [7] Jiang Y, Wang X, Li G, Li Q, Liu C, Chen X, Wang L, Li Y and Jiang C 2015 Diversity and anti-microbial activities of actinomycetes Associated with three species of Lichens. *American Journal of Bioscience* **3**(5): 171-177.
- [8] Nimnoi P, Pongsilp N and Lumyong S 2009 Endophytic actinomycetes Isolated from *Aquilaria crasna* Pierre ex Lec and screening of plant growth promoters production. *World Journal Microbiol Biotechnol* **26**: 193-203.
- [9] Tang S, Li W, Dong W, Zhang Y, Xu L and Liang C 2003 Study of the biological characteristic of Some Halophilic and Halotolerant Actinomycetes Isolated from Saline and Alkaline Soil. *Actinomycetol* **17**(1): 6-10.
- [10] Okkoro CK, Brown R, Jones A L, Andrews B A, Asenjo J A, Goodfellow M and Bull A T 2009 Diversity of culturable actinomycetes in hyper-arid soils of the atacama Desert, Chile. *Antonie van Leeuwenhoek* **95**: 121-133.
- [11] Liu C, Jiang Y, Wang X, Chen D, Chen X, Wang L, Han L, Huang X and Jiang C 2017 Diversity, antimicrobial activity, and biosynthetic potential of cultivable actinomycetes

- associated with lichen symbiosis. *Microb Ecol. Springer Science and business media*.
- [12] Grube M and Berg G 2009 Microbial consortia of bacteria and fungi with focus on the lichen Symbiosis. *British Microbial Society***23**: 72-85.
- [13] Axenov-Gibanov DV, Voytsekhovskaya IV, Tokovenko B T, Protasov E S, Gamaiunov SV, Rebets Y V, Luzhetskyy A N, and Timofeyev M A 2016 Underground Lake and Moonmilk Speleothem from the Biggest Conglomeratic Karstic Cave in Siberia as Source of Novel Biologically Active Compounds. *Plos One***11**(2): 1-12.
- [14] Lisdiyanti, P, Otoguro M, Ratnakomala S, Lestari Y, Hastuti R D, Triana E, Katsuhiko A and Widyastuti Y. 2010. *Actinokinesporabaliensis* sp. nov., *Actinokinesporacibodasensis* sp. nov. and *Actinokinesporacianjurensis* sp. nov., isolated from Soil and Plant Litter. *International Journal of Systematic and Evolutionary Microbiology***60**: 2331-2335.
- [15] Sujarit K, Kudo T, Ohkuma M, Pathom-Aree W and Lumyong S 2016 *Streptomyces palmae* sp. nov., isolated from oil palm (*Elaeisguineensis*) rhizosphere soil. *International Journal of Systematic and Evolutionary Microbiology* **66**: 3983-3988.
- [16] Sulistiyani T R and Widhyastuti N 2011 Isolation, selection, and molecular identification of antibiotic producer. *Actinomycetes. Widyariset***14**(3): 541-548.
- [17] Suneetha V, Karthick R and Prathusha K 2011 Isolation and identification of *Streptomyces* ST1 and ST2 strains from Tsunami affected soils: Morphological and biochemical studies. *J Oceanogr Mar Sci***2**(4): 96-101.
- [18] Brock T D, Madigan M T, Martinko J M and Parker J 2002 *Biology of microorganisms seventh Edition*. Prentice-Hall, Inc. New Jersey.
- [19] Davis W W and Stout T R 1971 Disc Plate Method of Microbiological Antibiotic Assay. *Applied Microbiology***4** (22): 659-665.
- [20] Scherlach K and Hertweck C 2009 Trigering cryptic natural product biosynthesis in microorganisms. *Org Biomol Chem* **7**: 1753-1760.
- [21] Jeske O, Surup F, Ketteni ßM, Rast P, Förster B, Jogler M, Wink J and Jogler C 2016 Developing Techniques for the Utilization of Planctomycetes As Producers of Bioactive Molecules. *Frontiers in Microbiology* **7**: 1-14

Comparative Studies Between Hydrothermal Carbonation and Torrefaction for Biofuel Production from Poultry Litter

Rafail Isemin

Tambov State Technical University
106, Sovetskaya Street, Tambov,
Russia, 392000
+74752639446
risemin@gmail.com

Aleksandr Mikhalev

Tambov State Technical University
106, Sovetskaya Street, Tambov,
Russia, 392000
+74752630446
malex_v@list.ru

Oleg Milovanov

Tambov State Technical University
106, Sovetskaya Street, Tambov,
Russia, 392000
+74752630446
milowanov.o@yandex.ru

Dmitry Klimov

Tambov State Technical University
106, Sovetskaya Street, Tambov,
Russia, 392000
+74752630446
marcelldm@mail.ru

Natalia Muratova

Tambov State Technical University
106, Sovetskaya Street, Tambov,
Russia, 392000
+74752630446
mns@admin.tstu.ru

Kristina Krysanova

Joint Institute for High Temperatures,
Russian Academy of Sciences
13, Izhorskaya Street, Moscow,
Russia, 127412
+74954857981
vermont.content@gmail.com

Yuri Teplitskii

A. V. Luikov Heat and Mass Transfer
Institute
15, P. Brovka Street, Minsk, Belarus,
220072
+375172842480
tep@hmti.ac.by

Anatolii Greben'kov

A. V. Luikov Heat and Mass Transfer
Institute
15, P. Brovka, Minsk, Belarus,
220072
+375172842480
tep@hmti.ac.by

Vadim Kogh-Tatarenko

Tambov State Technical University
106, Sovetskaya Street, Tambov,
Russia, 392000
+74752639446
vadim6873@yandex.ru

ABSTRACT

The results of comparative experiments on the production of biofuel from poultry litter (PL) by the method of low-temperature pyrolysis (Torrefaction) and hydrothermal carbonization are presented. Comparison of the obtained results shows that as a result of hydrothermal carbonation of PL (processing temperature 180-210 °C, treatment time 240 minutes), the carbon content in the manure can be increased by 1.35 times, and the oxygen content is reduced in 2.2 times, the lower heat of combustion of the fuel obtained, which is similar in its characteristics to lignites, can be increased by 1.25 times to 19.7 MJ/kg. As a result of low-temperature pyrolysis in the fluidized bed at a temperature of 300 °C in a nitrogen medium and superheated water vapor, the carbon content can be increased by 1.16 times, and the oxygen content is reduced in 2.8 times. The lowest heat of combustion of the fuel produced can be increase by 1.13 times to 18.8 MJ/kg. Considering that the technology of PL treatment by low-temperature pyrolysis in the fluidized bed requires significantly less processing time (360-480 seconds), this technology can be

fully considered as an alternative to hydrothermal carbonization.

CCS Concepts

Applied computing → Physical sciences and engineering → Engineering

Keywords

Poultry litter; Torrefaction; Hydrothermal carbonization; Fluidized bed; Fixed bed; Superheated vapor

1. INTRODUCTION

PL is a heterogeneous feedstock consisting of bedding material, urine, feathers and waste feed, and is the most suitable manure feedstock for thermal conversion processes [1]. Notwithstanding, the advantages of PL for increasing soil fertility, there are environmental concerns about its over application on agricultural sites which may result in human and animal health risks through leaching of nitrates and other pollutants into groundwater [2].

Developing environmentally beneficial uses for animal byproducts for application to land would help to alleviate problems associated with their management. Disposal technology for biowaste has clearly indicated that thermochemical conversion processes have the capability to convert animal by-products into combustible gases, bio-oils and solid products, which can be used as a soil amendment/fertilizer [3, 4]. Accordingly, thermal conversion technologies, including pyrolysis, gasification, combustion and hydrothermal carbonization (HTC), are being used to convert biomass and/or biowaste into useful products while addressing compliance with environmental emission norms. HTC a relatively new process for biomass carbonization, usually performed at 180–375 °C under auto-generated pressures [5], has

Permission to make digital or hard copies of all or part of this work for personal or classroom use is granted without fee provided that copies are not made or distributed for profit or commercial advantage and that copies bear this notice and the full citation on the first page. Copyrights for components of this work owned by others than ACM must be honored. Abstracting with credit is permitted. To copy otherwise, or republish, to post on servers or to redistribute to lists, requires prior specific permission and/or a fee.
ICBBB '19, January 7-9, 2019, Singapore, Singapore
Copyright 2019 ACM 978-1-4503-6654-0/19/01...\$15.00

DOI: <https://doi.org/10.1145/3314367.3314372>

been gaining attention, because energy-intensive predrying is not necessary [6] Moreover, the hydrochar (HTC char) has a higher heating value compared to the biochar produced from slow-pyrolysis or conventional carbonization at the same temperature [7].

However, HTC process takes place at high pressure, which complicates and increases the cost of equipment for this process. The duration of HTC process takes up to several hours. HTC process produces large amounts of water that is contaminated with biomass and requires disposal.

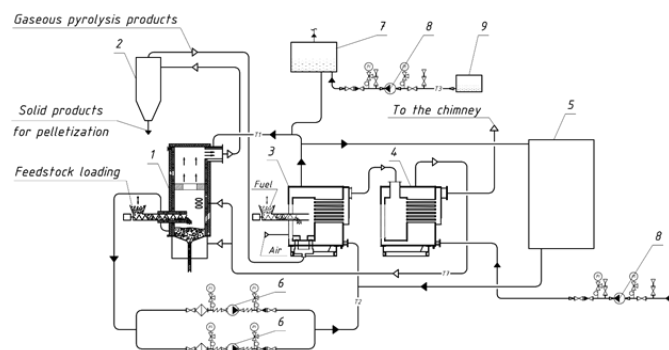
The results of studies of the low – temperature pyrolysis (torrefaction) process of various agricultural wastes in the fluidized bed of sand and other materials are known, showing that the duration of pyrolysis can be reduced to 200 – 250 seconds, and the heating rate of biomass is increased accordingly. The product is processed evenly without the risk of charring [8, 9, 10].

Earlier, we proposed to carry out the PL decontamination by the means of torrefaction [11]. The process was carried out in a Hearth - type reactor, in which finished pellets made from PL were subjected to torrefaction at a temperature of 155-250 °C. It has been shown that after the poultry litter pelletization and heat treatment at a temperature of 250 °C for 60 minutes it is possible to completely remove the pathogenic microflora in it.

The disadvantage of the proposed technology is the low rate of heat treatment.

Now we are suggested realizing the torrefaction of the PL in a fluidized bed.

The proposed scheme for the PL treatment is shown in Figure 1.



1 – Torrefaction reactor, 2 – Cyclone, 3 – Thermocracking reactor, 4 – Steam boiler, 5 – Power generation unit, 6, 8 – Pumps, 7 - Expansion tank for high-temperature heat carrier, 9 – Storage tank for high-temperature heat carrier

Figure 1. The proposed scheme for the PL treatment

The torrefaction of the PL is offered to be carrying out in the reactor 1 with a fluidized bed of inert material (quartz sand, for example).

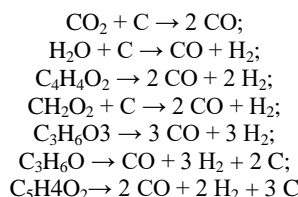
The PL can be fed to torrefaction reactor either in the original form or in the pellet form.

In the first case, solid pyrolysis products are removed from the reactor 1 together with the gas mixture into the cyclone 2, where they are separated from the gas stream and sent on the granulation.

In the second case, PL pellets along with the inert material are unloaded through the lower discharge pipe installed under the fluidized bed. Then the finely dispersed material is returned to the fluidized bed by means of the pneumatic conveying system, whereas the decontaminated pellets are sent to the consumer.

Gaseous products, are sent to the thermal cracking reactor 3, in which these products are processed into synthesis gas.

The following reactions take place in the hot activated carbon bed, which make it possible to obtain a synthesis gas with a high content of carbon monoxide and hydrogen [12]:



The synthesis gas obtained is being burned in the same reactor furnace, which causes heating of the high-temperature heat carrier, used to heat the pyrolysis reactor 1, cyclone 2, and also as the primary heat carrier in the Rankine organic cycle plant 5, by means of which the electrical energy is generated.

The high-temperature heat carrier is being heated to 350-400 °C in thermal cracking reactor 3. The flue gases temperature reaches 550 - 650 °C beyond the reactor and their heat is used for generating water steam with an excess pressure of 0.07 MPa in the boiler 4. Then this steam is superheated to the required temperature by means of a superheater (the superheater is not shown at the scheme), which also uses the heated in the reactor 3 a high-temperature heat carrier.

According to the described scheme, all the gas from the torrefaction reactor is supplied to the thermal cracking reactor, i.e. pyrolysis gaseous products and spent superheated water steam. It may also be offered variant that water steam is condensed, and only non-condensable gaseous pyrolysis products are sent to the thermal cracking reactor. In this case, water heated during steam condensation to above 95 °C temperature can also be used to generate electrical energy using a Rankine organic cycle plant. Calculations show that for the low-temperature pyrolysis of the poultry litter with initial moisture of 20% in quantity 1 t/h, 4 t/h of superheated to 300 °C water steam is required. By condensing this steam, thermal energy sufficient to generate 250 kW of electrical energy can be obtained. In turn, this amount of electricity will be enough to granulate 1 t/h of decontaminated poultry litter.

The described scheme for the PL treatment and for its gaseous products utilization was adopted by us during the implementation project of construction a demonstration plant for the processing of PL.

The realization of the project had required the following studies implementation, which results are set out in this article:

- study of the co-fluidization process for quartz sand and PL pellets.;
- study of the torrefaction process for PL pellets in a fluidized bed, that is fluidized by superheated water steam;
- the thermal cracking process investigation of non-condensable gaseous products of PL torrefaction;

- study of pathogenic microflora content in the PL before and after its treatment by torrefaction method.

The objective of this study is to conduct on torrefaction of PL in a fluidized bed and comparative experiments on HTC of PL.

2. EXPERIMENTAL UNIT

The scheme of the experimental unit for torrefaction PL process study is given at Figure 2.

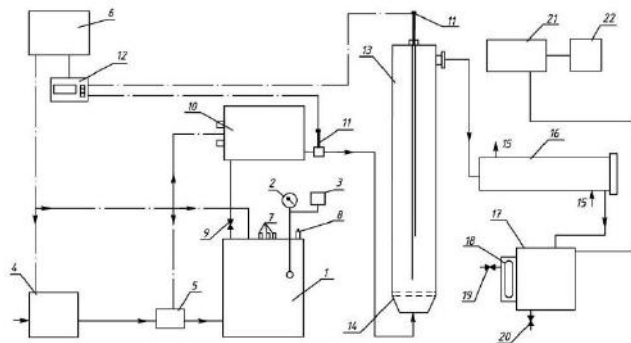


Figure 2. Scheme of experimental unit for torrefaction PL process study

The unit includes a steam electric boiler 1, equipped with a pressure gauge 2, steam pressure sensors 3 in the boiler 1 and a pipeline 4 for water supply. The pipeline 4 is equipped with a valve 5, eliminating the flow of steam into the pipeline 4 when the water pressure in it falls. The automation system and regulation 6 manages the operation of the boiler with the help of the sensor 7, which monitors the water level in the boiler. The safety valve 8 and the control valve 9 regulate the water pressure in the boiler and exclude the increase of this pressure over the permissible limits.

Behind the boiler there is an electric superheater 10, equipped with thermocouples 11 and temperature controllers 12. Superheated steam with the required temperature is fed to the reactor 13 to study the low-temperature pyrolysis of the litter in the boiling layer, equipped with a gas distribution grid 14. The gaseous pyrolysis products together with the waste water vapor enter the refrigerator 16, which is cooled by water entering the pipelines 15. The condensed products enter the container 17, equipped with an observation window 18 and 19, 20 valves for condensate discharge. Non-condensable gases enter the gas tank 21, followed by the gas analyzer "VarioPlus SinGaz" 22.

The unit works as follows. The water vapor produced in the boiler 1 with an overpressure of less than 0.07 MPa and a temperature of 117 °C enters the electric superheater 10, where it is heated to the required temperature. The superheated steam enters the reactor for low-temperature pyrolysis 13, where quartz sand is transferred to the fluidized state. The reactor 13 is made of stainless steel and has a diameter of 80 mm and a height of 800 mm. The walls of the reactor are thermally insulated. Quartz sand has a particle size of 0.16 – 0.25 mm. The reactor 13 is provided with a feeder to feed into the boiling PL layer after the layer temperature reaches the required value. The number of PL, loaded into the reactor, was 20 – 23 g. During the pyrolysis of PL we continuously measured the content in the gases behind the refrigerator 16 carbon dioxide, carbon monoxide, CH₄ by means of hydrogen analyzer "VarioPlus SynGaz". The experiment stopped when the gas analyzer stopped recording the release of these gases. After completion of the experiment, the reactor was purged for 2 hours

with cold nitrogen, after which pellets from the litter were unloaded from it.

During the experiments, the bed of inert material could be in a stationary or fluidized state. In this case, instead of superheated steam as a gas medium and coolant, nitrogen heated to the required temperature in the superheater could be used.

Steam consumption was determined by the amount of condensate after cooling the condensed pyrolysis products. This amount of steam was included and evaporated during pyrolysis moisture contained in the pellets. However, since the original pellets contained a small amount of moisture and the mass of the portions of the pellets loaded into the reactor, was not large, this amount of moisture does not significantly affect the accuracy of determining the steam consumption. The nitrogen flow rate was determined using a flow meter.

HTC process was carried out in a laboratory steel reactor of periodic action at 180-210 °C; the duration of the process was 4 hours.

Thermal analyzer SDT Q600 was used to determine the moisture and ash content. SDT Q600 allows synchronous thermal analysis, which includes thermogravimetric, differential thermogravimetric analysis and differential scanning calorimetry. The calorific value was determined on the basis of elemental analysis, which was performed on the elemental analyzer Vario MICRO Cube. This analyzer is designed to simultaneously determine the elements C, H, N and S in the samples.

3. RESULTS AND DISCUSSION

Figure 3 shows the curves of changes in the concentration of CO₂, CO and CH₄ in non-condensable gases behind the unit at torrefaction PL in a fixed bed of quartz sand, purged with nitrogen at an average temperature of 300 °C. The reactor was loaded with 50 g of PL, the nitrogen flow rate was 5 l/min.

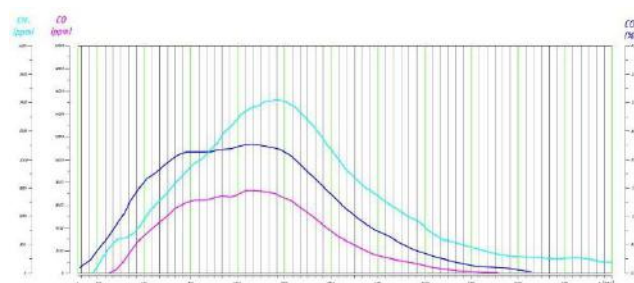


Figure 3. Curves of changes in the concentration of CO₂, CO and CH₄ in non-condensable gases behind the unit at torrefaction PL in a fixed bed of quartz sand, purged with nitrogen at temperature of 300 °C

As can be seen from Figure 3, the time of torrefaction PL in such layer, judging by the curves of the change in the concentration of non-condensing gases, takes 2400 seconds, and the time of the most intensive process takes 1000 seconds.

In the fluidized bed, converted to a fluidized state with hot nitrogen (nitrogen flow rate of 5 l/min, mass loaded into the PL reactor is 20 g), the duration of the most active phase of torrefaction is approximately 240 seconds, and the process itself is basically completed in 480 seconds (Figure 4). I. e., in the nitrogen medium, the duration of the torrefaction PL process in the fluidized bed reduced by about 5 times, and the duration of the most intensive process is reduced by 4.2 times.

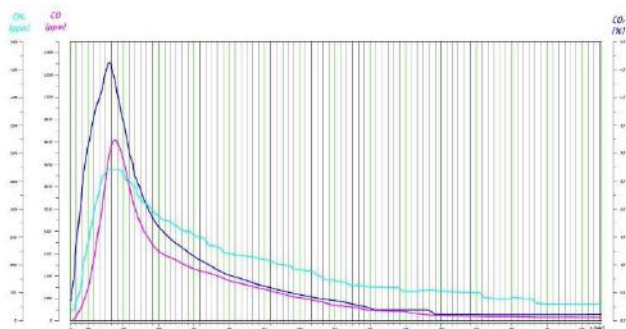


Figure 4. Curves of changes in the concentration of CO₂, CO and CH₄ in non-condensable gases behind the unit at torrefaction PL in the fluidized bed of quartz sand particles in nitrogen medium at 300 °C

In the fluidized bed, liquefied by superheated water vapor, the duration of the torrefaction PL process is reduced to 360 seconds, and the duration of the most active phase of the process – up to 120 seconds (Figure 5).

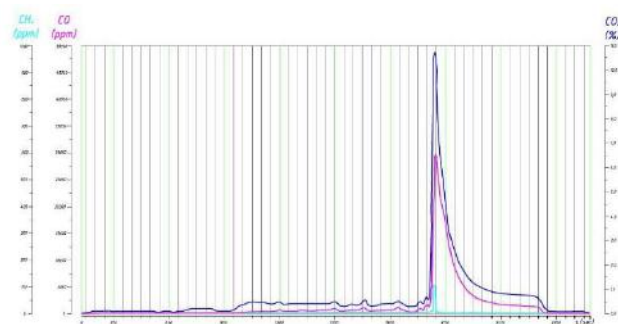


Figure 5. Curves of changes in the concentration of CO₂, CO and CH₄ in non-condensable gases behind the unit at torrefaction PL in the fluidized bed of quartz sand particles, windswept by superheated steam at 300 °C

Table 1 shows the main characteristics of PL before and after torrefaction.

As can be seen from Table 1, PL after torrefaction at a temperature of 300 °C the oxygen content in the sample is reduced 2.4 - 2.8 times with such a sharp decrease in the oxygen concentration of PL, after its thermal treatment in a nitrogen atmosphere in a fixed bed of particles of inert material, in a nitrogen atmosphere in a fluidized bed of inert material in the superheated steam in a fluidized bed of inert material.

With increasing hydrothermal carbonization temperature, the mass yield of biochar decreased. At 180 °C mass yield was 57.88%, and at 210 °C decreased to 47.4%.

Table 2 presents the results of chemical analysis of PL content after HTC depending on HTC temperature.

Comparison of the results shows that as a result of hydrothermal carbonation of the PL (processing temperature 180-210 °C, processing time 240 minutes), the carbon content in the PL can be increased by 1.35 times, and the oxygen content is reduced by 2.2 times, the lower calorific value of the resulting fuel can be increased by 1.25 times to 19.7 MJ/kg.

Table 1. Main characteristics of PL before and after torrefaction

Material	Determined Characteristics						
	C, %	H, %	N, %	S, %	O, %	Ash A, %	LCV, MJ/kg
Row PL	41,4	5,7	4,8	0,8	30,7	16,6	16,7
PL after torrefaction (fixed bed, N ₂)	47,6	3,7	6,3	0,96	10,9	30,5	18,9
PL after torrefaction (fluidized bed, N ₂)	46,7	3,7	6,3	0,98	11,6	30,7	18,5
PL after torrefaction (fluidized bed, steam)	48,2	3,63	4,65	0,9	12,5	30,1	18,8

Table 2. Results of chemical analysis of PL content after HTC depending on HTC temperature

Temperature of HTC, °C	PL content, % mass (on dry substance)			
	C	H	N	O
180	49,1	5,5	3,31	24,28
190	49,7	5,5	3,5	22,47
200	50,3	5,35	3,63	17,5
210	55,3	5,56	3,97	13,8

Both the O/C and H/C atomic ratios of the hydrochar as shown in Table 3 decreased with increasing treatment temperature and time. The O/C atomic ratio fell to a greater extent than the H/C, providing strong evidence that decarboxylation reaction occurred during the torrefaction and HTC and suggests that decarboxylation reactions are more important than dehydration reactions [13].

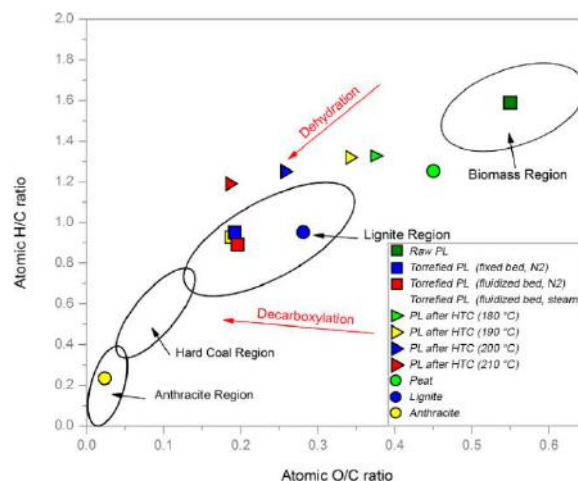


Figure 6. Van Krevelen diagram

The Van Krevelen diagram (Figure 6) was used to present the elemental composition of different materials. It also provides an insight into the possible reaction pathways for the formation of hydrochars and their fuel quality [14]. In this figure, typical zones for lignite, coal, anthracite and biomass, and major possible reactions (dehydration and decarboxylation) are indicated.

Table 3. The ratio (H/C) and (O/C) for the original and heat-treated PL in comparison with similar characteristics for other types of fuel

Material	H/C	O/C
Raw PL	1.641	0.557
Torrefied PL after torrefaction (fixed bed, N ₂)	0.926	0.172
PL after torrefaction (fluidized bed, N ₂)	0.944	0.186
PL after torrefaction (fluidized bed, steam)	0.897	0.194
PL after HTC (180 °C)	1.335	0.371
PL after HTC (190 °C)	1.319	0.339
PL after HTC (200 °C)	1.267	0.261
PL after HTC (210 °C)	1.198	0.187

As a result of torrefaction at a temperature of 300 °C in nitrogen and superheated water vapor, the carbon content can be increased by 1.16 times, and the oxygen content reduced by 2.8 times. The lower heat of combustion of the fuel can be increased by 1.13 times to 18.8 MJ / kg. Given that the technology of processing biomass by low – temperature pyrolysis in the fluidized bed requires much less processing time (360-480 seconds), this technology can be considered as an alternative to hydrothermal carbonization.

4. ACKNOWLEDGMENTS

The work was supported by the Ministry of science and higher education of the Russian Federation (Agreement № 074 – 11 – 2018 – 018 from May 29, 2018).

5. REFERENCES

- [1] Ghanim, B.M., Pandey, D.S., Kwapinski, W., Leahy, J.J. 2016. Hydrothermal carbonisation of poultry litter: effects of treatment temperature and residence time on yields and chemical properties of hydrochars. *Bioresour. Technol.* 216 (2016), 373–380.
- [2] Lynch, D., Henihan, A.M., Bowen, B., Lynch, D., McDonnell, K., Kwapinski, W., Leahy, J. 2013. Utilization of poultry litter as an energy feedstock. *Biomass Bioenergy* 49 (2013), 197–204.
- [3] Pandey, D.S., Kwapinska, M., Gómez-Barea, A., Horvat, A., Fryda, L.E., Rabou, L.P., Leahy, J.J., Kwapinski, W. 2016. Poultry litter gasification in a fluidized bed reactor: effects of gasifying agent and limestone addition. *Energy Fuels* 30 (2016), 3085–3096.
- [4] Taupe, N., Lynch, D., Wnetrzak, R., Kwapinska, M., Kwapinski, W., Leahy, J. 2016. Updraft gasification of poultry litter at farm-scale-A case study. *Waste Manage.* 50 (2016), 324–333.
- [5] Danso-Boateng E., Shama G., Wheatley A.D., Martin S.J. and Holdich R.G. 2015 Hydrothermal carbonization of sewage sludge: Effect of process conditions on product characteristics and methane production. *Bioresour Technol.* 177 (2015), 318–327.
- [6] He C., Gianni A., and Wang J.Y. 2013. Conversion of sewage sludge to clean solid fuel using hydrothermal carbonization: Hydrochar fuel characteristics and combustion behavior. *App Energy* 111 (2013), 257–266.
- [7] Kambo H.S., Dutta A. 2015. A comparative review of biochar and hydrochar in terms of production, physico-chemical properties and applications. *Renew Sust Energ Rev.* 45 (2015), 359–378.
- [8] Brachi P., Chirone R., Miccio F., Miccio M., Ruoppolo G. 2018. Valorization of orange peel residues via fluidized bed torrefaction: comparison between different bed materials. In *Proceeding of the 23th International Conference on Fluidized Bed Conversion*. Seoul, Korea, 977 – 987.
- [9] Brachi P., Chirone R., Miccio F., Miccio M., Ruoppolo G. 2015. Fluidized Bed Torrefaction of Industrial Tomato Peels: Set – Up of a New Batch Lab – Scale Test rig and Preliminary Experimental Results. In *Proceeding of the 22th International Conference on Fluidized Bed Conversion*, Turku, Finland, 438 – 447.
- [10] Brachi P, Miccio F, Miccio M, Ruoppolo G. 2016. Torrefaction of Tomato Peel Residues in a Fluidized Bed of Inert Particles and a Fixed-Bed Reactor, *Energy Fuels* 30 (2016), 4858-4868.
- [11] Isemin R., Mikhalev A., Milovanov O., Stepantsova L., Solopov V. 2017. Development of the Technology of Poultry Litter Treatment into Organics Fertilizer through its Decontamination by the Low – Temperature Pyrolysis Method, *International Journal of Chemical Engineering and Application* (2017), 144 – 188.
- [12] Lavrenov V. A., Larina, O. M., Sinelshchikov V. A., and Sytchev G. A. 2016 Two-Stage Pyrolytic Conversion of Different Types of Biomass into Synthesis Gas *High Temperature* (2016,) 892–898.
- [13] Poerschmann J., Baskyr I, Weiner B., Koehler R., Wedwitschka H., Kopinke F. – D. 2013 Hydrothermal carbonization of olive mill wastewater *Bioresour. Technol.*, (2013) 581-588
- [14] Kambo H. S., Dutta A. 2015 A comparative review of biochar and hydrochar in terms of production, physico-chemical properties and applications *Renewable Sustainable Energy Rev.*, (2015) 359-378.

ICBBB 2019

Statistical Ecology

Ecological Informatics Approach to Analyze Habitat Preferences of *Auricularia delicata* (Italic) in Bingungan Forest, Turgo Natural Forest Conservation Area

Dwiki Prasetya

Department of Biology, Yogyakarta State University
Jl. Colombo No.1, Karangmalang, Yogyakarta, Indonesia
+6281239193032

dwiki412fmipa@student.uny.ac.id

Tien Aminatun

Department of Biology, Yogyakarta State University
Jl. Colombo No.1, Karangmalang, Yogyakarta, Indonesia
+6282138267965

tien_aminatun@uny.ac.id

ABSTRACT

Based on our previous research, *Auricularia delicata* has been detected as unique and important local mushroom in economic and ecological values which were newly recorded in Turgo tropical forest ecosystem, with exactly restricted distribution only in Bingungan forest. This research aimed to know habitat preferences of *Auricularia delicata* by using ecological informatics approach regarding to management forest-fungi efforts. To yield communicative interpretation, we used some analyses from Pearson correlation among physical and chemical characteristics of substrate as *Auricularia delicata* habitat, Bray-Curtis similarity and distance indices, NMDS (Non-Metric Multidimensional Scaling) ordination, hierarchical clustering with UPGMA (Unweighted Pair Group Method with Arithmetic Mean) and non-hierarchical clustering with K-means, till we could categorize habitat preferences from the very good, good, poor, and very poor categories.

CCS Concepts

Applied computing → Life and medical sciences → Bioinformatics

Keywords

Statistical Ecology, *Auricularia delicata*, Habitat Preferences

1. INTRODUCTION

The decision to monitor *Auricularia delicata* macrofungi species in Bingungan forest is one effort of macrofungi conservation in tropical rainforest ecosystems. In addition, the forest being protected and conserved by Mount Merapi National Park (TNGM). *Auricularia delicata* is known as “keprok” mushroom which has potential values to fulfill nutrition for Turgo people. *Auricularia delicata* is a type of macrofungi belonging to the jelly macrofungi group. The results of the survey conducted by Prasetya et al. in 2017[1] showed that macrofungi jelly in Bingungan forest had a second ecological importance value after

© 2019 Association for Computing Machinery. ACM acknowledges that this contribution was authored or co-authored by an employee, contractor or affiliate of a national government. As such, the Government retains a nonexclusive, royalty-free right to publish or reproduce this article, or to allow others to do so, for Government purposes only.

ICBBB '19, January 7–9, 2019, Singapore, Singapore

© 2019 Association for Computing Machinery.

ACM ISBN 978-1-4503-6654-0/19/01...\$15.00

DOI: <https://doi.org/10.1145/3314367.3314382>

agarics macrofungi group, with sequences of 89% and 138% of total 300%. *Auricularia delicata* had the highest frequency (0.7), with an ecological importance value of 71%. Interestingly, *Auricularia delicata* was only found in Bingungan forest, not distributed in the other forests of Turgo area such as Tritis forest or Turgo forest. This fungus undergoes a process of fruiting in the rainy season to the early dry season.

The importance of fungi in ecosystems is in the following four major functions: (1) As decomposers, fungi drive the global carbon cycle. (2) As mycorrhizal symbionts, they form absorptive accessories to roots, linking the activities of separate plants and underpinning primary production in forests, heathlands, and grasslands. (3) Food sources for many wildlives. (4) As parasites, they regulate population dynamics of their hosts [2][3].

The forest fungi management is a concept to conserve priority macrofungi in edible, rare, or unique categories [4]. Monitoring is done in terms of habitat preferences and population dynamics. Those methods are suitable to the concepts of macrofungi habitat modeling. Therefore, we may describe clearly enough about where macrofungi grow, and what kind of habitat characteristics would influence the fruiting process. Thus, the habitat and ecosystem management which support sporocarp formation of *Auricularia delicata* can be maintained.

2. METHODS

2.1 Study Area

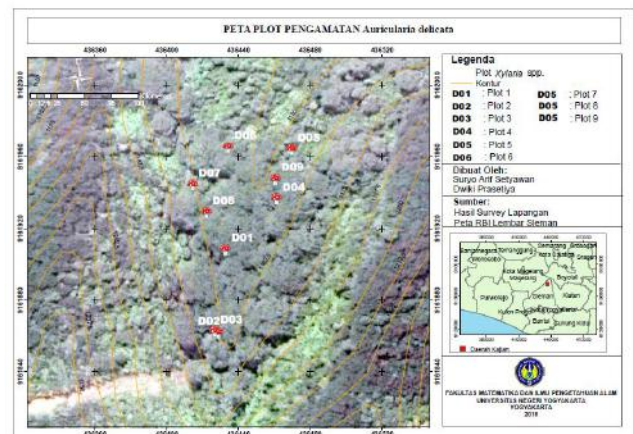


Figure 1. Map of permanent sampling plots. The mushrooms symbols show sampling plots area

This research was carried out in Bingungan forest, Turgo Natural Forest Conservation Area, Mount Merapi National Park. Bingungan Forest is located at the altitude of 1169-1193 m above the sea level with the coordinate points of 04° 36.422' South Latitude - 04° 36.450' South Latitude, 916° 19.06' West Longitude - 916° 18.70'. The data were collected on nine permanent plots that had been predetermined and coded as D01, D02, D03, D04, D05, D06, D07, D08, and D09 that showed in Figure 1.

2.2 Data Analysis

To determine habitat preferences, the Pearson correlation analysis is used for among variables, those are tree species, decay class, C organic, N total, C/N ratio, holocellulose, alphacellulose, betacellulose, gammacellulose and lignin. Then these variables

are analyzed further using the Bray-Curtis distance and similarity indices. Afterwards visualized by NMDS (Non-Metric Multidimensional Scaling) ordination method. After knowing the distance and similarity among plots/habitats, clustering is done using UPGMA (Unweighted Pair Group Method with Arithmetic Mean) and K-means based on Bray-Curtis distance and similarity indices. Finally, habitat preferences can be categorized ranging from the very good, good, poor, and very poor categories.

3. FINDINGS AND DISCUSSION

3.1 Habitat Preferences Analysis

Firstly, we are looking forward correlation between physical and chemical characteristics of substrates as *Auricularia delicata* habitat.

Table 1. All measured variables of substrates as *Auricularia delicata* habitat. This table represents characteristics of each plot sampling

Plot	Species	C %	N %	C/N %	Holo %	Alfa %	Gama%	Beta %	Lignin %	Decay	Dtot
D01	<i>Mallotus paniculatus</i>	52,89	1,37	38,60	53,11	33,63	19,48	46,89	42,58	4	2668
D02	<i>Erythrina</i> sp.	55,83	0,86	64,91	43,01	23,07	19,94	56,99	50,84	3	247
D03	<i>Mallotus paniculatus</i>	50,16	2,42	20,72	25,28	16,79	8,49	74,72	46,40	3	703
D04	<i>Mallotus paniculatus</i>	52,38	2,02	25,93	45,75	15,91	29,84	54,25	39,78	4	3018
D05	<i>Macaranga triloba</i>	57,55	0,76	75,72	56,27	23,9	32,37	43,73	25,86	4	1393
D06	<i>Mallotus paniculatus</i>	50,89	1,19	42,76	55,03	33,46	21,57	44,97	37,91	0	55
D07	<i>Podachaenium</i> sp.	49,56	3,33	14,88	64,54	32,72	31,82	35,46	31,98	0	60
D08	<i>Mallotus paniculatus</i>	49,3	1,42	34,71	53,79	27,21	26,58	46,21	27,43	4	953
D09	<i>Macaranga triloba</i>	56,81	0,79	71,91	54,03	25,19	28,84	45,97	45,68	3	264

Table 2. Pearson correlation analysis among variables of substrates as *Auricularia delicata* habitat. The numbers marked with the blue color that mean strong-very strong positive correlation between variables. Meanwhile the numbers marked with thered color that mean strong-very strong negative correlation betweenvariables

	C	N	C/N	Holo	Alfa	Gamma	Beta	Lignin	Decay	Species	Dtot
C		-0,72	0,91	0,07	-0,19	0,27	-0,07	0,20	0,39	0,35	0,06
N	-0,72		-0,88	-0,04	-0,01	-0,05	0,04	-0,11	-0,42	0,16	-0,02
C/N	0,91	-0,88		0,16	-0,01	0,25	-0,16	0,07	0,30	0,27	-0,16
Holo	0,07	-0,04	0,16		0,73	0,80	-1	-0,59	-0,33	0,54	-0,09
Alfa	-0,19	-0,01	-0,01	0,73		0,18	-0,73	-0,27	-0,52	0,21	-0,27
Gamma	0,27	-0,05	0,25	0,80	0,18		-0,80	-0,61	-0,03	0,59	0,09
Beta	-0,07	0,04	-0,16	-1	-0,73	-0,80		0,59	0,33	-0,54	0,09
Lignin	0,20	-0,11	0,07	-0,59	-0,27	-0,61	0,59		0,02	-0,24	-0,06
Decay	0,39	-0,42	0,30	-0,33	-0,52	-0,03	0,33	0,02		-0,34	0,66
Species	0,35	0,16	0,27	0,54	0,21	0,59	-0,54	-0,24	-0,34		-0,43
Dtot	0,06	-0,02	-0,16	-0,09	-0,27	0,09	0,09	-0,06	0,66	-0,43	

Table 2 shows a positive (simultaneous) or negative (inverse) relationship among the variables of habitat preferences of substrates which were overgrown with *Auricularia delicata* based on the Pearson correlation analysis of calculated number from Table 1 The closer the values to +1 or -1, the greater the

correlation between those variables. According to Sugiyono [5], the interpretation of correlation coefficients can be categorized into very low ($\rho = 0.00 - 0.199$), low ($\rho = 0.20 - 0.399$), medium ($\rho = 0.40 - 0.599$), strong ($\rho = 0.60 - 0.799$), and very strong ($\rho = 0.80 - 1,000$). From Table 2 we would focus more on the

correlation of number of fruit bodies production during observation (Dtot) to the other variables. According to **Table 2** a strong correlation with production of *Auricularia delicata* fruit bodies is decay class, which means that the higher the decay class, the more fruit bodies may be produced on the substrates. The correlation analysis is still continued to see the significance between variables through the p value (p value <0.05). If the p value is <0.05, the relationship between these variables can be generalized to all *Auricularia delicata* population, if the p value is > 0.05, the relationship between two variables is not significant.

Table 3 proves that the p value of the correlation between the decay class and the total density of *Auricularia delicata* fruit

Table 3. P values of Pearson Correlation analysis among variables of substrates as *Auricularia delicata* habitat. The numbers marked with the blue color that mean strong (positive)-significant correlation between variables. Meanwhile the numbers marked with the red color that mean strong(negative)-significant correlation between variables

	C	N	C/N	Holo	Alfa	Gamma	Beta	Lignin	Decay	Species	Dtot
C		0,02691 6	0,00060 36	0,84257	0,61846	0,4659	0,84257	0,59319	0,29705	0,34306	0,8767 4
N	0,02		0,00136 32	0,90263	0,97091	0,88486	0,90263	0,75874	0,25298	0,66438	0,9533 9
C/N	0,00060 4	0,00136 3		0,66659	0,97893	0,51537	0,66659	0,84115	0,4324	0,47195	0,6713 5
Holo	0,84257	0,90263	0,66659		0,02482 9	0,00863 3	3,29E- 35	0,08975 5	0,37234	0,13076	0,7987 5
Alfa	0,61846	0,97091	0,97893	0,02482 9		0,62782	0,02482 9	0,46578	0,14571	0,5835	0,4800 8
Gamma	0,4659	0,88486	0,51537	0,00863 3	0,62782		0,00863 3	0,07617 1	0,93484	0,08821	0,8140 9
Beta	0,84257	0,90263	0,66659	3,29E- 35	0,02482 9	0,00863 3		0,08975 5	0,37234	0,13076	0,7987 5
Lignin	0,59319	0,75874	0,84115	0,08975 5	0,46578	0,07617 1	0,08975 5		0,93933	0,52676	0,8600 9
Decay	0,29705	0,25298	0,4324	0,37234	0,14571	0,93484	0,37234	0,93933		0,36936	0,0500 62
Species	0,34306	0,66438	0,47195	0,13076	0,5835	0,08821	0,13076	0,52676	0,36936		0,2364 8
Dtot	0,87674	0,95339	0,67135	0,79875	0,48008	0,81409	0,79875	0,86009	0,05006 2	0,23648	

bodies is more than 0.05, that is 0.050062, which means that there is no significance correlation between these two variables, no causal relationship. This means that strong relationship between these two variables may occur on a particular substrate/plot or period. The correlation between habitat preference variables can also be concluded through the correlation plot in **Figure 2**, which states that if the color of the variable plot gets closer to blue, the correlation becomes stronger and more positive (simultaneous), and if the color of the variable plot gets closer to red, the correlation becomes stronger and negative (inverse). The plot which is crossed means that the correlation between variables is not significant.

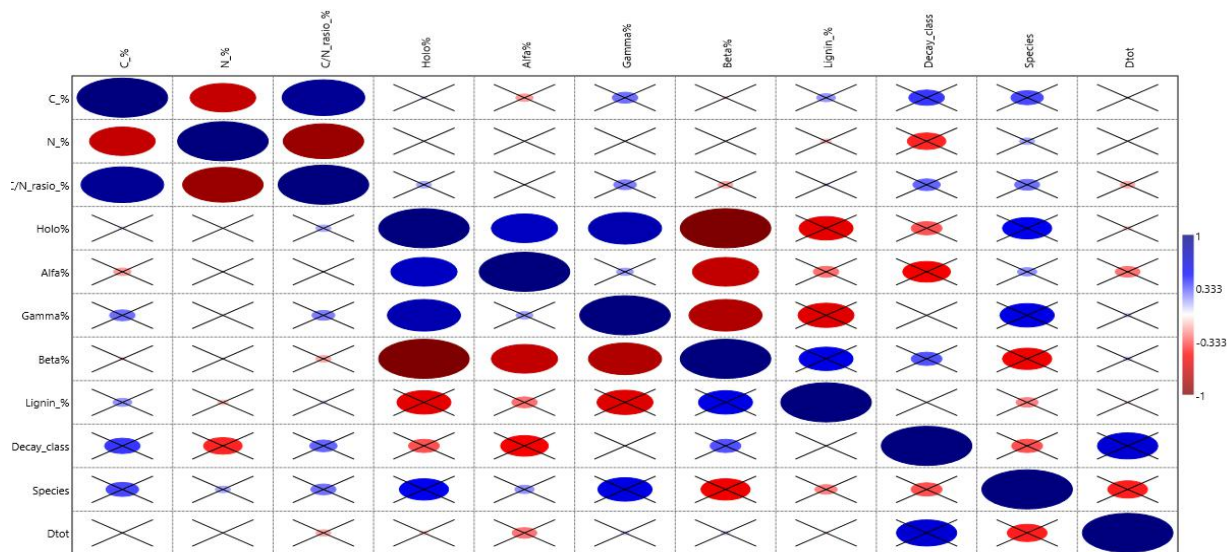


Figure 2. Pearson correlation plot of all measured variables of substrates as *Auricularia delicata* habitat

Analysis of habitat preferences is deeply interpreted through analysis of similarity and distance Bray-Curtis indices to determine how similar habitats of the substrates which overgrown with *Auricularia delicata* fruit bodies.

$$SI = \frac{2W}{(A + B)} \times (100\%)$$

Explanation:

SI : Similarity index

W : The smallest value of parameters measured in the two points / plots that are compared

A : The total value of parameters measured at plot A

B : The total value of parameters measured at plot B

The selection of the Bray-Curtis similarity index is based on the goodness of applying this index to calculate various parameters, whether it be species abundance or physical and chemical factors of various sampling [6]. To get dissimilarity or distance index we have to use an equation $DI = (1 - SI) \times 100\%$, DI (dissimilarity index) and SI (similarity index).

Table 4. Habitat preferences similarity based on Bray-Curtis index. The numbers marked with the blue color mean the highest similarity among plots

	D01	D02	D03	D04	D05	D06	D07	D08	D09
D01		0,293785	0,469798	0,934495	0,708181	0,203075	0,182113	0,58135	0,307021
D02	0,293785		0,627462	0,260902	0,463403	0,701053	0,626877	0,55302	0,944918
D03	0,469798	0,627462		0,435581	0,673723	0,403647	0,384077	0,829393	0,621306
D04	0,934495	0,260902	0,435581		0,654606	0,165235	0,158358	0,530199	0,269208
D05	0,708181	0,463403	0,673723	0,654606		0,311177	0,294957	0,827414	0,497404
D06	0,203075	0,701053	0,403647	0,165235	0,311177		0,887972	0,403175	0,708616
D07	0,182113	0,626877	0,384077	0,158358	0,294957	0,887972		0,382591	0,65494
D08	0,58135	0,55302	0,829393	0,530199	0,827414	0,403175	0,382591		0,583118
D09	0,307021	0,944918	0,621306	0,269208	0,497404	0,708616	0,65494	0,583118	

Table 5. Habitat preferences dissimilarity index based on Bray-Curtis index. The numbers marked with the red color that mean the highest distance among plots

	D01	D02	D03	D04	D05	D06	D07	D08	D09
D01		0,706215	0,530202	0,065505	0,291819	0,796925	0,817887	0,41865	0,692979
D02	0,706215		0,372538	0,739098	0,536597	0,298947	0,373123	0,44698	0,055082
D03	0,530202	0,372538		0,564419	0,326277	0,596353	0,615923	0,170607	0,378694
D04	0,065505	0,739098	0,564419		0,345394	0,834765	0,841642	0,469801	0,730792
D05	0,291819	0,536597	0,326277	0,345394		0,688823	0,705043	0,172586	0,502596
D06	0,796925	0,298947	0,596353	0,834765	0,688823		0,112028	0,596825	0,291384
D07	0,817887	0,373123	0,615923	0,841642	0,705043	0,112028		0,617409	0,34506
D08	0,41865	0,44698	0,170607	0,469801	0,172586	0,596825	0,617409		0,416882
D09	0,692979	0,055082	0,378694	0,730792	0,502596	0,291384	0,34506	0,416882	

From **Table 4** we can see how similar the plots which are represented by the index values, while **Table 5** we can find out among plots that have high or low dissimilarities. We try to interpret plot D01 that is very similar to D04 with the value of 93.44%, and D01 has the largest distance to D06 and D07 with the values of 79.69% and 81.78 %; plot D02 is very similar to D09 with the value 94.91% and D02 has the largest distance to D01 and D04 with the values of 70.62% and 73.90%; plot D03 is very similar to D08 with the value of 82.93% and D03 has the largest distance to D06 and D07 with the values of 59.63% and 61.59%; plot D04 is very similar to D01 with the value of 93.44% and D04 has the largest distance to D06 and D07 with the values of 83.47% and 84.16%; plot D05 is very similar to D08 with the value 82.74% and D05 has the largest distance to D06 and D07

with the values of 68.88% and 70.5%; plot D06 is very similar to D07 with the value 88.79% and D06 has the largest distance to D01 and D04 with the values of 79.69% and 83.47%; plot D07 is very similar to D06 with the value 88.79% and D07 has the largest distance to D01 and D04 with the values of 81.78% and 84.16%; plot D08 is very similar to D03 and D05 with the values of 82.93% and 82.74% and D08 has the largest distance to D06 and D07 with the values of 59.68% and 61.74%; plot D09 is very similar to D02 with the value of 94.91% and D09 has the largest distance to D01 and D04 with the values of 69.29% and 73.07%.

The results of these similarity and dissimilarity data analyses will be very helpful for multidimensional ordination techniques. This ordination is a way to summarize data in the coordination

form. The results of the ordinated data analysis will be presented in the form of a graph that displays the points as the representative of the sampling plot studied. The plots or sampling points are placed with their position directly close to the level of similarity, so that the coordinate points can explain whether they have a clustering pattern or not. In addition, deciding the pattern of group or cluster formation is based on personal considerations which apparently also depend on the researchers's understanding of the habitat conditions of study [7]. Ordination decided to visualize plots coordinates is NMDS (Non-Metric Multidimensional Scaling).

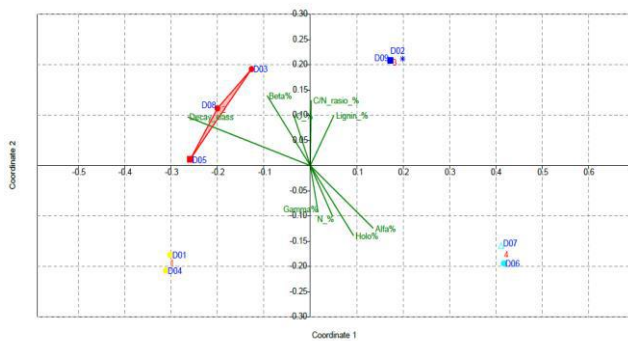


Figure 3. NMDS ordination of all plots based on Bray-Curtis similarity index with abiotic factors imaging (C, N, C/N ratio, lignin, alphacellulose, holocellulose, gammacellulose, betacellulose and decay class). Symbols: •*Mallotus paniculatus*; **Erythrina* sp.; ■*Macaranga triloba*; ▲*Podachaenium* sp

From the result of NMDS ordination graphs in **Figure 3**, it can be seen that there are clustering patterns in each quadrant. In quadrant I there is clustering formation between plot D02 and plot D09; clustering among plot D03, plot D05, and plot D08 in quadrant II; clustering between plot D01 and plot D04 in quadrant III; clustering between plot D06 and plot D07 in quadrant IV. It also can be summarized significance correlation between environmental variables and plot similarities. To ensure how similar and dissimilar among plots, the graph can be represented in **Table 6** and **Table 7** as follows:

Table 6. Plots coordination numbers based on NMDS graph. Each cluster has to be marked with representative color in graph: the blue color for cluster in quadrant I, the red color for cluster in quadrant II, the yellow color for cluster in quadrant III, and the aqua color for cluster in quadrant IV

Name	Coordinate 1	Coordinate 2
D01	-0.30246	-0.17669
D02	0.19916	0.21164
D03	-0.1267	0.19137
D04	-0.31199	-0.20797
D05	-0.2589	0.012553
D06	0.41705	-0.19394
D07	0.41156	-0.15881
D08	-0.20034	0.11341
D09	0.17263	0.20843

Table 7. The environmental variables coordination number based on NMDS graph

Name	Coordinate 1	Coordinate 2
C_ %	-0.1204	0.33621
N_ %	0.16401	-0.34358
C/N_rasio_ %	0.0064486	0.44056
Holo%	0.31738	-0.47228
Alfa%	0.46176	-0.42225
Gamma%	0.056858	-0.3146
Beta%	-0.31738	0.47228
Lignin%	0.17243	0.33739
Decayclass	-0.90053	0.32828

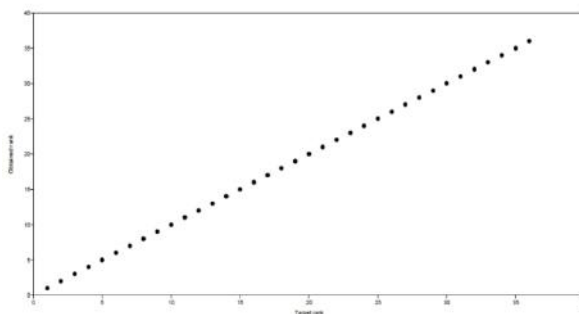


Figure 4. Sheppard plot of NMDS analysis shows that there is no stress in ranking process of the results. Stress value=0

NMDS can make few assumptions about the nature of the data. For example, the principal component analysis assumes linear relationships and reciprocal averaging assumes modal relationships. However, NMDS makes neither of these assumptions, so is well suited for a wide variety of data including environmental variables [8]. The best result is the one that reflects the rank-order of distances in the original dissimilarity and similarity calculation. The statistics that reflects how well the configuration represents the distances is called 'stress'. A smaller stress value means that a better NMDS ordination is calculated. **Figure 4** shows final stress values which should ideally be smaller than 10% and not larger than 30% [9].

In NMDS visualization above we only made a summary of the plots which are clustered, but unable to measure which cluster is the best and the worst and how many clusters really there are. To solve this distraction, it is recommended to do an analysis of the ecological distance by clustering methods. Clusters are formed with hierarchical clustering methods with the UPGMA ecological distance evaluation based on similarity Bray-Curtis index. Hierarchical clustering methods do not only cluster sites by species composition on each site, but it can also cluster the various clusters from various parameters that were formed earlier in the clustering process. Thus, hierarchical clustering methods provide a hierarchy for the similarity of sites [9]. The results of a hierarchical clustering can be used to classify plots as *Auricularia delicata* into groups. The classification is defined by choosing a certain distance level, or by choosing a fixed

number of clusters as an alternative way of using non-hierarchical clustering methods such as K-means.

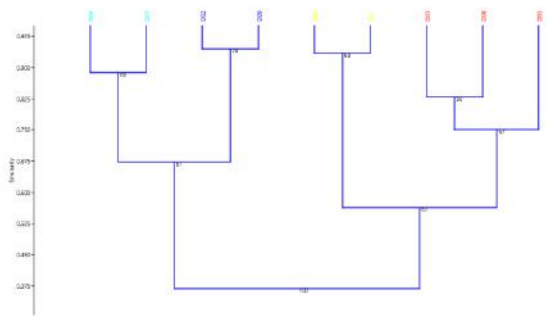


Figure 5. Clustering analysis result using hierarchical clustering (UPGMA method) based on Bray-Curtis similarity index. The plots are classified into 5 clusters, but from NMDS gives 4 representative clusters. N Bootstraps = 1000; Cophenetic correlation = 0, 8458

Table 8. Clustering analysis result using non hierarchical clustering (K-means) that classify plots into 4 groups when we choose 4 as fixed number clusters

Item	Cluster	Category
D01	1	Very good
D02	3	Poor
D03	2	Good
D04	1	Very good
D05	2	Good
D06	4	Very poor
D07	4	Very poor
D08	2	Good
D09	3	Poor

Based on the value of cophenetic correlation that classical dendrogram in **Figure 5** is very good and is a representative of the formed clusters. The closer value to 1 the more representative the relationship of the closeness of cluster [10]. From the results of the clustering in **Table 8** we can conclude after approaching the method that there are four habitat categories of *Auricularia delicata* in Bingungan forest, The **Very Good** group consists of plots D01 and D04; The **Good** group consists of plots D03, D05, and D08; The **Poor** group consists of plots D02 and D09; The **Very Poor** group consists of plots D06 and D07.

3.2 Habitat Characteristics and Fungal Strategies

Most of Basidiomycota group fungi can be categorized into white-rot fungi which prefer degrading lignin in the down woods to cellulose; the texture of down woods after being decayed would be fibrous and the color would be bleached [11]. *Auricularia delicata* produces a white rot on dead and decaying wood. It produces class II heme peroxidases such as lignin peroxidases LiP and manganese peroxidases MnP. dye-decolorizing peroxidases with manganese-independent

peroxidases activities have been demonstrated [12]. In fact the succession of the fruiting process of white-rot macrofungi was able to occur in all decay classes [13]. We found *Auricularia delicata* macrofungi were thriving on 3 and 4 decay classes at 3 species. They are *Mallotus paniculatus*, *Macaranga triloba*, and *Erythrina* sp. also as parasite at some tree species, like *Podachaeium* sp. and *Mallotus paniculatus*. Previous studies showed *Auricularia delicata* associated and form fruit bodies at rubber plantation (*Hevea brasiliensis*) and oak trees (*Quercus griffithii*) [14].

Auricularia delicata possibly can be found growing on fallen trees trunks or branches, and occasionally on the moss of living trees [15] and it is primarily found in wet forest [16]. In Bingungan Forest, most of all substrates as *Auricularia delicata* habitat are trunks which after being colonized some macrofungi not only *A. delicata* (some agarics and *Xylaria polymorpha* have been found), the trunks texture would be soft and fibrous, because of much lignin loss. Another case, evidently *A. delicata* is able as epiphyte organism (living on the surfaces of plants) on primary branches of *Mallotus paniculatus* and a trunk of *Podachaeium* sp. but their hosts are still alive. This fungal strategy is called biotroph which in the latter case one might be expected that though local digestion of host tissue may be necessary for penetration or establishment of the pathogen, only simple nutrients would be removed from the host [17]. This phenomena may explain the reason why that living tree (D06 and D07) belongs to the very poor category habitat for epiphyte *Auricularia delicata*; some show special adaptations to the plant surface, which is a challenging environment, being dry, waxy and exposed to direct sunlight and the natural response of plants to fungal pathogens is to produce defensive plant hormones such as salicylic acid, jasmonates, and ethylene [17][3]. So epiphytes are often pigmented (particularly melanised) to protect them from UV radiation, and the energy is most using in terms of survival. Thus, fruit bodies of *A. delicata* are not many to be produced.

If we take a look at the very good category habitat for *Auricularia delicata* those are D01 and D04 to produce fruit bodies, we will realize there are some similar characteristics of tree species (*Mallotus paniculatus*), chemical contents, decay class, and finally taking effect to fruit bodies production. Their characteristics is also close D05 (*Macaranga triloba*), but plot D05 has high C/N ratio about 75.7%. By increasing the C/N ratio of wood materials, it may reduce the ability of saprotrophic ormycorrhizal fungi to decompose the substrates [18].

4. CONCLUSION

We have determined successfully which the best substrate as *Auricularia delicata* in Bingungan Forest, Turgo Natural Forest Conservation Area based on ecological informatics approach that we use; from Pearson correlation, similarity and dissimilarity indices, ordination, and clustering methods. We suggest to use this approach to analyze another macrofungi habitat the next forward. Choosing ordination and clustering methods depends on particular conditions and the researchers' consideration.

5. ACKNOWLEDGMENTS

Thanks to the best partners who involved in this research on the same research team, Suryo Arif Setyawan and Junita Kurniawati.

6. REFERENCES

- [1] Prasetya, D., et al. 2017. *Eksplorasi Keanekaragaman Makrofungi Edible dan Non-Edible di Kawasan Hutan Hujan Tropis Bukit Turgo Merapi*. Research Report of PKM DIKTI-2017, Yogyakarta State University (Unpublished).
- [2] Molina R., Pilz., D., Smith J., Dunham S., . Dreisbach, T., O'dell T., and Castellano M. 2001. *Conservation and Management of Forest Fungi in The Pacific Northwestern United States: An Integrated Ecosystem Approach*. Department of Agriculture United States, Forest Service, Pacific Northwest Research Station, Portland, Oregon, US.
- [3] Dighton, J. 2016. *Fungi in Ecosystem Processes*. Second Edition. CRC press, Taylor & Francis Group, US.
- [4] Pilz D., and Molina R. 1996. *Managing Forest Ecosystem to Conserve Fungus Diversity and Sustain Wild Mushroom Harvests*. Department of Agriculture United States, Forest Service, Pacific Northwest Research Station, Portland, Oregon, U.S.
- [5] Sugiyono. 2007. *Statistik untuk Penelitian*. Alfabeta, Bandung.
- [6] Barbour, M.G., Burk, J.H., and Pilts, W.D. 1987. *Terrestrial Plant Ecology*. Second Edition. The Benyamin Cummings Publ., Co., Inc., California.
- [7] Djohan, T.S. 2016. *Petunjuk Praktikum Ekologi Lanjut*. Universitas Gadjah Mada, Yogyakarta, Indonesia.
- [8] Holland, S.M. 2008. *Non-Metric Multidimensional Scalling*. Department of Geology, University of Georgia, Athens.
- [9] Kindt, R. and Coe, R. 2005. *Tree Diversity Analysis: A Manual and Software for Common Statistical Methods for Ecological and Biodiversity Studies*. World Agroforestry Centre, Nairobi, Kenya.
- [10] Hammer, O. 2011. *Ecological Cluster Analysis with Past*. Natural History Museum, University of Oslo.
- [11] Srivastava, S., Kumar, R., and Singh, V.P. 2013. *Wood Decaying Fungi*. LAP Lambert Academic Publishing, New Delhi, India.
- [12] Floudas, D., et al. 2012. The Paleozoic Origin of Enzymatic Lignin Decomposition Reconstructed from 31 Fungal Genomes. *Science*. 336, 1715-1719.
- [13] Rajala, T. et al. 2012. Fungal Community Dynamics in Relation to Substrate Quality of Decaying Norway Spruce (*Picea abies* [L.] Karst.) Logs in Boreal Forests. *FEMS Microbiol. Ecol.* 81, 2 (Aug, 2012), 494-505.
- [14] Xing-Hong, W., Chaobin, Z., Pedro, F. and Changhe, Z. 2016. Screening and Characterization of *Auricularia delicata* Strain for Mushroom Production under Tropical Temperature Conditions to Make Use of Rubberwood Sawdust. *Research Journal of Biotechnology*. 11, 11 (Nov, 2016), 26-37.
- [15] Mata, M. 1999. *Macrohongos de Costa Rica*. Instituto Nacional de Biodiversidad (INBio), Santo Domingo, Heredia, Costa Rica.
- [16] Museo Nacional de Costa Rica. 2013. *Auricularia delicata*. In: *Ecobiosis 2013*. National Biodiversity Portal. Downloaded on 30 September 2018. <http://ecobiosis.museocostarica.go.cr/especies/ficha/1/3404>
- [17] Moore, D., Robson, G.D. and Trinci, A.P.J. 2011. *21st Century Guidebook to Fungi*. Cambridge University Press, UK.
- [18] Hätenschwiler, S. and Vitousek, P.M. 2000. The role of polyphenols in terrestrial ecosystem nutrient cycling. *TREE* 15, 238–243.

Author Index

A		H	
A. G. Zazybin	86	Hardik Joshi	58
A. Welivita	28	Hemant Sharma	48
A. Ye. Malmakova	86	J	
Agustina E. Susanti	91	Jianming Xie	22
Aleksandr Mikhalev	97	K	
Amjad Rehman	1	Khurram Ejaz	1
Amrita Jha	63	Kristina Kryanova	97
Anatolii Greben'kov	97	L	
Andrii Iakovliev	67	Le Sy Vinh	36
Anjana Umapathy	17	Liu Yaping	75
Anusha Sreenivasan	17	Liye Mei	12
Atul Bhaskar	67	M	
Aussama Soontrunnarudrungsri	82	Malinee Sriariyanun	82
B		Mani Baskaran	8
B Narasinga Rao	17	Miaomiao Jiang	22
Brajesh Kumar Jha	53, 58, 63	Mohd Shafy Mohd Rahim	1
C		N	
C. S. Suchand Sandeep	8	N. U. Kystaubayeva	86
Chaowei Cheng	12	Nadim Rana	1
Chu Jie	75	Natalia Muratova	97
D		Nguyen Thi Phuong Thao	36
D. A. Meedeniya	28	O	
Devanshi D. Dave	53	Oleg Milovanov	97
Divya S. Nairy	17	P	
Dmitry Klimov	97	Patchanee Yasurin	82
Dwiki Prasetya	102	Preeyapa Sripromma	82
E		Puspita Lisdiyanti	91
Emiliya Kalamiyets	75	G	
G		Guishan Zhang	
Guishan Zhang	43		

Q		U	
Qichao Yu	22	Usama Ijaz Bajwa	1
R		V	
Rafail Isemin	97	V. K. Yu	86
Rungnattakan Ploenkutham	82	Vadakke Matham Murukeshan	8
S		Vadim Kogh-Tatarenko	
S Natarajan	17		97
S. A. P. A. Rukshan	28	W	
Sarangapani Sreelatha	8	W. Mangunwardoyo	91
Shanti Ratnakomala	91	Wu Peng	75
Shiping Liu	22	X	
Srinandan Dasmahapatra	67	Xianhua Dai	43
Suksan Amornraksa	82	Xiaopeng Guo	12
Suvaluk Asavasanti	82	Xun Jie Jeessmond Hong	8
T		Y	
T. E. Li	86	Yuri Teplitskii	97
Tien Aminatun	102	Z	
Tin Aung	8	Zhao Bo	75